UNIVERSITÀ DEGLI STUDI DI CATANIA

DIPARTIMENTO DI SCIENZE CHIMICHE

DOTTORATO IN SCIENZA DEI MATERIALI E NANOTECNOLOGIE

Antonio Abbadessa

Hybrid Nano-systems Based on PEGylate Porphyrins: Synthesis, Characterization and Theranostic Applications

---

PhD Thesis

Tutor: **Chiar.mo Prof. Placido G. Mineo**

ANNO ACCADEMICO 2017-2018

Summary

Preface

"*A friend of mine (Albert R. Hibbs) suggests a very interesting possibility for relatively small machines. He says that, although it is a very wild idea, it would be interesting in surgery if you could swallow the surgeon. You put the mechanical surgeon inside the blood vessel and it goes into the heart and "looks" around (Of course the information has to be fed out). It finds out which valve is the faulty one and take a little knife and slice it out. Other small machines might be permanently incorporated in the body to assist some inadequately-functioning organ. Now come the interesting question: How do we make such a tiny mechanism? I leave that to you…*"[1]

Figure 1.1.1: Richard Feynman

This quote comes from the conference "***There's a Plenty of Room at the Bottom***" held by physicist Richard Feynman (***Fig. 1.1.1***) at a meeting of the American physical society in Caltech on December 29, 1959. Feynman considered the possibility of direct manipulation of individual atoms as a more powerful option in synthetic chemistry than those used at the moment. Feynman gave a visionary talk on "*smallness*" and how miniaturization would lead to new technical applications. He was already talking about nanotechnology and even a pre-figured "*nanomedicine*" when he quoted, as shown above, one of his colleagues. He was probably thinking of a "mini-robot" surgeon, but the idea of having a doctor inside the body is an excellent metaphor for the use of medical nanosystems for evaluation and/or diagnostic treatment. Over the last twenty years, the list of applications of nanomaterials in biology, chemistry, and medicine has increased exponentially. The visionary discourse of Feynman can be considered as the beginning of nanotechnological progress that, in our days, translates into applications in many fields of nanometric devices.

With particular attention to the medical field, the birth and use of nanometric systems, such as nanoparticles, have helped develop a new branch of biomedicine: the theranostics.

This term indicates all those systems through which diagnosis and therapy can be carried out simultaneously, something that resembles the surgeon imagined by Feynman.

[1] *Feynman RP.* http://calteches.library.caltech.edu/1976/1/1960Bottom.pdf

Introduction

Theranostics

In a society in which technological progress seems to know no boundaries, understanding the functioning of the human body on a molecular scale and the ability to intervene in a pre-symptomatic, acute or chronic phase of a disease, are the focal points that biomedical field aims to implement. In the scientific imaginary, the goal is to create highly reliable and sensitive recognition systems, as well as being able to transport and administer drugs or, at best, to be therapeutic systems themselves. This is the so-called principle of the three F "find, fight and follow" which translates into the concepts of early diagnosis, therapy and control of the therapy itself, also known as Theranostics.

John Funkhouser, the Chief Executive Officer of PharmaNetics, used the term “Theranostics” for the first time in 1998 as “the ability to affect therapy or treatment of a disease state”. Accordingly, theranostics as a treatment strategy for individual patients encompasses a wide range of subjects, including personalized medicine, pharmacogenomics, and molecular imaging, to develop an efficient, new targeted therapy, and to optimize drug selection via a better molecular understanding. Furthermore, theranostics aims to monitor the response to the treatment, to increase drug efficacy and safety, and to eliminate the unnecessary treatment of patients, resulting in significant cost savings for the overall healthcare system.[1]

Theranostics has recently become one of the keywords in cancer research,[2-15] based on the assumption that if cancer growth can be hindered during the diagnosis phase, subsequent treatment would be much simpler because cancer growth is delayed or reduced. Because the fast-growing cancer tissues form leaky vasculatures around themselves,[16, 17] researchers can use the enhanced permeability and retention (EPR) effect[16, 18-23] for effective delivery of anticancer agents. Thus, chemical research efforts pertaining to oncology have mainly focused on the synthesis of anticancer drugs and design of vehicles (e.g., polymer particles, liposomes), in which many anticancer drugs can be loaded to be delivered specifically to cancer tissues.

In the early phase of theranostics development, before 2005, an imaging function was simply added to these delivery vehicles loaded with therapeutic agents by attacking image contrast agents for use in methods such as computerized tomography (computed tomography), positron emission tomography (PET) and magnetic resonance imaging (MRI).

Cancer research has undergone a major change in recent decades. Cancer is no longer seen from a reductionist point,[19] where the focus is only on the tumor cells and the genes they contain. As outlined by Prof. Robert A. Weinberg,[24, 25] cancer cells interact with a complex mixture of surrounding immune cells, endothelial cells, neovascularization, and fibroblasts. Furthermore, cancer can acquire various survival strategies such as self-sufficiency in growth signals, evasion of apoptosis, development of insensitivity to antigrowth signals, sustained angiogenesis, metastasis and unlimited replication, which are considered the six distinctive signs of cancer.[28 29] It is well known that cancer shows high resistance in very adverse conditions. Even with chemotherapy and intensive radiotherapy, the complete elimination of cancer is an apparent goal; in many cases cancer, that has acquired resistance to the previous treatments, recurs.[26-28] This is because cancer can adapt quickly and to survive through a series of mutations. Therefore, it is possible to completely cure cancer by simply combining a therapeutic drug with an imaging agent. Various nanomaterials have been developed in attempts to addressing these problems. Nanomedicines are therapies based on nanoparticles made up of a variety of organic or inorganic nanomaterials for the treatment, diagnosis, monitoring and control of biological systems. Nanomaterials can be loaded with multiple types of drugs or possess themselves more intrinsic antitumor therapeutic skills. They can target surface-bound molecules on tumor cells and be further loaded with contrast agents for multimode images. The formulation of theranostic nanoparticles allows us to monitor the response to treatment and increase the efficacy and safety of the drug.[29, 30] Recently, new progress has been reported in the bio-application of nanomaterials. It includes significant improvement of MRI contrast using superparamagnetic nanoparticles with high magnetization values,[31-35] photoacoustic imaging with carbon nanotubes (CNTs),[30, 32-39] the photothermal effect of CNTs and other carbon nanomaterials such as graphene,[40-42] the photothermal effect of polymer nanoparticles and metallic nanoparticles (Plasmonic Photothermal Effect),[43, 44] nanoparticle-based effective gene-delivery vehicles,[45-58] nanocomposites applicable to multiple therapies,[59-62] elucidation of the removal process of nanomaterials from the body,[63-65] activatable therapeutic nanomaterials,[62, 64, 66-91] and a better understanding of nanotoxicology.[92-97] The most encouraging aspect of these new developments is that some of the current research efforts have started to implement the latest concepts of cancer, that is, theranostics is evolving to incorporate aspects of both molecular imaging [98-103] as well as personalized cancer therapy.

Nanomaterials started to be used extensively in the development of theranostic systems from 2006 and, by adopting Ferrari's classification, a theranostic nanoparticle can be dissected into

at least three components: biomedical payload, carrier, and surface modifier, depending on both their roles and locations, as shown in ***Figure 2.1.1***.

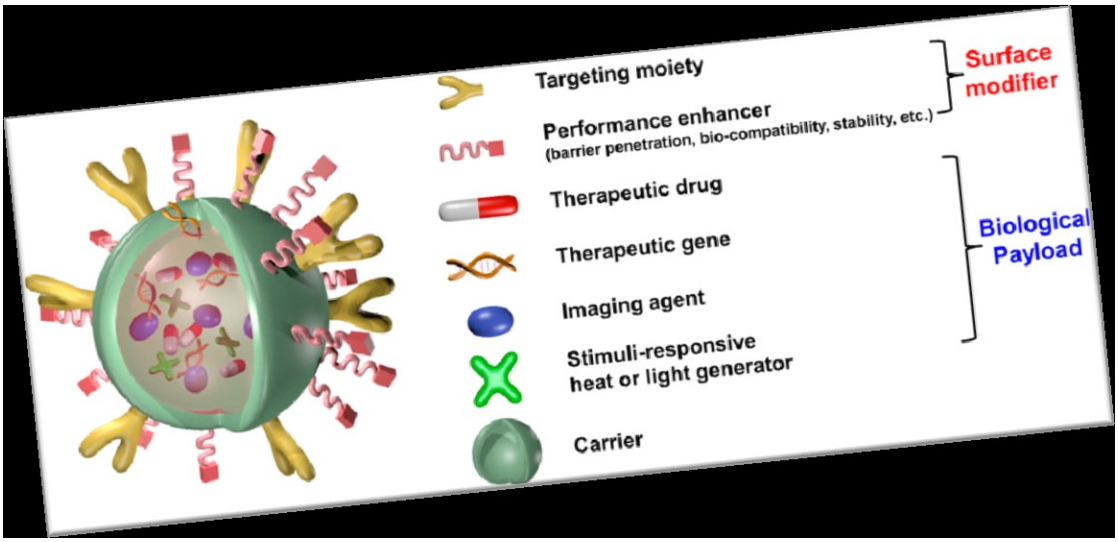

***Figure 2.1.1*:** Schematic illustration of multifunctional nanoparticles.

Biomedical "payloads" include imaging agents (e.g., organic dyes, quantum dots [QDs], upconversion particles [UCNPs], MRI contrast agents, CT contrast agents, etc.) and therapeutic agents (anticancer drugs, DNA, small interfering RNA [siRNA], proteins, hyperthermia-inducing nanoparticles, ROS-generating agents, etc.). The carrier should provide sufficient physical protection for the biological payloads under physiological conditions during delivery to the desired target site. Several organic and inorganic vectors have been developed. The carrier might be designed to become cancer-specifically disintegrated for better imaging or therapeutic efficacies. Finally, modifiers are attached to the surface of the carrier, which provide theranostic nanomaterials with additional properties, e.g., long circulation time, barrier-penetrating ability, and target-specific binding ability. The components for generating a theranostic nanoparticle along with material classifications and functions are listed in ***Table 2.1.2***.[104]

component	material	function
biomedical payload	imaging agents for optical, CT, MRI, PET, ultrasonic imaging (organic dye, QDs, UCNPs, magnetic materials, metal nanoparticles with SPR, CNT)	imaging enhancement
	therapeutic agents (anticancer drugs, DNA, siRNA, hyperthermal/photodynamic materials)	cancer cell death induction, gene up/downregulation
carrier	organic (lipid, natural/synthetic polymers)	monofunctional (protection of payloads, controlled release of drug/gene, biocompatibility, stimuli responsiveness)
	inorganic (hollow metal nanoparticles, hollow metal oxide nanoparticles, carbon nanostructures, porous Si or SiO_2 nanoparticles)	multifunctional (imaging ability added to above functions)
surface modifier	antibody	molecular imaging
	aptamer	target specific delivery
	peptide/protein	uptake enhancement
	small molecules	penetration of barrier
	charge-balancing molecules	signaling transduction
		stimuli responsiveness

Table 2.1.2: Material used in multifunctional nanoparticles.

Following the modern lines of development in theranostic field, the following doctoral project aims to synthesize new nanosystems based on metallic nanoparticles, such as gold and silver, to be used either singly in simpler systems, or coupled with magnetic systems, such as magnetite or maghemite, in order to obtain more complex structures like the core@shell type. In both cases, the nanoparticles systems will be functionalized with PEGylate porphyrin derivatives that would allow the final system to obtain: solubility in aqueous environment, penetration into the cell membranes and stealth-like properties towards the immune system.
These properties are conferred by the chains of polyethyleneglycol, linked covalently to the porphyrin core. Thanks to the fluorescence properties of these dyes, it is possible to reveal the system when it is inside the cells, and to give photo-cytotoxic characteristics, because the porphyrin ring is a photosensitizing agent: it is able to catalyze the singlet oxygen formation reaction (which is a cytotoxic species) if irradiated with a light of suitable wavelength.
Therefore, the project aims to synthesize a new device with assorted designs and having multiple properties usable in the theranostic field. Such properties are provided not only by the merging of several components but also by the reduced dimensions of the final systems.
Following will be shown in detail the unique and fascinating properties of the porphyrins and of the metallic and magnetic nanoparticles, which have led modern research to focus almost exclusively on their development and application in the theranostic field, and that have launched the present PhD project.

[1] Xie, H. G.; Frueh, F. W. Pers. Med. 2005, 2, 325
[2] Bardhan, R.; Lal, S.; Joshi, A.; Halas, N. J. Acc. Chem. Res. 2011, 44, 936.
[3] Cole, A. J.; Yang, V. C.; David, A. E. Trends Biotechnol. 2011, 29, 323.
[4] Davis, M. E.; Chen, Z. G.; Shin, D. M. Nat. Rev. Drug Discovery 2008, 7, 771.
[5] Grodzinski, P. Mol. Pharmaceutics 2009, 6, 1263.
[6] Janib, S. M.; Moses, A. S.; MacKay, J. A. Adv. Drug Delivery Rev. 2010, 62, 1052.
[7] Kelkar, S. S.; Reineke, T. M. Bioconjugate Chem. 2011, 22, 1879.
[8] Kievit, F. M.; Zhang, M. Adv. Mater. 2011, 23, H217.
[9] Lammers, T.; Aime, S.; Hennink, W. E.; Storm, G.; Kiessling, F. Acc. Chem. Res. 2011, 44, 1029.
[10] Minelli, C.; Lowe, S. B.; Stevens, M. M. Small 2010, 6, 2336.
[11] Park, K.; Lee, S.; Kang, E.; Kim, K.; Choi, K.; Kwon, I. C. Adv. Funct. Mater. 2009, 19, 1553.
[12] Petak, I.; Schwab, R.; Orfi, L.; Kopper, L.; Keri, G. Nat. Rev. Drug Discovery 2010, 9, 523.
[13] Riehemann, K.; Schneider, S. W.; Luger, T. A.; Godin, B.; Ferrari, M.; Fuchs, H. Angew. Chem., Int. Ed. 2009, 48, 872.
[14] Xie, J.; Lee, S.; Chen, X. Adv. Drug Delivery Rev. 2010, 62, 1064.
[15] Yezhelyev, M.; Gao, X.; Xing, Y.; Alhajj, A.; Nie, S.; Oregan, R. Lancet Oncol. 2006, 7, 657
[16] Ferrari, M. Nat. Rev. Cancer 2005, 5, 161.
[17] Iyer, A. K.; Khaled, G.; Fang, J.; Maeda, H. Drug Discovery Today 2006, 11, 812.
[18] Maeda, H. Bioconjugate Chem. 2010, 21, 797.
[19] Maeda, H. Adv. Enzyme Regul. 2001, 41, 189.
[20] Maeda, H.; Bharate, G. Y.; Daruwalla, J. Eur. J. Pharm. Biopharm. 2009, 71, 409.
[21] Moorthi, C.; Manavalan, R.; Kathiresan, K. J. Pharm. Pharm. Sci. 2011, 14, 67.
[22] Tanaka, T.; Shiramoto, S.; Miyashita, M.; Fujishima, Y.; Kaneo, Y. Int. J. Pharm. 2004, 277, 39.
[23] Torchilin, V. Adv. Drug Delivery Rev. 2011, 63, 131
[24] Hanahan, D.; Weinberg, R. A. Cell 2000, 100, 57.
[25] Hanahan, D.; Weinberg, R. A. Cell 2011, 144, 646
[26] McKnight, J. A. Clin. Tech. Small. Anim. Pract. 2003, 18, 67.
[27] Steinherz, L. J.; Steinherz, P. G.; Tan, C. T. C.; Heller, G.; Murphy, M. L. J. Am. Med. Assoc. 2000, 6, 15.
[28] Zadik, Y.; Vainstein, V.; Heling, I.; Neuman, T.; Drucker, S.; Elad, S. J. Endocrinol. 2010, 36, 1588
[29] Lee, D.-E.; Koo, H.; Sun, I.-C.; Ryu, J. H.; Kim, K.; Kwon, I. C. Chem. Soc. Rev. 2012, 41, 2656.
[30] Lee, D. Y.; Li, K. C. P. Am. J. Roentgenol 2011, 197, 318
[31] Dong, W.; Li, Y.; Niu, D.; Ma, Z.; Gu, J.; Chen, Y.; Zhao, W.; Liu, X.; Liu, C.; Shi, J. Adv. Mater. 2011, 23, 5392.
[32] Ge, J.; Hu, Y.; Biasini, M.; Beyermann, W. P.; Yin, Y. Angew. Chem., Int. Ed. 2007, 46, 4342.
[33] Lee, J. H.; Huh, Y. M.; Jun, Y.-W.; Seo, J. W.; Jang, J. T.; Song, H. T.; Kim, S.; Cho, E. J.; Yoon, H. G.; Suh, J. S.; Cheon, J. Nat. Med. 2007, 13, 95.
[34] Lee, J-H.;Jang,J.-T.;Choi,J.-S.;Moon,S.H.;Noh,S.-H.;Kim, J.- W.; Kim, J.-G.; Kim, I.-S.; Park, K. I.; Cheon, J. Nat. Nanotechnol. 2011, 6, 418.
[35] Tadic, M.; Kusigerski, V.; Markovic´, D.; Panjan, M.; Milos´ evic˘, I.;´Spasojevic, V.´ J. Alloys Compd. 2012, 525, 28
[36] Hong, H.; Gao, T.; Cai, W. Nano Today 2009, 4, 252.
[37] Liu, Z.; Cai, W.; He, L.; Nakayama, N.; Chen, K.; Sun, X.; Chen, X.; Dai, H. Nat. Nanotechnol. 2007, 2, 47.
[38] Liu, Z.; Sun, X.; Nakayama-Ratchford, N.; Dai, H. ACS Nano 2007, 1, 50.
[39] Lu, F.; Gu, L.; Meziani, M. J.; Wang, X.; Luo, P. G.; Veca, L. M.; Cao, L.; Sun, Y.-P. Adv. Mater. 2009, 21, 139
[40] Ali-Boucetta, H.; Al-Jamal, K. T.; McCarthy, D.; Prato, M.; Bianco, A.; Kostarelos, K. Chem. Commun. 2008, 4, 459.
[41] Bhirde, A. A.; Patel, V.; Gavard, J.; Zhang, G.; Sousa, A. A.; Masedunskas, A.; Leapman, R. D.; Weigert, R.; Gutkind, J.S.; Rusling, J. F. ACS Nano 2009, 3, 307.
[42] Huang, X.; Yin, Z.; Wu, S.; Qi, X.; He, Q.; Zhang, Q.; Yan, Q.; Boey, F.; Zhang, H. Small 2011, 7, 1876.
[43] Yang, J.;Choi,J.;Bang,D.;Kim,E.;Lim,E.K.;Park,H.;Suh,J.S.; Lee, K.; Yoo, K. H.; Kim, E. K.; Huh, Y. M.; Haam, S. Angew. Chem., Int. Ed. 2011, 50, 441,
[44] X. Huang, M. A. El-Sayed, J. Adv. Res., 2010, 1, 13–28. X. Huang, M. A. El-Sayed, Alexandria Med. J., 2011, 47, 1–9.]
[45] Akinc, A.; Thomas, M.; Klibanov, A. M.; Langer, R. J. Gene Med. 2005, 7, 657.
[46] Chang,R.S.;Suh,M.S.;Kim,S.;Shim,G.;Lee,S.;Han,S.S.;Lee, K.E.; Jeon,H.;Choi, H. G.; Choi, Y.;Kim, C.W.; Oh, Y. K. Biomaterials 2011, 32, 9785.
[47] Chen, J.; Tian, H.; Guo, Z.; Xia, J.; Kano, A.; Maruyama, A.; Jing, X.; Chen, X. Macromol. Biosci. 2009, 9, 1247.
[48] Dong, H.; Ding, L.; Yan, F.; Ji, H.; Ju, H. Biomaterials 2011, 32, 3875.

[49] Kim, T. W.; Chung, H.; Kwon, I. C.; Sung, H. C.; Shin, B. C.; Jeong, S. Y. Int. J. Pharm. 2005, 295, 35.
[50] Lee, J. H.; Lee, K.; Moon, S. H.; Lee, Y.; Park, T. G.; Cheon, J. Angew. Chem., Int. Ed. 2009, 48, 4174.
[51] Lee, M.-Y.; Park, S.-J.; Park, K.; Kim, K. S.; Lee, H.; Hahn, S. K. ACS Nano 2011, 5, 6138.
[52] Lim, E.-K.; Yang, J.; Suh, J.-S.; Huh, Y.-M.; Haam, S. J. Mater. Chem. 2009, 19, 8958.
[53] Lv, H.; Zhang, S.; Wang, B.; Cui, S.; Yan, J. J. Controlled Release 2006, 114, 100.
[54] McIntosh, C. M.; Esposito, E. A.; Boal, A. K.; Simard, J. M.; Martin, C. T.; Rotell, V. M. J. Am. Chem. Soc. 2001, 123, 7626.
[55] Shim,G.;Han, S.E.;Yu, Y.H.;Lee,S.; Lee,H.Y.;Kim,K.;Kwon, I. C.; Park, T. G.; Kim, Y. B.; Choi, Y. S.; Kim, C. W.; Oh, Y. K. J. Controlled Release 2011, 155, 60.
[56] Stobiecka, M.; Hepel, M. Biomaterials 2011, 32, 3312.
[57] Yezhelyev, M. V.; Qi, L.; O'Regan, R. M.; Nie, S.; Gao, X. J. Am. Chem. Soc. 2008, 130, 9006.
[58] Zhang, P.;Yang,J.;Li,W.;Wang,W.;Liu,C.;Griffith,M.;Liu,W. J. Mater. Chem. 2011, 21, 7755.]
[59] Yang, J.; Lee, J.; Kang, J.; Oh, S. J.; Ko, H.-J.; Son, J.-H.; Lee, K.; Suh, J.-S.; Huh, Y.-M.; Haam, S. Adv. Mater. 2009, 21, 4339.
[60] Kim, E.; Jung, Y.; Choi, H.; Yang, J.; Suh, J. S.; Huh, Y. M.; Kim, K.; Haam, S. Biomaterials 2010, 31, 4592.
[61] Lim, E. K.; Huh, Y. M.; Yang, J.; Lee, K.; Suh, J. S.; Haam, S. Adv. Mater. 2011, 23, 2436.
[62] Yang,J.;Lee,C.H.;Ko,H.J.;Suh,J.S.;Yoon,H.G.;Lee,K.;Huh, Y. M.; Haam, S. Angew. Chem., Int. Ed. 2007, 46, 8836
[63] Fukumorii, Y.; Ichkawa, H. Adv. Powder Technol. 2006, 17, 1.
[64] Sharma, P.; Brown, S.; Walter, G.; Santra, S.; Moudgil, B. Adv. Colloid Interface Sci. 2006, 123−126, 471.
[65] Rösler, A.; Vandermeulen, G. W. M.; Klok, H.-A. Adv. Drug. Delivery Rev. 2001, 53, 95]
[66] Kim, T.; Cho, E. J.; Chae, Y.; Kim, M.; Oh, A.; Jin, J.; Lee, E. S.; Baik, H.; Haam, S.; Suh, J. S.; Huh, Y. M.; Lee, K. Angew. Chem., Int. Ed. 2011, 50, 10589.
[67] Yang, X.; Grailer, J. J.; Pilla, S.; Steeber, D. A.; Gong, S. Bioconjugate Chem. 2010, 21, 496.
[68] Min, K. H.; Kim, J. H.; Bae, S. M.; Shin, H.; Kim, M. S.; Park, S.; Lee, H.; Park, R.W.; Kim, I. S.; Kim, K.; Kwon, I.C.; Jeong, S.Y.; Lee,D. S. J. Controlled Release 2010, 144, 259.
[69] Walker, G. F.; Fella, C.; Pelisek, J.; Fahrmeir, J.; Boeckle, S.; Ogris, M.; Wagner, E. Mol. Ther. 2005, 11, 418.
[70] Schmaljohann, D. Adv. Drug Delivery Rev. 2006, 58, 1655. (87) Kim, J.-H.; Lee, T. R. Chem. Mater. 2004, 16, 3647.
[71] Shuhendler, A. J.; Staruch, R.; Oakden, W.; Gordijo, C. R.; Rauth, A. M.; Stanisz, G. J.; Chopra, R.; Wu, X. Y. J. Controlled Release 2012, 157, 478.
[72] Sershen, S. R.; Westcott, S. L.; Halas, N. J.; West, J. L. J. Biomed. Mater. Res. 2000, 51, 293.
[73] de Smet, M.; Langereis, S.; van den Bosch, S.; Grull, H. J. Controlled Release 2010, 143, 120.
[74] Oishi, M.; Tamura, A.; Nakamura, T.; Nagasaki, Y. Adv. Funct. Mater. 2009, 19, 827. (94) Yan, F.; Kopelman, R. Photochem. Photobiol. 2003, 78, 587.
[75] Urano, Y.; Asanuma, D.; Hama, Y.; Koyama, Y.; Barrett, T.; Kamiya, M.; Nagano, T.; Watanabe, T.; Hasegawa, A.; Choyke, P. L.; Kobayashi, H. Nat. Med. 2009, 15, 104.
[76] Schroeder, A.; Goldberg, M. S.; Kastrup, C.; Wang, Y.; Jiang, S.; Joseph, B. J.; Levins, C. G.; Kannan, S. T.; Langer, R.; Anderson, D. G. Nano Lett. 2012, 12, 2685.
[77] Graf, N.; Lippard, S. J. Adv. Drug Delivery Rev. 2012, 64, 993. (99) Lien, Y. H.; Wu, T. M. J. Colloid Interface Sci. 2008, 326, 517.
[78] Nam, J.; Won, N.; Jin, H.; Chung, H.; Kim, S. J. Am. Chem. Soc. 2009, 131, 13639.
[79] Sato, K.; Yoshida, K.; Takahashi, S.; Anzai, J. Adv. Drug Delivery Rev. 2011, 63, 809.
[80] Thomas, C. R.; Ferris, D. P.; Lee, J.-H.; Choi, E.; Cho, M. H.; Kim, E. S.; Stoddart, J. F.; Shin, J.-S.; Cheon, J.; Zink, J. I. J. Am. Chem. Soc. 2010, 132, 10623.
[81] Karg, M.; Hellweg, T. Curr. Opin. Colloid Interface Sci. 2009, 14, 438.
[82] Bardhan, R.; Chen, W.; Perez-Torres, C.; Bartels, M.; Huschka, R.M.; Zhao, L.L.; Morosan, E.;Pautler,R.G.;Joshi,A.;Halas,N.J. Adv. Funct. Mater. 2009, 19, 3901.
[83] Shimkunas, R. A.; Robinson, E.; Lam, R.; Lu, S.; Xu, X.; Zhang, X. Q.; Huang, H.; Osawa, E.; Ho, D. Biomaterials 2009, 30, 5720.
[84] Cheng, J.; Teply, B. A.; Jeong, S. Y.; Yim, C. H.; Ho, D.; Sherifi, I.; Jon, S.; Farokhzad, O. C.; Khademhosseini, A.; Langer, R. S. Pharm. Res. 2006, 23, 557.
[85] Gullotti, E.; Yeo, Y. Mol. Pharmaceutics 2009, 6, 1041.
[86] Zhou,L.;Cheng,R.;Tao,H.;Ma,S.;Guo,W.;Meng,F.;Liu,H.; Liu, Z.; Zhong, Z. Biomacromolecules 2011, 12, 1460.
[87] Kaiden, T.; Yuba, E.; Harada, A.; Sakanishi, Y.; Kono, K. Bioconjugate Chem. 2011, 22, 1909.
[88] Aryal, S.; Grailer, J. J.; Pilla, S.; Steeber, D. A.; Gong, S. J. Mater. Chem. 2009, 19, 7879.
[89] Van Dongen, S. F.; Verdurmen, W. P.; Peters, R. J.; Nolte, R. J.; Brock, R.; Van Hest, J. C. Angew. Chem., Int. Ed. 2010, 49, 7213.
[90] Goda, T.; Goto, Y.; Ishihara, K. Biomaterials 2010, 31, 2380.

[91] Byrne, J. D.; Betancourt, T.; Brannon-Peppas, L. Adv. Drug Delivery Rev. 2008, 60, 1615.
[92] Gupta, A. K.; Wells, S. IEEE Trans. Nanobiosci. 2004, 3, 66.
[93] Gupta, A. K.; Gupta, M. Biomaterials 2005, 26, 1565.
[94] Park, K. S.; Tae, J.; Choi, B.; Kim, Y. S.; Moon, C.; Kim, S. H.; Lee, H. S.; Kim, J.; Park, J.; Lee, J. H.; Lee, J. E.; Joh, J. W.; Kim, S. Nanomedicine-UK 2010, 6, 263.
[95] MacKay, J. A.; Li, Z. Adv. Drug Delivery Rev. 2010, 62, 1003.
[96] Mahmoudi, M.; Sant,S.;Wang,B.;Laurent,S.;Sen,T. Adv. Drug Delivery Rev. 2011, 63, 24.
[97] Shubayev, V. I.; Pisanic, T. R., II; Jin, S. Adv. Drug Delivery Rev. 2009, 61, 467.
[98] Jong, M. D.; Breeman, W. A. P.; Kwekkeboom, D. J.; Valkema, R.; Krenning, E. P. Acc. Chem. Res. 2009, 42, 873.
[99] Yoo, D.; Lee, J.-H.; Shin, T.-H.; Cheon, J. Acc. Chem. Res. 2011, 44, 863.
[100] MacKay, J. A.; Li, Z. Adv. Drug Delivery Rev. 2010, 62, 1003.
[101] Mahmoudi,M.;Sant,S.;Wang,B.;Laurent,S.;Sen,T. Adv. Drug Delivery Rev. 2011, 63, 24.
[102] Petros, R. A.; DeSimone, J. M. Nat. Rev. Drug Discovery 2010, 9, 615.
[103] Shubayev, V. I.; Pisanic, T. R., II; Jin, S. Adv. Drug Delivery Rev. 2009, 61, 467.
[104] Haam, S.; Lee, K.; Yang, J.; Huh, Y.-M. Nanocomposites, 1st ed.; Wiley-VCH: Weinheim, 2010

Porphyrins

The porphyrins are an important natural class of macrocyclic compounds that play a very important role in the metabolism of living organisms. They are found in different biological systems, and among the most important examples we can mention the Eme group (porphyrin ring containing a Fe^{2+} ion) of the hemoglobin (***Fig- 2.2.1***), responsible for the transport of oxygen in the blood or, as for the plant kingdom, the chlorophyll (***Fig. 2.2.2***), essential to the photosynthesis process.

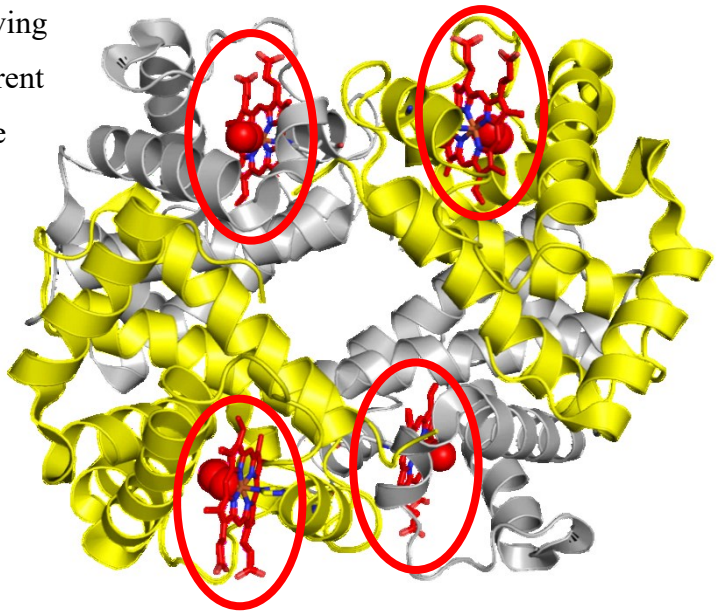

Figure2.2.1: Hemoglobin and heme structures

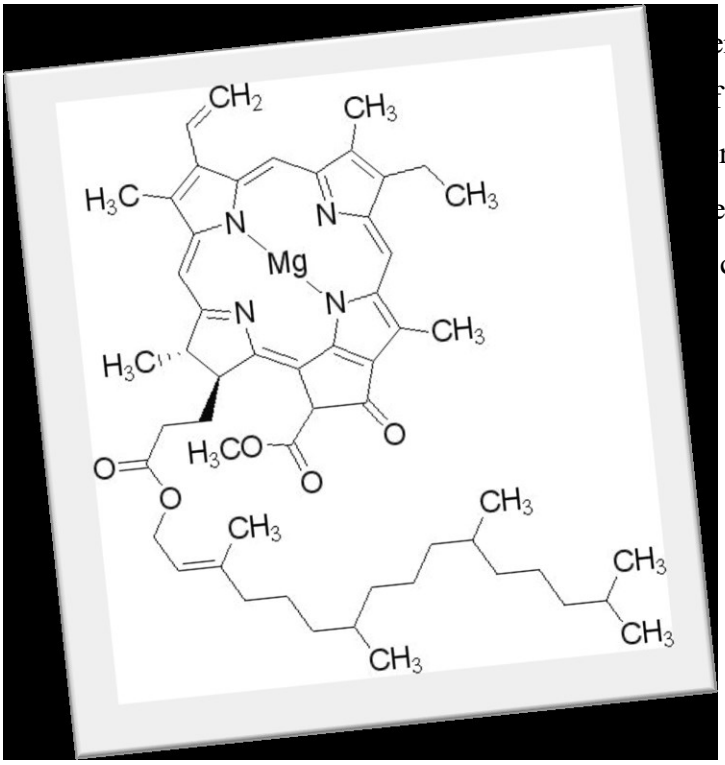

Figure 2.2.2: chlorophyll structure

ence the interest of research on the study f these systems and their essential roperties in biological processes such: electronic transfer (cytochrome c, cytochrome oxidase), catalysis, storage and transfer of oxygen (hemoglobin and myoglobin), complexation selection of varied species, and the initial phases of photochemical steps in photosynthesis.

The word porphyrin is derived from the Greek porphura meaning purple. They are in fact a large class of deeply colored pigments, of natural or synthetic origin, having in common a substituted aromatic macrocycle ring and consisting of four pyrrole rings linked by four methine bridges (***Fig.2.2.3***)[1].

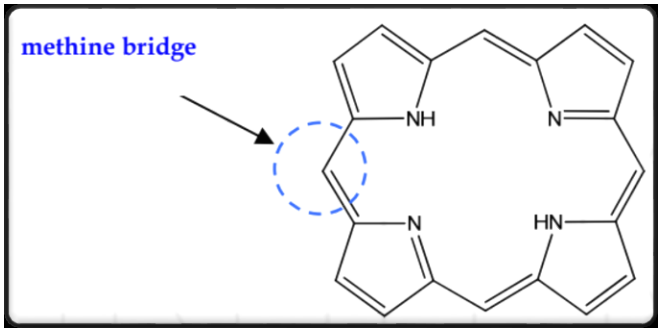

Figure 2.2.3: The structure of porphyrin.

The IUPAC nomenclature (***Fig. 2.2.4***) provides the numbering of all carbon atoms of the ring, including nitrogen atoms, so that the two saturated nitrogen atoms receive the numbers 21 and 23. The positions 1, 4, 6, 9, 11, 14, 16 and 19 are indicated as α-pyrrole, the positions 2, 3, 7, 8, 12, 13, 17 and 18 are called β-pyrroles and the positions 5, 10, 15 and 20 are called meso.

Any substituents formed by alkyl chains are indicated by assigning the number of the porphyrin carbon atom to which they are bound to all atoms of the chain, with an apex finally indicating the number of links of distance. The porphyrin macrocycle is a highly-conjugated molecule containing 22 π-electrons, but only 18 of them are delocalized according to the Hückel's rule of aromaticity (4n+2 delocalized π-electrons, where n= 4).

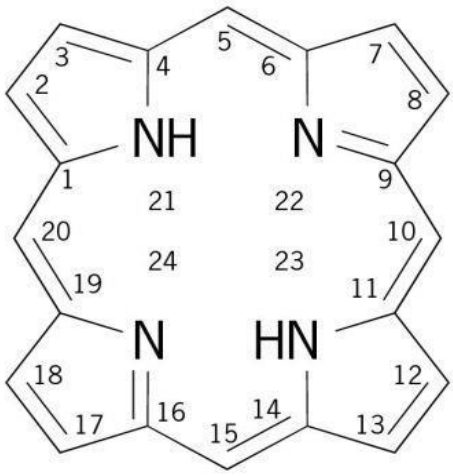

Figure 2.2.4: Nomenclature IUPAC of porphyrin ring.

The electronic delocalization also depends on the state in which the porphyrin is found (***Fig. 2.2.5***), which can present itself as:

- Free base
- Anionic form
- Complex Metal

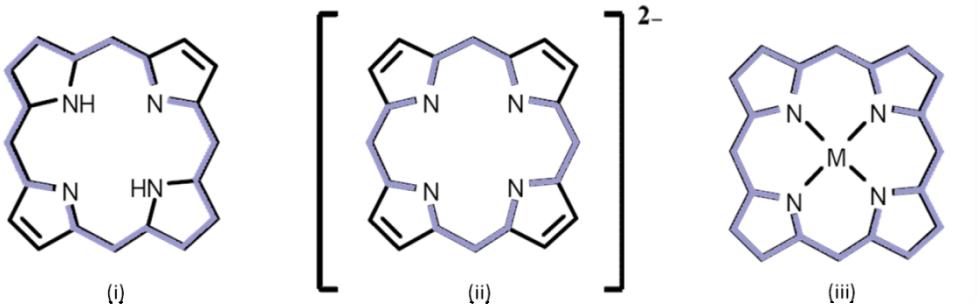

Figure 2.2.5: Delocalization of the π system in the porphyrin: (i) Free base (ii) Dianionics (iii) Complexed metal.

Theoretical and experimental studies have shown that the thermodynamically more stable forms for symmetric systems are the two trans-NH degenerate tautomers, and the proton migration between the two seems to proceed through a step-by-step mechanism for the less favored cis-NH tautomer (***Fig. 2.2.6***)

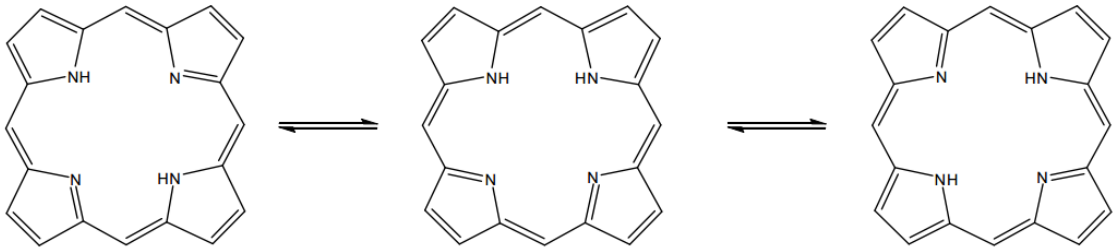

Figure 2.2.6: Tautomerism of Porphyrin Ring

Porphyrin structure supports a highly stable configuration of single and double bonds with aromatic characteristics that permit the electrophilic substitution reactions typical of aromatic compounds such as halogenation, nitration, sulphonation, acylation, deuteration, formylation. Nevertheless, in the porphyrins there are two different sites on the macrocycle where electrophilic substitution can take place with different reactivity:[1] positions 5, 10, 15 e 20, called meso, and positions 2, 3, 7, 8, 12, 13, 17 and 18, called β-pyrrole positions. The activation of these sites depends on the porphyrins electronegativity that can be controlled by the choice of the metal to coordinate to the central nitrogen atoms. For this reason, the introduction of divalent central metals produces electronegative porphyrin ligands and these complexes can be substituted on their meso-carbon. On the other hand, metal ions in electrophilic oxidation states (e.g. Sn IV) tend to deactivate the meso-position and to activate the β pirrole to electrophylic attack. The chemical characteristics of substituents in β-pyrrole and meso-position determine the water and/or organic solvent solubility of porphyrins.

It was recognized early that the intensity and colour of porphyrins are derived from the highly conjugated π-electron systems and the most fascinating feature of porphyrins is their characteristic UV-visible spectra that consist of two distinct regions: in the near ultraviolet and in the visible region. It has been well documented that changes in the conjugation pathway and symmetry of a porphyrin can affect its Uv-Vis absorption spectrum.[1, 2, 3, 4, 5] The absorption spectrum of porphyrins has long been understood in terms of the highly successful "four-orbital" (two highest occupied π orbitals and two lowest unoccupied π* orbitals) model first applied in 1959 by Martin Gouterman that has discussed the importance of charge localization on electronic spectroscopic properties and has proposed the four-orbital model in the 1960 to explain the absorption spectra of porphyrins.[3, 6] It has been well documented that changes in the conjugation pathway and symmetry of a porphyrin can affect its Uv-Vis absorption spectrum.

The electronic absorption spectrum of a typical porphyrin consists therefore of two distinct regions. The first involves the transition from the ground state to the second excited state ($S_0 \rightarrow S_2$) and the corresponding band is called the Soret or B band and has a molar extinction coefficient about 10^5 M^{-1} cm^{-1}. The range of absorption is between 380-500 nm, depending on whether the porphyrin is β or meso-substituted. The second region consists of a weak transition to the first excited state ($S_0 \rightarrow S_1$) in the range between 500-750 nm (the Q bands) having a molar extinction coefficient about 10^4 M^{-1} cm^{-1} (***Fig. 2.2.7***).

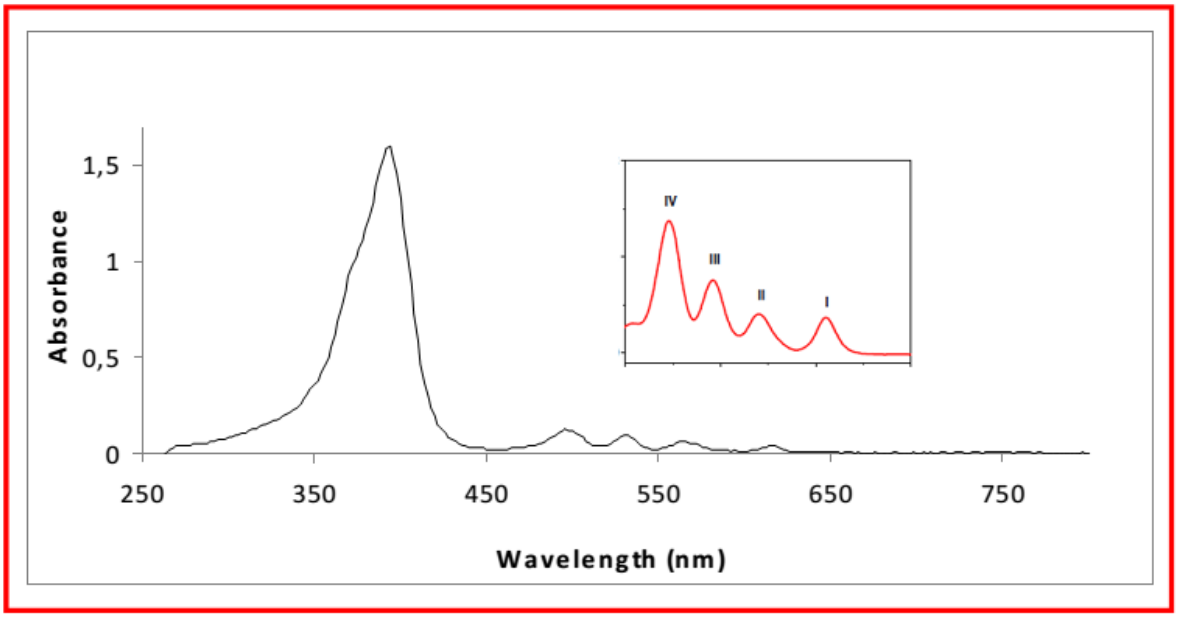

Figure 2.2.7: Uv-Vis spectrum of porphyrin, in insert the enlargement of the Q region between 480-720 nm.

According to Gouterman's theory, the absorption bands in porphyrin systems arise from transitions between two HOMOs and two LUMOs, and it is the identities of the metal center and the substituents on the ring that affect the relative energies of these transitions. The HOMOs were calculated to be $\mathbf{a_{1u}}$ and $\mathbf{a_{2u}}$ orbitals, while the LUMOs were calculated to be a degenerate set of $\mathbf{e_g}$ orbitals. Transitions between these orbitals gave rise to two excited states. Orbital mixing form two states of energy, one with higher energy state with greater oscillator strength, giving rise to the Soret band, and a lower energy state with less oscillator strength, giving rise to the Q-bands (***Fig. 2.2.8***).

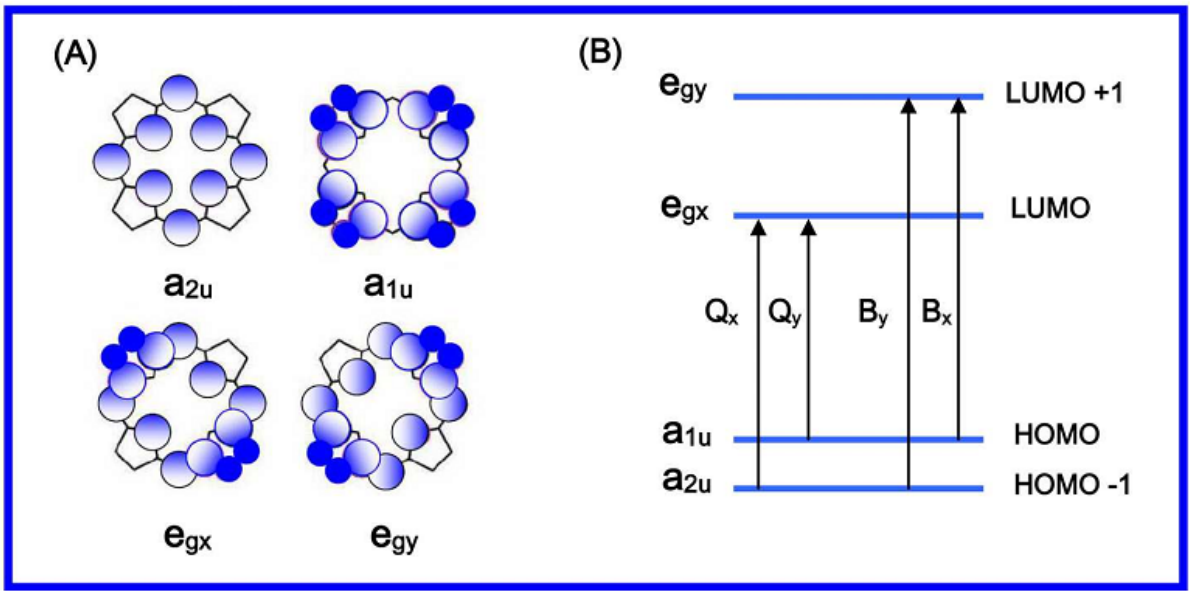

Figure 2.2.8: Porphyrin HOMOs and LUMOs. (A) Representation of the four Gouterman orbitals in porphyrins. (B) Drawing of the energy levels of the four Gouterman orbitals upon symmetry lowering from D_{4h} to C_{2V}. The set of e_g orbitals gives rise to Q and B bands

The relative intensity of Q bands is due to the kind and the position of substituents on the macrocycle ring. When the relative intensities of Q bands are such that IV > III > II > I, the spectrum is said etio-type and porphyrins called *etioporphyrins*. This kind of spectrum is found in all porphyrins in which six or more of the β-positions are substituted with groups without π- electrons. Substituent with π-electrons, attached directly to the β-positions, gave a change in the relative intensities of the Q bands, such that III > IV > II > I. This is called *rhodo-type* spectrum (rhodoporphyrin) because these groups have a "reddening" effect on the spectrum by shifting it to longer wavelengths.

However, when these groups are on opposite pyrrole units, the reddening is intensified to give an *oxo-rhodo-type* spectrum in which III > II > IV > I. On the other hand, when mesopositions are occupied, the *phyllo-type* spectrum is obtained, in which the intensity of Q

bands are IV > II > III > I .[2]

While variations of the peripheral substituents on the porphyrin ring often cause minor changes to the intensity and wavelength of the absorption features, protonation of two of the inner nitrogen atoms or the insertion/change of metal atoms into the macrocycle usually results in a strong change of the visible absorption spectrum. When porphyrinic macrocycle is protonated or coordinated with any metal, there is a more symmetrical situation than in the porphyrin free base and this produces a simplification of Q bands pattern for the formation of two Q bands (***Fig. 2.2.9***).

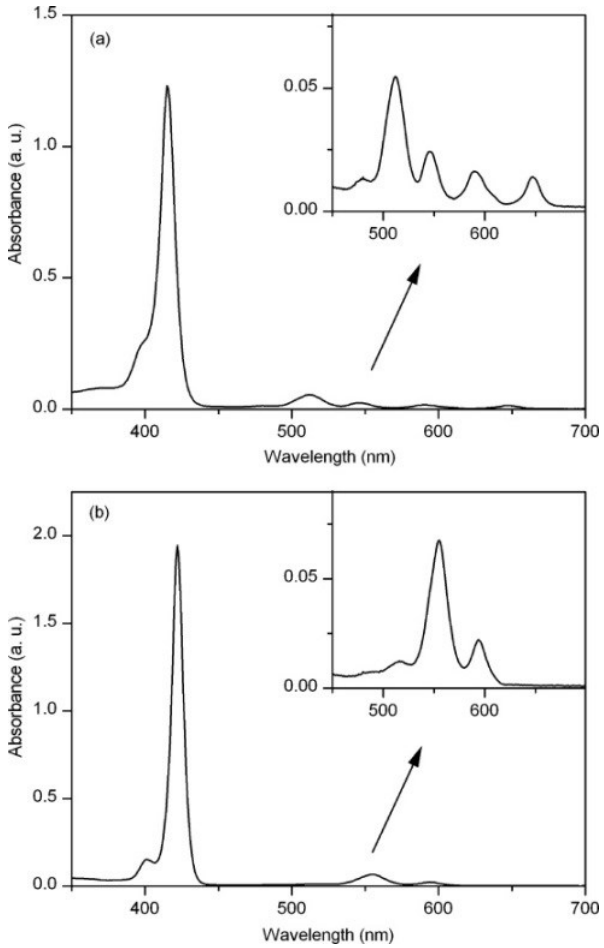

Figure 2.2.9: Typical Uv-Vis spectrum of (A) free-base porphyrin and (B) metallic porphyrin.

Neglecting the overall charge of the macrocycle, a monomeric free-base porphyrin H_2-P in aqueous solution can add protons to produce mono H_3-P^+ and dications H_4-P^{2+} at very low pH, or lose protons to form the centrally monoprotic H-P^- at pH about 6 or aprotic P^{2-} species at pH ≥ 10 (***Figure 2.2.10***). These chemical forms of porphyrin may exist in equilibrium, depending upon the pH of the solution and can be characterized from the change of the electronic absorption spectrum. The change in spectra upon addition of acid or basic

substances can generally be attributed to the attachment or the loss of protons to the two imino nitrogen atoms of the pyrrolenine-like ring in the free-base.[7, 8]

The N-protonation induced a red-shifts that are consistent with frontier molecular orbital calculations for protonated porphyrins.

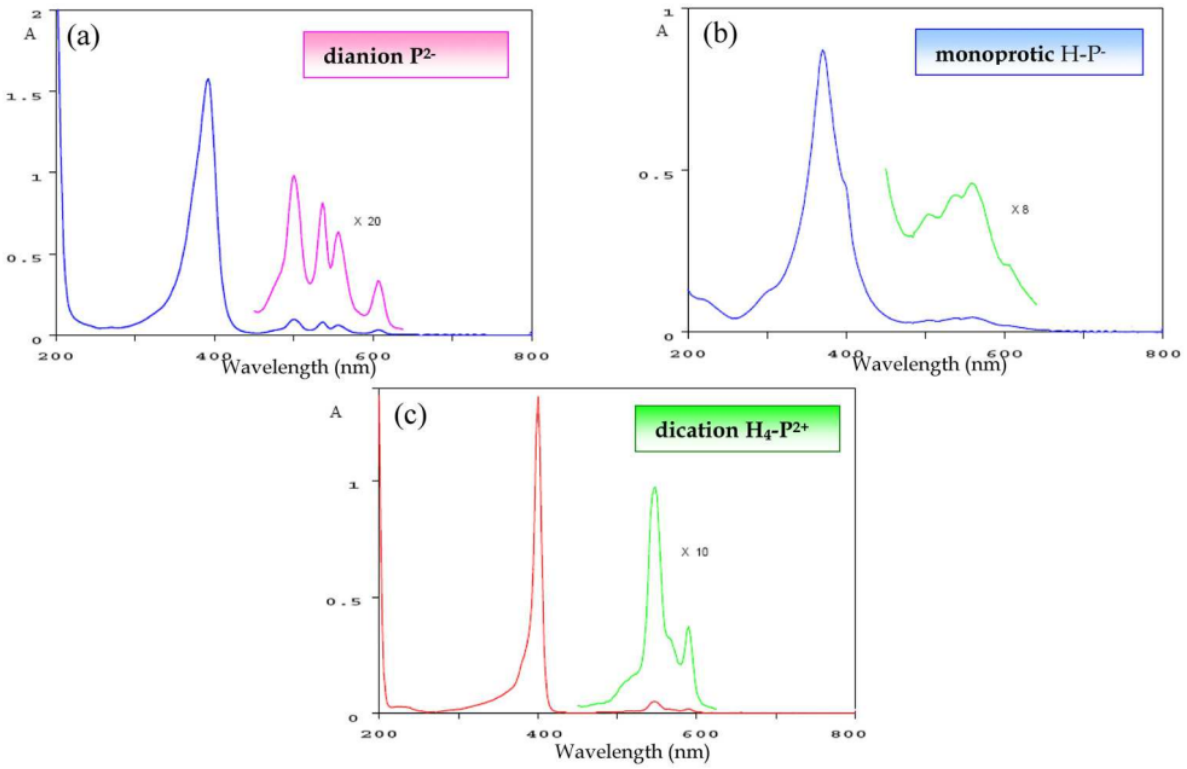

Figure 2.2.10: Typical Uv-Vis spectrum of dianion P^{2-} (pH about 10) monoprotic $H\text{-}P^{-}$ (pH about 6) and dication $H_4\text{-}P^{2+}$ porphyrin (pH about 1)

Upon addition of acid, the spectral pattern of porphyrins changes from the four Q-band spectrum, indicating D_{2h} symmetry for free-base porphyrin, to a two Q-band spectrum for the formation of dications $H_4\text{-}P^{2+}$, indicating D_{4h} symmetry, typical of porphyrin coordinated to a metal ion through the four N-heteronuclei. In addition, in all cases, the intense Soret band is red-shifted (to an extent dependent on the meso-substituents).

Furthermore, the porphyrins also show fluorimetric spectrum properties, in particular for the porphyrins found in the free form, the fluorescence spectrum shows two peaks, one at 658nm, very intense, and another, weaker, at 714nm, in different solvents.

As for the absorption spectrum, also in the case of fluorescence, the wavelength of the emission maximum is influenced by the substituents present in the porphyrin ring, as well as by the presence of metals in the porphyrin core. An example is the zinc- porphyrin, whose spectrum shows a strong fluorescence peak at 610nm, which corresponds to the transition (0;

0), that is from the fundamental S_1, to the fundamental S_0; and another peak at 650nm for the transition (1; 0), that is from the fundamental S_1, to the excited S_0.

Furthermore, the position of the fluorescence bands is not influenced by the type of solvent.

Porphyrins can also exist in a complex form, giving rise to very peculiar characteristics. The formation reaction of the metal-porphyrins is one of the most important processes both from the analytical and bioinorganic point of views. Through the degree of formation of a whole series of metal-porphyrins, it is possible to understand the kinetic study on the different complexity of metal ions. Furthermore, the kinetics of metal-porphyrins formation with different metal ions is essential to understand the in vivo complexation processes that lead to the formation of natural metal-porphyrins. Generally, the porphyrins are synthesized in free form and subsequently the metallation reaction is carried out. When a metallic M^{n+} ion is inserted into the cavity of the porphyrinic ring in its free form H_2P, the species $MP^{(n-2)}$ is formed, according to the equation:

$$M^{n+} + H_2P \leftrightarrow MP^{(n-2)} + 2H^+$$

During the formation of the metal-porphyrins there is a variation of color with the consequent transformation of the Uv-Vis spectrum, especially in the Q bands area. In fact, the two Q bands that are obtained are called α and β, and depending on their relative intensities it is possible to understand the stability of the complex formed; in the moment in which α> β the metal forms a stable planar square complex with the porphyrin; in the other case, when β> α (eg with Ni (II), Pd (II), Cd (II)) the metals are easily replaced by protons, thus indicating a not very stable complex.

The size of the porphyrinic ring makes it perfectly suitable to bond almost all metal ions. In fact, a large number of metals can be inserted at the center of the macrocycle, forming a whole series of metal-porphyrins that play a key role in different biochemical processes from photosynthesis to oxygen transport and various redox reactions. Depending on the size, the charge, the spin multiplicity and the type of metal ion, regular metal-porphyrins are formed which are kinetically inert complexes. This is the case of many of the natural metal-porphyrins in which, for the "perfect" dimensions, the metallic center is located inside the plane of the tetra-pyrrole ring. This is what happens when the cationic ray falls within the range between 55-80 pm.

The group of symmetry to which the porphyrins in the free form belong is the D_{2h}, with the two hydrogens allocated diagonally to the pyrrolic nitrogen; differently, the metal-porphyrins

in their regular form are highly symmetrical. However, if the radius of the ion that is bound is too large (about 80-90 pm) the arrangement is not perfect with an exit from the ring plane, with distortion and loss of symmetry. Thus, the sitting-atop metal-porphyrins are formed, which have characteristics both in spectroscopic and kinetic properties.

A growing interest has arisen recently regarding the supramolecular complexes of π conjugated systems for their potential applications in optoelectronics and in the field of photovoltaics. The molecular aggregates of several types of dyes have been studied as conductive organic compounds, as markers in biological or artificial membranes and also as materials with nonlinear optical properties useful for optical devices.

Recently, porphyrin assembly has been used for light-driven energy transduction systems, copying the photophysical processes of photosynthetic organisms.[9, 10, 11, 12, 13]

The aggregation and dimerization of porphyrins and metalloporphyrins in aqueous solution have been widely investigated[14, 15] and it has been deduced that it is dependent strictly on physical-chemical characteristics, such as ionic strength, pH, and solvent composition; the combination of these factors can facilitate the aggregation processes.[10] The aggregation of porphyrins changes their spectral and energetic characteristics. The diverse chemical and photophysical properties of porphyrins are in many cases due to their different aggregation mode and, because of interchromophoric interactions, perturbations in the electronic absorption spectra of dyes occur. Deviations from Beer's law are often used to investigate the porphyrin aggregation in solution. Because the aggregates of porphyrins show peculiar spectroscopic properties, the molecular associations of porphyrins were generally investigated using Uv-Vis absorption and fluorescence spectroscopy.[16]

The characteristic of porphyrin molecule with 22 π-electrons causes a strong π–π interaction,[17] facilitating the formation of two structure types: "H-type" with a hypsochromic shift of the B band and "J-type" with bathochromic shift of the B band, with respect to those of monomer (***Fig. 2.2.11***).

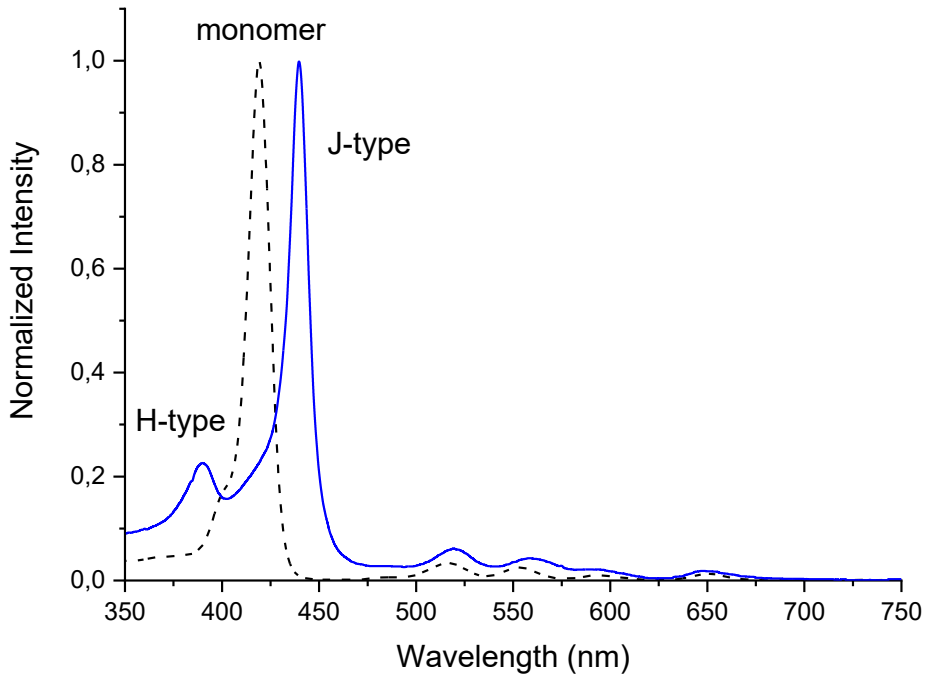

Figure 2.2.11: Typical Uv-Vis spectrum H-type and J-type aggregates.

The J-type aggregates (side-by-side) are formed for transitions polarized parallel to the long axis of the aggregate, while H-type (face-to-face) for transitions polarized perpendicular to it (***Fig. 2.2.12***)

J-aggregates are formed with the monomeric molecules arranged in one dimension such that the transition moment of the monomers is parallel and the angle between the transition moment and the line joining the molecular centers is zero.[18] The strong coupling of monomers results in a coherent excitation with a red-shift relative to the monomer band (***Fig. 2.2.13***).

H-aggregates are again a one-dimensional arrangement of strongly coupled monomers, but the transition moments of the monomers are perpendicular (ideal case) to the line of centers. Unlike J-aggregates, the arrangement in H-aggregates is face-to-face. The dipolar coupling between monomers leads to a blue shift of the absorption band (***Fig. 2.2.13***)[19, 20].

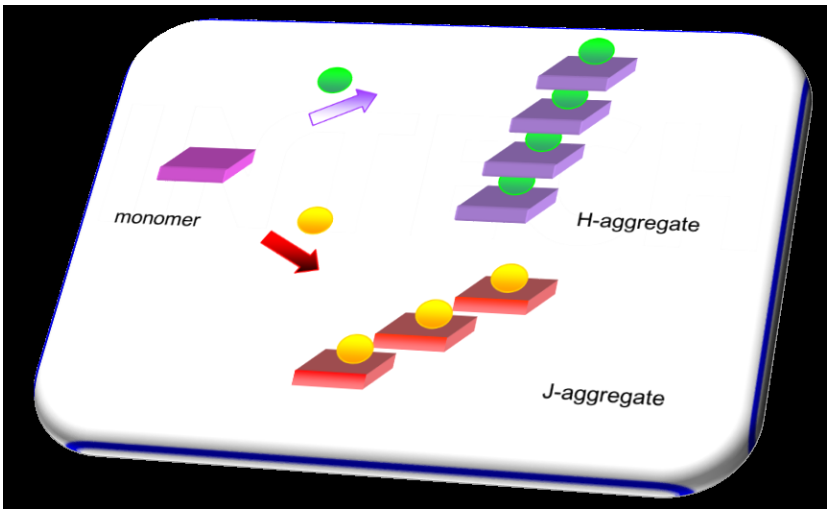

Figure 2.2.12: geometric representation of J and H aggregates.

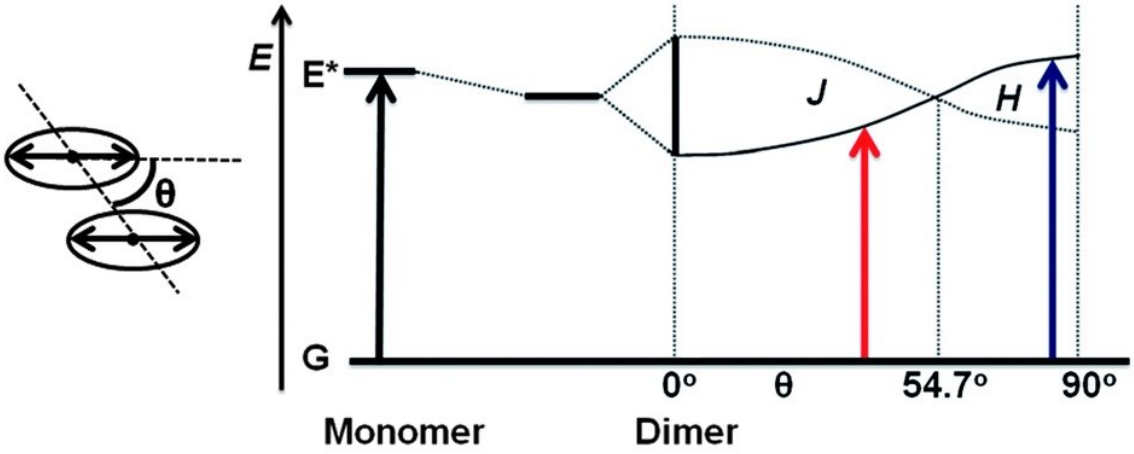

Figure 2.2.13: J and H aggregate formation scheme with respective angles and energies

It has been known for nearly a century that some porphyrins and related compounds can selectively localize in a wide variety of tumors.[21]

This property, along with the usual low-dark toxicities of porphyrin macrocycles, led to their initial choice as the most promising PDT photosensitizers, compared with several other aromatic macrocycles (such as acridine, fluorescein, eosin, and rhodamine).[22]

Porphyrin-based compounds possess a number of key photochemical, photophysical and biological properties that make them highly desirable for medical applications: they absorb strongly in the visible region of the optical spectrum, are fluorescent, are non-toxic in the dark, have high chemical stability, have affinity for serum proteins, have favorable pharmacokinetic properties, and form very stable complexes with a variety of metal ions while retaining their in vivo tumor-localization properties. For these reasons, several

porphyrin-type compounds are currently in various stages of preclinical or clinical development as phototherapeutic agents.

PDT consists of the irradiation of a tumor-localized photosensitizer, with the light of appropriate wavelength, to form an excited triplet state (via a singlet) which reacts with molecular oxygen and other substrates to generate highly cytotoxic species (e.g. singlet oxygen, superoxide anion, hydroxyl radicals) that cause irreversible destruction of tumor cells.[23, 24, 25, 26, 27, 28]

Highly reactive transient species such as singlet oxygen have a limited range in tissue (< 0.1 mm for singlet oxygen), so toxicity is restricted to the immediate area/volume in which the photosensitizing drug is localized. Therefore, porphyrin-PDT is a localized approach to the treatment of cancer, which ideally induces selective tumor cell destruction with minimal side effects, in contrast to more conventional types of treatments such as chemotherapy and radiotherapy.

The cytotoxic species generated intracellularly upon activation of porphyrin-type sensitizers cause tumor cell death by necrosis and/or by apoptosis (programmed cell death).[29, 30] Porphyrin-induced apoptosis in tumors is primarily correlated with mitochondrial photodamage [31, 32, 33, 34, 35, 36] and usually occurs rapidly, probably as a result of a cascade-like cell killing process, leading to a rapid loss of treated tissue.[37, 38]

Although the mechanisms responsible for porphyrin tumor-selectivity are not yet completely understood, their association to plasma proteins, particularly to low-density lipoproteins (LDL),[39, 40, 41] the high content of macrophages in tumor cells (which in some cases account for 20-50% of the total tumor cell population),[42, 43, 44, 45, 46] and the lower intracellular pH,[47, 48, 49] have all been proposed to participate in the selective uptake of these compounds in tumors. The LDL-bound porphyrins can bind to LDL receptor sites, which are abundantly expressed on the membranes of actively growing and proliferating tumor cells, and be internalized by endocytosis, or by non-receptor-mediated processes.[50, 51]

Porphyrin compounds have a strong propensity for aggregation in aqueous solutions and tumor-associated macrophages have been shown to ingest porphyrin aggregates. Hydrophobic porphyrin molecules and their aggregates can also enter tumor cells both by passive diffusion through the plasma membrane and/or by fluid-phase endocytosis. The binding of porphyrin-based drugs to collagen, as well as to albumin, globulins, elastin, and high-density lipoproteins (HDL) have also been observed.[52, 53, 54, 55]

In particular, hydrophilic porphyrin compounds show little affinity for binding to LDL, but they bind strongly to albumin. The high vascular permeability and inefficient lymphatic clearance of neoplastic tissues can also partly account for the tumor-targeting ability of

porphyrin systems.[56, 57] The intracellular localization of porphyrins is a key factor in determining the efficiency of tumor-cell destruction by PDT. Porphyrin compounds usually either have a general cytoplasmic localization or preferentially accumulate in certain organelles, such as the lysosomes, the mitochondria, the endoplasmic reticulum, the Golgi apparatus, and to a certain extent, in the nuclei of tumor cells. Porphyrin molecules (neutral, cationic and anionic) have been shown to bind to mitochondrial benzodiazepine receptors, and therefore, to be internalized and localized to some extent in this critically important organelle.[58, 59, 60, 61]

In general, porphyrin-type compounds display multiple localization sites within the cell, which might account for their effectiveness in tumor cell destruction. The intracellular re-localization of porphyrin sensitizers upon brief light exposure has also been reported, and this redistribution process might play an important role in PDT-induced cell killing.[62, 63]

In addition, porphyrins and their diamagnetic metal complexes are highly fluorescent, and this property enables the detection of tumors by fluorescence imaging.[64, 65, 66, 67, 68, 69]

The use of a fluorescent sensitizer in PDT allows the combination of diagnosis and therapy, as well as effective treatment planning. Furthermore, paramagnetic metal complexes of porphyrin-based compounds [for example Mn(III) and Gd(III)] have been shown to be effective contrast agents for magnetic resonance imaging (MRI),[70, 71, 72, 73, 74, 75, 76] thus enabling detection by a highly efficient and non-invasive technique.

However, despite the multiple potential uses, and in particular in the biomedical field, one of the problems related to the use of porphyrin compounds is the insolubility in water.

In order to overcome this issue, various solutions have been designed and applied. The most common one uses ionic porphyrins but, unfortunately, these systems can interact with biological compounds, such as proteins and DNA, altering their correct functioning.

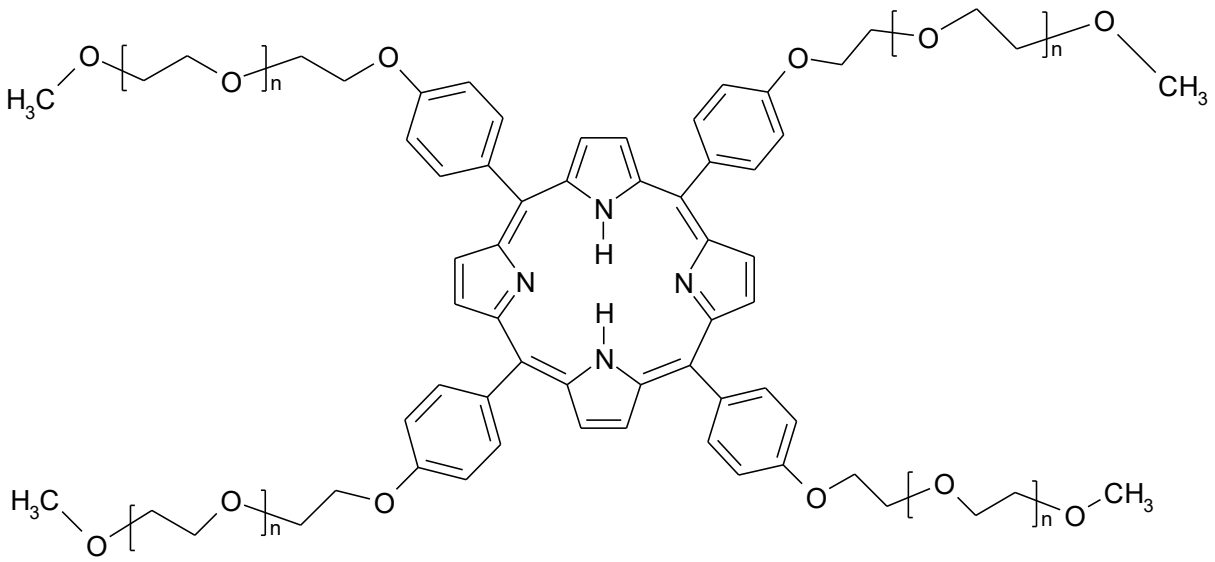

Figure 2.2.14: Structure of 5.10.15.20 tetrakis {p-[ω-methoxy -poly (ethylene oxide)] phenyl} porphyrin

The researchers, in the university laboratory in which I have done my PhD's work, to synthesized an uncharged water-soluble porphyrin, used the hydrophilic properties of polyethylene glycol chains, which, bound to the porphyrinic units (***Fig. 2.2.14***), make them water-soluble without affecting their biocompatibility, an essential property for moving in biological environments and allowing, for example, the crossing cellular membranes, leaving the photophysical and photochemical properties unaltered[77, 78, 79, 80].

[1] Milgrom, L.R. (1997) *The Colours of Life*, OUP, Oxford
[2] Gouterman, M. J.; Chem. Phys. 1959, 30, 1139
[3] Whitten, D. G; Lopp, I. G.; Wildes, P. D. J. Am. Chem. Soc. 1968, 90, 7196
[4] Nappa, M. J. S.; Valentine,. J. Am. Chem. Soc. 1978, 100, 5075
[5] Wang, M.-Y. R.; Hoffman, B. M. J. Am. Chem. Soc. 1984 106, 4235.
[6] Gouterman, M. J. Mol. Spectroscopy, 1961, 6, 138
[7] M. Gouterman, Optical spectra and electronic structure of porphyrins and related rings. In The Porphyrins, 2nd Ed.; Dolphin, D., Ed; Academic Press: New York, 1978; Volume 3.
[8] Giovannetti, R.; Alibabaei, L.; Pucciarelli, F. Inorganic. Chim. Act. 1961,363, 1561
[9] Choi, M.-S.; Aida, T.; Luo, H.; Araki, Y.; Ito, O. Angew. Chem., Int. Ed. 1961, 42, 4060.
[10] Choi, M.-S.; Aida, T.; Yamazaki, I.; Yamazaki, T. Angew. Chem., Int. Ed. 2004, 43, 150
[11] Choi, M.-S.; Aida, T.; Yamazaki, I.; Yamazaki, T. Angew. Chem., Int. Ed. 2001, 40, 194
[12] Choi, M.-S.; Aida, T.; Yamazaki, I.; Yamazaki, T. Chem. Eur. J. 2002, 8, 2667.
[13] Luo, H.; Choi, M.-S.; Araki, Y.; Ito, O.; Aida, T. Bull. Chem. Soc. Jpn. 2005, 78, 405
[14] Borissevitch, I.E.; Gandini, S.C.; J. Photochem. Photobiol. B: Biol. 1998, 43, 112
[15] Pasternack, R.F.; Gibbs, E.J.; Antebi, A.; Bassner, S.; Depoy, L.; Turner, D.H.; Williams, A.; Laplace, F.; Lansard, M.H.; Merienne, C.; Perrée-Fauvet, M. J. Am. Chem. Soc. 1985, 107, 8179
[16] Ohmo, O.; Kaizu, Y.; Kobayashi, H. J. Chem. Phys. 1993, 99, 4128.
[17] Van de Craats, A.M.; Warman, J.M. Adv. Mater. 2001, 12, 130.
[18] Bohn, P. W. Annu. Rev. Phys. Chem. 1993, 44, 37.
[19] Czikklely, V.; Forsterling, H. D.; Kuhn, H. Chem. Phys. Lett. 1970, 6, 207.
[20] Nuesch, F.; Gratzel, M. Chem. Phys. 1995, 193, 1.
[21] Hausman, W. Biochem. Z., 1909, 14, 275-278
[22] Bonnett, R. Rev. Contemp. Pharmacother., 1999, 10, 1-17
[23] Dougherty, T. J.; Gomer, C. J.; Henderson, B. W.; Jori, G.; Kessel, D.; Korbelik, M.; Moan, J.; Peng, Q. J. Natl. Cancer Inst., 1998, 90, 889-905.
[24] Schnitmaker, J. J.; Bass, P.; van Leengoed, M. L. L. M.; van der Meulen, F. W.; Star, W. M.; van Zaudwijk, N. J. Photochem. Photobiol. B: Biol. 1996, 34, 3-12.
[25] Hahn, S. M.; Glatstein, E. Rev. Contemp. Pharmacother. 1999, 10, 69-74.
[26] Hsi, R. A.; Rosenthal, D. I.; Glatstein, E. Drugs, 1999, 57, 725-734.
[27] Webber, J.; Herman, M.; Kessel, D.; Fromm, D. Annals Surg. 1999, 230, 12-23.
[28] Webber, J.; Herman, M.; Kessel, D.; Fromm, D. Langenbeck's Arch. Surg. 2000, 385, 299-304.
[29] Waldman, T.; Zhang, Y.; Dillehay, L.; Yu, J.; Kinzler, K.; Vogelstein, B.; Williams, J. Nature Med. 1997, 3, 1034- 1036.
[30] Mason, M. D. Rev. Contemp. Pharmacother. 1999, 10, 25- 37.
[31] Luo Y.; Kessel, D. Photochem. Photobiol. 1997, 66, 479- 483.
[32] Oleinick, N. L.; Evans, H. H. Radiat. Res. 1998, 150 (Suppl.), S146-S156.
[33] Kessel, D.; Luo, Y. J. Photochem. Photobiol. B: Biol. 1998, 42, 89-95;
[34] Kessel, D.; Luo, Y. Cell Death and Differentiation, 1999, 6, 28-35.
[35] Varnes, M. E.; Chiu, S.-M.; Xue, L.-Y.; Oleinick, N. L. Biochem. Biophys. Res. Commun. 1999, 255, 673-679.
[36] Kessel, D.; Luo, Y.; Mathieu, P.; Reiners, Jr., J. J. Photochem. Photobiol. 2000, 71, 196-200.
[37] Agarwal, R.; Korman, N. J.; Mohan, R. R.; Feyes, D. K., Jawed, S.; Zaim, M. T.; Mukhtar, H. Photochem. Photobiol. 1996, 63, 547-552.
[38] Granville, D. J.; Levy, J. G.; Hunt, D. W. C. Photochem. Photobiol. 1998, 67, 358-362
[39] Kongshaug, M. Int. J. Biochem. 1992, 24, 1239-1265.
[40] Maziere, J. C.; Morliere, P.; Santus, R. J. Photochem. Photobiol. B: Biol. 1991, 8, 351-360.
[41] Obochi, M. O. K.; Boyle, R. W.; van Lier, J. E. Photochem. Photobiol. 1993, 57, 634-640
[42] Korbelik, M.; Krosol, G.; Olive, P. L.; Chaplin, D. J. Br. J. Cancer, 1991, 64, 508-512;
[43] Korbelik, M.; Krosol, G.; Chaplin, D. J. Cancer Res. 1991, 51, 2251-2255.
[44] Krosl, G.; Korbelik, M.; Dougherty, T. J. Br. J. Cancer, 1995, 71, 549-555.
[45] Hamblin, M. R.; Newman, E. L. J. Photochem. Photobiol. B: Biol. 1994, 23, 3-8.
[46] Brasseur, N.; Langlois, R.; La Madeleine, C.; Ouellet, R.; van Lier, J. E. Photochem. Photobiol. 1999, 69, 345-352
[47] Thomas, J. P.; Girotti, A. W. Photochem. Photobiol. 1989, 49, 241-247.
[48] Brault, D. J. Photochem. Photobiol. B: Biol. 1990, 6, 79- 86.
[49] Peng, Q.; Moan, J.; Cheng, L. S. Cancer Lett. 1991, 58, 29- 35.
[50] Jori, G.; Reddi, E. Int. J. Biochem. 1993, 25, 1369-1375.
[51] Allison, B. A.; Pritchard, P. H.; Levy, J. G. Br. J. Cancer, 1994, 69, 833-839.
[52] Villanueva, A.; Jori, G. Cancer Lett. 1993, 73, 59-64.

[53] Kessel, D. J. Photochem. Photobiol. B: Biol. 1997, 39, 81- 83.
[54] Kessel D.; Whitcomb, K. L.; Schulz, V. Photochem. Photobiol. 1992, 56, 51-56.
[55] Kessel, D.; Poretz, R. D. Photochem. Photobiol. 2000, 71, 94-96.]
[56] Dougherty, T. J.; Gomer, C. J.; Henderson, B. W.; Jori, G.; Kessel, D.; Korbelik, M.; Moan, J.; Peng, Q. J. Natl. Cancer Inst. 1998, 90, 889-905,
[57] Roberts, W.; Hasan, T. Cancer Res. 1992, 52, 924-930
[58] Verma, A.; Nye, J.; Snyder, S. H. Mol. Pharmacol., 1987, 84, 2256-2260. [66] Kessel, D. Cancer Lett., 1988, 39, 193-198.
[59] Singh, G.; Jeeves, W. P.; Wilson, B. C.; Jang, D. Photochem. Photobiol., 1987, 46, 645-649.
[60] Morgan, J.; MacDonald, I. J.; Oseroff, A. R. Photochem. Photobiol., 1998, 67, 26S.
[61] Kessel, D. Cancer Lett. 1988, 39, 193-198.
[62] Berg, K; Madslien, K.; Bommer, J. C.; Oftebro, R.; Winkelman, J. W., Moan, J. Photochem. Photobiol. 1991, 53, 203-210.
[63] Wood, S. R.; Holroyd, J. A.; Brown, S. B. Photochem. Photobiol. 1997, 65, 397-402
[64] Mang, T. S.; McGinnis, C.; Liebow, C.; Nseyo, U. O.; Crean, D. H.; Dougherty, T. J. Cancer, 1993, 71, 269-276.
[65] Moan, J.; Berg, K.; Steen, H. B.; Warloe, T.; Madslien, K. In Photodynamic Therapy, Henderson, B.; Dougherty, T., Eds., Marcel Dekker, New York, 1992, pp 19-36.
[66] Trepte, O.; Rokahr, I.; Andersson-Engels, S.; Carlsson, K. J. Microsc. 1994, 176, 238-244.
[67] Hebeda, K. M.; Wolbers, J. B.; Sterenborg, H. J. C. M.; Kamohorst, W.; van Gemert, J. J. C.; van Alphen, H. A. M. J. Photochem. Photobiol. B: Biol. 1995, 27, 85-92.
[68] Campbell, D. L.; Gudgin-Dickson, E. F.; Forkert, P. G.; Pottier, R. H.; Kennedy, J. C. Photochem. Photobiol. 1996, 64, 676-682.
[69] Wang, I.; Clemente, L. P.; Pratas, R. M. G.; Cardoso, E.; Clemente, M. P.; Montan, S.; Svanberg, S.; Svanberg, K. Cancer Lett. 1999, 135, 11-19
[70] Megnin, F.; Faustino, P. J.; Lyon, R. C.; Lelkes, P. I.; Cohen, J. S. Biochim. Biophys. Acta, 1987, 929, 173-181.
[71] Marzola, P.; Cannistraro, S. Physiol. Chem. Phys. Med. NMR 1987, 19, 279-282.
[72] Bockhorst, K.; Els, T.; Kohno, K.; Hoehn-Berlage, M. Acta Neurochir. Suppl. 1994, 60, 347-349.
[73] Sessler, J. L.; Kral, V.; Hoehner, M. C.; Chin, K. O. A.; Davilla, R. M. Pure Appl. Chem. 1996, 68, 1291-1295;
[74] Young, S. W.; Fan, Q.; Harriman, A.; Sessler, J. L.; Dow, W. C.; Mody, T. D.; Hemmi, G. W.; Hao, Y.; Miller, R. A. Proc. Natl. Acad. Sci. 1996, 93, 6610-6615.
[75] Rosenthal, D. E.; Nurenberg, P.; Becerra, C. R.; Frenkel, E. P.; Carbone, D. P.; Lum, B. L.; Miller, R.; Engel, J.; Young, S.; Miles, D.; Renschler, M. F. Clin. Cancer Res. 1999, 5, 739-745.
[76] Aime, S.; Botta, M.; Gianolio, E.; Terreno, E. Angew. Chem. Int. Ed. 2000, 39, 747-750.
[77] Mineo, P.; Faggio, C.; Micali, N.; Scamporrino, E.; Villari, V. RSC Advances, 2014, 4, 19389
[78] Mineo, P.; Vitalini, D.; Scamporrino. E. Macromol. Rapid Commun., 2002, 23, 681.
[79] Angelini, N.; Micali, N.; Villari, V.; Mineo, P.; Scamporrino, E.; Vitalini, D. Physical Review E, 2005,71, 21915
[80] Scamporrino, E.; Mineo, P.; Dattilo, S.; Vitalini, D.; Spina, E. Macromol. Rapid Commun. 2007, 28, 1546-1552

Metallic Nanoparticles

Nanoparticles (NPs) are tiny materials having size ranges from 1 to 100 nm. They can be classified into different classes based on their properties, shapes or sizes. The distinct groups include fullerenes, metal nanoparticles, ceramic nanoparticles, and polymeric nanoparticles. Nanoparticles possess unique physical and chemical properties due to their high surface area and nanoscale size. Their optical properties are reported to be dependent on the size, which imparts different colors due to absorption in the visible region. Their reactivity, toughness and other properties are also dependent on their unique size, shape, and structure. Due to these characteristics, they are suitable candidates for several applications, which include catalysis, imaging, medical applications, energy-based research, and environmental applications. Metallic nanoparticles have different physical and chemical properties from bulk metals (lower melting points, higher specific surface areas, specific optical properties, mechanical strengths, and specific magnetizations), properties that might prove attractive in various industrial applications.

Of particular importance, the optical properties are one of the fundamental attractions and characteristics of nanoparticles. For example, a 20 nm gold nanoparticle has a characteristic wine-red color. A silver nanoparticle is yellowish gray. Platinum and palladium nanoparticles are black.

Not surprisingly, the optical characteristics of nanoparticles have been used since time immemorial in sculptures and paintings even before the 4th century AD.

Figure 2.3.1: Lycurgus cup reveals a brilliant red when light passes through its sections of glass containing gold-silver alloyed nanoparticles.

The most famous example is the Lycurgus cup (fourth century AD) illustrated in ***Figure 2.3.1***. This extraordinary cup is the only complete historic example of a very special type of glass, known as dichroic glass, that changes color when held up to the light. The opaque green cup turns to a glowing translucent red when the light is shone through it internally (i.e., light is incident on the cup at 90° to the viewing direction). Analysis of the glass revealed that it

contains a very small quantity of tiny (~ 70 nm) metal crystals of Ag and Au in an approximate molar ratio of 14:1, which give it these unusual optical properties. What gives the Lycurgus Cup its special color display is the presence of these nanocrystals.

Nanotechnology is easily evident in various old churches. A well-known application of early nanotechnology is the ruby red color that was used for stained glass windows during the Middle Ages. Beautiful examples of these applications can be found in glass windows of many Gothic European cathedrals, among which the León Cathedral (Spain) (***Figure 2.3.2***) represents one of these unique masterpieces, located on the medieval French pilgrimage path to Santiago de Compostela (Spain); its impressive 2000 m^2 colored windows offer a unique view that certainly warrants a visit. Of course, the medieval artisans were unaware that they were using nanotechnology.

Figure 2.3.2: Stained glass windows in the cathedral of Leon in Spain

They just knew that a particular process produced a beautiful effect. For example, the stained glass of a wonderful rose can be seen at the world heritage Cathédrale Notre-Dame de Chartres in France. The stained glass made in medieval times is displayed in ***Figure 2.3.3***. Later chemistry clarified the reasons behind the generation of the color. These vivid colors were controlled by the size and the form (or shape) of the nanoparticles of gold and silver.

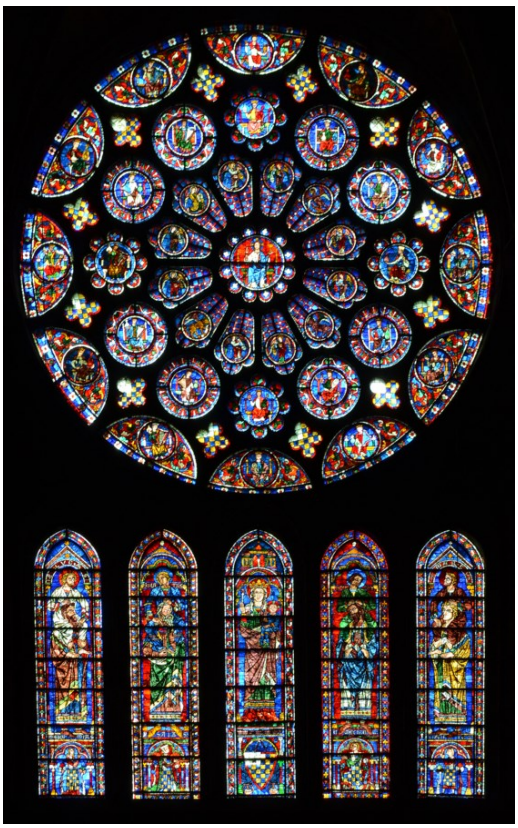

The relation between particles and their associated colors has been discussed recently by Jin and coworkers[1] in an article of 22 February 2005, the New York Times[2] summarized the relationship between the color of stained glass and the size/shape of the nanoparticles (***Figure 2.3.4***). After several decades, the ingredients present in the stained glass (colored glass) of various churches were clarified after the development of analytical instruments.

Figure 2.3.3: Rosace nord stained glass changes color depending on the morphology and size of Silver and Gold nanoparticles.

The current technology that deals with nanoparticles, or simply nanotechnology, began from the special optical phenomenon and the establishment of a theory to describe the various physical phenomena that were followed after the development of analytical instruments.

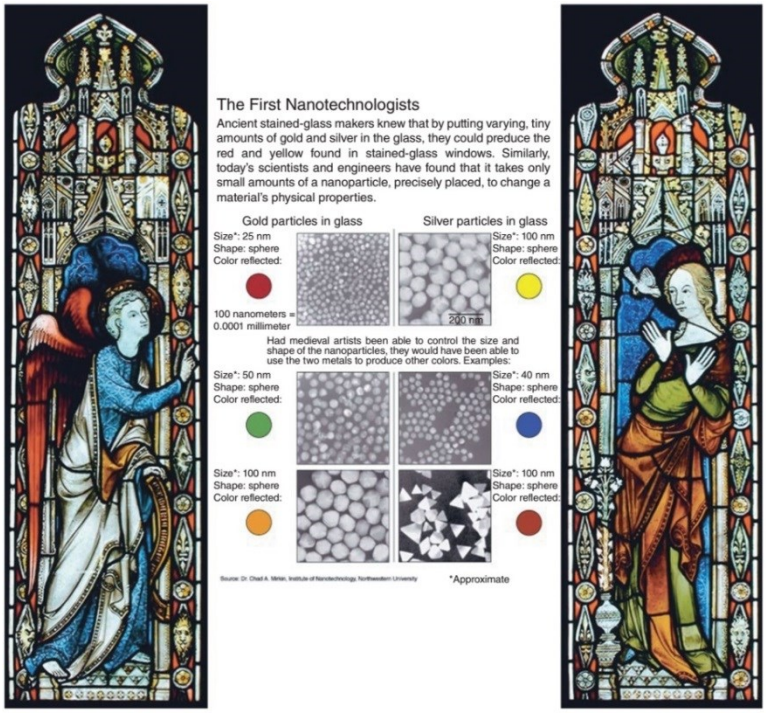

Figure 2.3.4: Comparison of the effect of size and shape of nanoparticles on the coloring of stained glass (Stained Glass Museum, Great Britain)

These interesting optical properties of nanoparticles are due to their unique interaction with light. In the presence of the oscillating electromagnetic field of the light, the free electrons of the metal nanoparticles undergo an oscillation with respect to the metal lattice. This process is resonant at a particular frequency of the light and is termed localized surface plasmon resonance (LSPR).

When a small spherical metallic nanoparticle is irradiated by light, the oscillating electric field causes the conduction electrons to oscillate coherently. This is schematically pictured in ***Figure 2.3.5***.

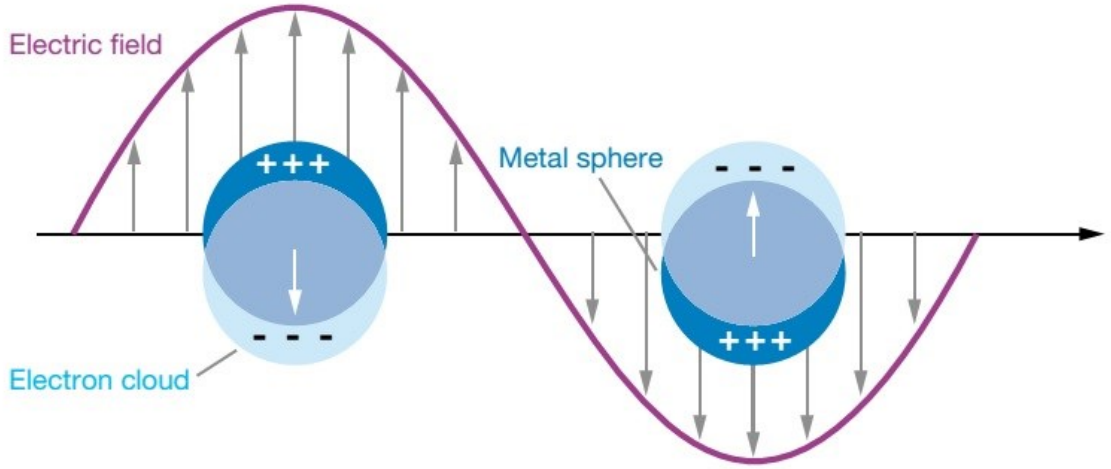

Figure 2.3.5: Scheme of the plasmonic oscillation for a spherical particle. The movement of the conduction electron cloud with respect to the nuclei is shown

When the electron cloud is displaced relatively to the nuclei, a restoring force arises from Coulomb attraction between electrons and nuclei that results in oscillation of the electron cloud relative to the nuclear framework. The oscillation frequency is determined by four factors: the density of electrons, the effective electron mass, and the shape and size of the charge distribution. The collective oscillation of the electrons is called the dipole plasmon resonance of the particle (sometimes denoted “dipole particle plasmon resonance” to distinguish from plasmon excitation that can occur in bulk metal or metal surfaces). Higher modes of plasmon excitation can occur, such as the quadrupole mode where half of the electron cloud moves parallel to the applied field and half moves antiparallel.

Furthermore, the intensity of the return force is influenced by the substance surrounding the nanoparticle and by its dielectric constant. To better explain the phenomenon, we exploit the analogy of the movement of the electronic cloud with respect to the nuclei using a mass-spring model. Just as the frequency of oscillation of the spring depends on the density, the shape and the consistency of the connected mass, so the oscillation of the electronic cloud

depends on the density, the shape and the size of the charge distribution. Moreover, just as a mass-spring system vibrates differently in the void rather than when it is immersed in a medium (such as water, oil, etc.), in the same way the electronic cloud oscillates differently also according to the consistency of the medium in which the particles are found. In other words, the oscillation of the free electrons is sensitive to the dielectric constant of the medium and to any variation thereof. In the absorption spectrum, can be observed a maximum absorption at the plasmonic resonance frequency, due to both the absorption and the scattering of light by the nanoparticles.

The value of the molar extinction coefficient for a single nanoparticle can be calculated using the Mie equation:[3]

$$E(\lambda) = \frac{(1+x)^2 8\pi^2 N a^3 \varepsilon_E^{3/2}}{3\lambda \ln(10)} \left[\frac{\varepsilon_i}{(\varepsilon_r + \varepsilon_E)^2 + \varepsilon_i^2} \right]$$

Where $E(\lambda)$ is the intensity of the extinction coefficient (due to absorption and scattering phenomena), N is the number of particles in the sensing area, a is the radius of the particles, χ is a factor related to the form of the nanoparticles, while εE is the dielectric constant of the medium adopted and ε_r and ε_i are respectively the real and imaginary part of the dielectric function of the metal. The equation highlights how the value of the resonance plasmon (LSPR) depends on the shape, size, and type of metal of which the nanoparticles are composed.

The frequency of oscillation of the free electrons following the interaction with the light radiation is specific to each metal and is called frequency of plasma. To obtain its value and the correlation with the dielectric constant, the Drude-Lorentz model is used, which couples the Lorentz model of a harmonic oscillator with that of Drude of electrical conductivity. The latter model considers the movement of electrons to conduction a metal as particles of an ideal gas. Such particles:

- Do not interact with each other;
- Own a density n;
- Collide with positive ions (which are considered stationary within the lattice) after a time τ, which slow down their motion.

The proposed model leads to the possibility of calculating the plasma frequency (ω_p) for an electron gas by the following relation:

$$\omega_p = \left(\frac{n_0\, e^2}{m_e \varepsilon_0}\right)^{1/2}$$

Where n_0 is the charge density, and it is the charge of the electron, m_e is the mass of the electron and ε_0 is the dielectric constant.

One of the reasons why nanoparticles are used is that their properties also depend on their size. To examine this dependence, we use a model adopted in quantum mechanics, that is, the particle in a potential hole; one can imagine the electrons of the nanoparticle as confined within a potential hole having the dimensions of the same nanoparticle. From the resolution of the Schrödinger equation for such a system we obtain the energy (understood as energy of the different electronic levels) of the wave function (electron) expressed by the following relation:

$$E_n = \frac{\hbar^2 \pi^2 n^2}{2ma^2}$$

Where *n* is the main quantum number, which assumes positive integers excluding the zero (n = 1,2, ... etc), with the size of the "potential hole", with *m* the mass and finally with *h* the constant of Planck divided *2π*.

This equation shows that *a* and *E* are inversely proportional. Often is necessary to know how the value of *ΔE* varies in function of *a*, to understand if the electronic transition will found to higher or lower values of energy. To do this, we calculate the value of *ΔE* between two energy states, for example *n* = 1 and *n* = 2, assigning different values to *a*.

The values obtained must be plotted in a graph, like that of ***Figure 2.3.6***, which will show us the trend of the curve, to understand if the value of the *ΔE* tends to decrease or increase as the value of *a* increases.

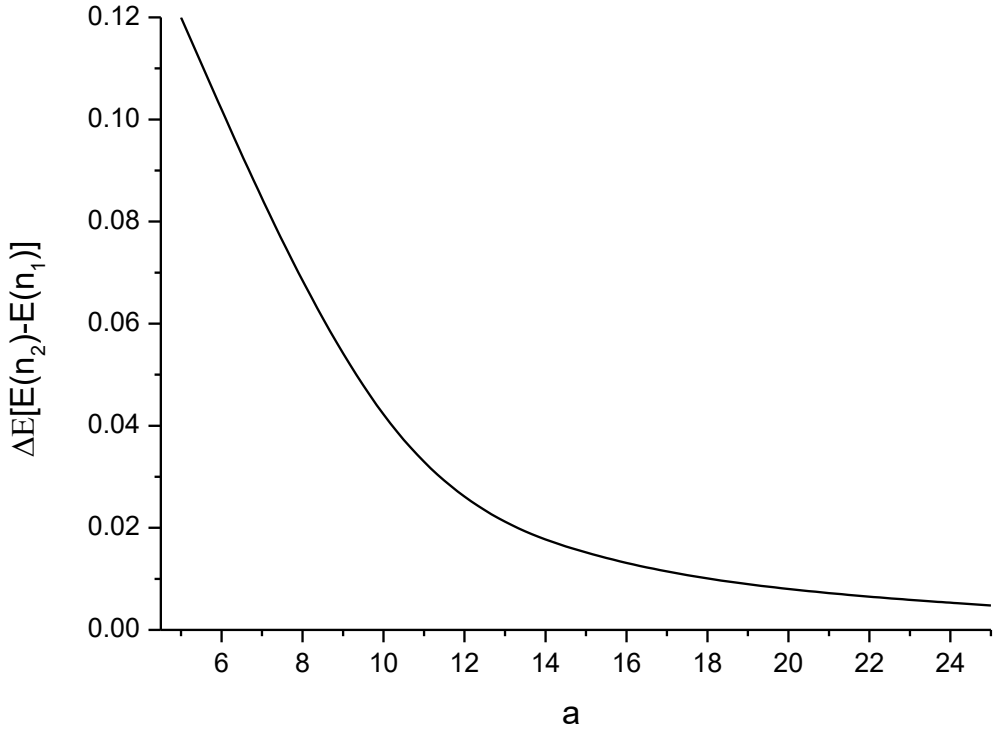

Figure 2.3.6: The graph shows the trend of the energy difference between two electronic levels (n = 2 and n = 1) as the value of a change (size of the potential hole). It is immediately clear that as the size of the potential hole decreases (which can be related to the size of the nanoparticles) the value of *ΔE* between the electronic levels increases (and vice versa) with consequent hypsochromic (or batochromic) shift of the maximum value of resonance plasmon absorption.

Therefore, decreasing the size of nanoparticles increases the distance between the different electronic levels, increases the energy that must be supplied, by radiation, to pass an electron from a fundamental level to an excited one; this involves the resonance plasmon energy to shift to higher values (blue shift). Vice versa, the increase in the size of the box, and the consequent decrease of *ΔE* of the electronic levels, results in a shift towards the red of the resonance plasmon.

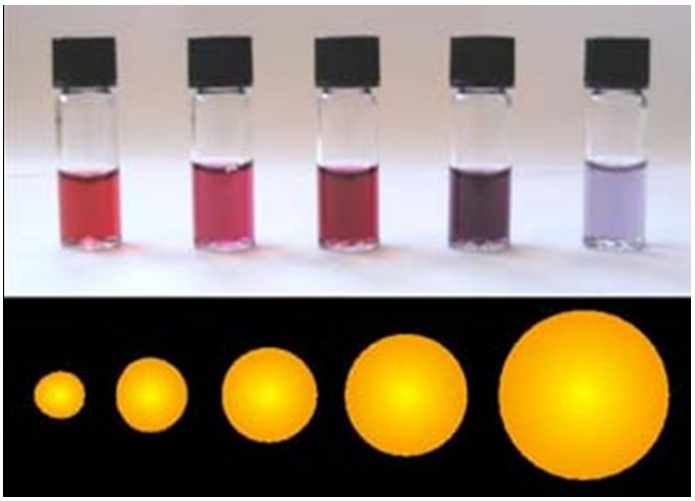

Figure 2.3.7: Gold nanoparticles; the figure shows the different colors depending on the different size of the nanoparticles.

This phenomenon, in the case of the nanoparticles of Gold and Silver, is visible to the naked eye when the value of the resonance plasmon there is in the visible range (***Fig. 2.3.7***).

Neoplastic disease, which frequency keeps increasing worldwide, causes a dramatic decline of life quality due to adverse effects of classic chemotherapy. The efficiency of systemic anticancer chemotherapy depends on the cell type and growth rate, tumor dimension, localization and vascularization, intracellular pH, and hipoxy.[4] The main obstacles frequently encountered in antitumor therapy (e.g., non-selective toxicity, low specificity, and stability, high rate of treatment resistance) may be partially overcome using nano-particulate systems[5] with targeted delivery. These may act as therapeutic or diagnostic agents, having to comply to optimal load, adequate plasmatic life, efficient bonding to the target cell/tissue, and controlled release.[6] Nanoparticles (NPs) are colloidal systems of submicron sized with a highly heterogeneous structure; following conjugation with biomolecular ligands, NPs may be used to target malignant tumors with high affinity and specificity. Moreover, their large surface area allows for their use as carriers for therapeutic/diagnostic agents.[7] Recently, metallic NPs have become a topic of interest in the scientific literature due to their physicochemical properties and intrinsic biological activity. Among metals, silver (Ag) displays the highest electrical and thermal conductivity.[8, 9, 10] Colloidal silver shows an excellent in vivo biodistribution[11, 12] and a very low toxicity;[13] in addition, it shows antitumor activity through mechanisms dependent on numerous factors including structure and size.[14] Silver antiproliferative activity was reported by in vitro studies on MCF-7 and MDA-MB-231 tumor cell lines (breast cancer)[7] and in vivo studies (glioblastoma)[15] as well. Gold nanoparticles show a unique set of properties that provide the possibility of building multifunctional platforms able to transport therapeutic agents with low water solubility and poor pharmacokinetic profile to the target and to sensitize cells and tissues to the treatment.[16] Literature study highlights several aspects that generate the necessity of a systematic approach of building metallic NP-based multifunctional platforms: induction, following conjugation, of an increased aqueous solubility of chemotherapic agents, optimization of their pharmacokinetic profile, accomplishment of target-specific and controlled release, as well as combination of a therapeutic and diagnostic effect in preliminary stages of tumor development.

Gold nanoparticles (AuNPs) exhibit a large range of physicochemical[17, 18, 19] and biological[20] parameters that enable them to function as contrast agents for molecular imaging and drug delivery agents, therefore exhibiting a theranostic approach in cancer management. Furthermore, AuNPs possess therapeutic potential, due to their unique physicochemical characteristics combined with their ability to target and destroy malignant cells. AuNPs with a

diameter within the range of 6-200 nm may infiltrate tumor cells through passive/active targeting,[21] the process being exploited in various procedures of killing cancer cells (***Figure 2.3.8***).

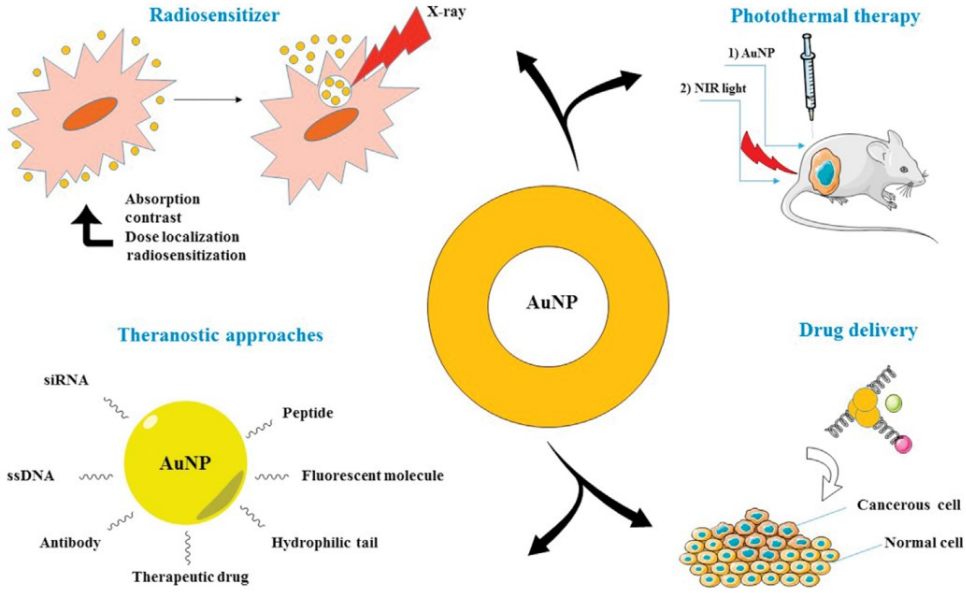

Figure 2.3.8: Various mechanisms of killing cancer cells by AuNPs

Ultrasmall AuNPs (2-15 nm) exhibit superior localization properties and deeper penetration into cancer cells or in vivo tumors in animal models;[22] particles between 2 and 6 nm show the highest tumor uptake and permeability. However, ultrasmall AuNPs may cause increased cell invasion and subsequent metastasis than larger AuNPs (20-40 nm), probably due to the upregulation of matrix metalloproteinase 9 and intercellular adhesion molecule-1.[23]

Recently, photothermal therapy (PTT) based on the nanotechnology has emerged as an appealing and minimally invasive therapeutic strategy for cancer treatment. It can deliver a specific amount of photoenergy directly into the tumor site to increase treatment efficiency and also minimize the damage to the surrounding healthy tissues.

Photothermal ablation of malignant tumors mediated by AuNPs stands as a selective, easily affordable, and highly effective tool in cancer therapy.[24] It consists of the hyperthermic treatment of cancer cells by NIR laser beams, using AuNPs as enhancers due to their ability to transform the absorbed energy into heat. As a result, the hyperthermic effect becomes significantly more intense and highly localized.[25] Spherical AuNPs may be used for the photothermal therapy of shallow cancers, such as skin cancer, by means of visible lasers.[17]

However, by conjugating gold spherical NPs with targeting adjuvant molecules, their ability to mediate photothermal ablation may be significantly increased. The combination of AuNPs

and laser irradiation resulted in increased intracellular levels of ROS, which accelerated cell death.[26]

Due to their large surface area and easy functionalization, AuNPs are involved in a diversity of studies as targeted/untargeted drug delivery agents for high drug load, enhanced cytotoxicity, and reduced effective dosage in cancer therapy.[27] The untargeted drug delivery is based on the passive cellular uptake with poor therapeutic results; higher therapeutic performance is achieved by conjugating AuNPs with tumor-targeting molecules.[28]

Targeting moieties may consist of monoclonal antibodies/antibody fragments, nonantibodies ligands (such as vitamins, carbohydrates, peptides, proteins, etc.) or aptamers.[29] Drugs are linked to AuNPs through covalent (pro-drugs) or non-covalent bonds (active molecules);[30] drug release can be triggered by endogenous or exogenous stimuli (***Figure 2.3.9***)

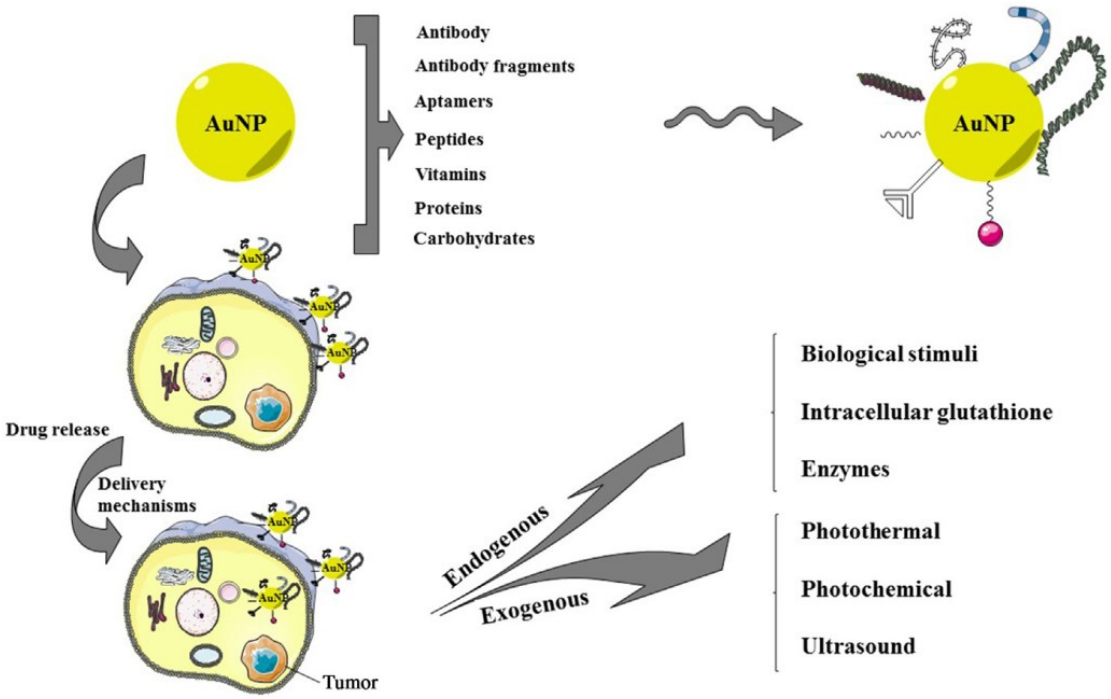

Figure 2.3.9: AuNPs as drug delivery platforms

The combination of gold nanoplatforms and active drugs may provide synergistic effects in cancer treatment.

Silver nanoparticles (AgNPs) have been widely used until now as antimicrobial agents in various industries,[31] with the antimicrobial activity displaying multiple valences: antibacterial, antifungal, antiviral.[32] Among noble metals, silver exhibits the highest efficiency of plasmon excitation which can also be tuned to various wavelengths in the visible domain. Plasmon resonance peaks for silver are sharper and slightly stronger compared to gold, thus providing

stronger photoabsorption effects.[33] Moreover, AgNPs provide various possibilities of surface functionalization and conjugation to diagnostic/therapeutic agents which make them attractive theranostic nanoplatforms.[32]

Silver proved to be more cytotoxic in vitro than gold, at concentrations above 5 mg/mL.[32]

The cytotoxic activity of AgNP on tumor cell lines is achieved through apoptotic and necrotic mechanisms that depend on their physicochemical parameters. The main drawback consists of their in vivo poor biocompatibility which can be overcome by conjugation with capping materials.[34] The unique physical (i.e., nanometric size) and optical (i.e., light scattering) properties enable AgNPs to act as in vitro/in vivo tools for cancer diagnostic and monitoring.[35] The absorption and scattering efficiency of both AuNP and AgNP has been evaluated by numerical simulation and discrete dipole approximation method;[36] the study reported a maximum efficiency for 20 nm (absorption) and 30 nm (light scattering) AgNPs that can be used in thermal and imaging procedures (Vis, NIR light).[35] An important aspect of malignant diseases is the presence of specific biomarkers in human serum. AgNPs may act as biosensors for the more accurate analytical determination of such tumor markers. Analyzing silver versus gold NPs, it has been shown that nanosilver exhibits higher molar extinction coefficient and stronger SERS ability; it is not as expensive as nanogold and can be detected easily by electrochemical methods.[37]

Despite of the metallic nanoparticles present unique properties for the application and synthesis of theranostic platforms, another class of nanoparticles has become part of this field in the last few years: we are talking about iron oxide nanoparticles, which can be used as diagnostics agents as well as treatments agent due to their magnetic properties.

[1] Jin, R.; Cao , Y.; Mirkin, C.A.; Kelly , K.L.; Schatz , G.C.; Zheng , J.G. Science 2001, 294, 1901 – 1903
[2] [http://www.nytimes.com/imagepages/2005/02/21/science/20050222_NANO1_GRAPHIC.html]
[3] Saglr, L.B; Ruvana, L.K.; Ruemmele, J.A.; Van Duyne, R.P. Nanomedicine 2011, 6, 1447-62.
[4] Amiji, M.M.; Lai, P.K.; Shenoy, D.B.; Rao, M. Pharm. Dev. Technol. 2002, 7, 195-202.
[5] Wong, H.L.; Bendayan, R.; Rauth, A.M.; Li, Y.; Wu, X.Y. Adv. Drug Deliv. Rev. 2007, 59, 491-504.
[6] Bae, Y.H.; Park, K. J. Control. Release 2011, 153, 198-205.
[7] Nguyen, V.L.; Cao, M.T.; Masayuki, N. Curr. Phys. Chem. 2014, 4, 173-194
[8] Rao, P.V.; Nallappan, D.; Madhavi, K.; Rahman, S.; Wei, L.J.: Gan, S.H.; Oxid. Med. Cell. Longev. 2016.
[9] Tran, H.Q.; Nguyen, V.Q.; Le, A.T. Adv. Nat. Sci: Nanosci. Nanotechnol. 2013, 4, (20 pp.).
[10] Afify, T.A.; Saleh, H.H.; Ali, Z.I.; Polym. Compos. 2015.
[11] Garza-Ocan˜as, L.; Ferrer, D.A.; Burt, J.; Diaz-Torres, L.A.; Cabrera, M.R.; Tamez Rodrı ´guez, V. Metallomics 2010, 2, 204-210.
[12] Stensberg, M.C.; Wei, Q.; McLamore, E.S.; Porterfield, D.M.,; Wei, A.; Sepu´lveda, M. S. Nanomedicine 2011, 6, 879-898
[13] Munger, M.A.; Radwanski, P.; Hadlock, G.C.; Stoddard, G.; Shaaban, A.; Falconer, J. Nanomedicine 2014.
[14] Zhang, X.F.; Liu, Z.G.; Shen, W.; Gurunathan, S. Int. J. Mol. Sci. 2016
[15] Urbanska, K.; Paja ´ ¸k, B.; Orzechowski, A.; Sokołowska, J.; Grodzik, M.; Sawosz, E. Nanoscale Res. Lett. 2015, 1, 98
[16] Dreaden, E.C.; Austin, L.A.; Mackey, M.A.; El-Sayed, M.A. Ther. Deliv. 2012, 3, 457-478.
[17] Capek, I. J. Surf. Sci. Technol. 2013, 29, 1-18.
[18] Huang, H.C.; Rege, K.; Heys, J.J. ACS Nano 2010, 4, 2892-2900.
[19] Zhang, Y.; Chu, W.; Dibaji Foroushani, A.; Wang, H.; Li, D.; Liu, J. Materials 2014, 7, 5169-5201
[20] Ahmad, M.Z.; Akhter, S.; Rahman, Z.; Akhter, S.; Anwar, M.; Mallik, N. J. Pharm. Pharmacol. 2013, 65, 634-651.
[21] Kodiha, M.; Wang, Y.M.; Hutter, E.; Maysinger, D.; Stochaj, U.; Theranostics 2015, 5, 357-370
[22] Huang, K.; Ma, H.; Liu, J.; Huo, S.; Kumar, A.; Wei, T. ACS Nano 2012, 6, 4483-4493.
[23] Liu, Z.; Wu, Y.; Guo, Z.; Liu, Y.; Shen, Y.; Zhou, P. PLoS One 9, 2014.
[24] Mocan, L.; Matea, C.T.; Bartos, D.; Mosteanu, O.; Pop, T.; Mocan, T. Clujul Med. 2016, 89, 199-202
[25] Li, J.-L.; Gu, M. J. Sel.Top. Quantum Electron. 2010, 16, 989-996
[26] Minai, L.; Yeheskely-Hayon, D.; Yelin, D. Sci. Rep. 2013, 3, 2146
[27] Dreaden, E.C.; Austin, L.A.; Mackey, M.A.; El-Sayed, M.A. Ther. Deliv. 2012, 3, 457-478.
[28] Ajnai, G.; Chiu, A.; Kan, T.; Cheng, C.-C.; Tsai, T.-H.; Chang, J. J. Exp. Clin. Med. 2014, 6, 172-178
[29] Jiao, P.F.; Zhou, H.Y.; Chen, L.X.; Yan, B. Curr. Med. Chem. 2011, 18, 2086-2102.
[30] Voliani, V.; Signore, G.; Nifosi, R.; Ricci, F.; Luin, S.; Beltram, F. Recent Pat. Nanomed. 2012, 2, 34-44.
[31] Abou El-Nour, K.M.M.; Eftaiha, A.; Al-Warthan, A.; Ammar, R.A.A. Arab. J. Chem. 2010, 3, 135-140.
[32] Tran, H.Q.; Nguyen, V.Q.; Le, A.T. Adv. Nat. Sci: Nanosci. Nanotechnol. 2013, 4, (20 pp.)
[33] Sironmani, A.; Kiruba, D. InTech, 2011.
[34] Sukumar, U.K.; Bhushan, B.; Dubey, P.; Matai, I.; Sachdev, A.; Packirisamy, G. Int. Nano Lett. 2013, 3, 45
[35] Austin, L.A.; Mackey, M.A.; Dreaden, E.C.; El-Sayed, M.A. Arch. Toxicol. 2014, 88, 1391-1417.
[36] Zhang, Y.J. Plasmonics 2011, 6, 393-397
[37] Chen, Z.; Leim, Y.; Chen, X. Microchim. Acta 2012, 179, 241-248.

Iron Oxide Nanoparticles

Iron oxides are common compounds which are widespread in nature and can be readily synthesized in the laboratory. Magnetic iron oxides have served humans for centuries. For example, the application of small iron oxide nanoparticles (IONPs) as a contrast agent for in vitro diagnostics has been practiced for nearly half a century.[1, 2, 3]In the past decade, the synthesis of magnetic IONPs has been intensively developed not only for its fundamental scientific interest but also for its many technological applications, such as targeted drug delivery, magnetic resonance imaging (MRI), magnetic hyperthermia and thermoablation, bioseparation, and biosensing.[4, 5, 6, 7]Particularly, bioapplications based on magnetic nanoparticles (NPs) have received considerable attention because NPs offer unique advantages over other materials. For example, magnetic IONPs are inexpensive to produce, physically and chemically stable, biocompatible, and environmentally safe.[8]

Eight iron oxides are known,[9] among these iron oxides, hematite (α-Fe_2O_3), magnetite (Fe_3O_4) and maghemite (γ-Fe_2O_3) are very promising and popular candidates due to their polymorphism involving temperature-induced phase transition. Each of these three iron oxides has unique biochemical, magnetic, catalytic, and other properties, which provide suitability for specific technical and biomedical applications.

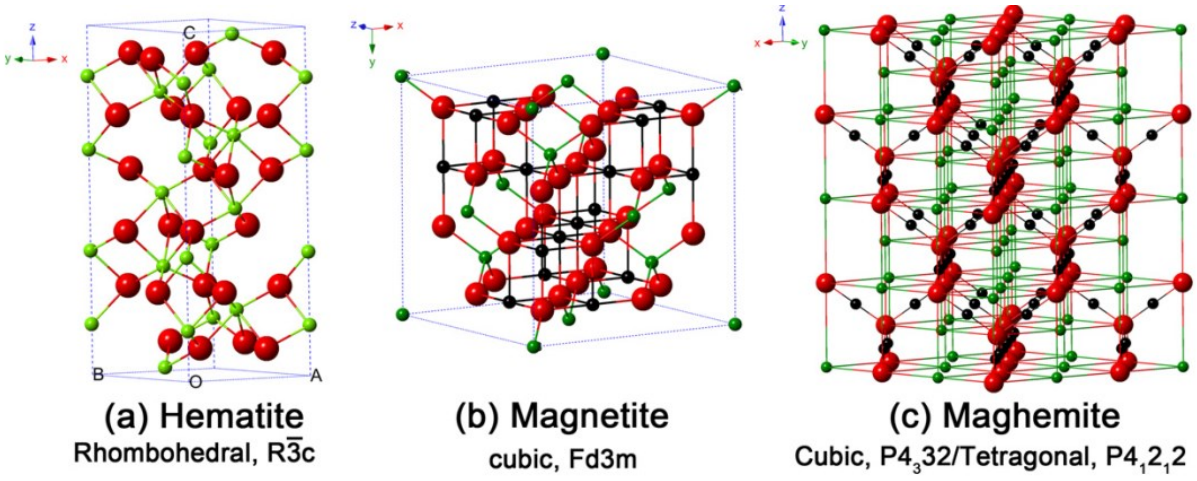

Figure 2.4.1: Crystal structure and crystallographic data of the hematite, magnetite, and maghemite (the black ball is Fe^{2+}, the green ball is Fe^{3+} and the red ball is O^{2-}).

Hematite (α-Fe_2O_3): as the most stable iron oxide and n-type semiconductor under ambient conditions, hematite (α-Fe_2O_3) is widely used in catalysts, pigments and gas sensors due to its low cost and high resistance to corrosion. It can also be used as a starting material for the synthesis of magnetite (Fe_3O_4) and maghemite (γ-Fe_2O_3), which have been intensively

pursued for both fundamental scientific interests and technological applications in the last few decades.[10] Hematite is an n-type semiconductor with a band gap of 2.3 eV, where the conduction band (CB) is composed of empty d-orbitals of Fe^{3+} and the valence band (VB) consists of occupied 3d crystal field orbitals of Fe^{3+} with some admixture from the O 2p non-bonding orbitals.[11] As shown in ***Figure 2.4.1a***, Fe^{3+} ions occupy two-thirds of the octahedral sites that are confined by the nearly ideal hexagonal close-packed O lattice.

Magnetite (Fe_3O_4): As shown in ***Figure 2.4.1b***, Fe_3O_4 has the face-centered cubic spinel structure, based on 32 O^{2-} ions and close-packed along the [111] direction. Fe_3O_4 differs from most other iron oxides in that it contains both divalent and trivalent iron. Fe_3O_4 has a cubic inverse spinel structure that consists of a cubic close-packed array of oxide ions, where all the Fe^{2+} ions occupy half of the octahedral sites and the Fe^{3+} are split evenly across the remaining octahedral sites and the tetrahedral sites. In stoichiometric magnetite FeII/FeIII = 1/2, and the divalent irons may be partly or fully replaced by other divalent ions (Co, Mn, Zn, etc). Thus, Fe_3O_4 can be both an *n*- and *p*-type semiconductor. However, Fe_3O_4 has the lowest resistivity among iron oxides due to its small bandgap (0.1 eV).

Maghemite (γ-Fe_2O_3): As shown in ***Figure 2.4.1c***, the structure of γ-Fe_2O_3 is cubic; each unit of maghemite contains 32 O^{2-} ions, 21⅓ Fe^{3+} ions, and 2⅓ vacancies. Oxygen anions give rise to a cubic close-packed array while ferric ions are distributed over tetrahedral sites (eight Fe ions per unit cell) and octahedral sites (the remaining Fe ions and vacancies). Therefore, the maghemite can be considered as fully oxidized magnetite, and it is an n-type semiconductor with a bandgap of 2.0 eV.

Understanding the correlation between the magnetic properties and the size and shape of IONPs is a prerequisite for widespread applications of magnetism in data storage and bio-separation areas. Generally, α-Fe_2O_3 has weak ferromagnetism at room temperature, while the saturation magnetization is often smaller than 1 emu g^{-1}. However, γ-Fe_2O_3 and Fe_3O_4 exhibit ferrimagnetism at room temperature, with the saturation magnetization reaching to 92 emu g^{-1}. It is noteworthy that many properties of IONPs depend on their size and shape. In general, IONPs become superparamagnetic at room temperature when the size of IONPs is below about 15nm, meaning that the thermal energy can overcome the anisotropy energy barrier of a single nanoparticle. However, aggregation among superparamagnetic IONPs is a common phenomenon. Hence, for protecting bare IONPs against aggregation, the magnetic properties can be tailored by the coating materials, such as Au, Ag, and Co_3O_4.

An unavoidable problem associated with magnetic IONPs in the size range is their intrinsic instability over longer periods, which manifests in two main ways:

- loss of dispersibility, where small NPs tend to aggregate and form large particles to reduce the surface energy; and
- loss of magnetism, where bare IONPs are easily oxidized in air due to their high chemical activity, especially Fe_3O_4 and γ-Fe_2O_3 NPs.

Therefore, it is crucial to develop a proper protection strategy to chemically stabilize bare IONPs against damage during or after the subsequent application. For biomedical applications, it is necessary to obtain water dispersible NPs, because most biological media are nearly neutral aqueous solutions. In view of the many strategies and their subsequent application, efforts have been devoted to fabricating four types of IONP-based materials, including the core-shell structure, matrix dispersed structure, Janus-type heterostructures and shell-core-shell structure ***(Figure 2.4.2***).

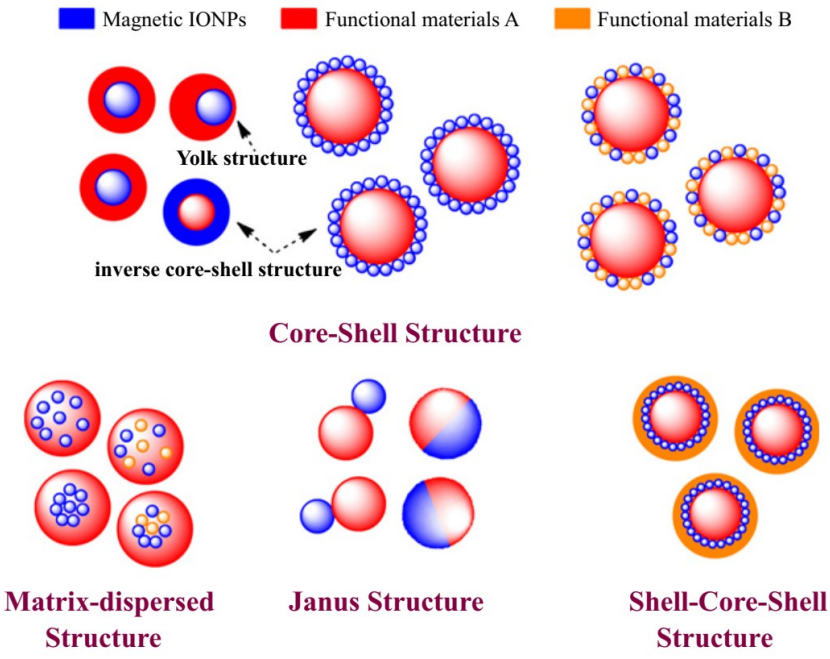

Figure 2.4.2: Typical morphologies of magnetic composite nanomaterials. Blue spheres represent magnetic IONPs, and the nonmagnetic entities and matrix materials are displayed in other colors. The nonmagnetic entity may provide the composite material with further functionalities and properties, providing multifunctional hybrid systems.

The most used materials for the functionalization of the nanoparticle surface are:

- *Small molecules and surfactants*: Organic molecules are used with different structure and length that usually have two groups that can be activated at the ends (e.s. -COOH, -SH, OH, $-NH_2$). In the case of metallic nanoparticles it is usual to use thiol molecules

for the S-Me binding force, whereas in the case of magnetic nanoparticles silane molecules are used since they do not interfere with the magnetic properties of the system.

- *Polymers*: Compared to small molecules or surfactants, the functionalization with polymers allows not only a greater number of activatable functional groups and greater colloidal stability but also plays an important role from the biological point of view (pharmacokinetics and biodistribution).[12] Precisely for this reason, there are different polymers, both of synthetic and natural origin, used for surface functionalization (***Table 2.4.3***)
- *Biomolecules*: Another functionalization strategy sees the anchoring on the surface of the nanoparticles of biomolecules, such as enzymes, antibodies, proteins, polypoid, etc, to increase their biocompatibility and targeting capacity.[13, 14, 15, 16, 17]

Table 2. Examples of smart polymer functionalized IONPs.

Type of stimulus	Polymers	Functional groups	Clinical products and examples
pH	Polypropylacrylic acid (PPAA), polyethacrylic acid (PEAA); Poly(methyl methacrylate) (PMMA) Poly (acrylic acid) (PAA)	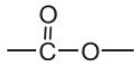	
	Chitosan	$-NH_2$ $-OH$	
	Poly(L-lysine), Poly(ethyleneimine) (PEI),	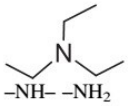	
	Poly(4-vinylpyridine), poly(2-vinylpyridine) (PVP) and poly(vinylamine) (PVAm)	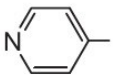	
			
Temperature	Poly(N-isopropylacrylamide) PNIPAAm	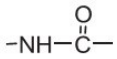	Pluronics® F127 Polox-amers® 407, Tetronics®
	Poly(N,N′-diethyl acrylamide), Poly(dimethylamino ethyl methacrylate)		PEG/PLGA, Regel ®
		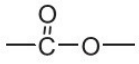	
			
	Polyethylene glycol (PEG)	–O–, –OH	T_1 MR Contrast Agent
Light	Polyethylene glycol (PEG)	–O–	
	Poly (lactic acid)	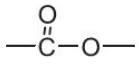	

Table 2.4.3: Type of Polymers used for the functionalization of nanoparticle systems. From left to right we have: the type of external stimulus that activates the polymer; the name of the polymer; the respective functional groups, and the examples of already patented clinical products.

In addition to functionalization with organic molecules, both small and large, the development of inorganic nanoparticles has recently been developed with a second inorganic system, in a core-shell type structure. This is mainly implemented to improve the stability over time of magnetic particles which may present aggregation phenomena (particles with too small dimensions aggregate forming clusters to reduce surface energy) or loss of magnetism (since the surface is oxidizable if exposed air).

The most common inorganic materials used to coat the magnetic nanoparticles are:[18, 19, 20]

- *Silica*: The silica coating is often used because it can better the dispersion in a solution of the magnetic nanoparticles, by isolating them and avoiding collapses due to the dipolar attraction. Moreover, the silica layer can increase the resistance of the same in an acid environment and the presence of silanol groups, if properly activated, would allow the anchoring on the surface of different organic molecules that would provide more specific properties to the final system.
- *Metals*: Metal nanoparticles (Au, Ag, Cu, Pd, Pt, etc) have a full range of interesting features (Localized Surface Plasmon Resonance and Surface-Enhanced Raman Scatting, SERS) and many of them, formed by Anisotropic metals, have been used in catalysis, as contrast in imaging, in medicine and in sensing. The possibility of combining the chemical-physical properties of magnetic and metallic nanoparticles has pushed research in this direction, obtaining optimal results in various fields, such as catalysis, biotechnology, and biomedicine. Furthermore, the metal shell is further functionalized with different charges, functional groups or organic molecules that increase its biocompatibility or specificity. Studies of literature have shown that the coating of Gold or Silver turns out to be one of the best options due to the low reactivity with magnetic NPs, thus maintaining the properties of both the coating and the magnetic NPs.[21]

Biocompatibility and toxicity of IONPs are important criteria to consider for their biomedical applications. Parameters determining biocompatibility and toxicity are the nature of the magnetically responsive component and the final size of the composite particles including their core and the coatings (shell). Ideally, composite IONPs must also have a high magnetization so that their movement in the blood can be controlled with an external magnetic field until it is immobilized close to the targeted pathologic tissue. Magnetic IONPs with a long blood retention time, biodegradability, and low toxicity have emerged as one of the primary nanomaterials for biomedical applications in vitro and in vivo. Some biomedical applications require surface functionalized, especially core-shell type, magnetic IONPs.

Nanoparticles coating is used to improve the physicochemical and biological properties of the final nanostructures. Bare IONPs tend to aggregate in physiological conditions, due to their hydrophobic nature and weakly charged surface, therefore coating is often used to avoid agglomeration.[22] The coating provides several advantages: core protection against corrosion and environmental degradation, anchorage points for potential targeting moieties, protection against particle aggregation, increased biocompatibility, colloidal stability, and enhanced release at the therapeutic site.[23] Inorganic materials, such as gold,[24] silica,[25] mesoporous hydroxyapatite[26] and organic materials, such as synthetic and natural polymers, surfactants,

and proteins[27], are usually used for coating or grafting the NPs. The hydrophilic polymer coating of IONPs enhances their water-solubility and biocompatibility and facilitates their chemical derivatization. PEG, dextran, chitosan, and starch[28] are highly used. PEGylated NPs are characterized by an enhanced permeability, stability, and prolonged half-life in the bloodstream, which increases target size localization.[29] Dextran/PEG coating provides superior in vitro biocompatibility and in vivo interaction with the biological system.[30] FERIDEX is a commercially available IONP, coated with dextran, designed to confer biocompatibility and aqueous stability in the saline environment of biological tissues.[31]

In recent years, SPIONs have emerged as one of the most promising tools for disease diagnosis and treatment monitoring. Magnetic NPs may also be used for labeling cells with weakly expressing biomarkers and for detection of bacteria.[32] NPs can be designed to fit the image purpose, due to their composition, size, shape and the possibility of shape functionalization to attach imaging agents; they can be targeted to the diseased region, allowing the contrast agent to penetrate into the cell/tissue/organ.[33] Magnetic NPs can be used in MRI, CT, PET, single-photon emission computed tomography (SPECT) and optical fluorescence.[34]

Magnetic NPs are used as contrast agents for MRI because of their superparamagnetic properties, which allow them to be magnetized only under the influence of an externally applied magnetic field, and to lose this magnetization once the field is deactivated.[35] [36] This property allows superparamagnetic iron oxide nanoparticles (SPIONs) to be used in MRI as negative contrast agents.[37]

Furthermore, SPIONs could locally convert external high-frequency field energy to thermal energy, which is called magnetic hyperthermia.[38] [39] [40]Magnetic hyperthermia induces cancerous cells undergoing apoptosis with a specific target under high-temperature conditions.[36] It also sensitizes cancer cells to radiation therapy or chemotherapy. Specifically, magnetic hyperthermia mediated by SPIONs can increase the temperature at the tumor center to greater than 40°C after exposure to the alternating magnetic field,[41] resulting in tumor growth inhibition in a human head and neck tumor xenograft model. SPION-facilitated magnetic hyperthermia has been translated into human patients in clinical trials.[42] Iron oxide NPs-mediated magnetic hyperthermia, triggered by the external magnetic field, not only ablated cancer cells but also increased the effectiveness of other treatments. In comparison with laser-triggered PTT, magnetic hyperthermia therapy is more promising in translation, due to the unlimited tissue penetration ability and reduced skin damage. Although there may be some concerns about the efficiency of magnetic-thermal conversion, it can be solved by radio-magnetic hyperthermia or chemo-magnetic hyperthermia-combined therapy.

Besides to accurately assess the efficiency of intratumoral drug delivery, especially NP-mediated drug delivery, noninvasive imaging is preferred in individual patients since human tumors have highly heterogeneous tumor blood vessel distributions and stromal drug delivery barriers. Such a precise oncology approach using image-guided drug delivery systems, or theranostic NPs, should allow timely assessment and adjustment of treatment strategies for cancer patients. In addition to the promising imaging property, theranostic NPs have been produced to carry a single therapeutic agent or the combination of two or more drugs,[43 44 45] including chemotherapy drugs, small-molecule agents, photosensitizers, and siRNAs. By labeling with additional imaging agents, intratumoral accumulation of theranostic NPs could be detected using a single or multimodal noninvasive imaging. As imaging NPs with high drug-loading capacity and low toxicity, SPIONs have become an attractive theranostic NP platform for the translational development of novel image-guided cancer therapeutic agents.

[1] Wu W.; He Q. G.; Jiang C. Z. Nanoscale Res. Lett. 2008, 3 397
[2] Gupta A. K.; Gupta M. Biomater. 2005, 26 3995
[3] Gilchrist R.; Medal R.; Shorey W. D.; Hanselman R. C.; Parrott J. C.; Taylor C. B. Ann. Surg. 1957, 146 596
[4] Yang L. J. Biomed. Nanotechnol. 2008, 4 439
[5] Lee N.; Hyeon T. Chem. Soc. Rev. 2012, 41 2575
[6] Laurent S.; Dutz S.; Häfeli U. O.; Mahmoudi M. Adv. Colloid Interface Sci. 2011, 166 8
[7] Cao M.; Li Z.; Wang J.; Ge W.; Yue T.; Li R.; Colvin V. L.; Yu W. W. Food Sci. Technol. 2012,27 47
[8] Lu A H; Salabas E. L.; Schuth F. Angew. Chem. Int. Edn. 2007, 46 1222
[9] Cornell R. M.; Schwertmann U. Am. J. of Anal. Chem., 2003, 6
[10] Wu W.; Xiao X. H.; Zhang S. F.; Zhou J. A.; Fan L. X.; Ren F.; Jiang C. Z. J. Phys. Chem. C 2010, 114 16092
[11] Zhang Z.; Boxall C.; Kelsall G. H. Colloids Surf. A 1993, 73 145
[12] Yang X. Q.; Grailer, J. J.; Rowland, I. J.; Javad, A.; Hurley, S. A.; Steeber, D. A.; Gong S. Q. 2010 31, 9065
[13] Samanta, B.; Yan, H.; Fischer, N. O.; Shi, J.; Jerry, D. J.; Rotello, V. M. J. Mater. Chem., 2008, 18, 1204
[14] Iwaki, Y.; Kawasaki H.; Arakawa, R. Anal. Sci., 2012, 28, 893
[15] Okuda, M.; Eloi, J-C.; Jones, S. E. W.; Sarua, A.; Richardson, R M.; Schwarzacher, W. Nanotechnology, 2012, 23, 415601
[16] Marcelo, G.; Muñoz-Bonilla, A.; Rodríguez-Hernández, J.; Fernández-García, M. Polym.Chem., 2013, 4, 558
[17] Xie, J.; Wang, J.; Niu, G.; Huang, J.; Chen, K.; Li, X.; Chen, X. Chem. Commun, 2010, 46, 433
[18] Zhao Y.; Zhang W.; Lin Y.; Du D. Nanoscale 2013, 5, 1121
[19] He X.; Tan L.; Chen D.; Wu X.; Ren X.; Zhang Y.; Meng X.; Tang F. Chem. Commun. 2013,49 4643
[20] Wang D-W et al J. Mater. Chem. B 2013, 1, 2934
[21] Wu, W.; Wu, Z.; Yu, T.; Jiang, C.; Kim, W-S. Adv. Drug Del. Rev. 2008, 60, 1307–1315].
[22] Nasiri, R.; Almaki, J.H.; Idris, A.B.; Majid, F.A.M.; Nasiri, M.; Salouti, M. et al. Mater. Sci. Eng. C 2016, 69, 1147-1158.
[23] Malekzadeh, A.M.; Ramazani, A.; Tabatabaei Rezaei, S.J.; Niknejad, H.; J. Colloid Interface Sci. 2017, 490, 64-73.
[24] Azhdarzadeh, M.; Atyabi, F.; Saei, A.A.; Varnamkhasti, B.S.; Omidi, Y.; Fateh, M. et al. Colloids Surf. B: Biointerfaces 2016, 143, 224-232.
[25] Sodipo, B.K.; Aziz, A.A. J. Magn. Magn. Mater. 2016.4, 16, 275-291.
[26] Aval, N.A.; Islamian, J.P.; Hatamian, M.; Arabfirouzjaei, M.; Javadpour, J.; Rashidi, M.-R. Int. J. Pharm. 2016, 509, 159-167
[27] Zhang, Y.; Newton, B.; Lewis, E.; Fu, P.P.; Kafoury, R.; Ray, P.C. et al. Toxicol. In Vitro 2015, 29, 762-768.
[28] Douziech-Eyrolles, L.; Marchais, H.; Herve´, K.; Munnier, E.; Souce´, M.; Linassier, C. et al. Int. J. Nanomed. 2007, 2, 541-550.
[29] Jokerst, J.V.; Lobovkina, T.; Zare, R.N.; Gambhir, S. Nanomedicine 2011, 6, 715-728.
[30] Sabareeswaran, A.; Ansar, E.B.; Harikrishna Varma, P.R.V.; Mohanan, P.V.; Kumary, T.V. Nanomedicine 2016, 12, 1523-1533.
[31] Cherukuri, P.; Glazer, E.S.; Curley, S.A. Adv. Drug Deliv. Rev. 2010, 62, 339-345
[32] Muluneh, M.; Issadore, D. Adv. Drug Deliv. Rev. 2014, 66, 101-109.
[33] Savla, R.; Minko, T. Adv. Drug Deliv. Rev. 2016.
[34] Thomas, R.; Park, I.K.; Jeong, Y.Y. Int. J. Mol. Sci. 2013, 14, 15910-15930
[35] Bean, C.P.; Livingston, J.D. J. Appl. Phys. 1959, 30, S120-S129
[36] Laurent, S.; Vander Elst, L.; Roch, A.; Muller, R.N. In: Carretta, P., Lascialfari, A. (Eds.), NMR-MRI, μSR and Mo¨ssbauer Spectroscopies in Molecular Magnets. Springer, Milan, 2007, pp. 71-87.
[37] Josephson, L.; Lewis, J.; Jacobs, P.; Hahn, P.F.; Stark, D.D. Magn. Reson. Imaging 1988, 6, 647-653.
[38] Hilger, I. Int. J. Hyperther. 2013, 29 (8), 828-834
[39] Lartigue, L.; Innocenti, C.; Kalaivani, T. et al. J. Am. Chem. Soc. 2011, 133 (27), 10459-10472.
[40] Torres-Lugo, M.; Rinaldi, C. Nanomedicine (Lond.) 2013, 8 (10), 1689-1707.
[41] Zhao, Q.; Wang, L.; Cheng, R. et al. Theranostics 2012 2, 113-121
[42] Maier-Hauff, K.; Ulrich, F.; Nestler, D. et al., J. Neurooncol. 2011, 103 (2), 317-324.
[43] Choi, K.Y.; Liu, G.; Chen, X. Nanoscale 2012a, 4 (2), 330-342.
[44] Choi, K.Y.; Jeon, E.J.; Yoon, H.Y. et al. Biomaterials 2012b, 33 (26), 6186-6193.
[45] Schleich, N.; Sibret, P.; Danhier, P. et al. Int. J. Pharmaceut. 2013, 447 (1-2), 94-101.

Aim of the Work

As described in the previous paragraphs, the interest in nanotechnologies and, in particular, in nanoparticles (NPs) is due to the ability to transport molecules of therapeutic interest in a protected form, controlling their blood circulation and tissue distribution. The composition of NPs is crucial in inducing physical/photophysical properties such as strong optical absorption (Au and Ag); photoluminescence, fluorescence or phosphorescence (Y_2O_3); magnetic moment (Fe or Co oxides) - useful in biomedical applications (labeling, detection, imaging, MRI, etc.) and that can be a starting point for uses ranging from sensing to personalized nanomedicine. From the specific functionalization of the surface of the NPs, it will be possible to program the type of interaction and the scope of application. In theranostics (one of the new strategies of personalized medicine), the interest in magnetic (Fe or Co oxides) and noble metal nanoparticles (Au, Ag) is remarkable, both for their magnetic and optical properties. In this context, parameters such as shape, size, and polydispersity of nanoparticles are extremely important. However, problems such as stability, biocompatibility, in vivo toxicity and efficiency in passive and/or active targeting remain completely unresolved. This project aims to address and solve these issues. The functionalization of nanoparticles with macromolecular systems capable of performing diagnostic, therapeutic and biocompatibility functions can make these NPs systems more efficients. Excellent results are expected by using, in a combined manner, porphyrin systems (for spectroscopic and photophysical properties capable, if exposed to suitable wavelength, to generate singlet oxygen), targeting/pharmaceutical agents and polyethylene glycol chains, essential in aqueous phase transmission, and also able to confer biocompatibility to the hybrid system (stealth effect).

The following PhD research project focuses mainly on the field of oncological therapies where the primary purpose of the research is to increase the effectiveness of treatments and to decrease the undesirable toxic side effects of current therapies, which indiscriminately affect both sick and healthy cells, causing often serious collateral damages.

The goal can be achieved by creating biocompatible smart systems that do not require carriers to function, but that are themselves able to "move" recognize and treat diseased tissues. These new multi-tasking molecules, therefore equipped with diagnostic and therapeutic properties, are part of the category of theranostics.

The research project proposes the development of new organic/inorganic hybrid nanosystems having a core-shell-shell structure, consisting of nanoparticles (NPs) (Ag, Au and/or Fe_3O_4@Au) in which PEGylate porphyrin systems are bounded on the surface. The choice of

synthesizing these hybrid systems stems from the possibility of exploiting the different properties of the individual components, combined into a single complex system.

The gold nanoparticles were chosen for the different properties in the teranostic field. AuNPs are good candidates for labelling applications because of their ability to interact strongly with visible light. Upon exposure to light, free electrons in gold atoms are excited to a state of collective oscillation known as surface plasmon resonance (SPR), conferring gold the ability to absorb and scatter visible light. In labelling applications, AuNPs are targeted and accumulated at the site of interest and based on their optical scattering properties, they enable visualization of the region under study. AuNPs may then be detected by any of the following ways: phase contrast optical microscopy, dark field microscopy, photothermal imaging, and photoacoustic imaging.

Furthermore, AuNPs attract particular interest because they possess enhanced absorption cross-sections. Their strong absorbance enables effective laser therapy with minimal "collateral damage" to the surrounding healthy tissue. The mechanism by which AuNPs exert their photothermal effect is through SPR and is called photothermal effect. The speed at which energy is converted and dissipated to the surrounding environment presents an efficient means of rapidly inducing hyperthermia in the vicinity of AuNPs following irradiation with light. Irreversible cell damage resulting from denaturation of proteins and disruption of cell membrane will occur in the areas subjected to high temperatures.

Silver nanoparticles were chosen thanks to their high thermal conductivity, plasmonic properties, chemical stability and antibacterial ability.

Another important feature of AgNPs is their involvement in cancer treatment.

The AgNPs are a promising tool as anticancer agents in diagnostics and probing, with strong effects against different cancer cell lines offering many advantages. Their better penetration, and the possibility to track AgNPs in the body make them a more efficient tool in cancer treatment with less risk compared to standard therapeutic procedures. The unique AgNP properties, such as easy surface functionalization, optical properties, reproducible synthetic routes and high surface: volume ratio, makes them suitable for cancer treatment. The optical properties can be tuned to have an absorption at specific wavelengths that is useful for imaging and photothermal applications in tissue. In addition, Ag NPs are used as an ablation tool for cancer cells due their ability to convert radiofrequencies into heat and can bring significant improvements in the antibacterial activity of this element, through specific effect such as an adsorption at bacterial surfaces

The magnetite core will provide the paramagnetic properties necessary for use in the Targeted Drug Delivery (NPs tissues via magnetic field), in Magnetic Resonance Imaging and

Magnetic Hyperthermia (the magnetic NPs may be subjected to an alternating magnetic field, overheating and thus determining cell death). The presence of gold serves both to stabilize the NPs of magnetite, thus overcoming the problem of the stability of these over time, and to give it photothermal properties (hyperthermia by light stimulation). The nanoscale dimensions of the complex system (40-100 nm) will allow the latter to perform passive targeting (EPR effect), while the external shell obtained by functionalization with the PEGylated porphyrins derivatives will induce the necessary water solubility and biocompatibility of the whole system. Given the excellent absorption spectroscopic properties, fluorescence (to monitor its presence inside the tissues) and photocytotoxicity (for the photodynamic therapy of tumors), it will be possible to strongly implement the field of application and efficiency of the nanohybrid systems.

Upon validation of the functioning of the system, and therefore of the project itself, the synthesis strategy can be adapted to functionalize and/or co-functionalize the nanoparticles also with active targeting agents (folic acid, oligopeptides, biotine, etc.) to limit the accumulation exclusively in diseased tissues endowed with specific receptors, further implementing the targeting properties described above.

In synthesis, the results obtained during my PhD research work, could be a fundamental starting point in order to developing systems for theranostic applications, exploiting both the nanoparticles and the porphyrin derivatives properties, thus to obtain multifunctional platforms for biomedical applications.

Experimental

Synthesis of 5,10,15, 20 tetrakis (p-hydroxyphenyl) porphyrin

The synthesis of 5,10,15,20 tetrakis (p-hydroxyphenyl) porphyrin (H_2TPP), whose structure is shown below (***Figure 3.1.1***), was carried out according to the method described by Little[1] using pyrrole and para-acetoxy benzaldehyde in boiling propionic acid as reagents.

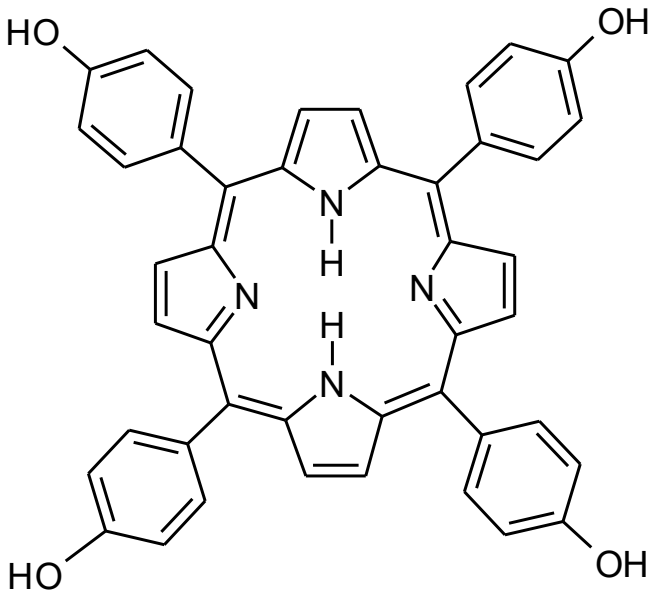

Figure 3.1.1: Structure of 5, 10,15, 20 tetrakis (p-hydroxy-phenyl) porphyrin.

As shown in ***Figure 3.1.2***, the synthesis takes place in two steps, in the first one there is the condensation of the porphyrin ring with the formation of 5,10,15,20 tetrakis (p-acetoxy-phenyl) porphyrin. Subsequently, after separation and purification, the condensation product undergoes a hydrolysis reaction (second step) which leads to the formation of H_2TPP.

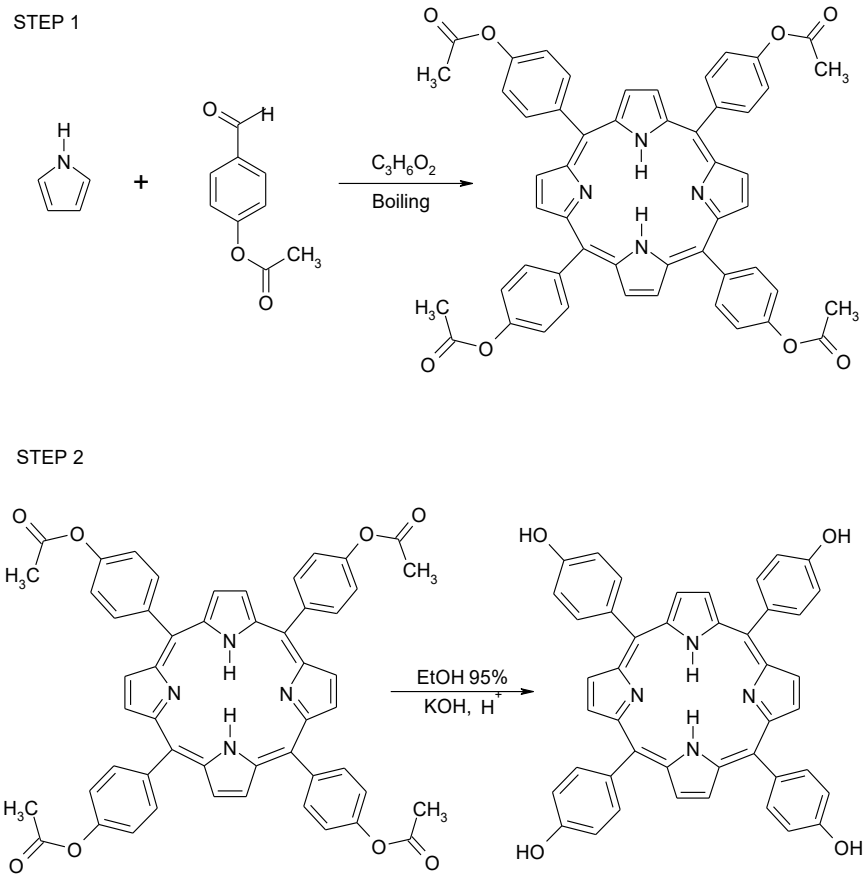

Figure 3.1.2: Scheme of synthesis of H_2TTP: The first step shows a condensation reaction between pyrrole and para-acetoxy benzaldehyde in an acid environment, which leads to the formation of 5,10,15,20 tetrakis (p-acetoxy-phenyl) porphyrin; The second step involves the hydrolysis of the acetoxy groups

Briefly, equimolar amounts of pyrrole and p-hydroxybenzaldehyde, respectively 32ml and 65ml, were solubilized in 730ml of propionic acid (see step 1). The solution was boiled for one hour and then left to cool, at first in the ice bath and then in the fridge at 5 °C for one night. The product obtained (of brown-black color) was filtered under vacuum and repeatedly washed with cold ethanol. The residue (violet in color) was left to further stir in ethanol and then filtered again to ensure that all unreacted material was removed. Finally, in order to eliminate any possible traces of solvent, the product was left in a vacuum stove (80°C) for one night. An aliquot of the final product was then solubilized in tetrahydrofuran and characterized by means of MALDI-TOF mass spectrometry to verify its composition.

In the related MALDI-TOF positive spectrum of ***Figure 3.1.3***, it can be evidenced, next to the peak at m/z 847 assigned to the tetra-acetoxy species, a second peak centered at m/z 804 due to the species with an already hydrolyzed acetoxy group.

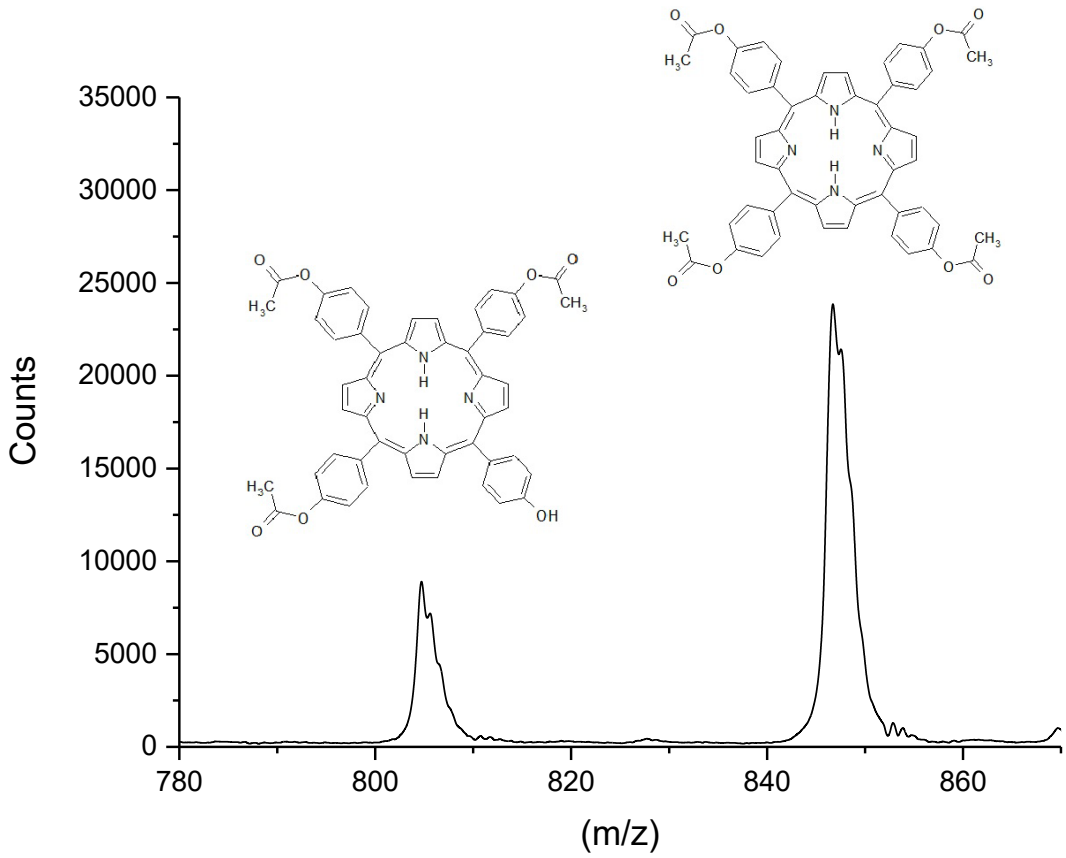

Figure 3.1.3: MALDI-TOF spectrum in positive of the product of the reaction to obtain the 5,10,15,20 tetrakis (p-acetoxy-phenyl) porphyrin (DCTB matrix.)

This was not a problem because the following step was the total hydrolysis of the acetoxyl groups to hydroxyl groups, to obtain the H_2TPP (see step 2). This was done by solubilizing the acetoxylated porphyrin in 300ml of 95% ethanol (5% H_2O) containing 15g of KOH. The reaction was left to reflux at 100 °C for half a day, monitoring the trend from time to time using MALDI-TOF analysis of small aliquots. When the MALDI-TOF spectrum shows that all the porphyrin was hydrolyzed, a quantity of glacial acetic acid equal to twice the KOH moles (30ml) was added to the solution to neutralize all the excess. The H_2TPP was recovered by filtration, performing different washings with cold ethanol that were not sufficient, in fact, they were detected, through TGA analysis, still impurities of acetic acid. To eliminate which, the product was left in a vacuum oven at 150 °C for one day. The resulting porphyrin was characterized by MALDI-TOF (***Fig. 3.1.4***) and ^{1}H-NMR (***Fig. 3.1.5***).

In the MALDI-TOF spectrum there are three peaks at m/z values of 679, 701 and 717 which correspond, respectively, to the protonate, sodiate and potassiate species of 5.10,15,20 tetrakis (p-hydroxyphenyl) porphyrin (H_2TPP).

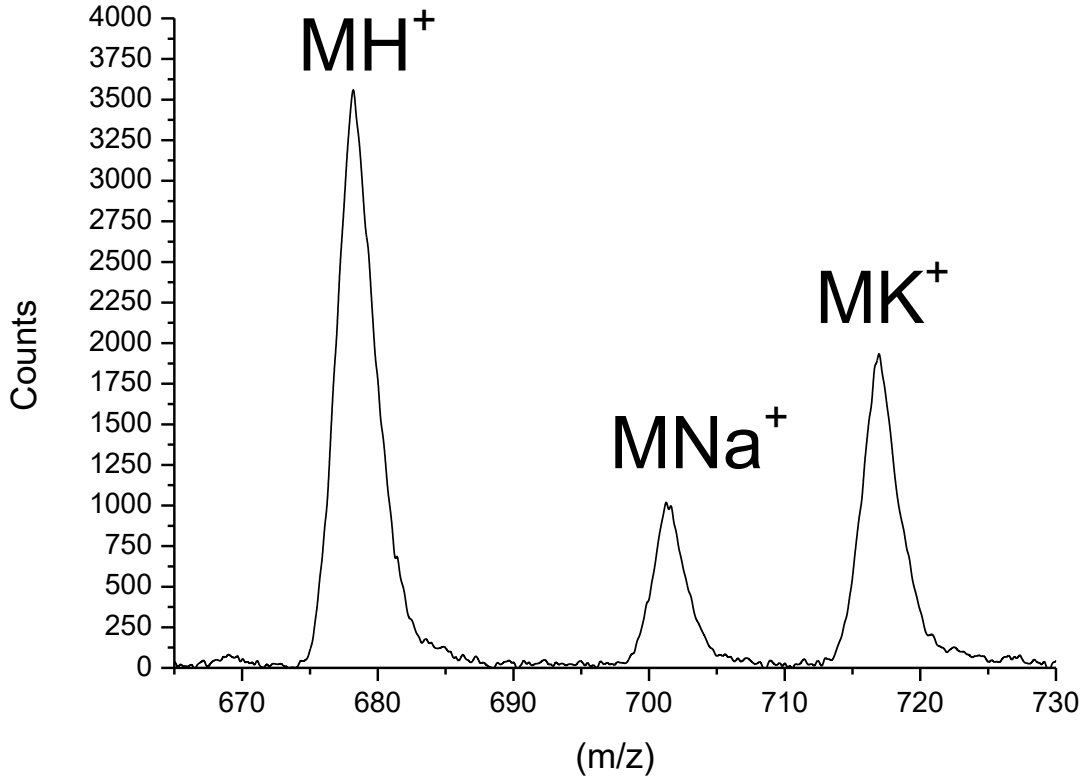

Figure 3.1.4: MALDI-TOF spectrum in positive from 5,10,15,20 tetrakis (p-hydroxy-phenyl) porphyrin using DCTB as a matrix.

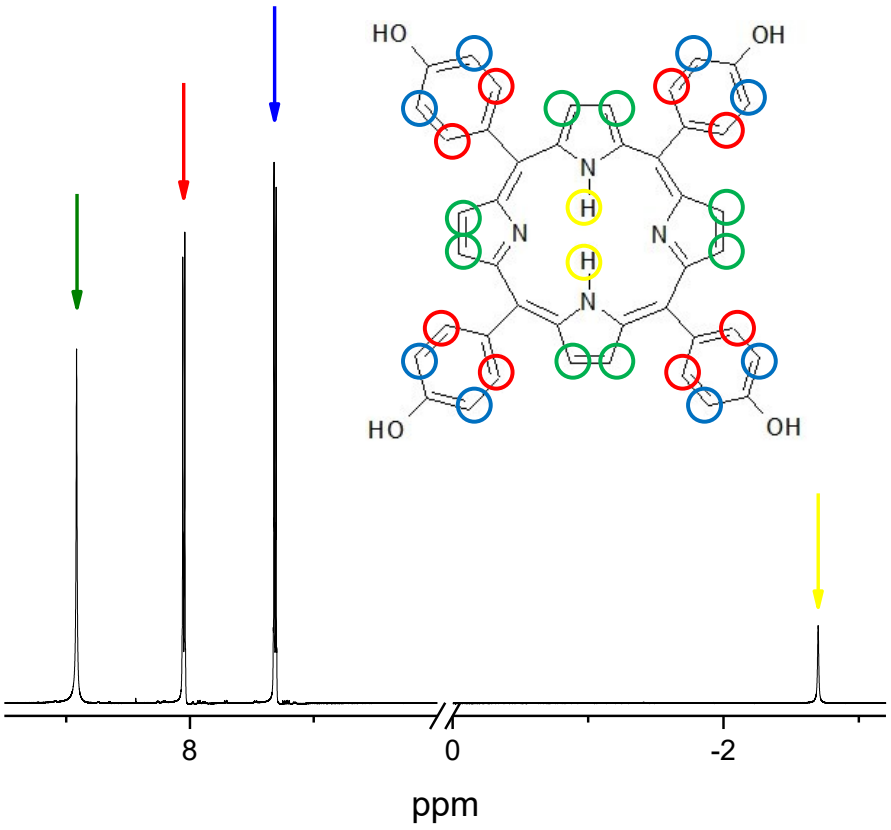

Figure 3.1.5: ^{1}H-NMR spectrum of H_2TPP in acetone-d_6.

The ^{1}H-NMR spectrum [500 MHz, $(CD_3)_2CO$, 27 °C] of the H_2TPP shows the following peaks:

a singlet at 8.91ppm corresponding to the hydrogens in the pyrrole β position (green circles); a doublet at 8.05 and 8.04 ppm, respectively, relative to the hydrogens in position β with respect to the phenolic OH group (red circles); a second doublet at values of 7.32 and 7.30 ppm relative to the hydrogens in position α with respect to the phenolic OH (blue circles); a singlet at -2.69 ppm relative to the hydrogens linked to pyrrolic nitrogens (yellow circles). The signals corresponding to the hydrogens of the phenolic OH groups are not reported for possible confusion and overlap with the signals relating to traces of water present in the solvent.

The spectroscopic properties of H_2TPP, and in particular its molar extinction coefficient, were obtained by Uv-Vis spectroscopy using 5 solutions at different concentrations (respectively $2.5*10^{-7}$ M, $5*10^{-7}$ M, $7{,}5*10^{-7}$ M, $1*10^{-6}$ M and $1.25*10^{-6}$ M) in acetone (***Fig. 3.1.6***). In the spectrum (***Fig. 3.1.6***) we can see a band, with a maximum of 419 nm, corresponding to the Soret and further four bands, with maximums at 651, 595, 553 and 516 nm, which corresponds to the expected Q-bands. In the same figure is shown the graph of the calibration

line obtained by plotting on the abscissa axis the value of the concentrations of the solutions and on the axis of the ordinates the value of the relative maximum absorbance peaks at 419 nm. Through the Lambert and Beer law, it was thus possible to calculate the value of the molar extinction coefficient (ε=419280 M^{-1} cm^{-1}).

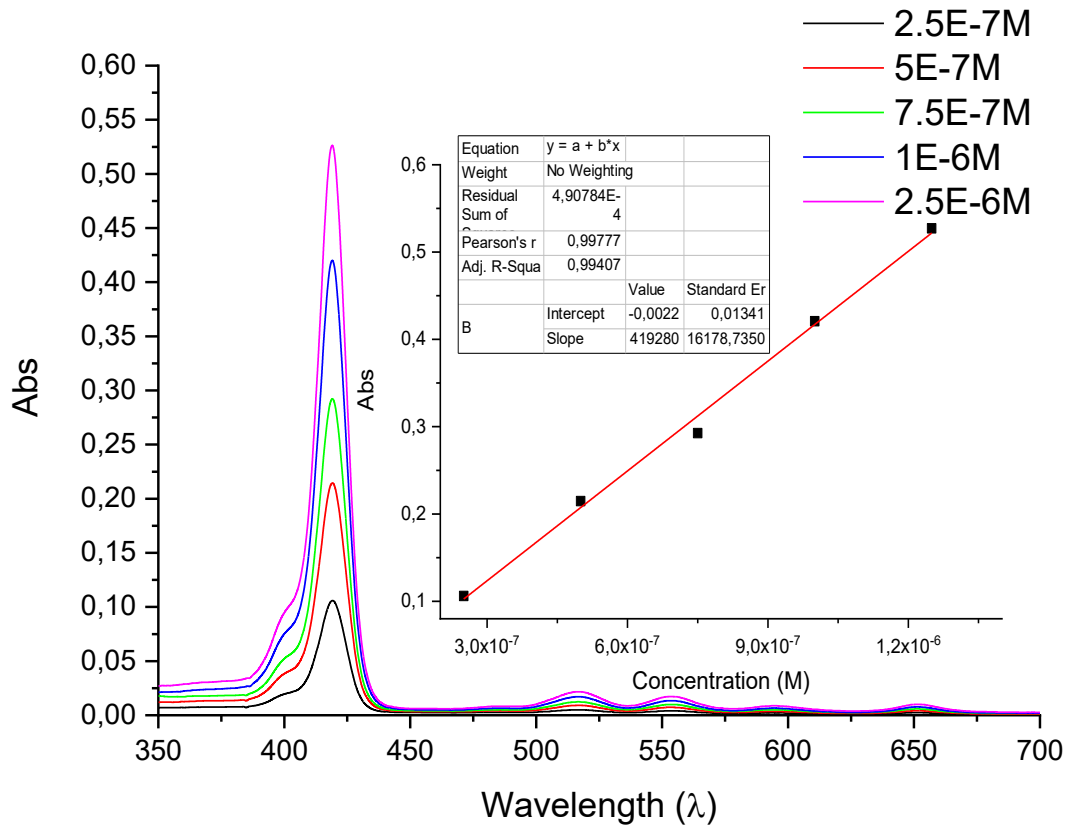

Figure 3.1.6: Uv-Vis spectra of $P(OH)_4$ solutions in acetone. The box shows the calibration line obtained by plotting the maximum absorbance values at 419 nm as a function of the concentration of the solutions (shown in the legend). From the table we see that the value of the angular coefficient of the line, which corresponds to the value of ε is 49280 M^{-1} cm^{-1}.

The fluorescence properties of H_2TPP were also verified by effecting the emission spectrum of a $1*10^{-6}$ M solution in acetone, after excitation with a wavelength of 419 nm, corresponding to the maximum absorption of the Soret band (***Fig. 3.1.7***).

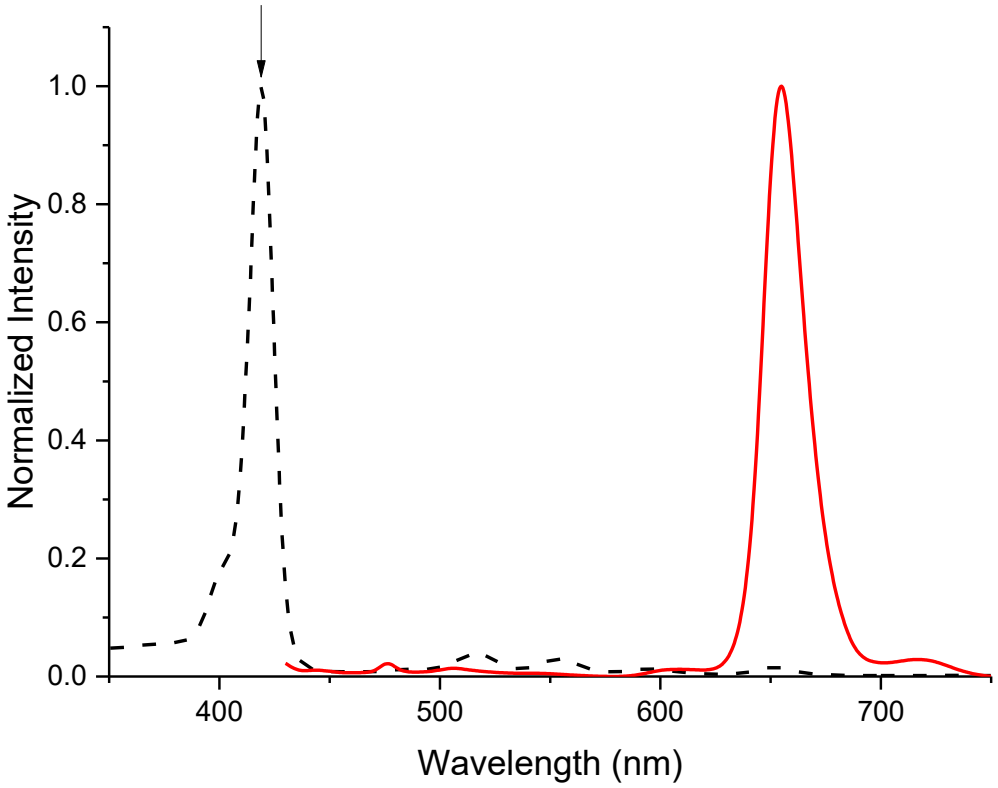

Figure 3.1.7: In red, the fluorescence spectrum of a solution of $P(OH)_4$ ($c = 1*10^{-6}$ M) in acetone. In black, the Uv-Vis spectrum of the same solution. The arrow indicates the wavelength at which the sample is excited (419 nm, maximum Soret Band) to obtain the fluorescence spectrum.

In compliance with the literature data, the above fluorescence spectrum shows a signal with maximum emission at 654 nm, typical of this type of porphyrins.

[1] Little, R. G.; Anton, J.A.; Loach, P.A.; Ibers, J.A. Journal of Heterocycl. Chem., 1975, 12, 343-349.

Synthesis of Synthesis of 5,10,15 tri {p- [ω-methoxy-poly (ethylene oxide)] phenyl} -20- (p-hydroxyphenyl) porphyrin.

The synthesis of PEGylated derivatives is necessary to make the water-soluble porphyrin system[1]. As reported in previous works, it was chosen an etherification reaction, in a basic environment, between H_2TTP porphyrin and chlorinated poly (ethylene glycol) mono-methyl ether (PEGMEC). Polyethylene glycol with different molecular weights can be used. In this work, the PEGMEC-350 and the PEGMEC-750 systems were used: the first consists of oligomers having an average of 7 repetitive units, while the second has about 15 repeating units. The use of PEGMEC with different molecular mass allows to explore the solubility limits in H_2O of the various derivatives. For the synthesis of water-soluble porphyrin derivatives, two different methods have been approached, both leading to the formation of a mixture of varied species, each having a porphyrin ring as a core and a different number of polyethylene glycol chains bound in peripheral position, as shown in the following scheme (***Fig. 3.2.1***).

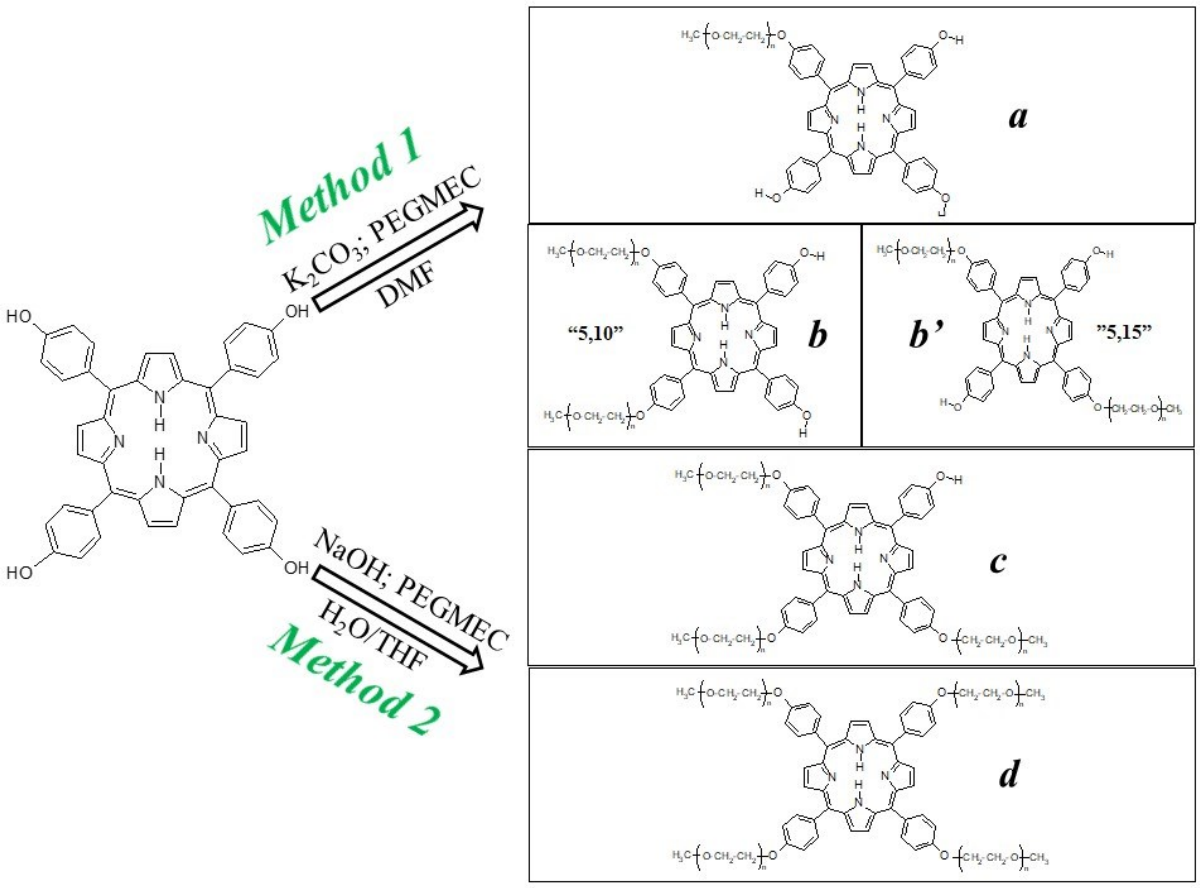

Figure 3.2.1: Synthesis scheme of porphyrin derivatives.

Briefly, in the following the synthesis procedures are reported:

Method 1: 0.6272 gr of H_2TPP (0.925mM), 1.230 gr of PEGMEC-350 (3.51mM) and 0.520 gr of K_2CO_3 (3.75mM) were solubilized in anhydrous DMF and left to reflux, under stirring at 135 °C. Potassium carbonate is necessary for the salification of the phenol groups of the porphyrin to improve the nucleophilic attack at PEGMEC. The reaction was monitored by MALDI-TOF spectrometry (***Fig. 3.2.2***) and when the conversion into the tri-substituted product was judged to be optimal (after about 3 hours) the reaction was stopped.

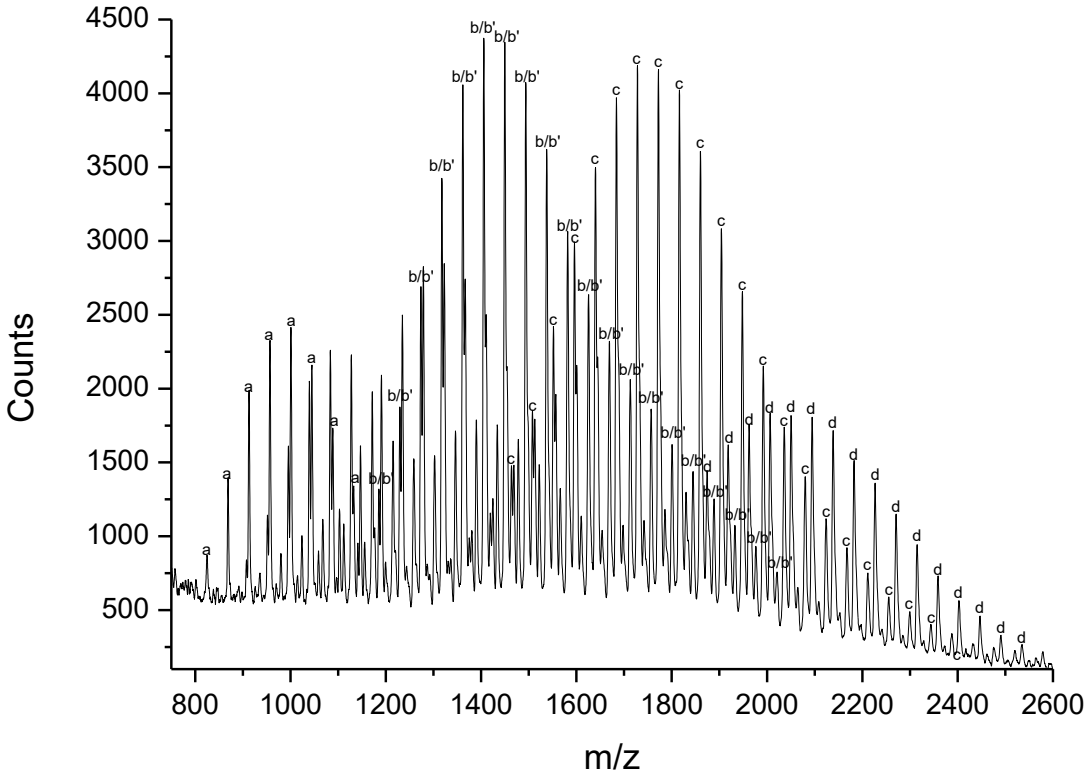

Figure 3.2.2: MALDI-TOF spectrum in positive of the reaction made with method 1 (scheme of figure 3.2.1) with DCTB matrix. In the spectrum are shown the 4 distributions corresponding to the differently substituted species (see diagram Fig.3.2.1).

In the positive MALDI-TOF spectrum of ***Figure 3.2.2***, there are four distributions corresponding to the species shown in ***Figure 3.2.1***. The first distribution (a) is centered at a m/z value of 1000 corresponding to the mono-substituted species, more specifically with peaks at m/z values of 869+n44 and 980+n44, in the MH^+ and MNa^+ forms, respectively with n=0-12. The second distribution (b/b') is centered at a m/z value of 1400 and corresponds to a mix of the two substituted isomers ("5,10" and "5,15"). The peaks are at m/z values of

1146+n44, 1212+n44 and 1229+n44 due, respectively, to the species MH^+, MNa^+ and MK^+, with n=0-20. The third distribution (c) refers to the tri-substituted compound, with peaks centered at m/z 1727, signals at m/z 1507+n44 due to the MK^+ species with n=0-22. The peaks relative to the species MH^+ and MNa^+ are not sufficiently resolved by overlapping with those of the previous and subsequent distributions. The fourth distribution (d) is centered at the m/z value of 2093 with very clear signals due to the peaks at m/z 1785+n44 relative to the species MK+, with n=0-17. Also, in this case, the peaks of the species MH^+ and MNa^+ are not solved.

The product obtained was acidified with glacial acetic acid and dried by rotavapor. The dichloromethane (CH_2Cl_2) was added to the residue, in order to solubilize only the reaction products and not the formed salts. This was dried by rotavapor and then further dried in a 80 °C vacuum oven overnight. The product was further poured in ethyl ether, to avoid any trace of unreacted PEGMEC, and finally left in a vacuum oven again for another day. The tri-substituted species was then separated from the other reaction products by silica gel column chromatography using a mixture consisting of 98% of chloroform, 1% ethanol and 1% triethylamine as an eluting phase (***Fig. 3.2.3***).

Figure 3.2.3: Chromatographic column on silica gel of reaction products.

The structural characterization of the expected product, the third band eluted from the column, was performed by MALDI-TOF mass spectrometry (***Fig.3.2.4***) and ^{1}H-NMR (***Fig.3.2.5***)

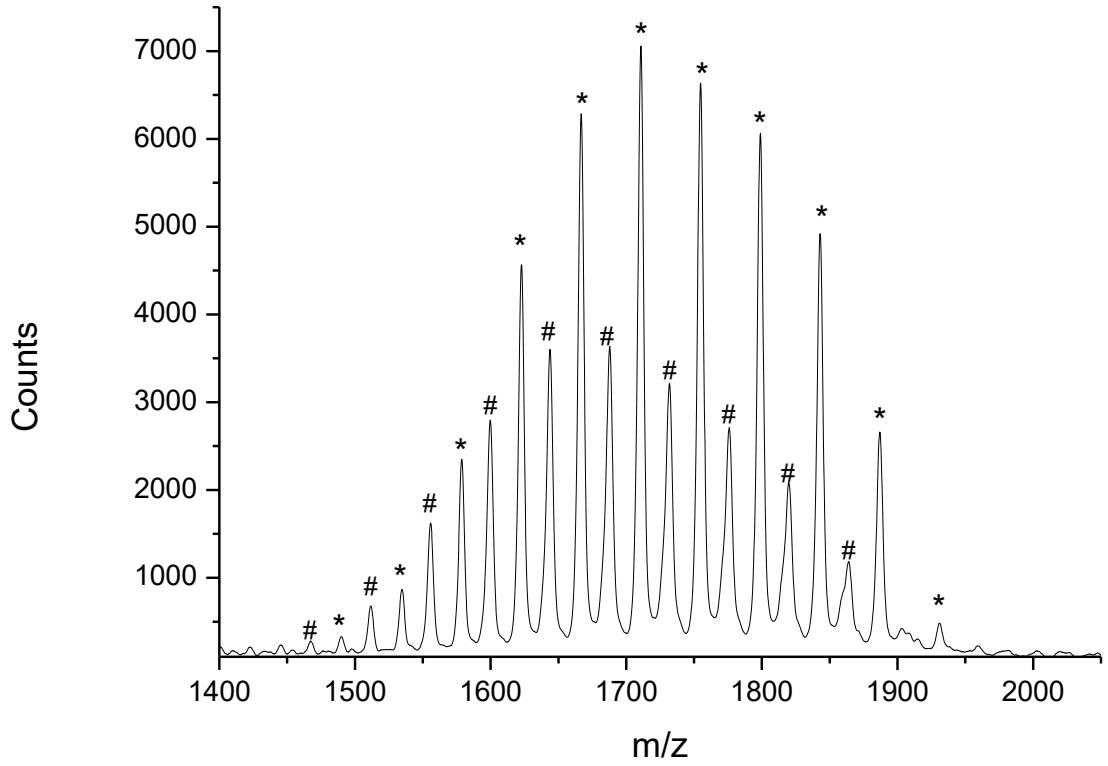

Figure 3.2.4: MALDI-TOF spectrum of 5,10,15 tri {p- [ω-methoxy-poly (ethylene oxide)] phenyl} -20- (p-hydroxyphenyl) porphyrin using DCTB as a matrix.

In the spectrum of ***Figure 3.2.4***, it is evident the distribution of the peaks centered at values of m/z of 1700 and, in particular, the peaks are found at m/z values of 1491+n44 and 1468+n44 with n= 0-13, corresponding to the species MH^+ (#) and MNa^+ (*), respectively.

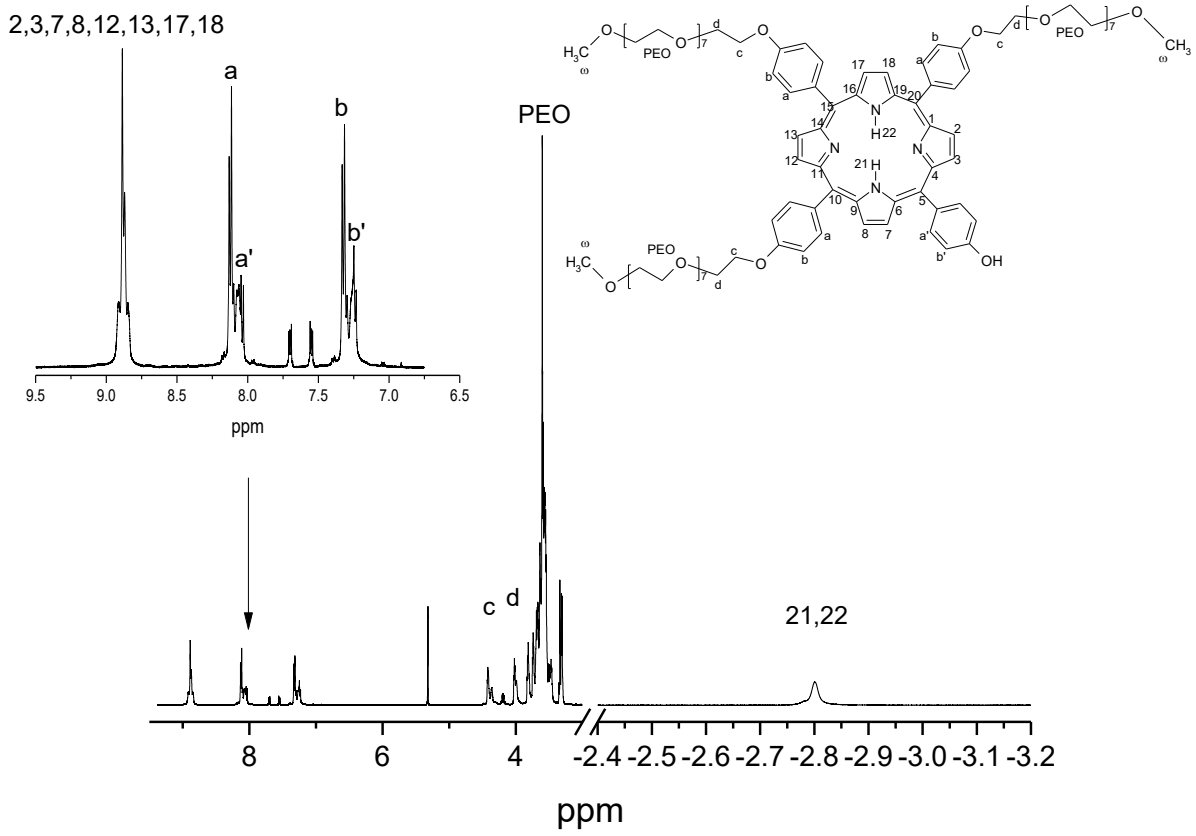

Figure 3.2.5: ^{1}H-NMR spectrum in CD_2Cl_2 of P(PEG350)$_3$

Figure 3.2.5 shows the ^{1}H-NMR spectrum (500 MHz, CD_2Cl_2, 27 °C) of the 5,10,15-p(ω-methoxy-polyethyleneoxyphenyl)-20-p(hydroxyphenyl) porphyrin (P(PEG350)$_3$) with the relative signals attribution. The discussion on the spectrum is reported later along with that of the species P(PEG750)$_3$, given the similarity of the two compounds.

Also, the spectroscopic properties of the P(PEG350)$_3$ have been studied both in an organic solvent and in water. However, it was not possible to calculate the value of ε in water solution because the porphyrin generates J and H aggregates that interfere with the intensity of the Soret band, distorting the value of ε. The following are the Uv-Vis spectra, (***Fig. 3.2.6***) (***Fig.3.2.7***) with the relative calculation of ε for the solutions in acetone, and the fluorescence spectra (***Fig. 3.2.8***) (***Fig. 3.2.9***) for the solutions of P(PEG350)$_3$ (c=1*10^{-6} M) in water and in acetone.

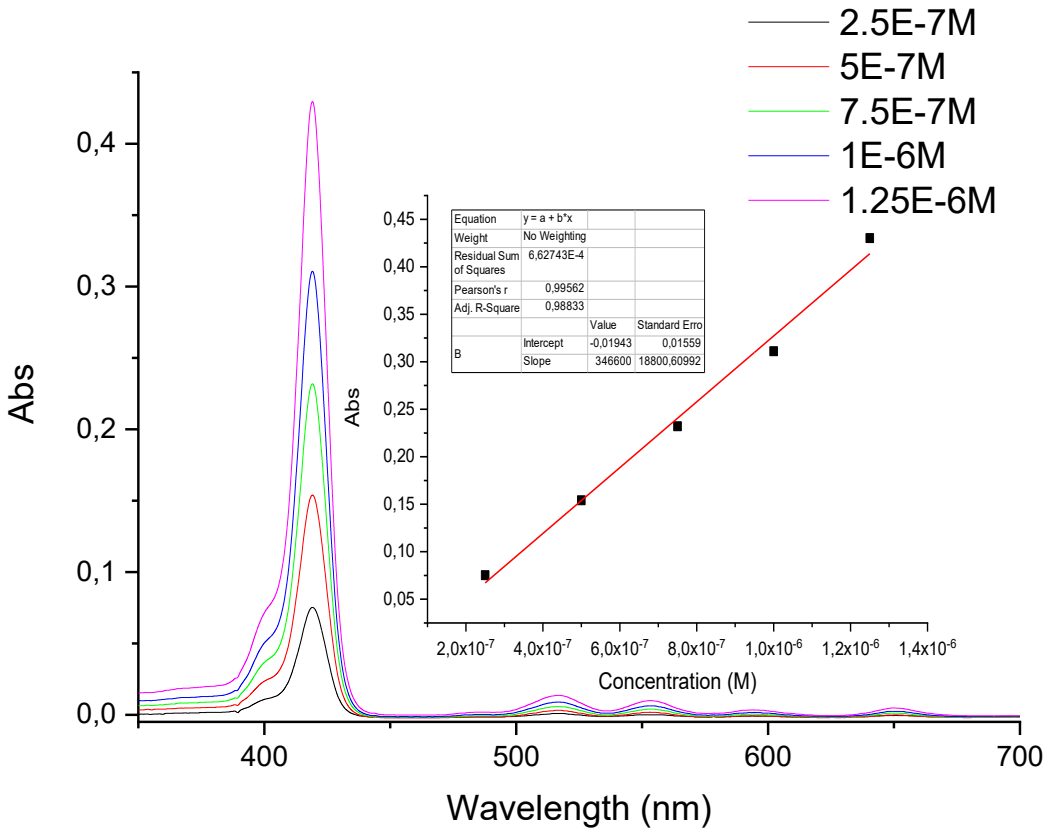

Figure 3.2.6: Uv-Vis spectra of P(PEG-350)$_3$ solutions in acetone. In the inset, the calibration line was obtained by plotting the maximum absorbance values at 419 nm as a function of the concentration of the solutions (shown in the legend). From the table we see that the value of the angular coefficient of the line, which corresponds to the value of ε is 346600 $M^{-1}cm^{-1}$.

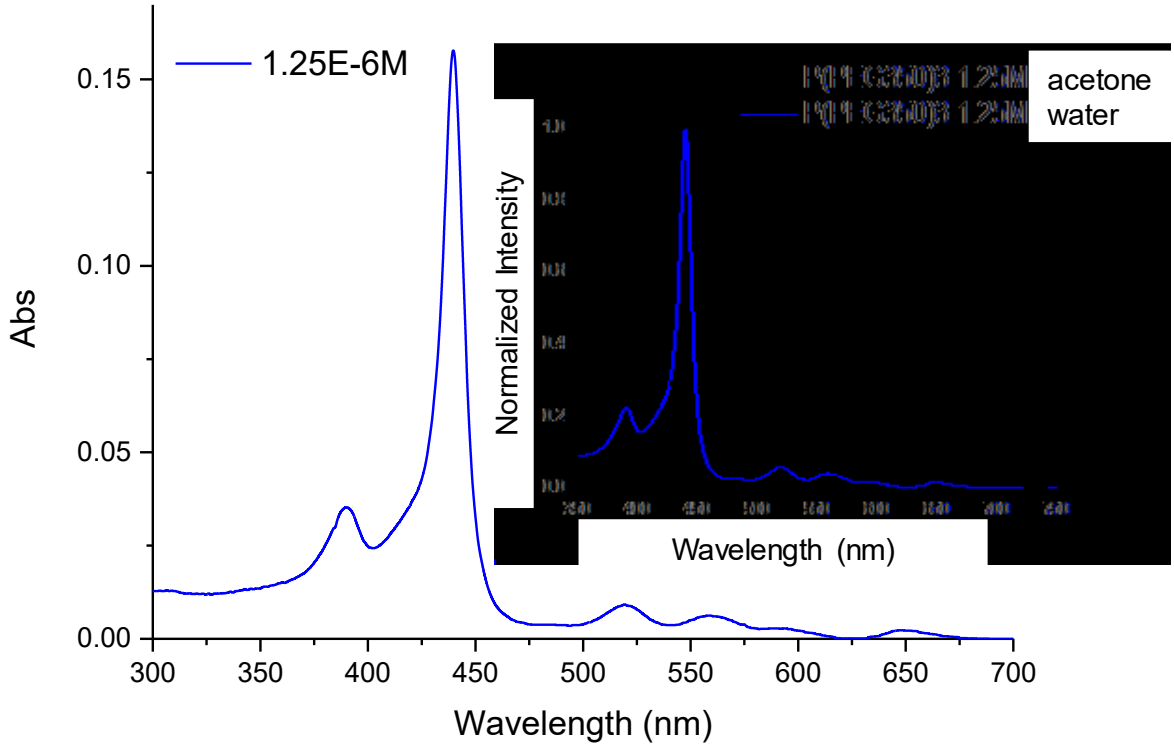

Figure 3.2.7: Uv-Vis spectra of P(PEG-350)$_3$ in water solution. In the inset shows the comparison between Uv-Vis spectra of P(PEG-350)$_3$ in acetone and water solution.

As seen from the Uv-Vis spectra, the absorption intensity in water is much lower than that in acetone at the same concentration. Moreover, the Soret band (419 nm in acetone) disappears completely, replaced by two new bands at 389 nm and 440 nm, respectively, due to the formation of the H and J aggregates. Similarly, the shape of the Q bands is also slightly different.

The fluorescence emission spectra of the same solutions related to an excitation at the wavelength corresponding to the maximum absorption of the Soret band are shown below, namely 419 nm for the sample in acetone and 440 nm for that in water.

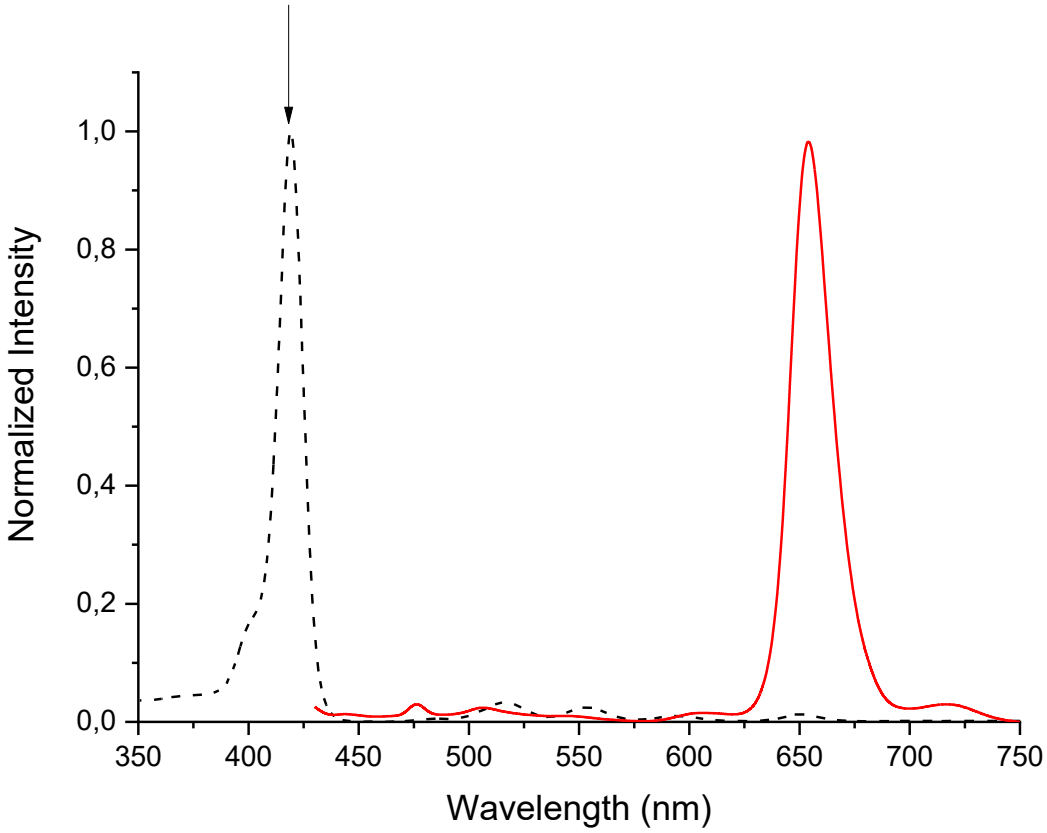

Figure 3.2.8: In red, the fluorescence spectrum of a solution of $P(PEG350)_3$ ($c=1*10^{-6}$ M) in acetone. In black, Uv-Vis absorption spectrum of the same solution. The arrow indicates the wavelength at which the sample is excited (419 nm maximum Soret Band) to obtain the fluorescence spectrum.

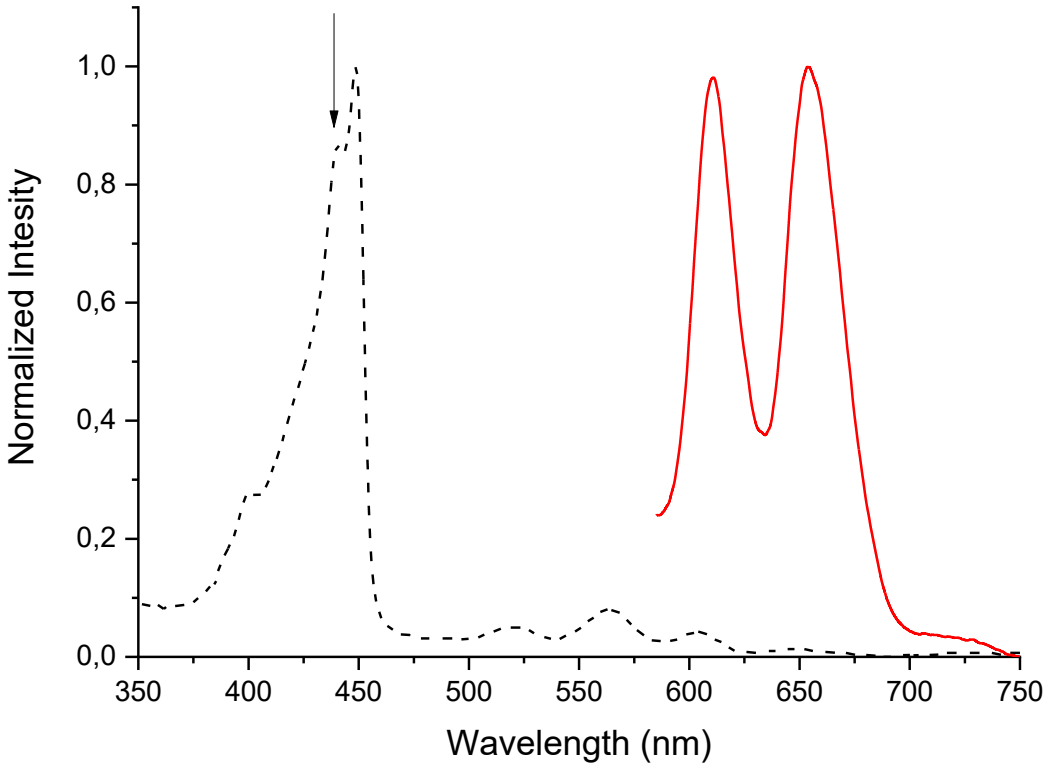

Figure 3.2.9: In red, the fluorescence spectrum of a solution of $P(PEG350)_3$ ($c=1*10^{-6}$ M) in water. In black, Uv-Vis spectrum of the same solution. The arrow indicates the wavelength at which the sample is excited (439 nm maximum Soret Band) to obtain the fluorescence spectrum.

Fluorescence spectra consist of a more intense peak at 654 nm, and other much lower peaks at at 610nm due to the presence of an artefact. In fact, using a filter at 405 nm, before the detector, the signal at 610 disappear.

The comparison between the two spectra shows that the porphyrin derivative maintains the fluorescence properties in an aqueous solution, as well as in organic solvent. The synthesis method described above had the advantage of obtaining the desired product in a brief time. In fact, the reaction lasted about three hours in total. Nevertheless, the procedure presented some problems: the difficulty of removal of the solvent (DMF) and the difficult purification from the salts that are formed.

For these reasons and driven by the need to use less polluting synthesis methods, a different synthetic approach in aqueous media has been used, although this has required longer times.

Method 2: Two solutions were prepared: one of 0.505 gr (0.744 mM) of H_2TPP in 6ml of an aqueous solution of 0.5 M NaOH; the other of 1.663gr (2.2 mM) of PEGMEC-750 in 6ml of a solution H_2O/THF 50:50. The PEGMEC solution was then added to porphyrin solution and left to react at reflux and under constant stirring. Also in this case the reaction was monitored

by means of MALDI-TOF MS, to verify the reaction progress (***Fig 3.2.10***), adding little amount of NaOH to move the reaction towards the formation of the products, and other THF to replace the one lost during the reaction. After three days the progress of the reaction was judged to be optimal and was stopped adding glacial acetic acid, until the color of the solution changed from purple to green. The solution was then roto-evaporated and dyed under vacuum at 80°C. The residue was solubilized in CH_2Cl_2, to separate the formed salts, and filtered. The filtrate was first concentrated and then poured into ethyl ether to eliminate excess PEGME.

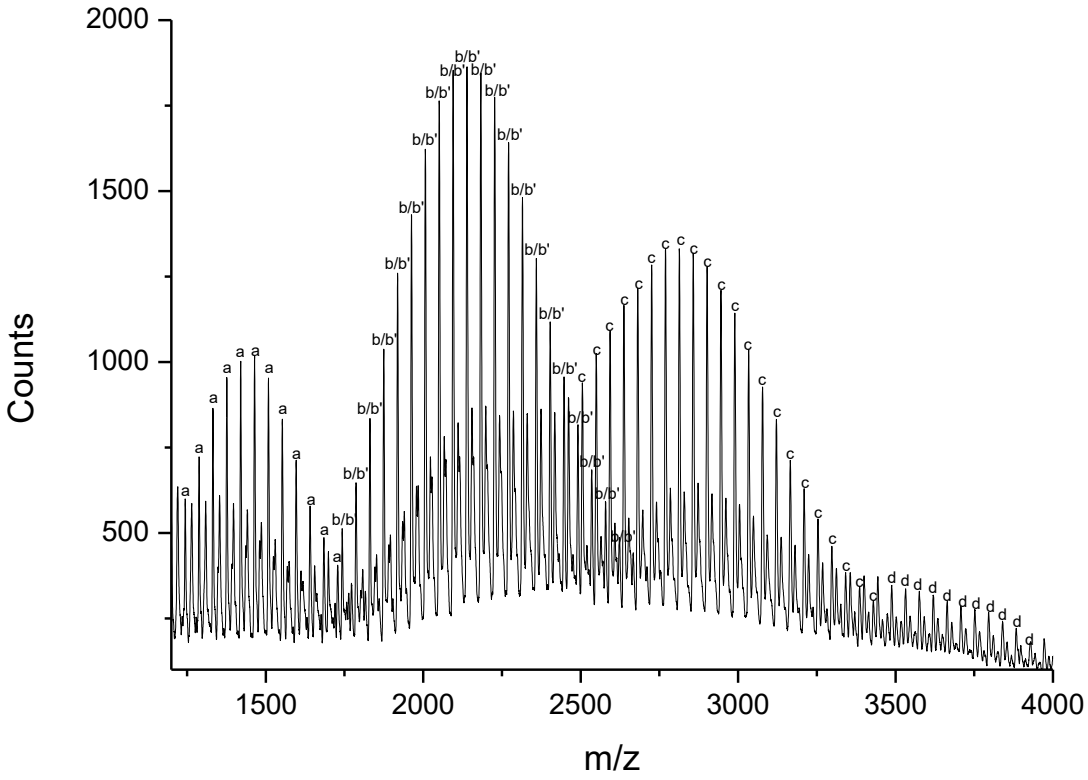

Figure 3.2.10: MALDI-TOF spectrum of the reaction mix H_2TPP and PEGMEC-750 in H_2O/THF. DCTB matrix.

In the mass spectrum, shown in ***Figure 3.2.10,*** there are four distributions, corresponding to the species shown in ***Figure 3.2.1*** and having PEGME-750 as peripheral chain. The first of these distributions (a) is centered a m/z 1420 and is corresponding to the mono-substituted species, with peaks at m/z values of 1200+n44 and 1265+n44, for the species MNa^+ and MH^+ respectively, with n=10-20. The second distribution (b/b') is centered at a m/z value of 2139 and corresponds to the mixture of the two substituted isomers ("5,10" and "5,15") with signals at 1743+n44 (MNa^+) and 1847+ n44 (MH^+), with n=8-26. Also in this case, the compound subjected to the synthesis corresponds to the third distribution (c) centered at m/z 2813 with

peaks at m/z 2417+n44 (MNa^+) and 2656+n44 (MK^+) with n=10-25. The fourth and last distribution (d) is at m/z 3617 with peaks at m/z 3441+n44, relative to the MNa^+ species, with n=16-24. The peaks of the species MH^+ and MNa^+ are not solved and difficult to evaluate.

The reaction mixture was separated by means of silica gel column chromatography, using $CHCl_3$ (96%), $(C_2H_5)_3N$ (2%) and CH_3CH_2OH (2%) as eluent mixture. The second eluted product, corresponding to $P(PEG750)_3$, was dried by roto-evaporator and under vacuum oven, and, finally, solubilized in CH_2Cl_2 and precipitated in ethyl ether. The characterization of 5,10,15-tri-{p-[ω-methoxy-poly (ethylene oxide)] phenyl}-20-(p-hydroxyphenyl) porphyrin $P(PEG750)_3$ was performed by means of MALDI-TOF MS (***Fig 3.2.11***) and ^{1}H-NMR (***Fig. 3.2.12***).

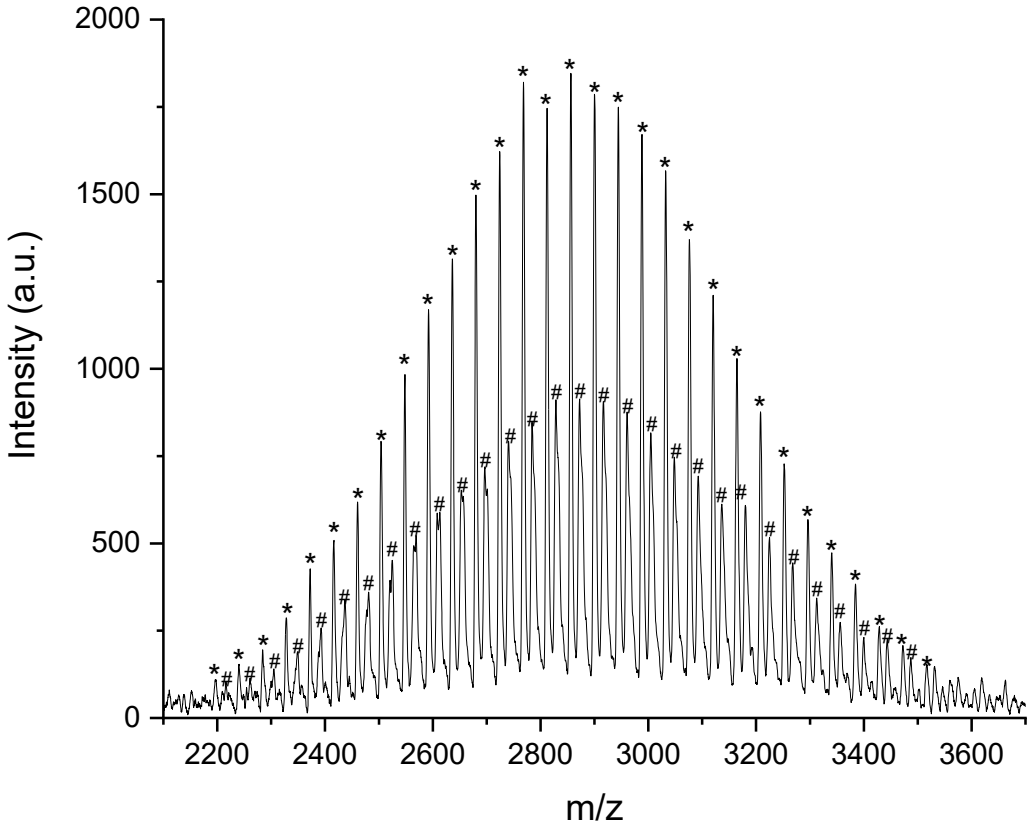

Figure 3.2.11: MALDI-TOF spectrum of 5,10,15 tri {p- [ω-methoxy-poly (ethylene oxide)] phenyl} -20- (p-hydroxyphenyl) porphyrin, $P(PEG750)_3$

In the spectrum of ***Figure 3.2.11***, it is evident the distribution of the peaks centered at values of m/z of 2855 and, in particular, the peaks are found at m/z values of 2855+n44 and 2871+n44 with n= 0-15, corresponding to the species MNa^+ (*) and MK^+ (#), respectively.

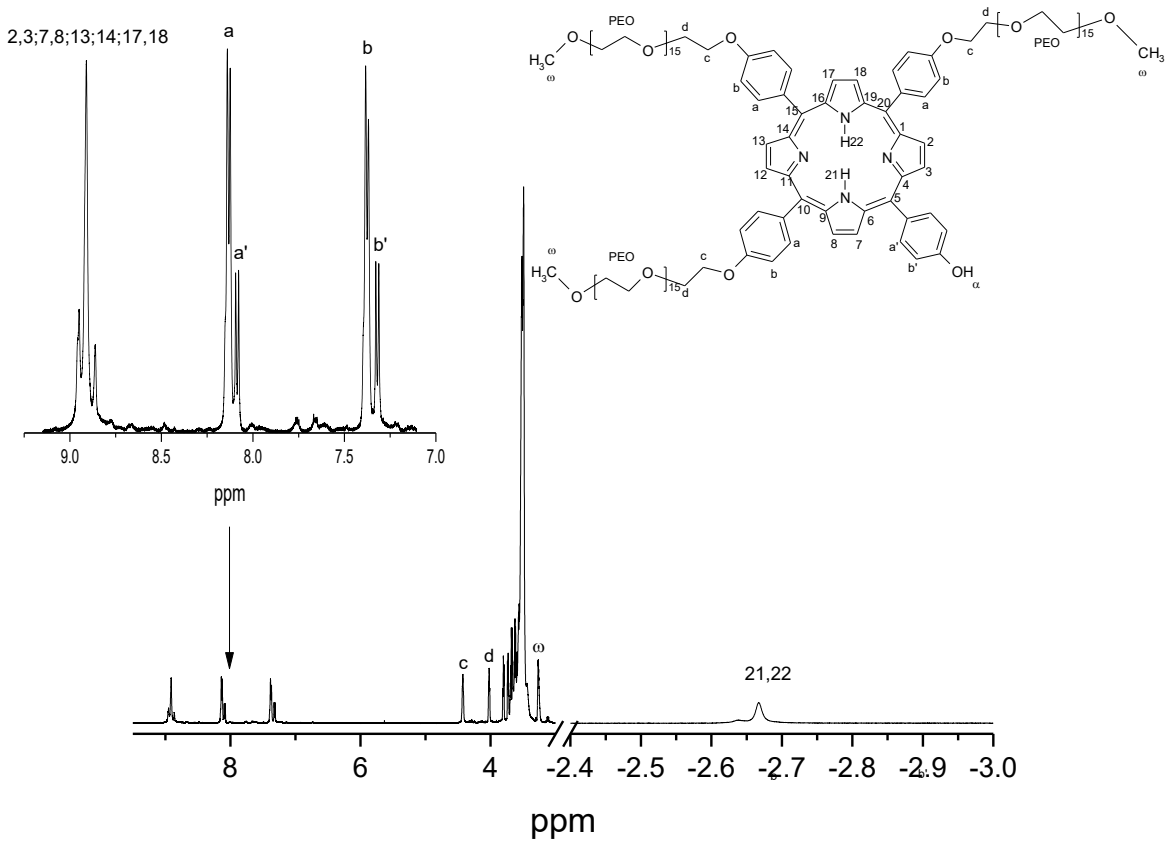

Figure 3.2.12: ^{1}H-NMR spectrum of P(PEG 750)$_3$. The spectrum was acquired using acetone-d6 as solvent.

The attribution of ^{1}H-NMR signals [500 MHz, $(CD_3)_2CO$, 27 ° C] related to P(PEG750)$_3$ is shown in ***Figure 3.2.12***: a multiplet at 8.92 ppm, relative to pyrrolic hydrogens in the β position (2,3,7,8,12,13,17,18), a doublet with a value of 8,13 ppm, relative to the hydrogens of the phenyls substituted with the PEGs in position β (a), a doublet proximal to 8.08ppm relative to the phenol hydrogens in position β (a'); a doublet at 7.37ppm relative to the hydrogens in position α of the substituted phenyls (b) and a doublet at 7.32ppm relative to the hydrogens of the phenol in position α (b'); a singlet with values of 4.42 ppm relative to CH_2 linked to phenolic oxygen (c), and another singlet relative to CH_2 immediately following (d) to values of 4.02 ppm. In the range between 3.8 and 3.4 ppm there are a series of multiplet relative to the hydrogens of the polyethylene oxide (PEO) chain. Finally, at -2.66 pmm there is a singlet related to the hydrogens linked to pyrrolic nitrogens (21,22). Signal assignment was also performed by analyzing the cross-peaks of the ^{1}H-^{1}H-ROESY spectrum (***Fig. 3.2.13***) and ^{1}H-^{1}H-COSY (***Fig. 4.2.14***).

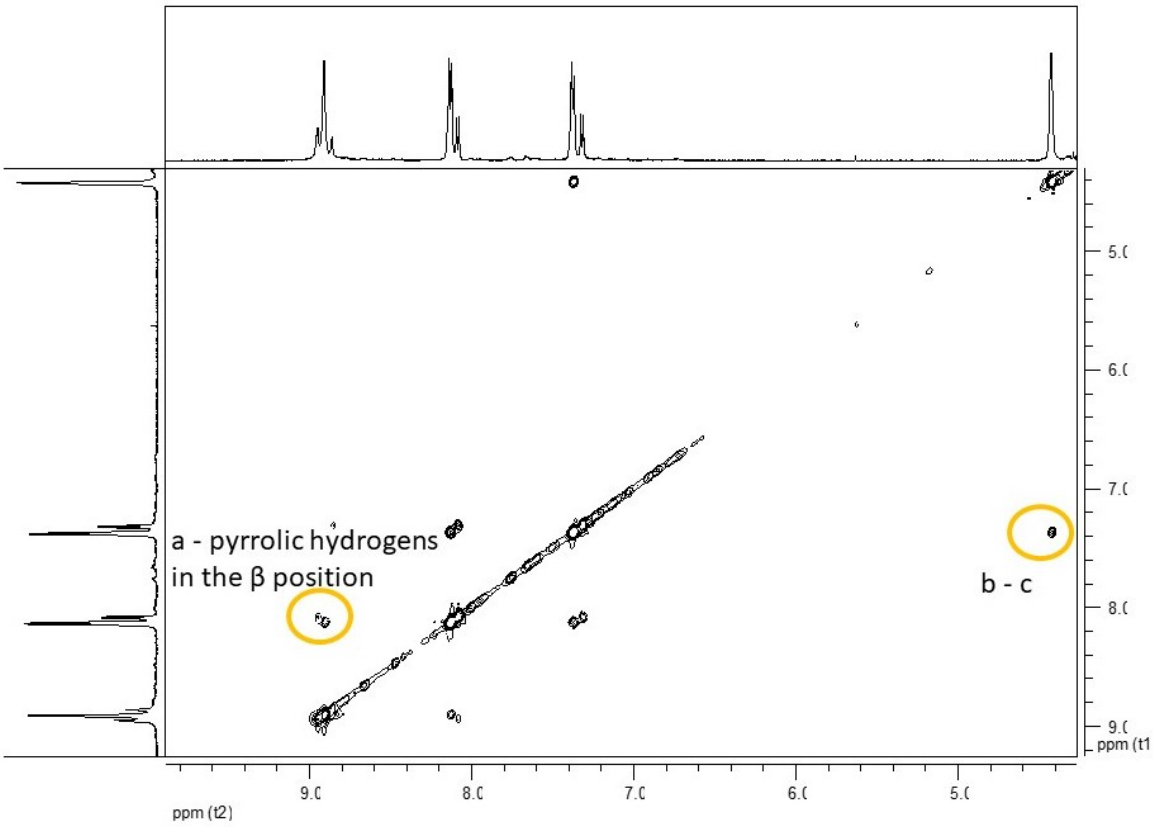

Figure 3.2.13: ^{1}H-^{1}H-ROESY spectrum of P (PEG750)$_3$ in acetone-d6.

The ^{1}H-^{1}H-ROESY spectrum (***Fig. 3.2.13***) shows the correlations between the pyrrolic CH in the β position (2,3,7,8,12,13,17,18) and the phenyls CH in α position (a), and the correlation between the hydrogens of the phenyls in β position (b) and the PEG's CH_2 linked to phenolic oxygen (c).

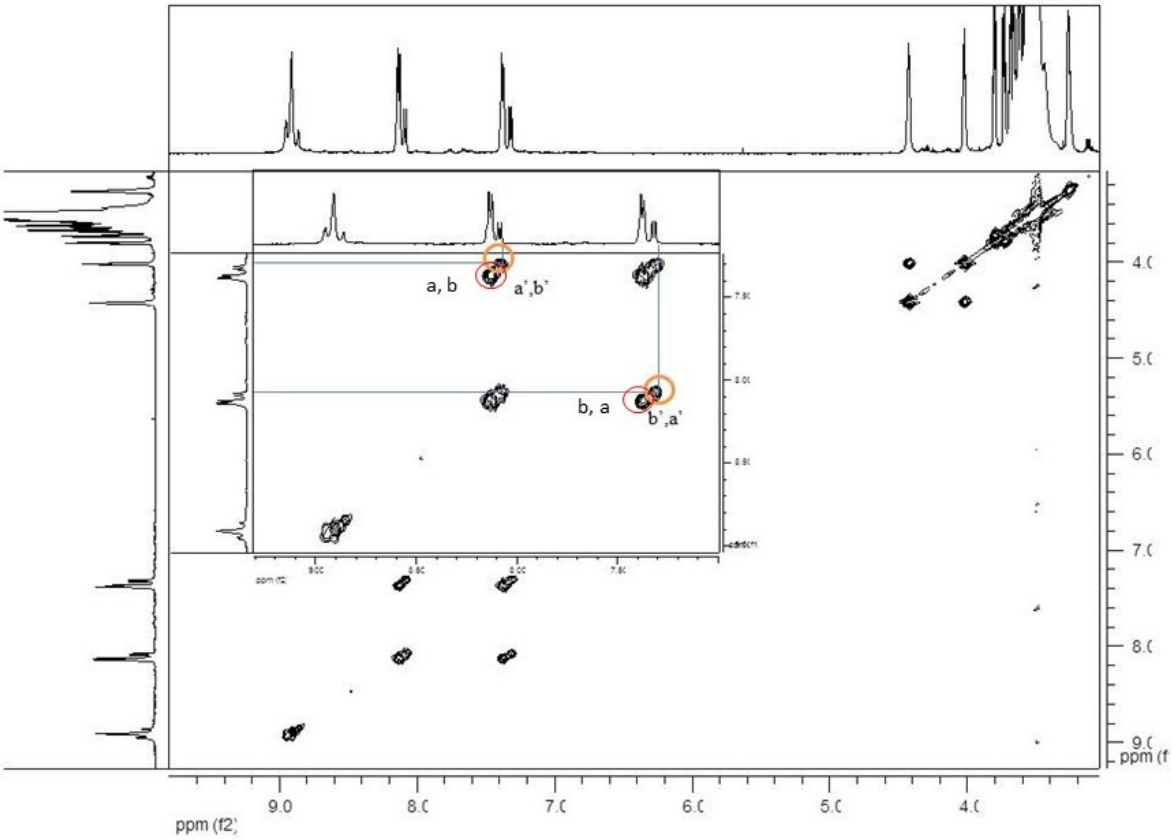

Figure 3.2.14: ^{1}H-^{1}H-COSY spectrum of P (PEG750)$_3$ in acetone-d6. The inset shows the magnification of the signals in the range of 7-9ppm and the related correlations.

The ^{1}H-^{1}H-COSY spectrum (***Fig. 3.2.14***) show the correlations between the two phenyl (a – b) CH, and between the two phenolic CH (a' – b').

Spectroscopic properties have also been studied for P(PEG750)$_3$. As in the previous case, the spectra were acquired in acetone and in water, at the same concentration, to compare the results obtained. Following, the Uv-Vis spectra of P(PEG750)$_3$ in acetone, with different concentration and the relative calculation of ε (***Fig.3.2.15 and inset***), and in water (***Fig. 3.2.16***):

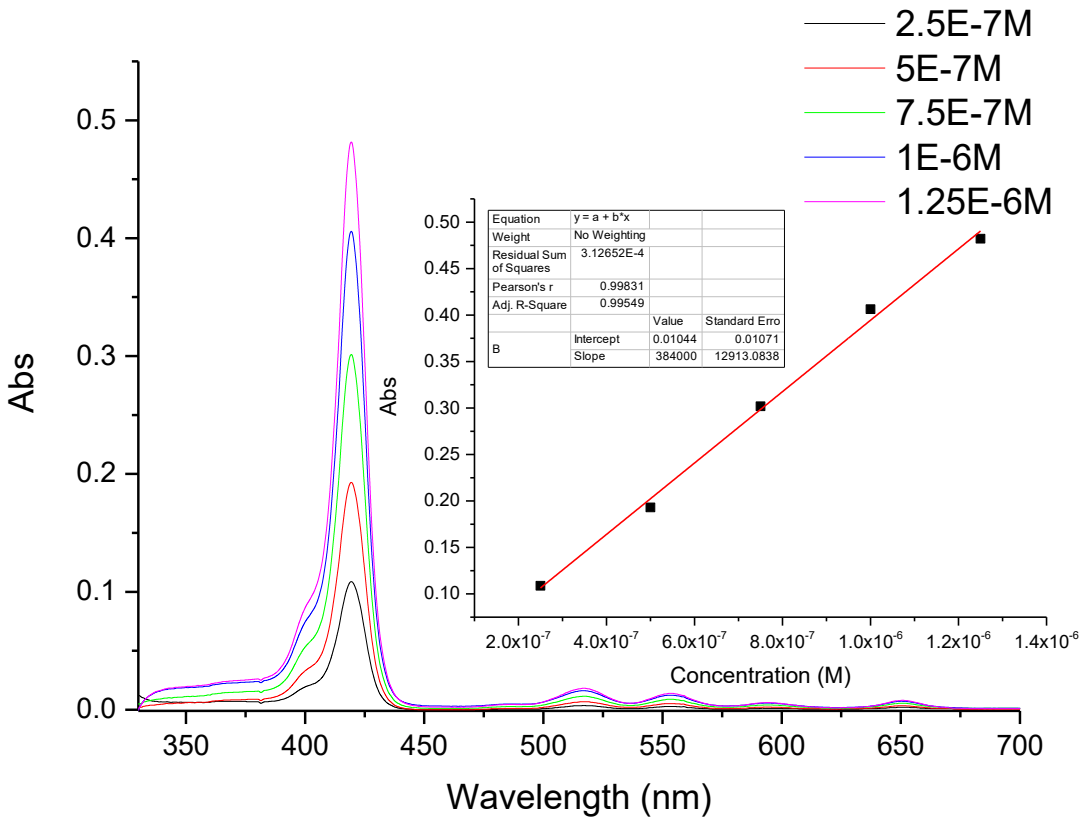

Figure 3.2.15: Uv-Vis spectra of P(PEG-750)$_3$ solutions in acetone. The inset shows the calibration line obtained by plotting the maximum absorbance values at 419 nm as a function of the concentration of the solutions (shown in the legend). From the table, we can observe that the value of the angular coefficient of the line, which corresponds to the value of ε, is 384000 M^{-1} cm^{-1}.

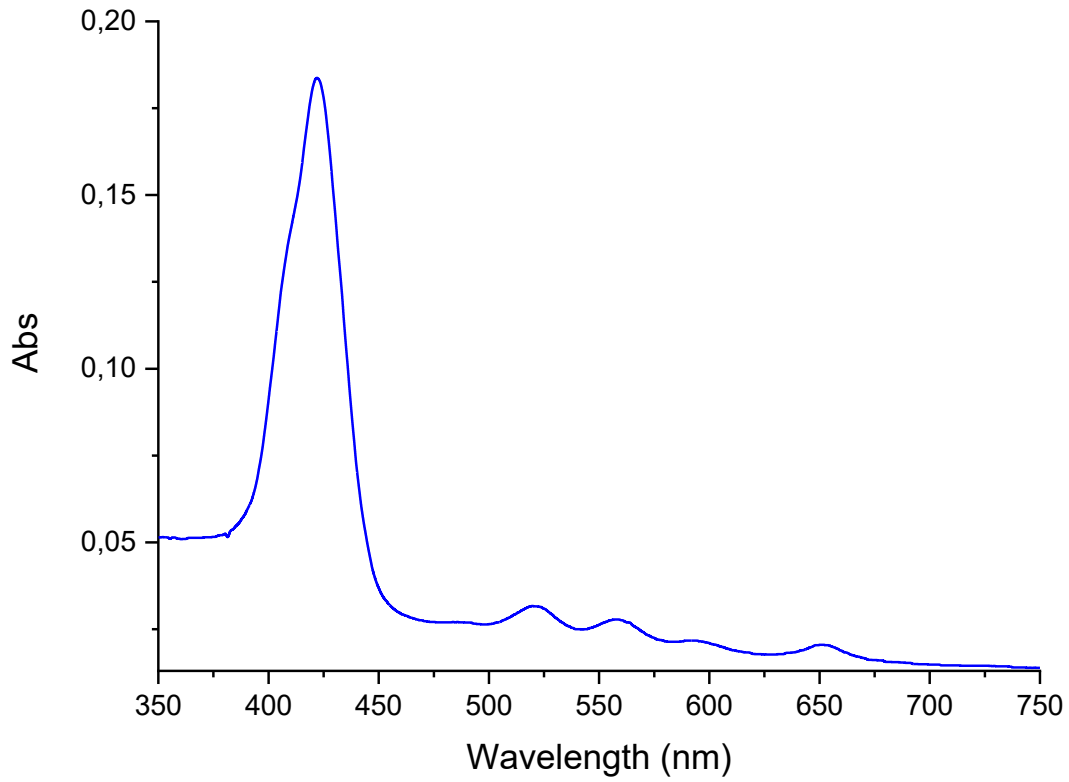

Figure 3.2.16: Uv-Vis spectra of P(PEG-750)$_3$ solutions in water.

The comparison between the spectra shows a behavior very similar to that of P(PEG350)$_3$, with a greater absorption intensity in acetone than in water. Compared to P(PEG350)$_3$, the intensity of the spectrum in water is relatively higher, to indicate a higher solubility of P(PEG750)$_3$, with a shape of the spectrum very close to that obtained in organic solvent, due to the lower formation of aggregates of type J and H, probably because the longer PEG chains limit the approach and stacking. Also in this case, the calculation of ε was not done in water, also because the Soret band is subject to a shift towards the blue as the concentration of the solution increases and to the appearance of a shoulder at about 405 nm to indicate the formation of the H-type aggregate. Another proof of the formation of the aggregates is the scattering in the red-region, observed in the spectrum.

The two fluorescence emission spectra for P(PEG750)$_3$ in acetone and water are reported in (***Fig. 3.2.17***) and (***Fig.3.2.18***), respectively.

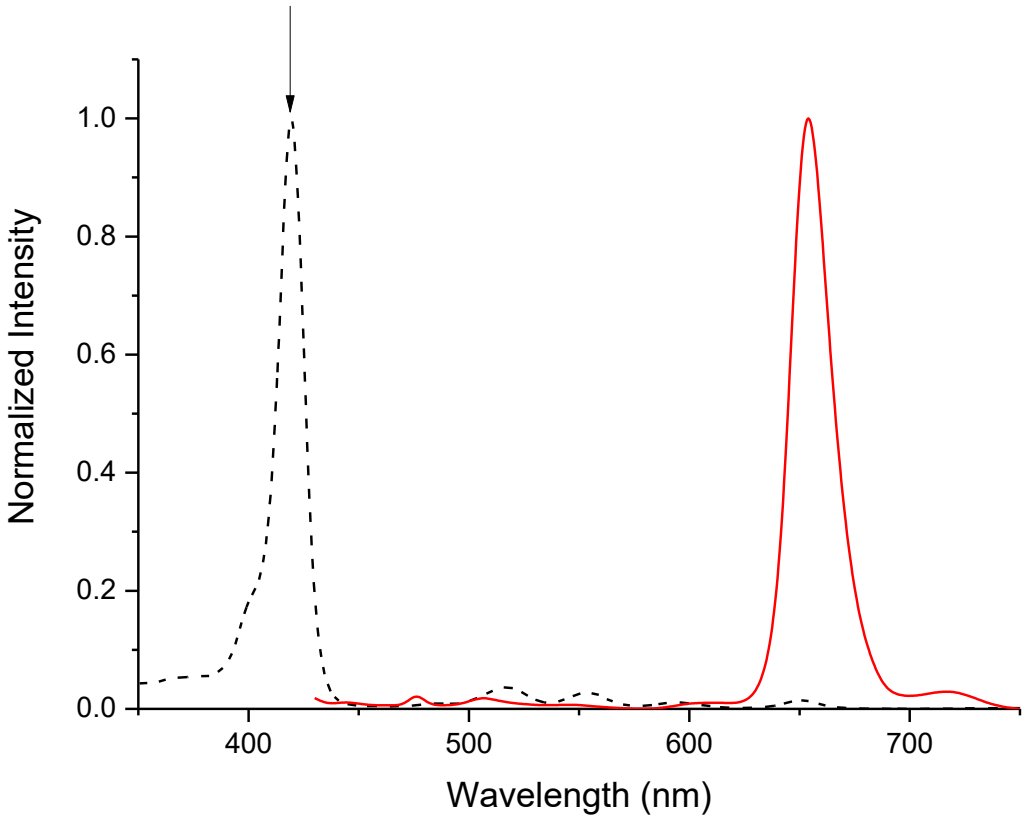

Figure 3.2.17: In red, the fluorescence spectrum of a $P(PEG750)_3$ solution ($c=1*10^{-6}$ M) in acetone. In black, Uv-Vis absorption spectrum of the same solution. The arrow indicates the wavelength where the sample is excited (422 nm maximum Soret Band) to obtain the fluorescence spectrum.

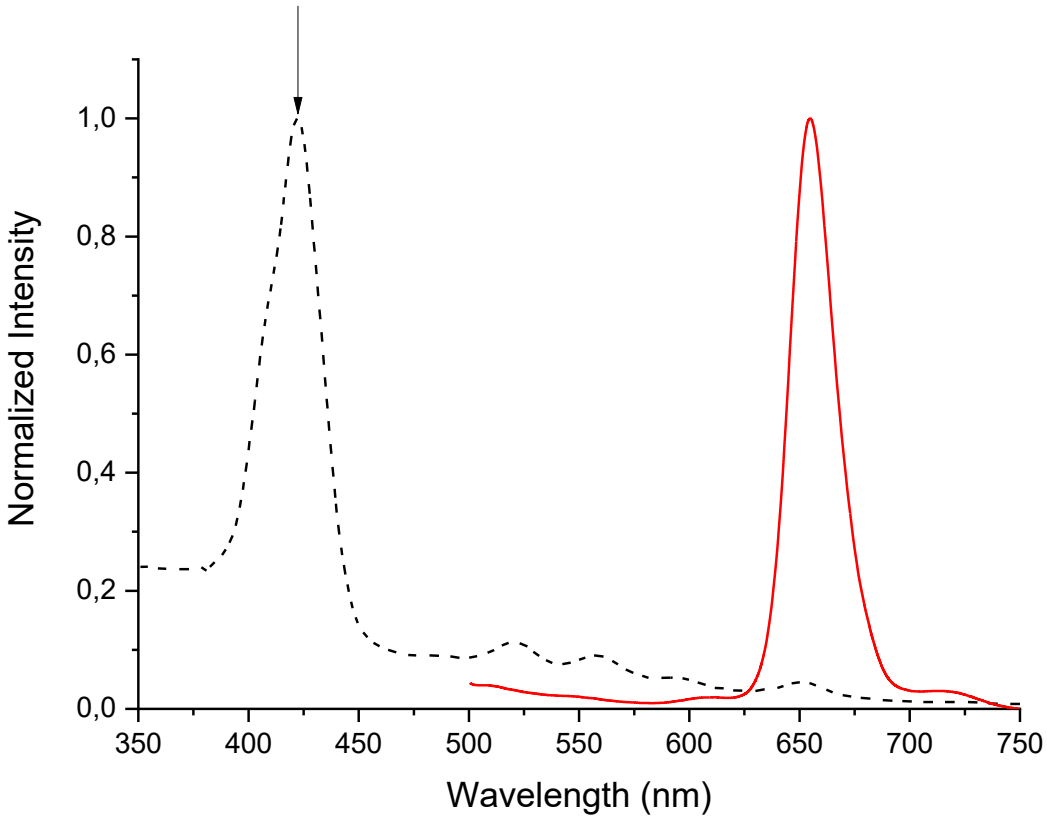

Figure 3.2.18: In red, the fluorescence spectrum of a solution of $P(PEG750)_3$ ($c=1*10^{-6}$ M) in water. In black, Uv-Vis absorption spectrum of the same solution. The arrow indicates the wavelength where the sample is excited (422 nm, maximum of the Soret Band) to obtain the fluorescence spectrum.

The greater water solubility of $P(PEG750)_3$ compared to $P(PEG350)_3$, is indicated by the intensity of the fluorescence signal which is higher for the former.

[1] Mineo, P.; Scamporrino, E.; Vitalini, D. Macromol. Rapid Commun., 2002, 23, 681–687.

Synthesis, functionalization and characterization of silver nanoparticles

Widely Silver nanoparticles have been investigated because they exhibit unusual optical, electronic, and chemical properties, depending on their size and shape, thus opening many possibilities with respect to technological applications. The silvers nanoparticles are one of the inorganic nanomaterials which are good antimicrobial agents. The researchers found that the bactericidal nanomaterials have opened a new epoch in pharmaceutical industries. Silver nanoparticles are the metal of choice as they hold the promise to kill microbe's effectively and effect on both extracellularly as well intracellularly. A variety of preparation techniques have been reported for the synthesis of silver NPs; notable examples include, laser ablation, gamma irradiation, electron irradiation, chemical reduction, photochemical methods, microwave processing, and biological synthetic methods. We have chosen to use a synthesis based on chemical reduction, for its simplicity and economy.

The synthesis of the silver nanoparticles (***Figure 3.3.1***), and their functionalization with the porphyrin derivatives (***Figure 3.3.2***), is carried out in 3 steps as shown in the following diagram:

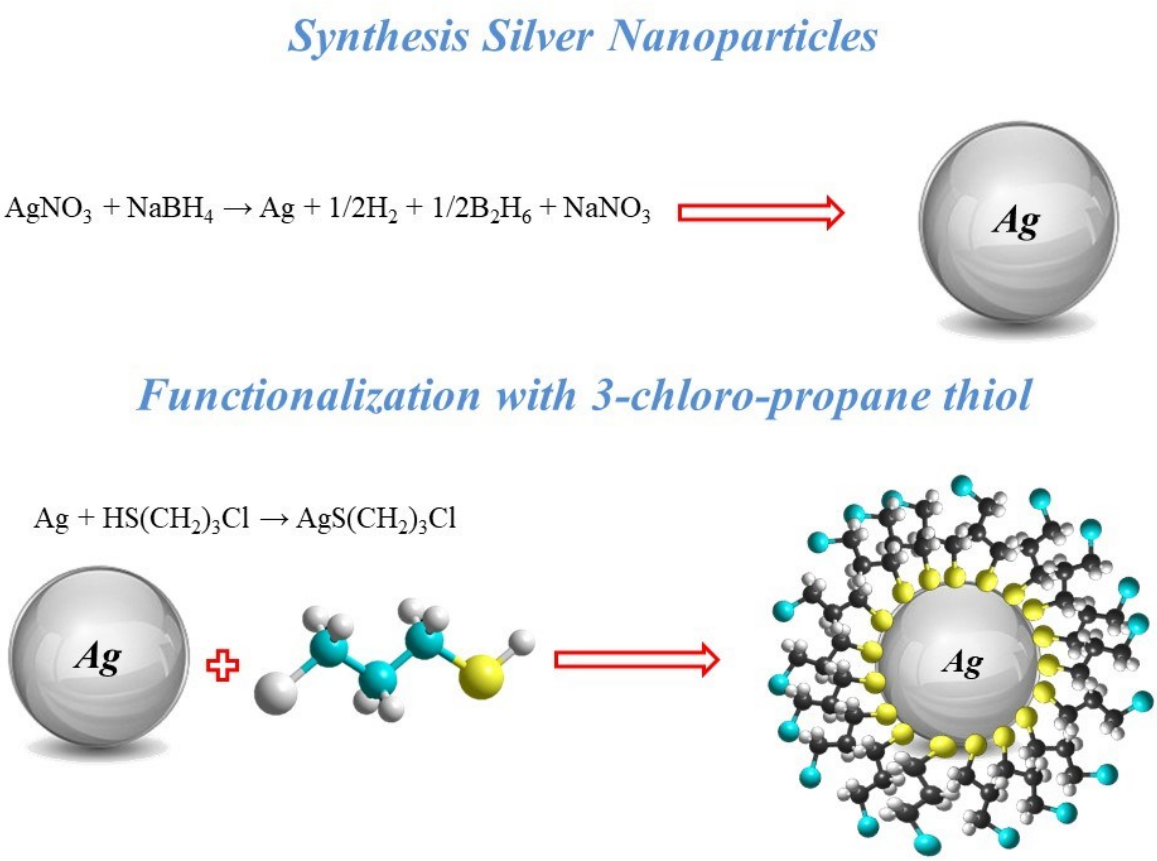

Figure 3.3.1: Synthesis scheme of silver nanoparticles and functionalization with 3-chloro-propanethiol.

Functionalization with P(PEG350)$_3$ o P(PEG750)$_3$

$$AgS(CH_2)_3Cl + P(PEG350)_3 \rightarrow AgS(CH_2)_3O\text{-}P(PEG350)_3$$

The previous reactions are valid also if is used P(PEG750)$_3$ as reactant

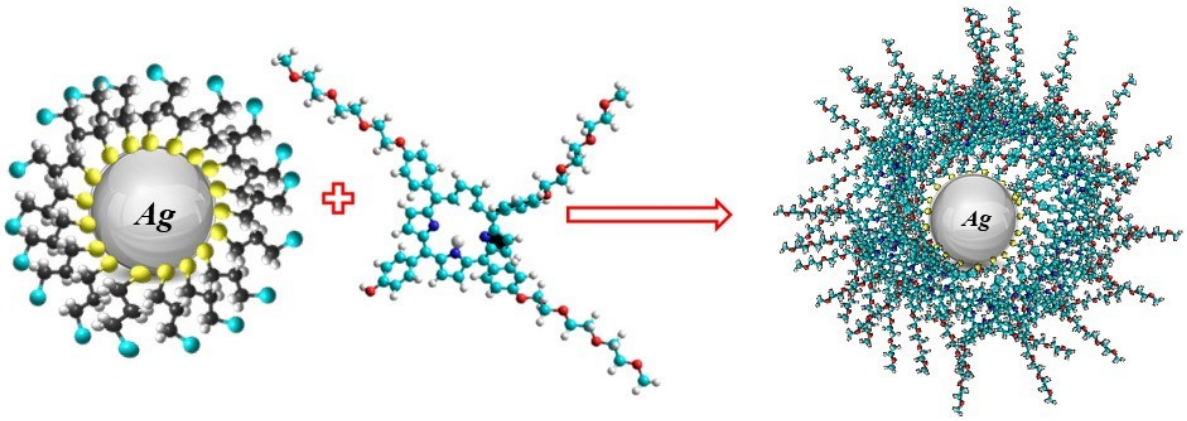

Figure 3.3.2: Functionalization scheme of AgNPs@ClPT with porphyrin derivatives

The synthesis of silver nanoparticles was performed by reducing silver nitrate with Sodium borohydride according to the following reaction: [1]

$$AgNO_3 + NaBH_4 \rightarrow Ag + 1/2H_2 + 1/2B_2H_6 + NaNO_3$$

Briefly: at 750 ml of a 2 mM solution of $NaBH_4$, placed under constant and vigorous stirring, 250 ml of a 1 mM solution of $AgNO_3$ were added at a constant rate. During the addition, the color of the solution goes from colorless to pale yellow and finally to gold yellow, as shown in the following images (***Fig. 3.3.3***).

Figure 3.3.3: Synthesis of silver nanoparticles (AgNPs). In the photo you notice the progress of the reaction: the photo on the left was taken about 2-3 minutes after of reaction, the photo on the right about 10 minutes after the reaction.

After the reaction (about 30 minutes) the colloidal suspension was kept in the fridge at 5 °C, so as to keep it stable for several months. In order to get an evidence of the presence of the plasmone and to gain information on the dimensions of the nanoparticles, a Uv-Vis characterization was performed. Although a first index of the size of the nanoparticles can be obtained from the color of the solution, the experimental confirmation is based on the wavelength of the plasmonic peak; moreover, the width of the peak is an index of the size polydispersity (***Fig. 3.3.4***).

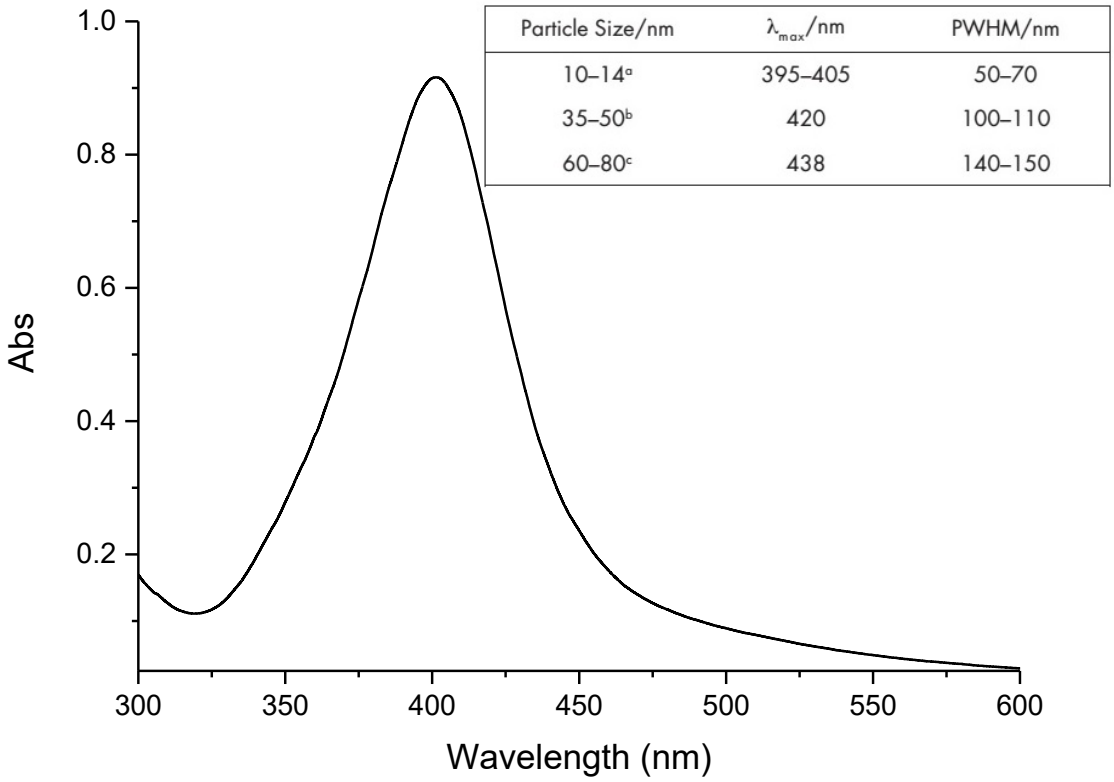

Figure 3.3.4: UV-vis spectrum of AgNPs. Diluted sample 1: 3.

As shown by the Uv-Vis spectrum of ***Figure 3.3.4***, the plasmonic peak has a maximum at 399 nm. From the values shown in the table of the same figure, according to literature data, we can suppose that the dimensions of the nanoparticles range from 10nm to 14nm. These data have been confirmed experimentally by the technique of Dynamic light scattering (DLS) (***Fig.3.3.5***).

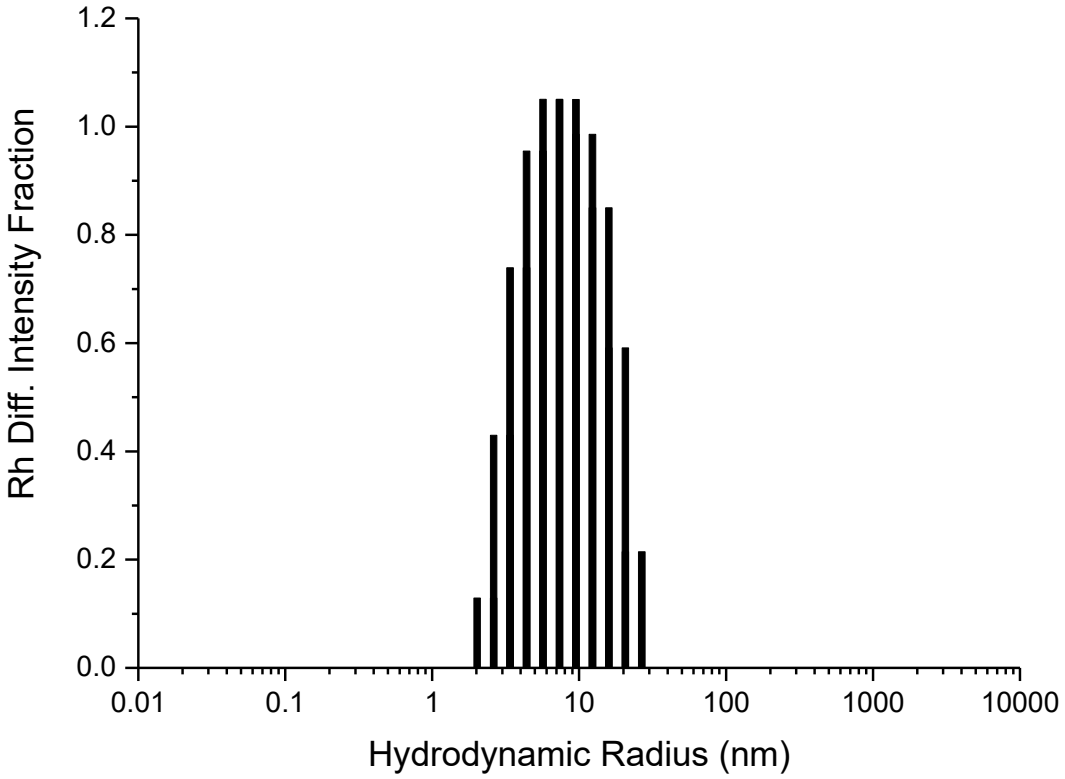

Figure 3.3.5: Size distribution of AgNPs in water

R_H average provided by the DLS technique is about 10.4nm ± (0.4%), a value that agrees with values found in literature (***see figure 3.3.4***) for a plasmonic peak at 400 nm, even if the distribution is wide enough. The possible fluorescence properties of AgNPs have also been studied and it has been seen that they do not show these.

The step that follows is about the functionalization of the particles with a thioled linker, which is carried out by two methods, known in literature, but used in a slightly modified form. ***Figure 3.3.6*** briefly describes the summary procedures:

Method 1

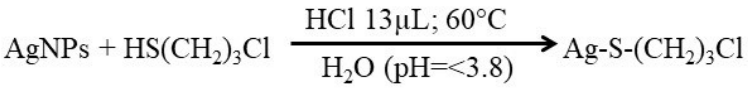

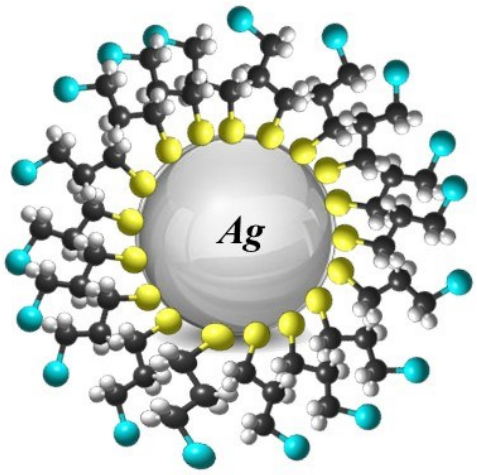

Method 2

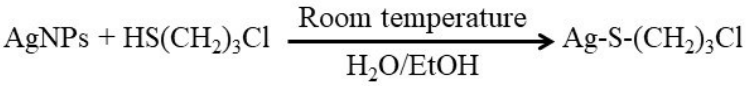

Figure 3.3.6: Scheme of the two methods of functionalization of the nanoparticles with the thioled ligand.

Method 1[2]: Briefly, HCl 1M was added to a 10 mL of an aqueous solution of AgNPs (0.27 mg), placed into a vial, in order to regulate the pH at about 3.7. Then 40µL ($4.1*10^{-4}$mol) of 3-chloro-1-propanethiol were added and the mixture heated at 60 °C for 3 h under vigorous stirring.

The obtained solution, cooled to room temperature, was centrifuged at 5000 rpm for 15 min. The residue was separated from surnatant, sonicated in ethanol, and centrifuged for 2 more times. The final product AgNPs@ClPT was maintained under vacuum at 60 °C for 24 h and then suspended in acetone and analyzed by means UV-Vis (***Fig.3.3.7***) and DLS (***Fig.3.3.8***) techniques.

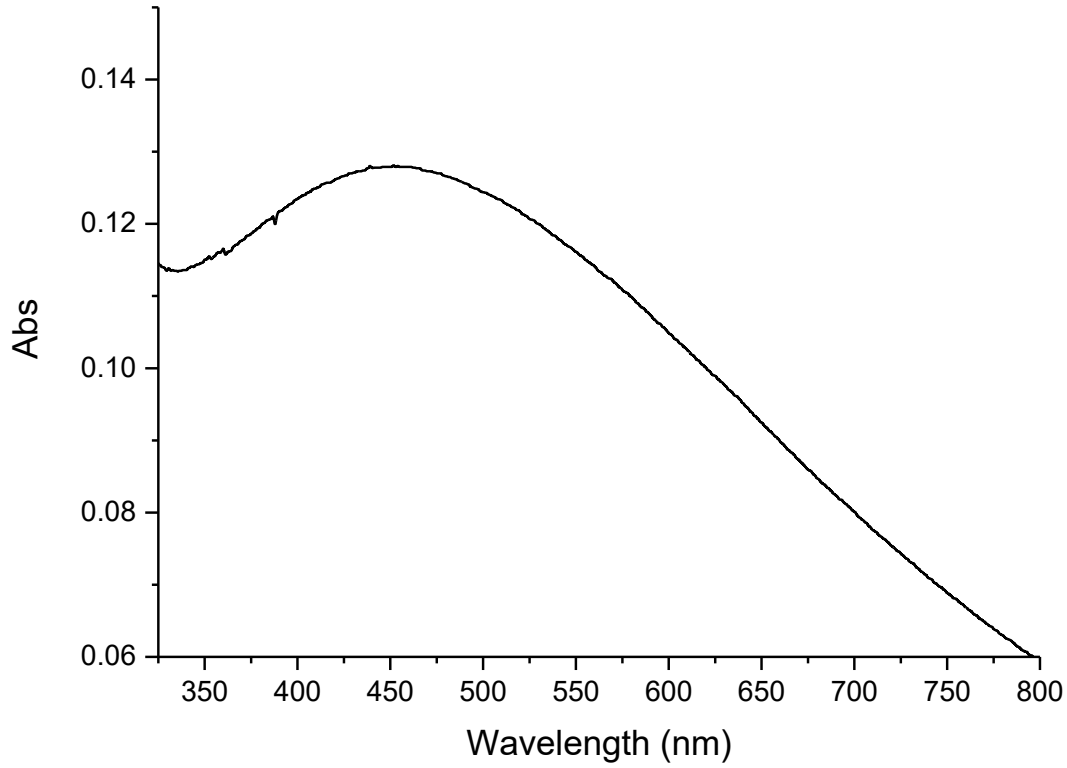

Figure 3.3.7: Uv-Vis spectrum of AgNPs after functionalization with 3-chloro-propanethiol in acetone (method 1).

The Uv-Vis spectrum of ***Figure 3.3.7*** shows an extended peak along the whole Uv-Vis spectrum, probably due to an aggregation of the particles through lipophilic interaction. One possible explanation could be the extensive functionalization of some systems that produce functionalized particles with different sizes. The dimensions of these were obtained through DLS (***Fig.3.3.8***).

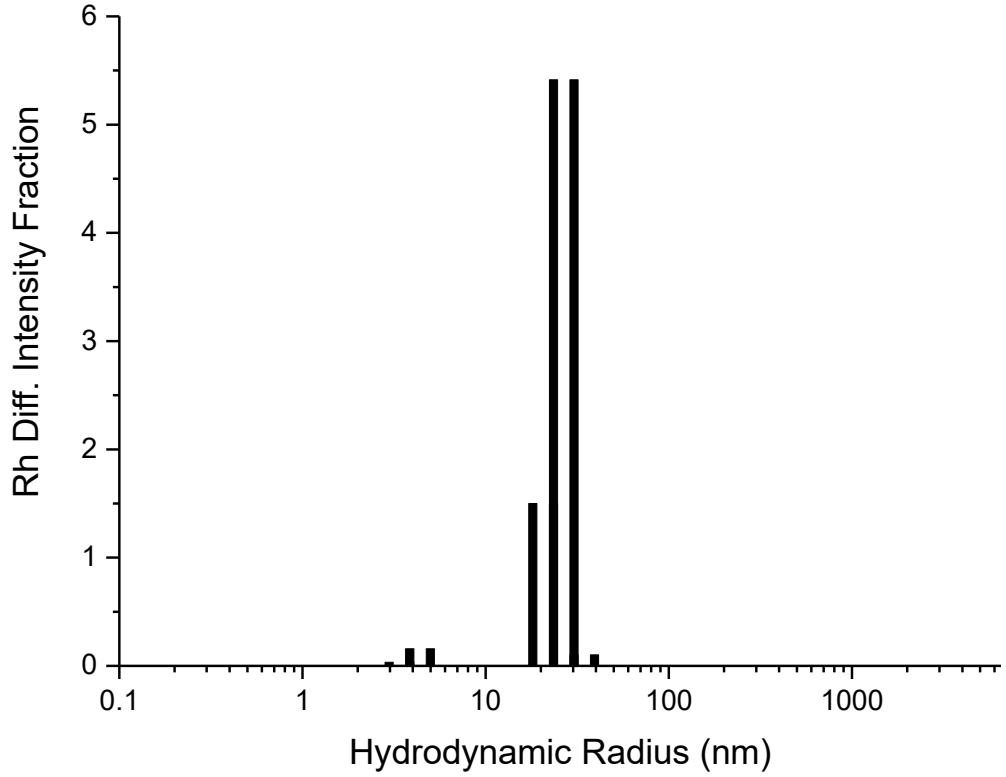

Figure 3.3.8: Size distribution of AgNPs@ClPT in acetone (method 1).

The DLS spectrum in ***Figure 3.3.8*** shows a R_H average about 4 nm, possibly due to non-functionalized nanoparticles or partially functionalized, while there is a second much more intense distribution at values of 36.9nm (± 1.7nm), approximately three times larger than that of bare nanoparticles. For these reasons, it is possible to assume the successful functionalization of the particles, and also the possible aggregation of these systems as previously mentioned.

Method 2 [3]: A 10 ml of AgNPs, are added 2 ml of a solution of 3-chloro-propanethiol in ethanol (40μL thiol in 2ml of ethanol) and left to react under vigorous stirring at room temperature for 2.5 hours. The obtained solution, cooled to room temperature, was centrifuged at 5000 rpm for 15 min; the residue was separated from supernatant, sonicated in ethanol, and centrifuged for 2 more times. The final product AgNPs@ClPT was maintained under vacuum at 60 °C for 24 h and then suspended in acetone and analyzed by means UV-Vis (***Fig. 3.3.9***) and DLS (***Fig. 3.3.11***) techniques.

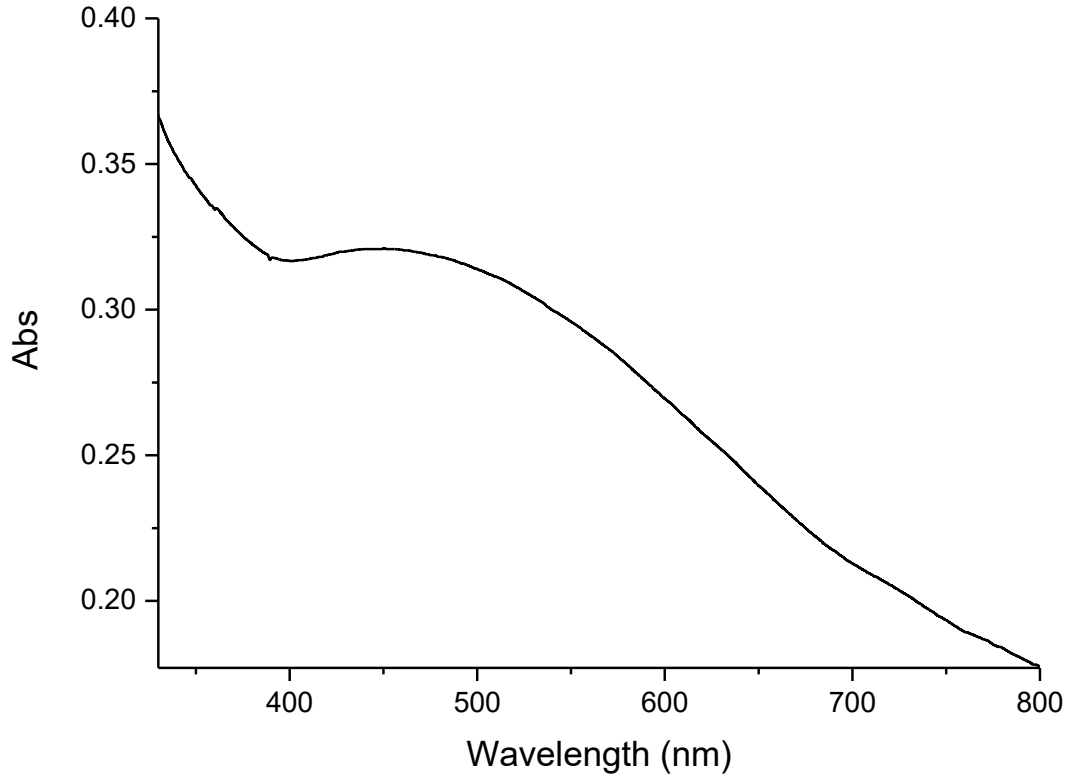

Figure 3.3.9: Uv-Vis spectrum of AgNPs after functionalization with 3-chloro-propanethiol in acetone (method 2).

Even for the Uv-Vis spectrum of ***Figure 3.3.9***, that refers to the second method of functionalization, it shows an extended peak along the whole Uv-Vis spectrum, due to an aggregation of the particles through lipophilic interaction, as in the first case. This leads to a high dimensional distribution of nanoparticles. In order to verify this hypothesis, a second test was performed, by monitoring the form of resonance plasmon peak during the progress of the reaction. The obtained results are shown in ***Figure 3.3.10***.

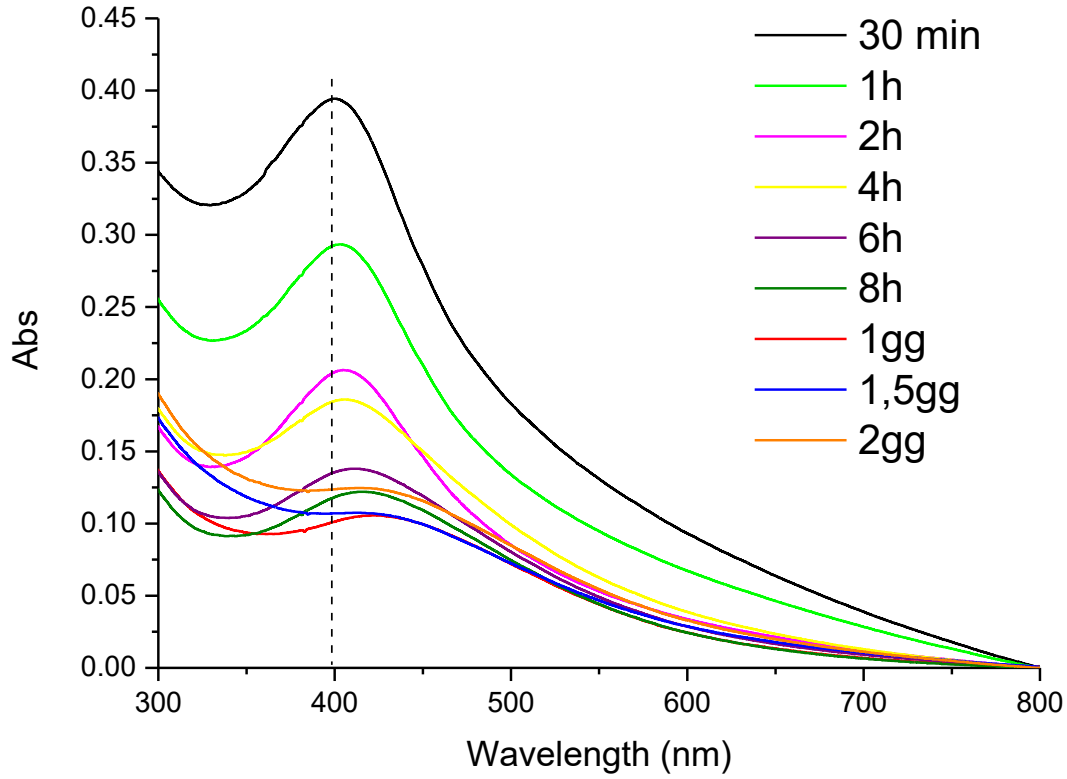

Figure 3.3.10: Monitoring of resonance plasmon peak of AgNPs during the functionalization reaction with 3-chloro-propanethiol.

The monitoring of the plasmon resonance peak shows a widening of the peak during the progress of the reaction. This can be explained as the formation of larger objects, not only because of the functionalization of the surface, but also to the aggregation of these functionalized systems due to lipophilic interactions. After several monitoring tests it was decided that the optimal reaction time is two and a half hours. In this case, a very good compromise between the plasmonic signal and the degree of functionalization is obtained.

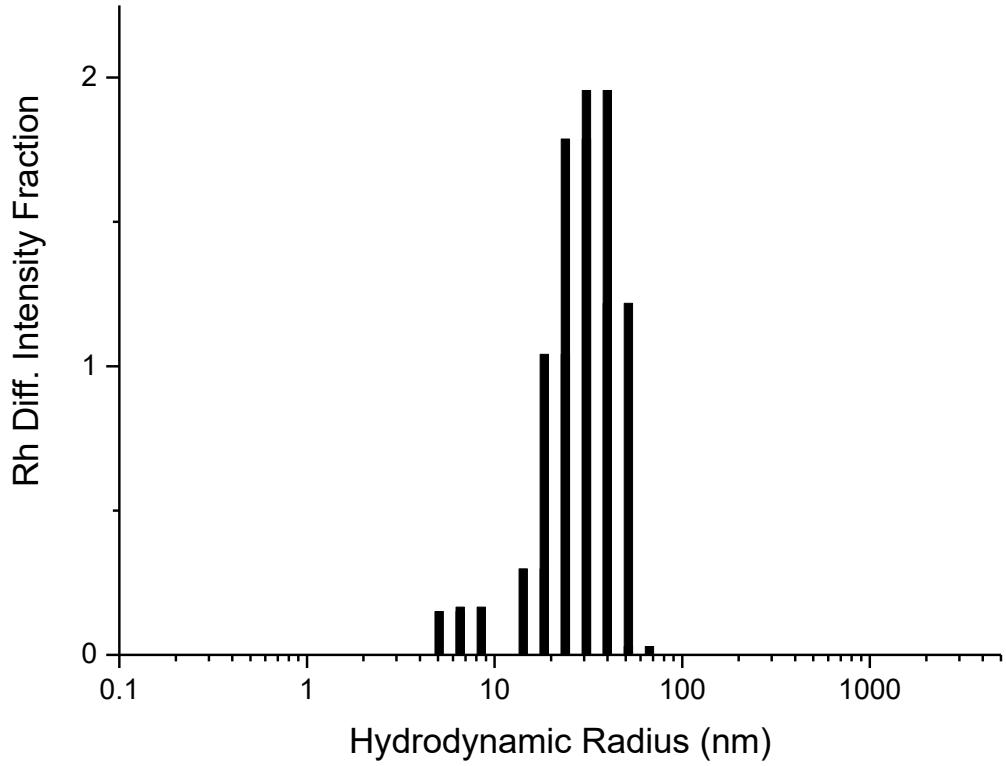

Figure 3.3.11: Size distribution of AgNPs@ClPT in acetone (method 2).

The DLS spectrum of ***Figure 3.3.11*** also shows, as for the previous sample, a first R_H average at values of about 8.5 nm, index of a part of the sample not, or partially, functionalized, and, a second R_H average at 48.5 nm (± 1.7nm), index of a successful functionalization. The value also allows us to hypothesize that we can obtain a more boosted functionalization by using method 2.

The third step of the synthetic process concerned the covalent bond, through a nucleophilic substitution reaction, of 5,10,15 tri (p-[ω-methoxy-poly (ethylene oxide)] phenyl}-20-(p-hydroxyphenyl) porphyrin [$P(PEG350)_3$ or $P(PEG750)_3$] at the AgNPs@ClPT's surface.

For both methods of formation of AgNPs@ClPT, described above, the functionalization with the porphyrin provides the following procedure [(for the sake of brevity, an example of functionalization with $P(PEG350)_3$ will be reported using method 1 (***see diagram 3.3.6***) and one with $P(PEG750)_3$ using method 2 (***see diagram 3.3.6***)]:

Briefly, 5 mg of AgNPs@ClPT were dispersed in a vial with 10 mL of acetone, 5mL of triethylamine and 5 mg of $P(PEG350)_3$, and the mixture held at boiling point for 24 h. Then, to separate the unreacted $P(PEG350)_3$, the solution (cooled at 25 °C) was centrifuged at 9000

rpm for 15min and the colored supernatant was eliminated. AgNPs@P(PEG350)$_3$ residue was solubilized in acetone, sonicated again for 5 min and centrifuged; this procedure was repeated twice. The final product AgNPs@P(PEG350)$_3$ was put under vacuum at 60 °C for 24 h and characterized by UV-Vis (***Figure 3.3.12***), fluorescence (***Figure 3.3.14***), TEM (***see result and discussion***) and DLS techniques (***Figure 3.3.13***).

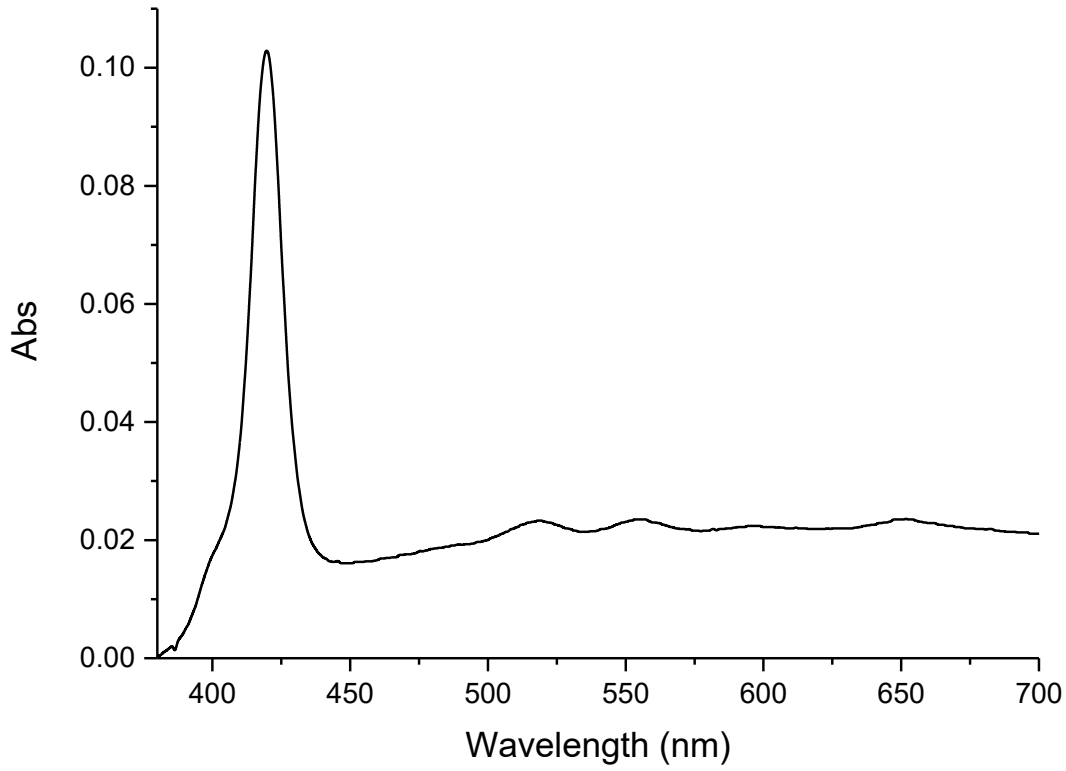

Figure 3.3.12: UV-Vis spectrum of AgNPS functionalized with 3-chloro-propanethiol (method 1) and P(PEG350)$_3$ in acetone.

The Uv-Vis spectrum of AgNPs functionalized with P(PEG350)$_3$ shows typical porphyrin signals: the peak corresponding to the Soret at 419.5 nm and the four Q-bands at values of 518, 555, 596 and 650 nm. However, the presence of a scattering signal is noticeable, due to the diffusion of light caused by the presence of the nanoparticles, the signal that partially covers the typical signals of the Q-bands. Also, The DLS analysis was then performed to verify the expected increase in the size of the nanoparticles due to the functionalization and compared to the previous measurements (***Fig 3.3.13***).

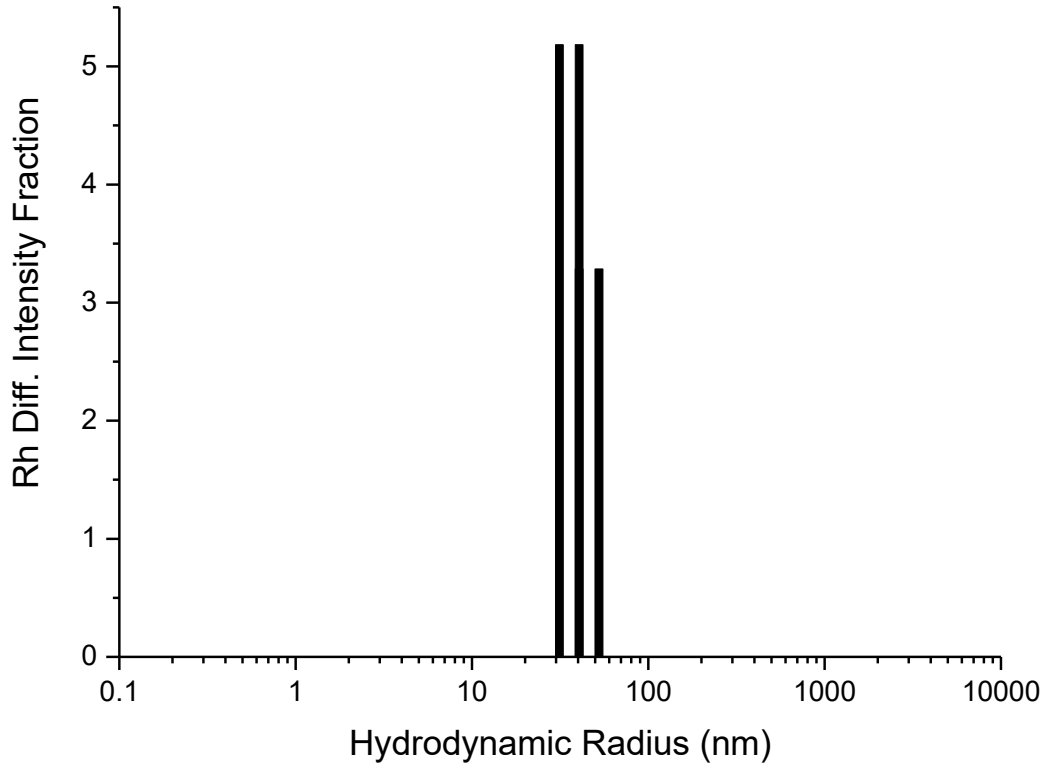

Figure 3.3.13: Size distribution AgNPs functionalized with 3-chloro-propanethiol (method 1) and $P(PEG350)_3$ in acetone.

Figure 3.3.13 shows sizes distribution of AgNPs@$P(PEG350)_3$, the value of R_H average is about 47.4nm (± 2.2%). The increase in sizes, if compared with the AgNPs@ClPT value of about 10 nm, makes one think of a successful functionalization with porphyrin derivative. The fluorescence experiment of the AgNPs@$P(PEG350)_3$ was also performed, using acetone as solvent. The relative spectrum is shown in the ***Figure. 3.3.14***.

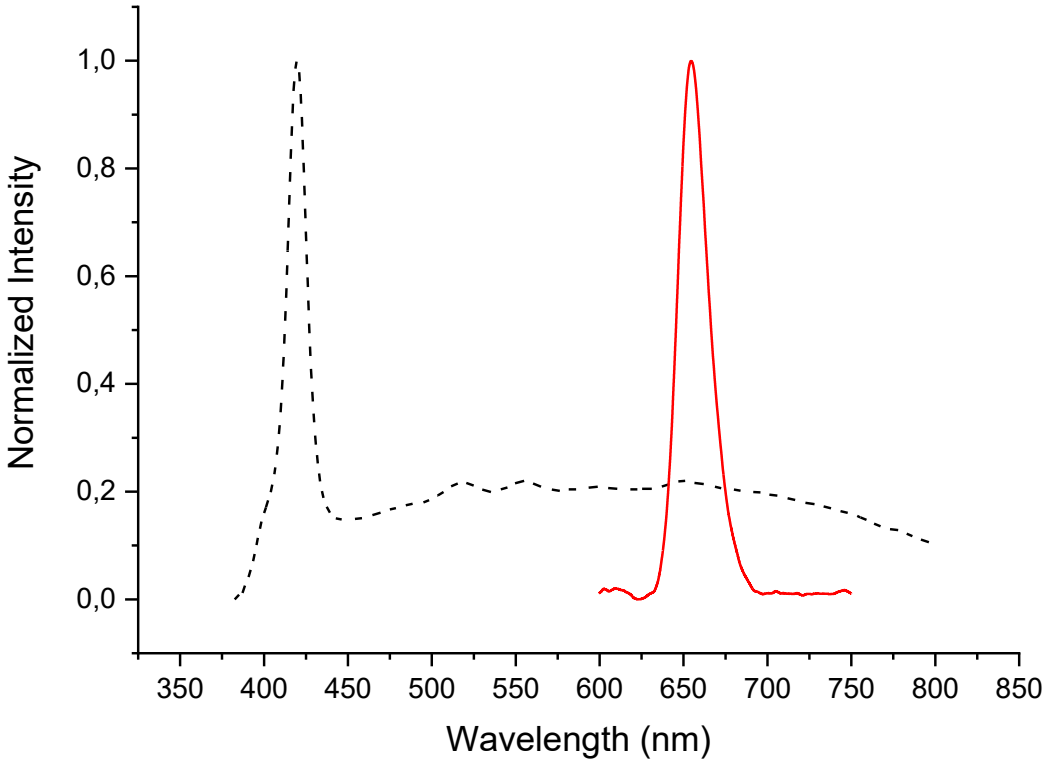

Figure 3.3.14: In black, Uv-Vis spectrum of AgNPs functionalized with 3-chloro-propanediol (method 1) and P $(PEG350)_3$ in acetone, in red, the corresponding fluorescence spectrum of the same solution (λ_{exc}=419nm).

Since, by analyzing nanoparticles as such and those of thiolate, no fluorescence signal was detected, the fluorescence peak observed at 654nm is a reliable indication of the presence of porphyrin units, even if it has still to be verified that these are actually bound to nanoparticles. The aqueous suspension of the sample was also analyzed, and the Uv-Vis and fluorescence spectra are shown in ***Figure 3.3.15*** and ***Figure 3.3.16***, while the corresponding spectrum of DLS is shown in ***Figure 3.3.17***.

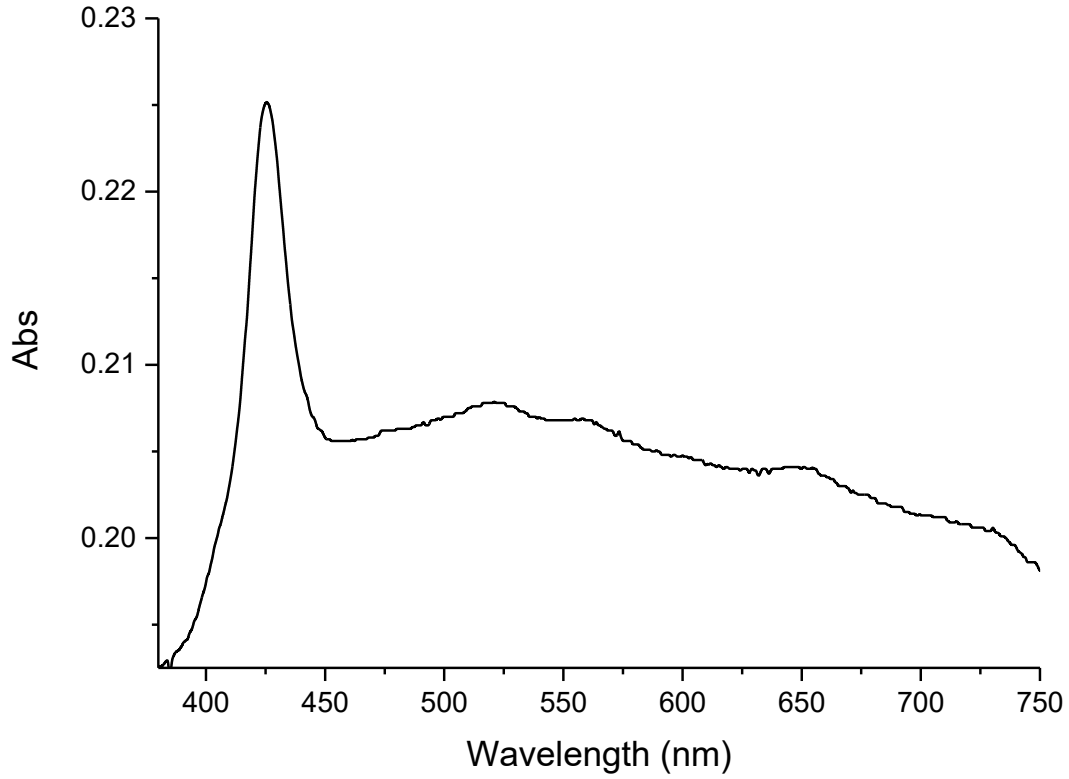

Figure 3.3.15: UV-Vis spectrum of AgNPs functionalized with 3-chloro-propanethiol (method 1) and $P(PEG350)_3$ in water.

The Uv-Vis spectrum of ***Figure 3.3.15***, shows a red-shift of the porphyrin Soret band at 425nm typical of the aqueous solvent. The wide scattering signal depends on the presence of the nanoparticles, or on the tendency of the porphyrinic species to give aggregates, even if they are bound to the surface of the nanoparticles. The dimensions of the objects under examination were calculated by means of DLS, suspending the sample in water to verify any differences with the same sample in acetone.

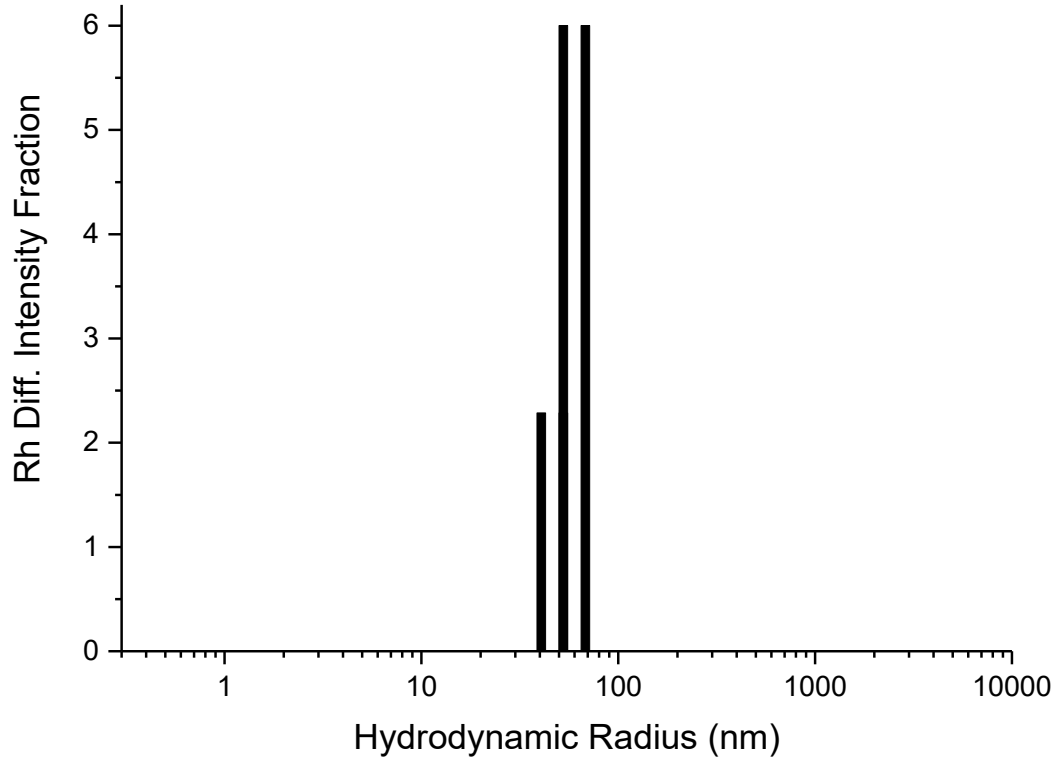

Figure 3.3.16: Size distribution AgNPs functionalized with 3-chloro-propanethiol (method 1) and $P(PEG350)_3$ in water.

In ***Figure 3.3.16*** we can notice that the R_H average of the functionalized nanoparticles changes from about 47.4nm (± 2.2 %) in acetone to 71.0 (± 0.3%) in water. The explanation of this phenomenon can be found in the possible formation of aggregates in water due to the porphyrin-porphyrin interaction.

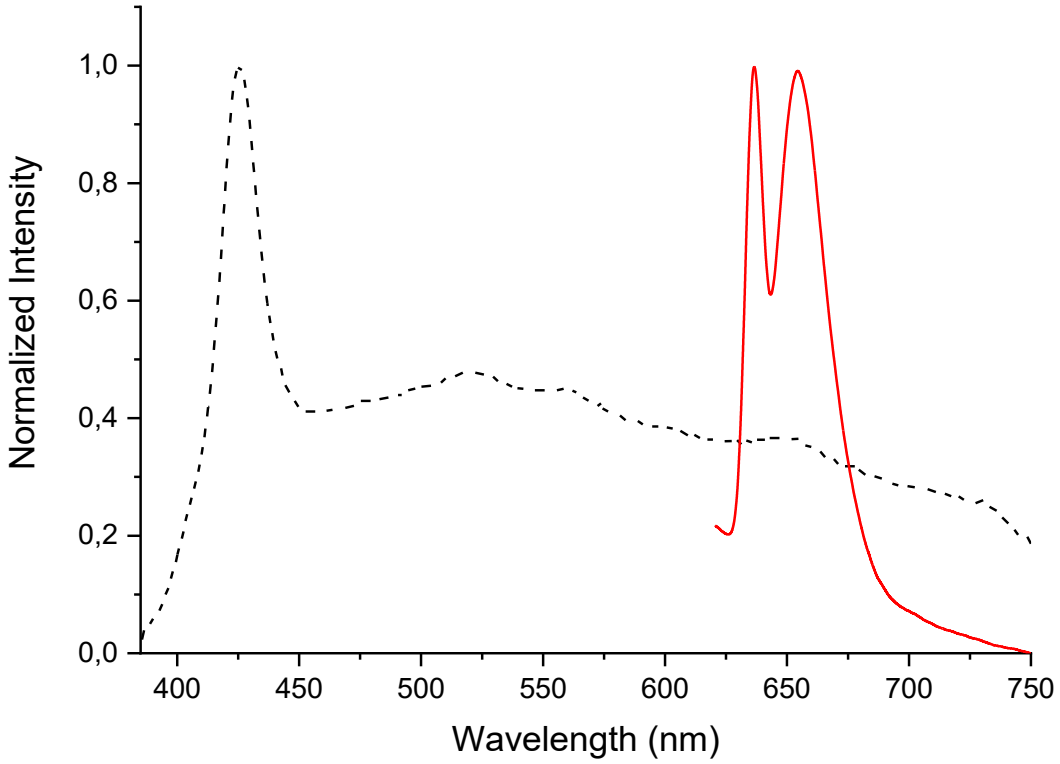

Figure 3.3.17: In black, the Uv-Vis spectrum of AgNPs functionalized with 3-chloro-propanethiol (method 1) and P(PEG350)$_3$ in water. In red, the fluorescence spectrum of the same solution (λ_{exc}=425nm).

The fluorescence spectrum of the sample in water solution, ***Figure 3.3.17***, shows a peak at 654 nm, evidence of the presence of the porphyrin on the particles' surface. Instead, the signal at 636nm is due to the presence of an artefact. In fact, using a filter at 405 nm, before the detector, the signal at 636 disappear.

As previously described, the characterizations referring to the functionalization reaction of AgNPs@ClPT with P(PEG750)$_3$ are now reported using AgNPs@ClPT obtained with the second functionalization method (*see diagram 3.3.6*). ***Figure 3.3.18*** shows the Uv-Vis spectrum of the particles, dispersed in acetone.

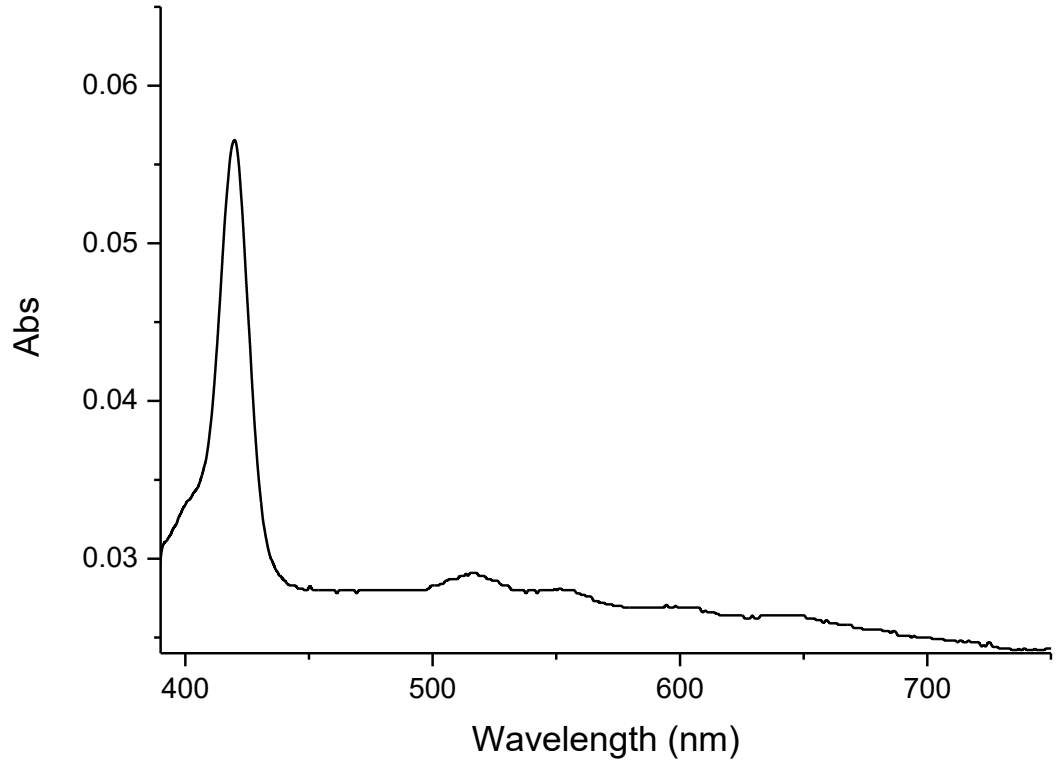

Figure 3.3.18: UV-Vis spectrum of AgNPs functionalized with 3-chloro-propanethiol (method 2) and $P(PEG750)_3$ in acetone solution.

The Uv-Vis spectrum of ***Figure 3.3.18*** shows the typical porphyrin signals confirming its presence. Moreover, unlike the same sample (spectrum not shown for the sake of brevity) in which the coupling agent was bound by method 1, the signals coming from the Q bands are clearer, and the overall intensity is higher, confirming the greater effectiveness of this method compared to the previous one. The dimensions of these systems were obtained through DLS (***Fig.3.3.19***)

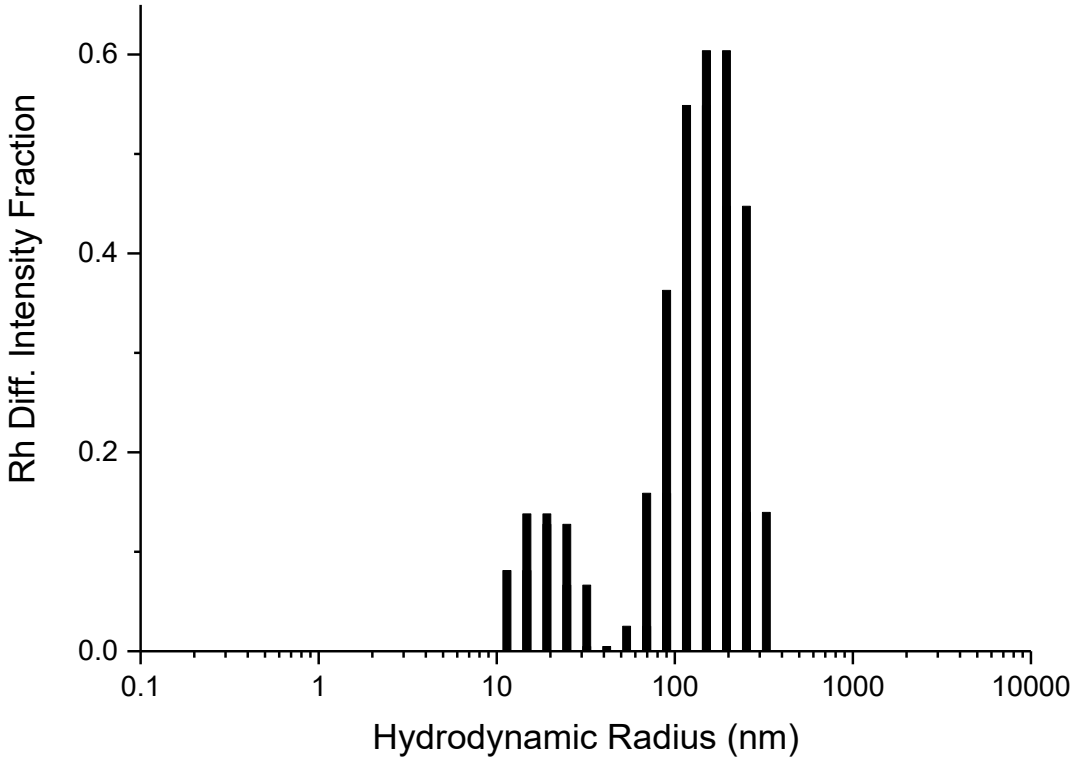

Figure 3.3.19: Size distribution AgNPs functionalized with 3-chloro-propanethiol (method 2) and $P(PEG750)_3$ in acetone.

From the DLS spectrum of ***Figure 3.3.19*** we can notice two R_H averages, the first at values of about 30 nm due to partially or non-functionalized particles; the second distribution is centered at 120 nm and confirms once again the most efficient functionalization obtained with this method.

The same solution was also characterized by fluorescence (***Fig. 3.3.20***).

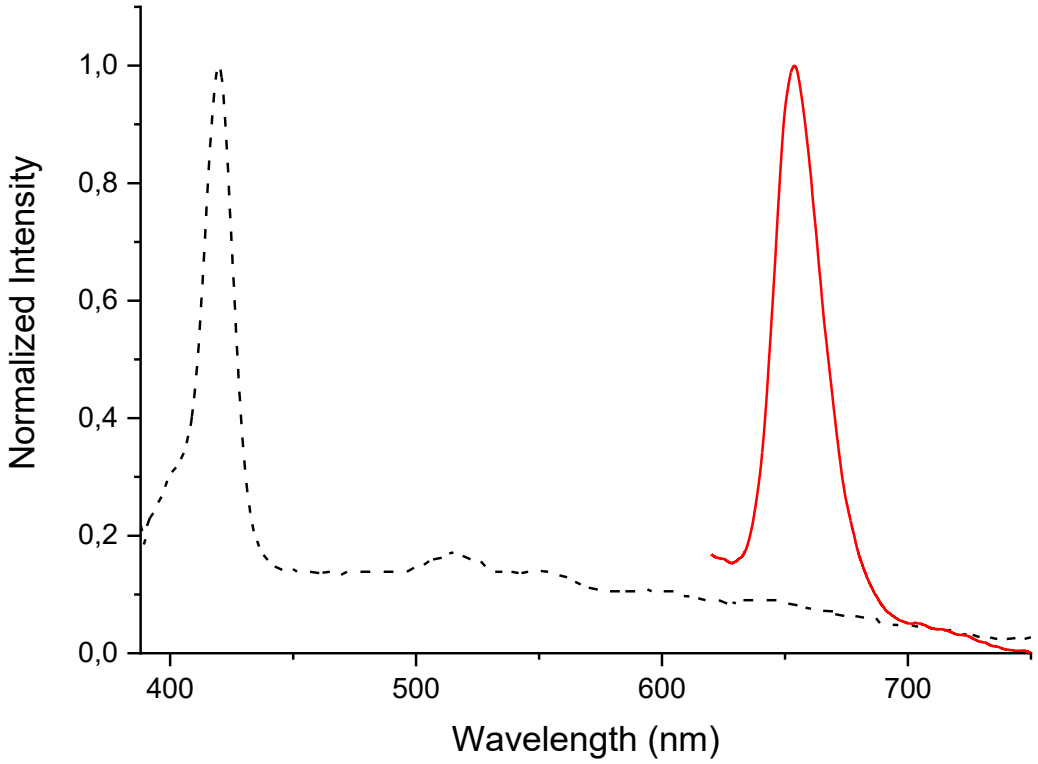

Figure 3.3.20: In black, the Uv-Vis spectrum of AgNPs functionalized with 3-chloro-propanethiol (method 2) and $P(PEG750)_3$ in acetone. In red, the fluorescence spectrum (λ_{exc}=419nm) of the same solution.

The fluorescence spectrum, ***Figure 3.3.20***, shows the typical peak of emission of the porphyrin at 654nm (λ_{ecc}=419nm). The aqueous suspension of the same sample was also analyzed, and the spectra of Uv-Vis (***Fig. 3.3.21***), of fluorescence (***Fig. 3.3.22***) and DLS (***Fig. 3.3.23***), are shown below.

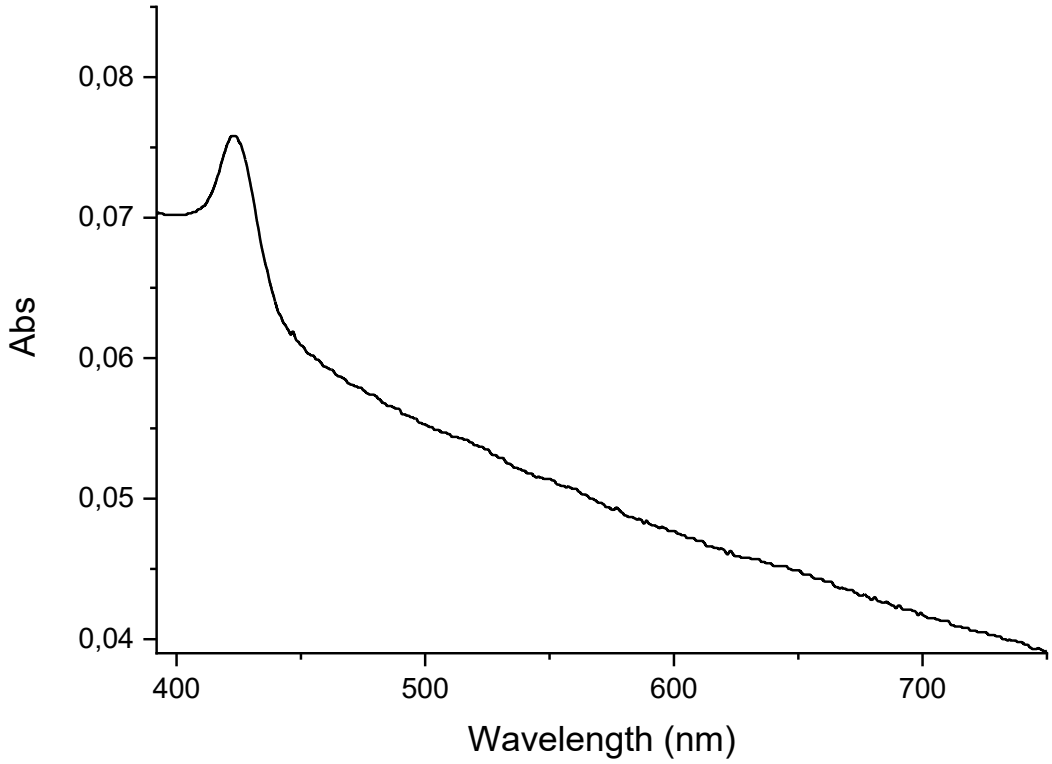

Figure 3.3.21: UV-Vis spectrum of AgNPs functionalized with 3-chloro-propanethiol (method 2) and $P(PEG750)_3$ in water.

From the spectrum of ***Figure 3.3.21*** we notice the presence of the Soret band. Also, the Q bands signal disappears because it is covered by the scattering phenomenon.

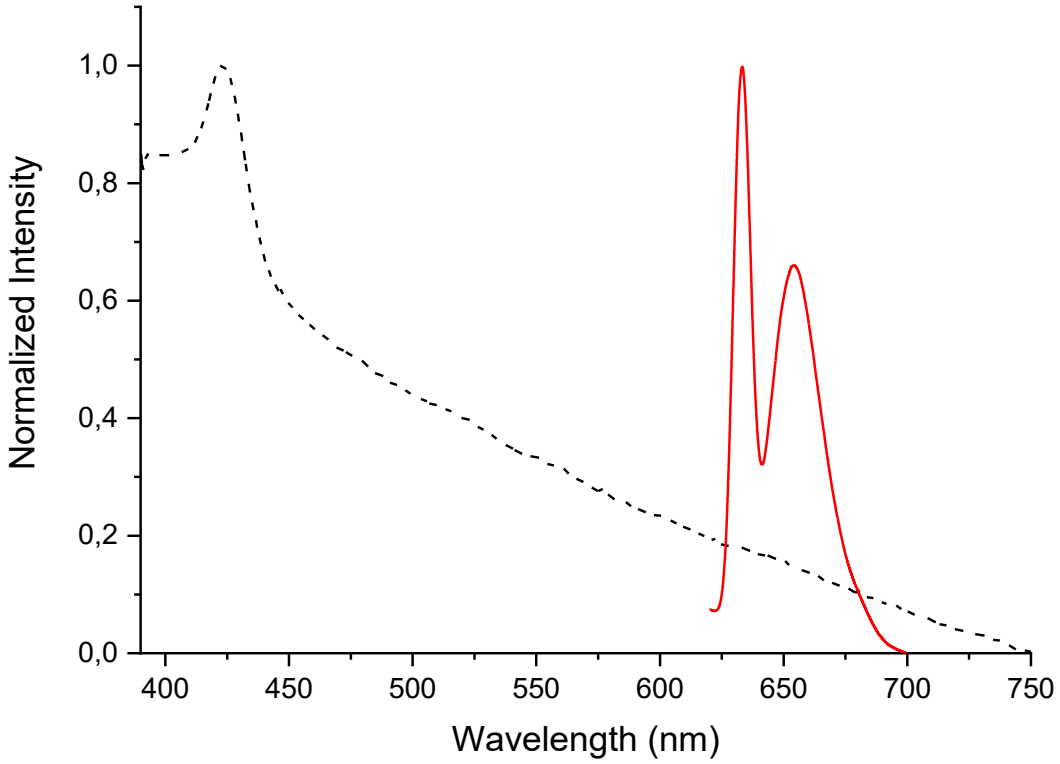

Figure 3.3.22: In black, the Uv-Vis spectrum of AgNPs functionalized with $P(PEG750)_3$ in water. In red, the corresponding fluorescence spectrum (λ_{exc}=425nm) of the same solution.

The fluorescence spectrum, ***Figure 3.3.22***, acquired in water, shows the typical peak of emission of the porphyrin at 654 nm, and, the signal at 636 nm is due to the presence of an artefact, as previously discussed with regard to ***figure 3.3.17***.

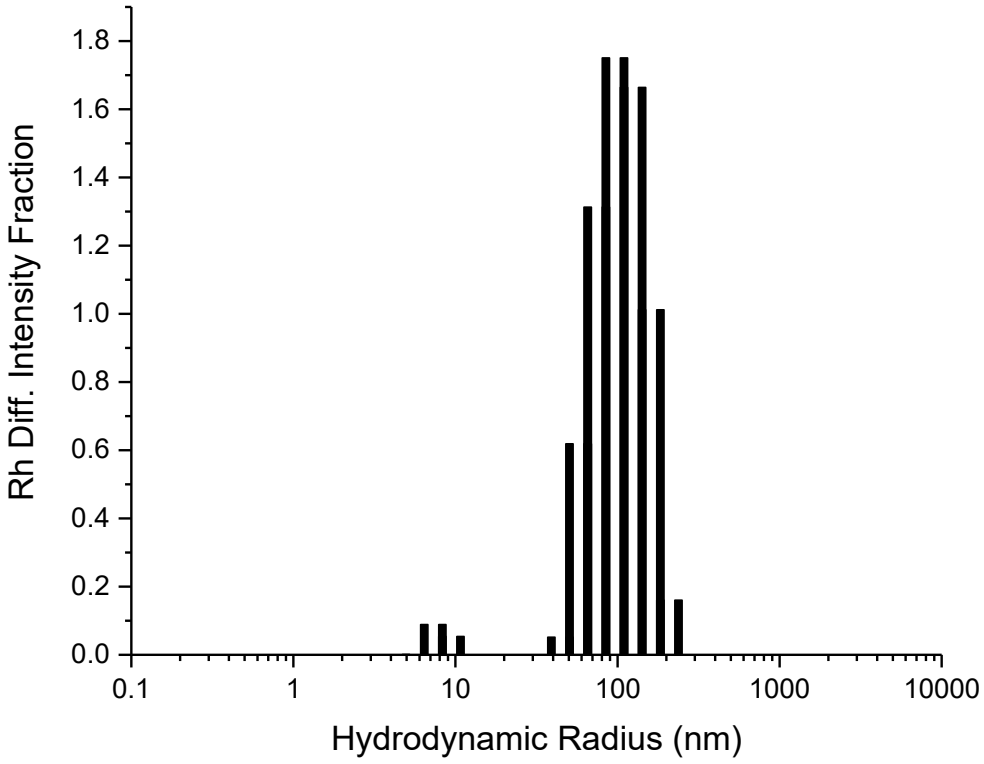

Figure 3.3.23: Size distribution AgNPs functionalized with 3-chloro-propanethiol (method 2) and $P(PEG750)_3$ in water.

From the DLS spectrum of ***Figure 3.3.23*** we notice two R_H averages, the first at values of about 10 nm, due to partially or non-functionalized particles; the second distribution is centered at 100 nm, and it confirms once again the most efficient functionalization obtained with this method.

[1] Basu, S; Jana, S.; Pande, S. T. Pal, J. of Col. and Int. Sci., 2008, 321, 288–293.
[2] Uzer, A.; Can, Z.; Akin, I.; Ercag, E.; Apak, R. Anal. Chem., 2014, 86, 351−356.
[3] McFarland, A.D.; Van Duyne, R.P. Nano Lett., 2003, 3, 1057-1062.

Synthesis, functionalization and characterization of gold nanoparticles

Colloidal gold is very attractive for several applications in biotechnology because of its unique physical and chemical properties. Many different synthesis methods have been developed to generate gold nanoparticles (AuNPs).

Techniques for making different AuNPs can be categorized into two principles, the “bottom up” method or “top down” methods. The bottom up method includes nanosphere lithography, chemical, photochemical, electrochemical, templating, sonochemical and thermal reduction techniques. This method involves assembly of atoms (produce by reduction of ions) into desired nanostructures. Top down methods such as photolithography and electron beam lithography, requires the removal of matter from the bulk material to get the desired nanostructure. While both methods can generate AuNPs of desired shape and size, each have their own drawbacks, (e.g., poor monodispersity in case of bottom up methods, and extensive waste of material in top down methods). the synthesis chosen by us falls into the category of bottom up methods, in particular that of chemical reduction.

The figures below show the scheme of synthesis (***Figure 3.4.1***) and functionalization (***Figure 3.4.2***) of gold nanoparticles:

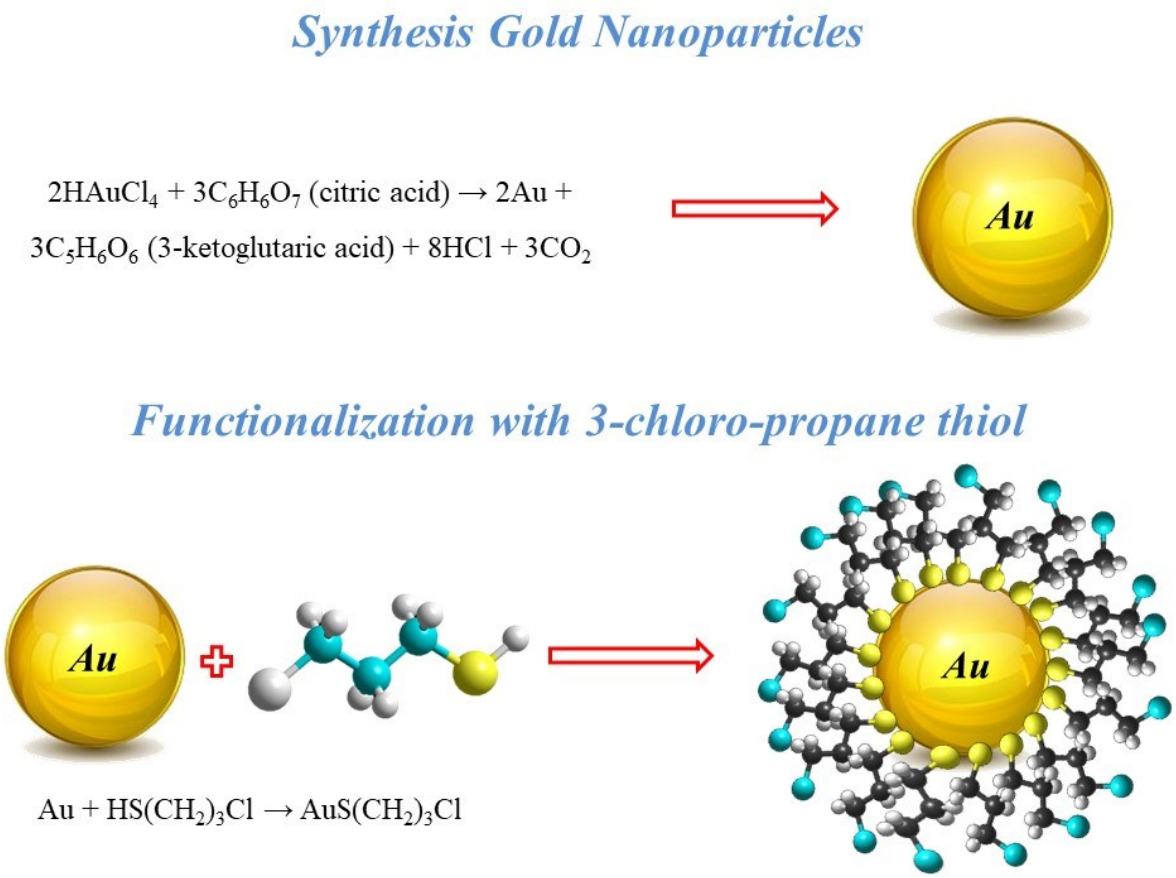

Figure 3.4.1: Scheme of gold nanoparticles synthesis and functionalization with 3-chloro-propanethiol.

Functionalization with P(PEG350)$_3$ o P(PEG750)$_3$

$$AgS(CH_2)_3Cl + P(PEG350)_3 \rightarrow AgS(CH_2)_3O\text{-}P(PEG350)_3$$

The previous reactions are valid even if $P(PEG750)_3$ is used as a reactant

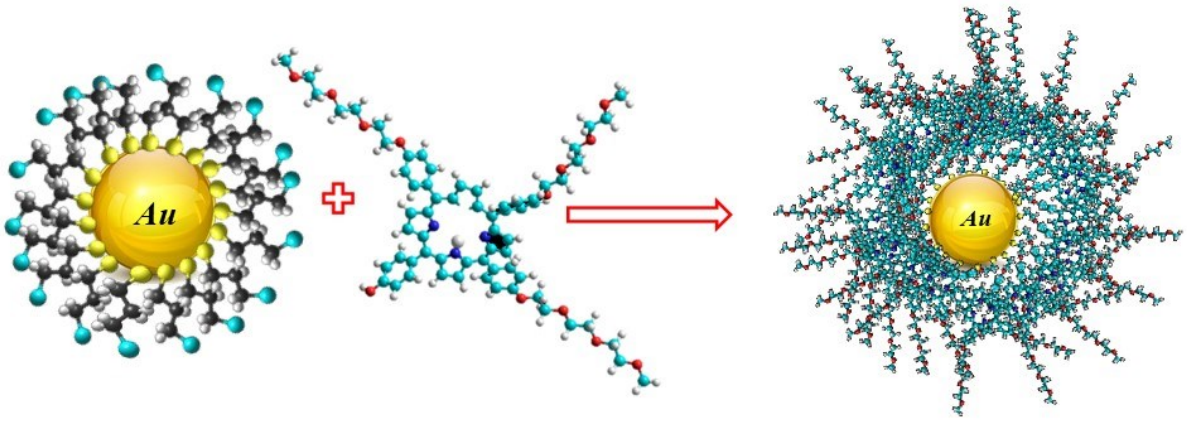

Figure 3.4.2 scheme of the functionalization of AuNPs@ClPT with porphyrin derivatives

The synthesis of the gold nanoparticles was carried out following the method introduced by Turkevic in 1951[1] and perfected by Frens in 1970[2]. This method exploits the reduction of tetrachloroauric acid with sodium citrate according to the following reaction:

$$2HAuCl_4 + 3C_6H_6O_7 \text{ (acido citrico)} \rightarrow 2Au + 3C_5H_6O_6 \text{ (acido 3-chetoglutarico)} + 8HCl + 3CO_2$$

Briefly, chloroauric acid ($HAuCl_4$, 17 mg, 1mM) and 50mL of water were placed into a three-neck flask and hold to reflux under vigorous stirring. Then 5 mL of sodium citrate (38.8 mM) were added. Immediately, the color of the solution changed from light yellow to red. The AuNPs solution was refluxed for further about 10 min then, always under stirring, cooled to ambient temperature. The final solution was stored at 4 °C and AuNPs characterization performed by means of UV-Vis (***Figure 3.4.4***) and DLS analysis (***Figure 3.4.6***).

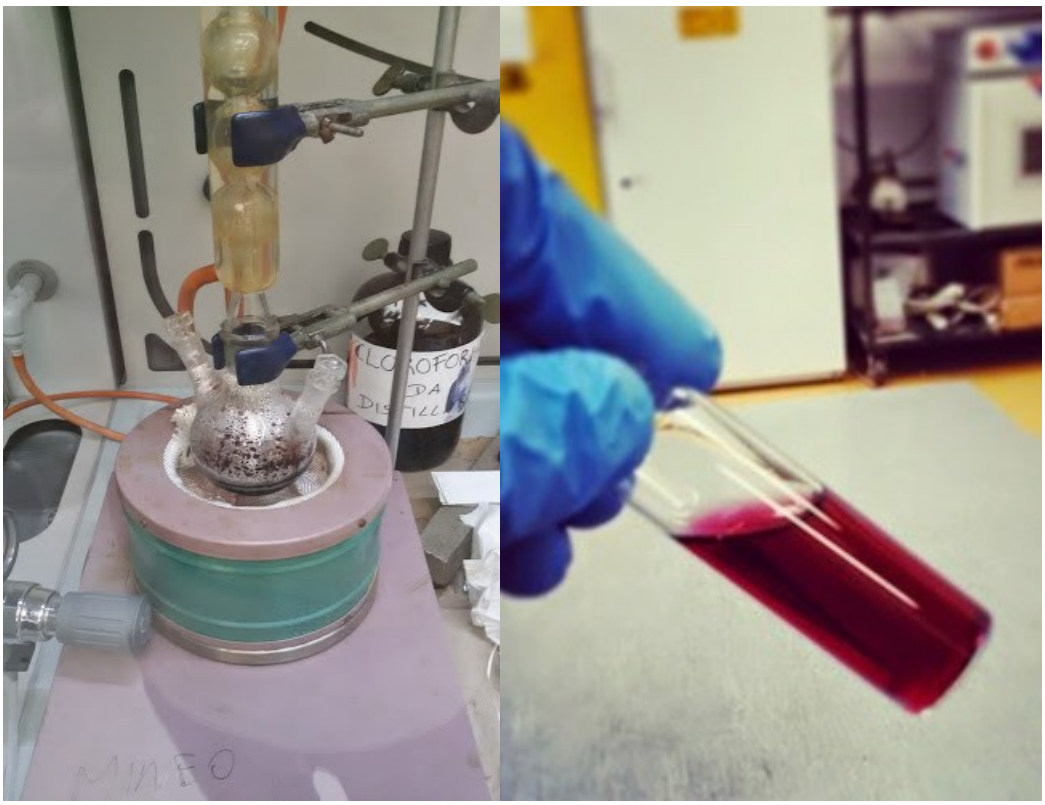

Figure 3.4.3: On the left, the AuNPs synthesis; on the right, AuNPs after being transferred to a vial, the ruby red color of the nano-particles is better noted.

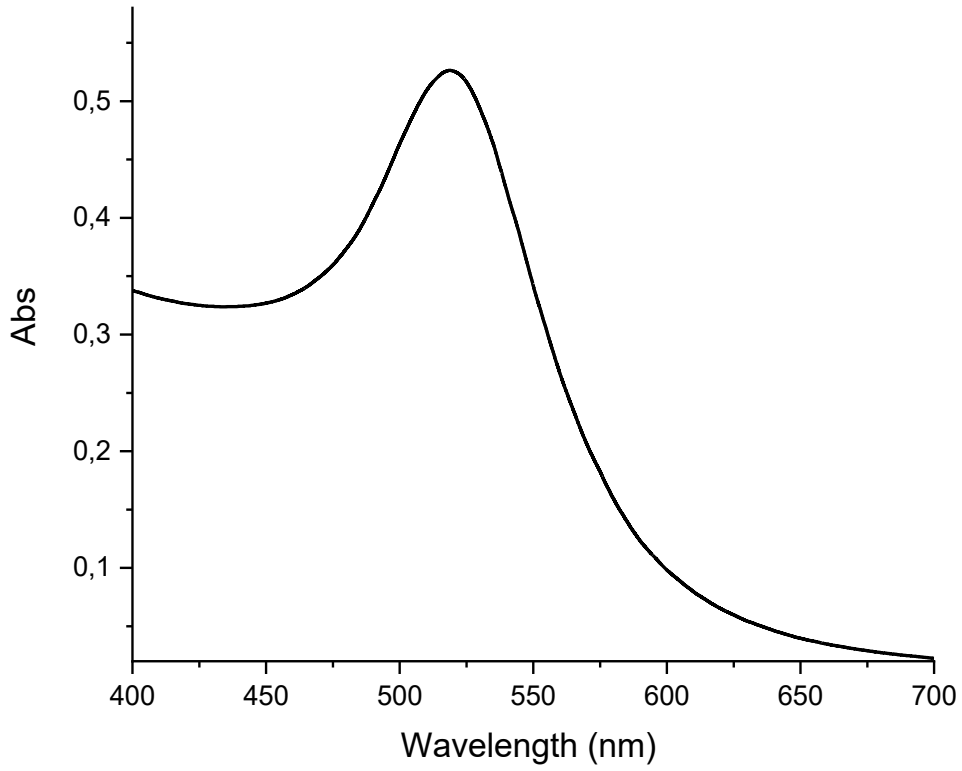

Figure 3.4.4: Uv-Vis spectrum of AuNPs in acqueous solution.

Also for the colloidal gold solution, a first approximate information on the dimensions can be deduced based on the color of the solution. A more exact evaluation can be made by examining the absorption spectrum, shown in ***Figure 3.4.4***, which shows how the value of the resonance plasmon is at wavelength values centered at 518.5nm. By comparing these data with those found in literature, and particularly with those shown in the ***Table 3.4.5***[3], it can be assumed that the size of the nanoparticles is about 12 nm. The table shows the correlation between size, color and wavelength from data obtained with different techniques: Uv-Vis (λab), Resonance Rayleigh Scattering (λRRS), Resonance non-linear Scattering or Second-Order Scattering (λSOS) and Frequency -Doubling Scattering (λFDS).

No.	Mean diameter, *D* (nm)	Color	λ_{max} (nm)				Number of Au atom in a gold nanoparticle
			λ_{ab}	λ_{RRS}	λ_{SOS}	λ_{FDS}	
1	12	Orange–red	520	286	480	310	5.33×10^4
2	19	Red	522	286	480	310	2.12×10^5
3	24	Red	524	286	480	310	4.27×10^5
4	33	Red	528	286	480	310	1.11×10^6
5	41	Red–purple	530	286	480	310	2.13×10^6

Table 3.4.5: Correlation table of colors, sizes and absorption wavelengths of AuNPs.

The Uv-Vis data was compared with the one derived from dynamic light scattering (DLS). Before being analyzed with DLS, the samples of AuNPs were filtered with 0.2μm (Teflon) filters. The obtained measurements confirm the literature data reported in the previous table; in particular, the plasmonic peak fall at 518.5nm, then dimensions close to 12nm, and the DLS data indicate dimensions of 11.6 nm ± (0.9%), (***Fig. 3.4.6***).

Moreover, as seen from the picture, the color of the AuNPs is red, as shown in the Table 3.4.5.

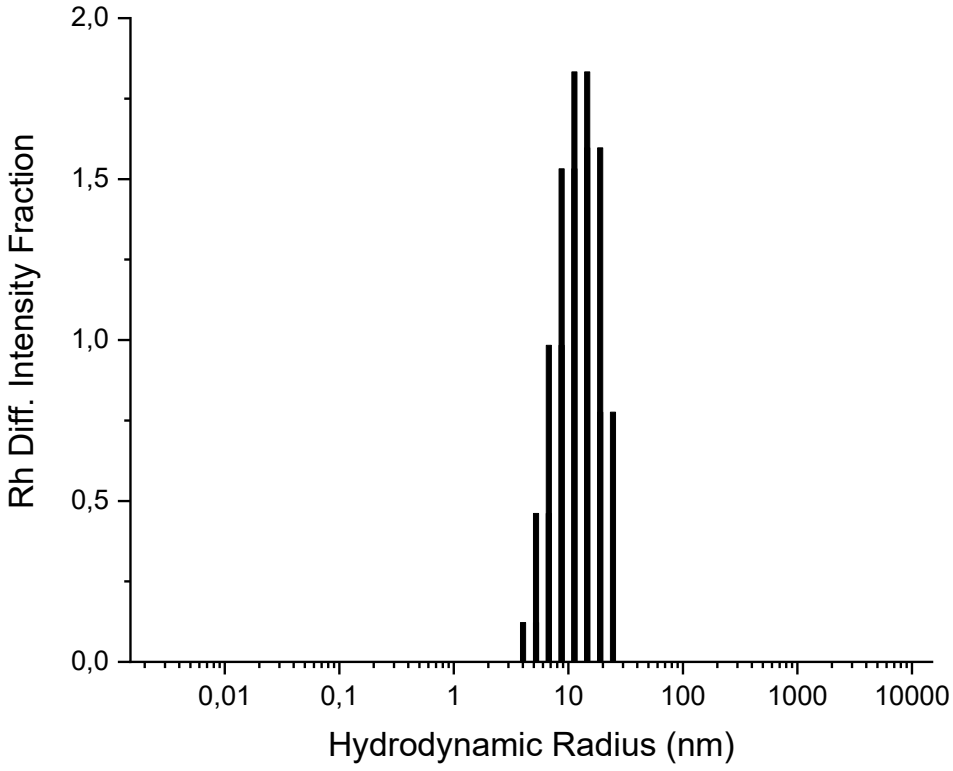

Figure 3.4.6: Size distribution of AuNPs in water.

The R_H average of AuNPs, shown in ***Figure 3.4.6***, is much narrower than R_H average of AgNPs. The possible reason explanation for this result is the filtering of AuNPs with 0.2 μm filters. The fluorimetric properties have also been studied for the AuNPs solution and the system does not show any fluorescence.

The next step concerns the functionalization of AuNPs with a thioled linker. The procedures adopted for the functionalization step are the same described for the AgNPs, known as method 1 and method 2. Therefore, only the scheme (***Figure 3.4.7***) and the relative spectroscopic data are reported.

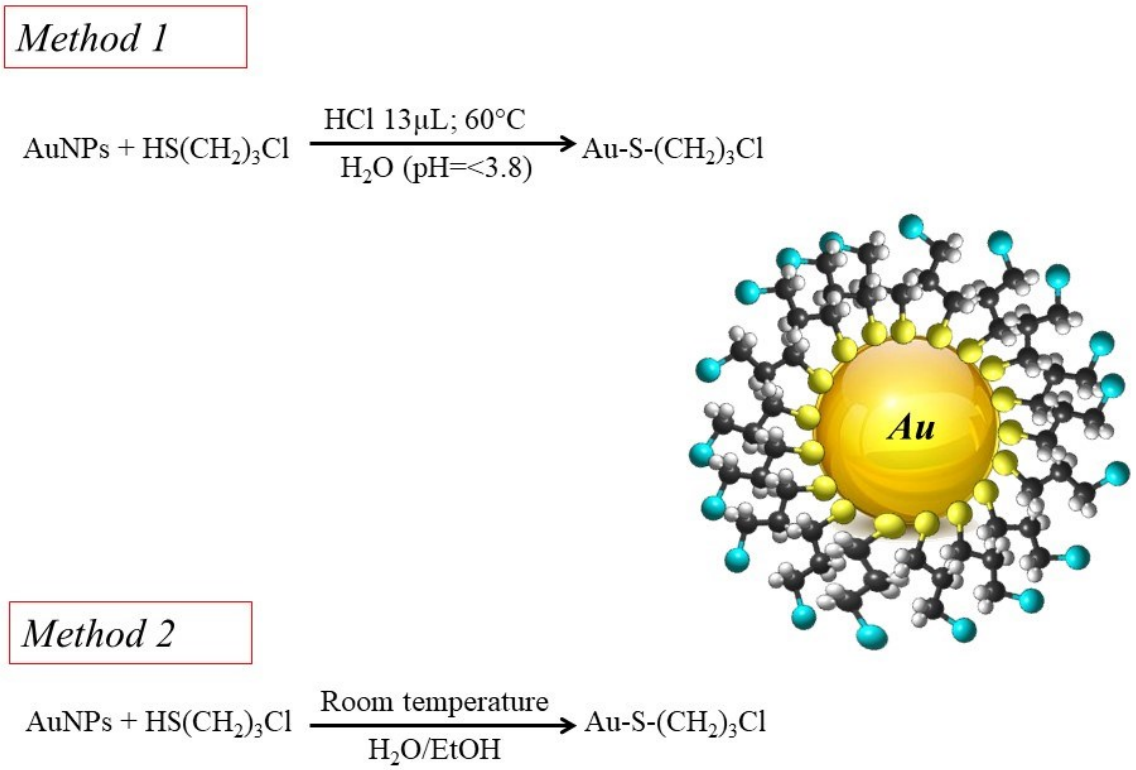

Figure 3.4.7: Scheme of the two methods used for the functionalization of the nanoparticles with the thioled coupling agent.

Figure 3.4.8 shows the UV-Vis spectrum in acetone of AuNPs functionalized with 3-chloro-propanethiol (method 1) acquired after purifying the product by centrifugation and drying in a vacuum oven.

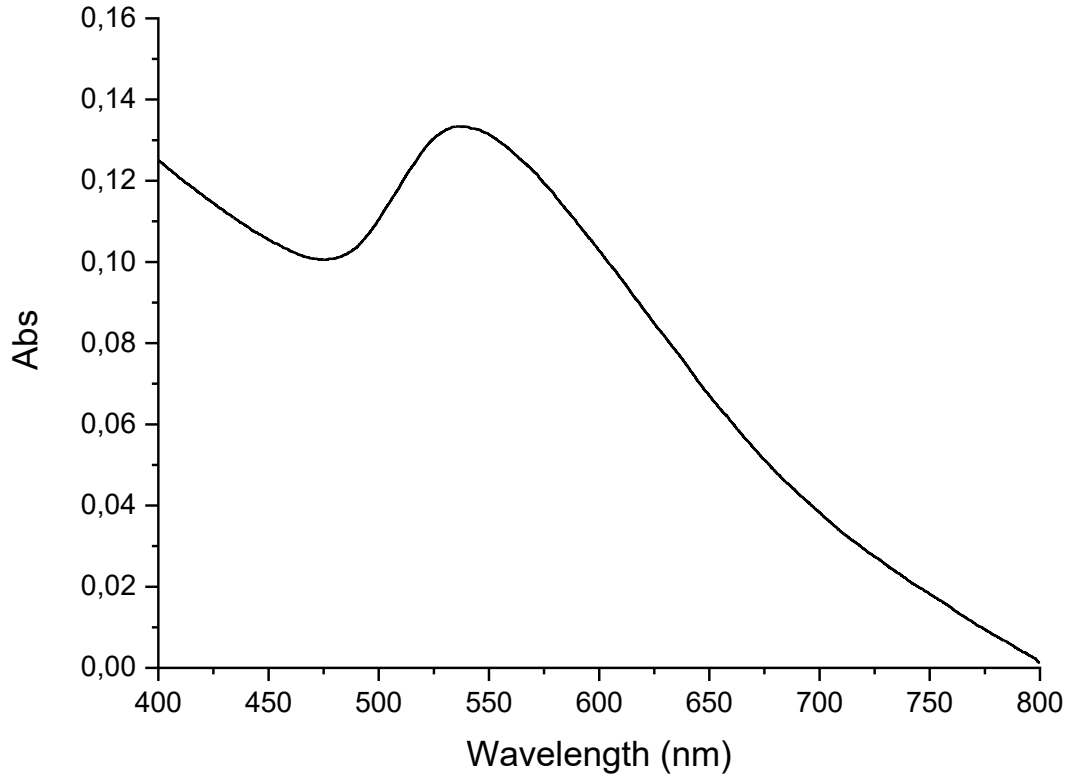

Figure 3.4.8: Uv-Vis spectrum in acetone solution of AuNPs after functionalization with 3-chloro-propanethiol (method 1).

Due to the large poly-dispersion, these particles in acetone solution exhibited a UV-vis (***Figure 3.4.8***) broad band centered at about 535 nm. Also in this case, the resonance plasmon peak enlargement, probably, is due to the aggregation of the nanoparticles generates from lipophilic interactions. To confirm that hypothesis a DLS experiment was performed (***see Figure 3.4.9***).

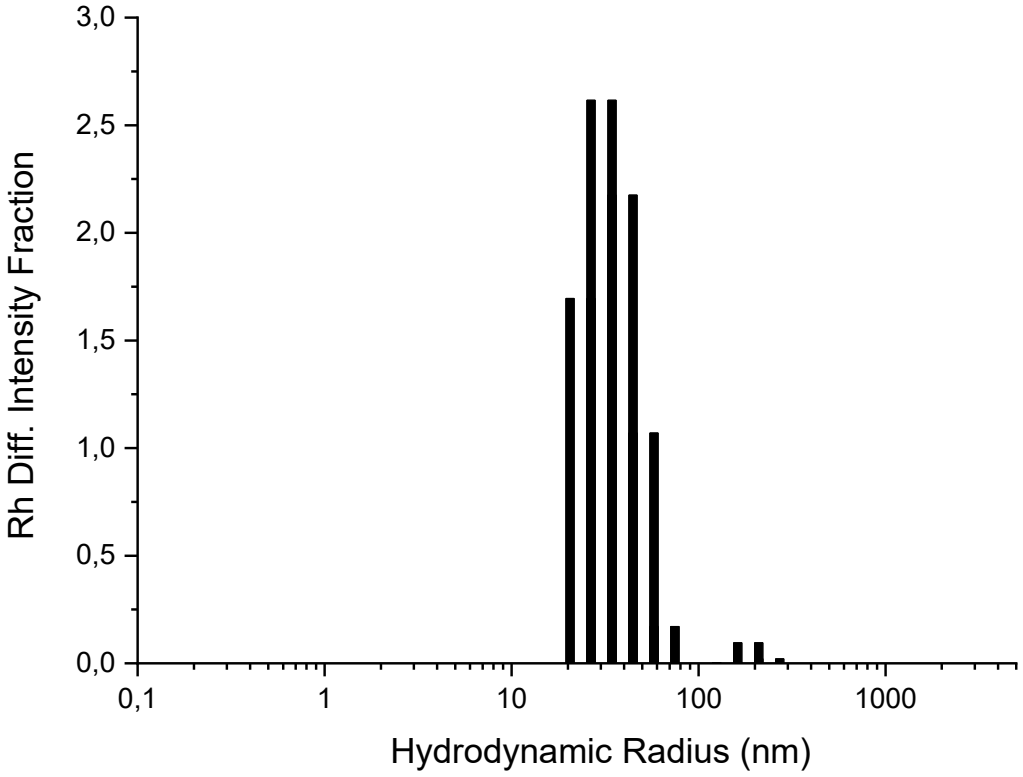

Figure 3.4.9: Size distribution, in acetone solution, of AuNPs functionalized with 3-chloro-propanethiol (method 1)

In particular, the DLS measurements in acetone shows a R_H average of 35nm (***Figure 3.4.9***), thus confirms the hypothesis of self-aggregation of AuNsP@ClPT particles.

In adding, another sample of AuNPs was functionalized with 3-chloro-propanethiol using the method 2 reported in the previous chapters.

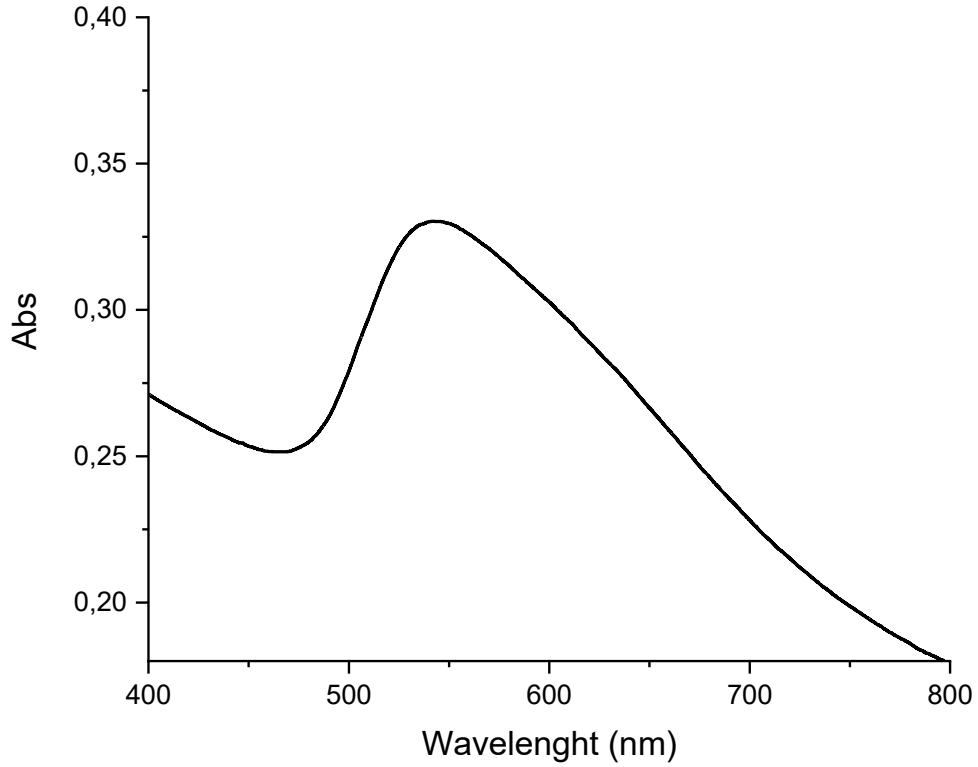

Figure 3.4.10: Uv-Vis spectrum, in acetone solution, of AuNPs after functionalization with 3-chloro-propanethiol in acetone (method 2).

The UV-Vis (***Figure 3.4.10***) spectrum of this new sample dispersed in acetone is very similar to the previous one, with the peak slightly shifted to values of 541.5 nm.

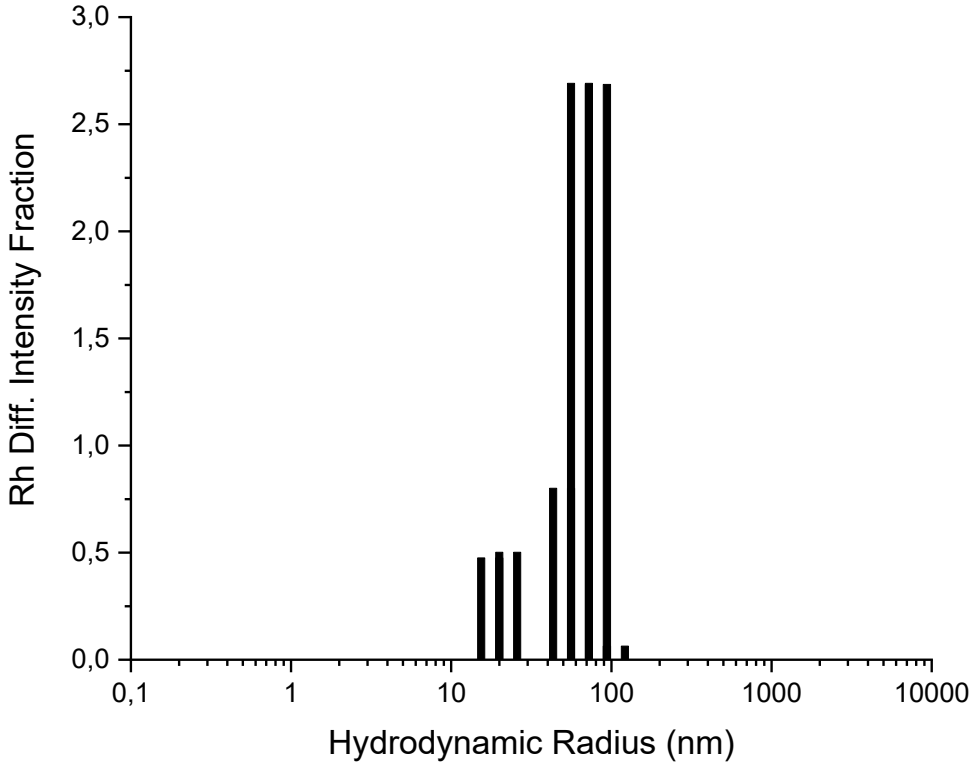

Figure 3.4.11: Size distribution, in acetone solution, of AuNPs after functionalization with 3-chloro-propanethiol (method 2).

The DLS spectrum (***Figure 3.4.11***), obtained for the sample AuNPs functionalized with 3-chloro-propanethiol using the method 2, shows two families of distributions: the first one is centered at values of about 20 nm, very similar to the previous sample; the second one, centered at values of about 70 nm, indicating that, by using this method, we can obtain a higher functionalization of the surface of the nanoparticles as expected from the red shift of the Uv-Vis spectrum.

The third step of the synthesis process concerned the covalent bond, through a nucleophilic substitution reaction, of 5,10,15 tri-(p-[ω-methoxy-poly(ethylene oxide)] phenyl}-20-(p-hydroxyphenyl) porphyrin [$P(PEG350)_3$ or $P(PEG750)_3$] on the AuNPs@ClPT surface.

For both methods of formation of AuNPs@ClPT, as described above, the functionalization with the porphyrin provides the used procedures. For the sake of brevity, an example of functionalization with $P(PEG350)_3$ will be reported using method 1 (*see diagram 3.4.7*) and one with $P(PEG750)_3$ using method 2 (*see diagram 3.4.7*):

Briefly, 5 mg of AuNPs@ClPT were dispersed in a vial with 10 mL of acetone, 5mL of triethylamine and 5 mg of $P(PEG350)_3$, and the mixture held at boiling point for 24 h. In this

conditions, condensation reaction between the OH phenolic group in position 20 of Porf@PEG and the chloride of the 3-chloro-propan thiolate moiety occurred. Then, to separate the unreacted $P(PEG350)_3$, the solution (cooled at 25 °C) was centrifuged at 9000 rpm for 15min and the colored supernatant was eliminated. $AuNPs@P(PEG350)_3$ residue was solubilized in acetone, sonicated again for 5 min and centrifuged; this procedure was repeated twice. The final product $AuNPs@P(PEG350)_3$ was put under vacuum at 60 °C for 24 h and characterized by UV-Vis, fluorescence, TEM (***see result and discussion***) and DLS techniques.

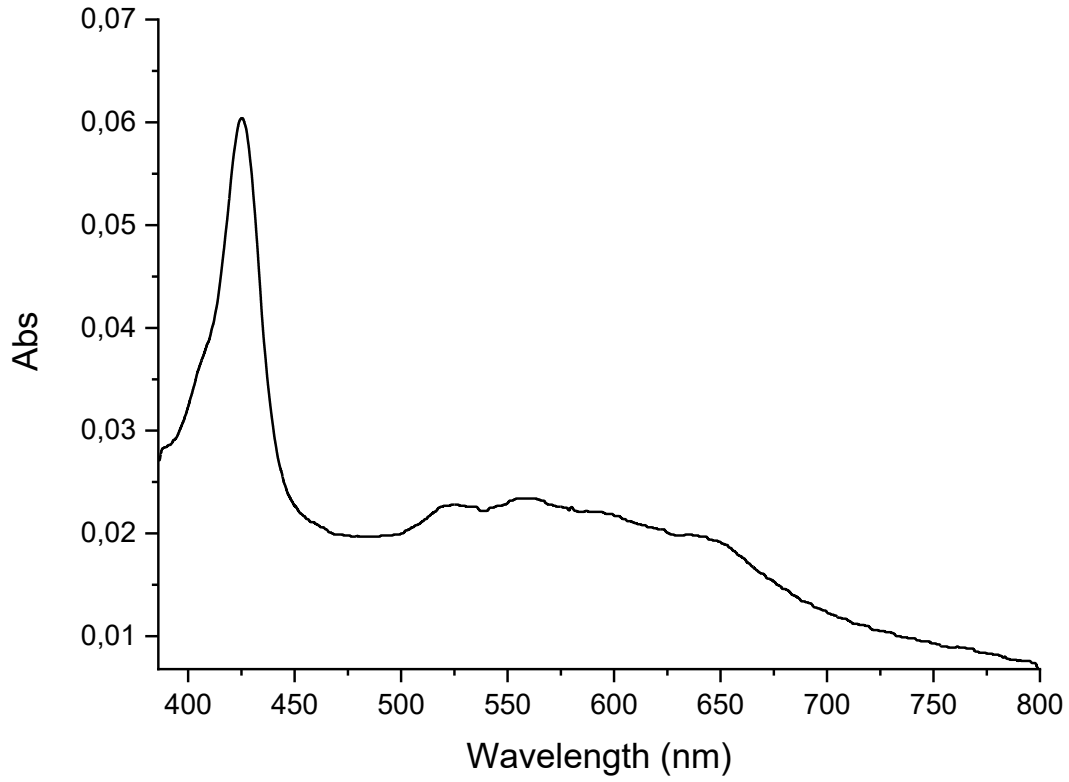

Figure 3.4.12: Uv-Vis spectrum, in acetone solution, of AuNPs after functionalization with 3-chloro-propanethiol (method 1) and $P(PEG350)_3$.

The Uv-Vis spectrum of the $AuNPs@P(PEG350)_3$ in acetone solution, reported in ***Figure 3.4.12***, shows the typical signals of the Porf@PEG moieties. In particular, the absorption due to the B-band (at 425 nm) and the Q-bands (in the range 500-675 nm) is evident. It is noticeable that in the range of the Q-bands a hump, due to the contribution of the SPR of modified AuNPs , is also present. Moreover, due to the aggregation phenomenon, the DLS analysis showed a value of R_H average of 50 nm (***Figure 3.4.13***).

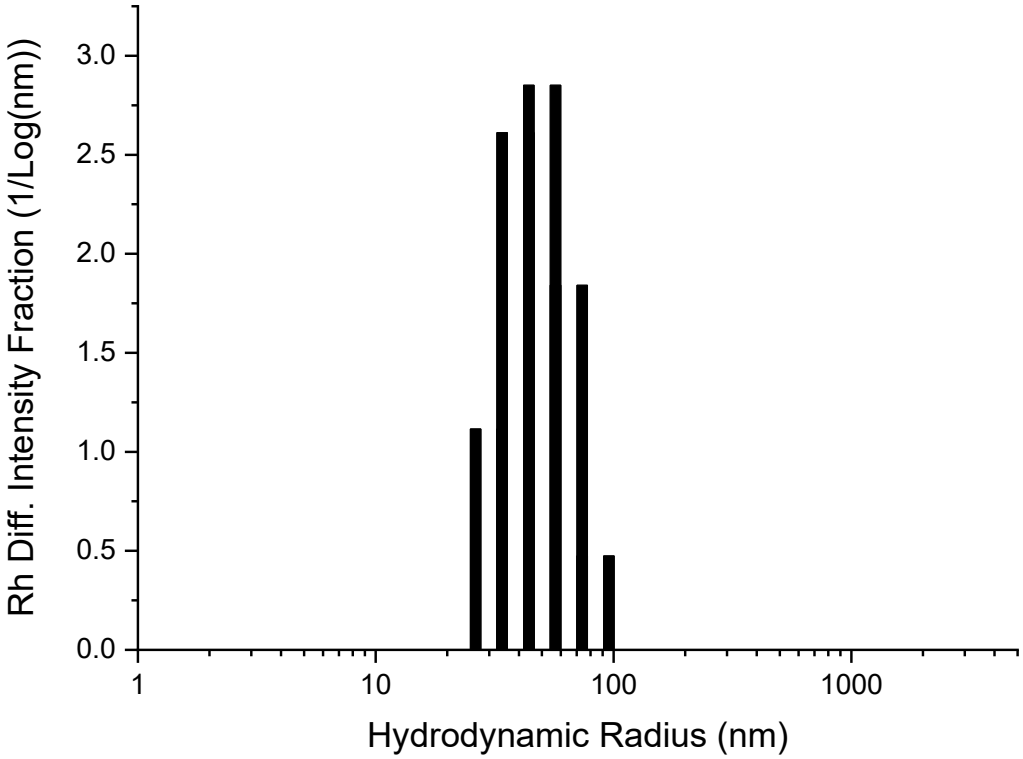

Figure 3.4.13: Size distribution, in acetone solution, AuNPs after functionalization with 3-chloro-propanethiol (method 1) and $P(PEG350)_3$.

Finally, as a consequence of the increasing of interactions between functionalized AuNPs (formation of aggregates), the Uv-Vis spectrum in aqueous solution of AuNPs@$P(PEG350)_3$, reported in ***Figure 3.4.14***, shows a decrease of the B-band intensity and a strong increase of the signal in the 550-800 nm range (broadening of plasmon resonance band).

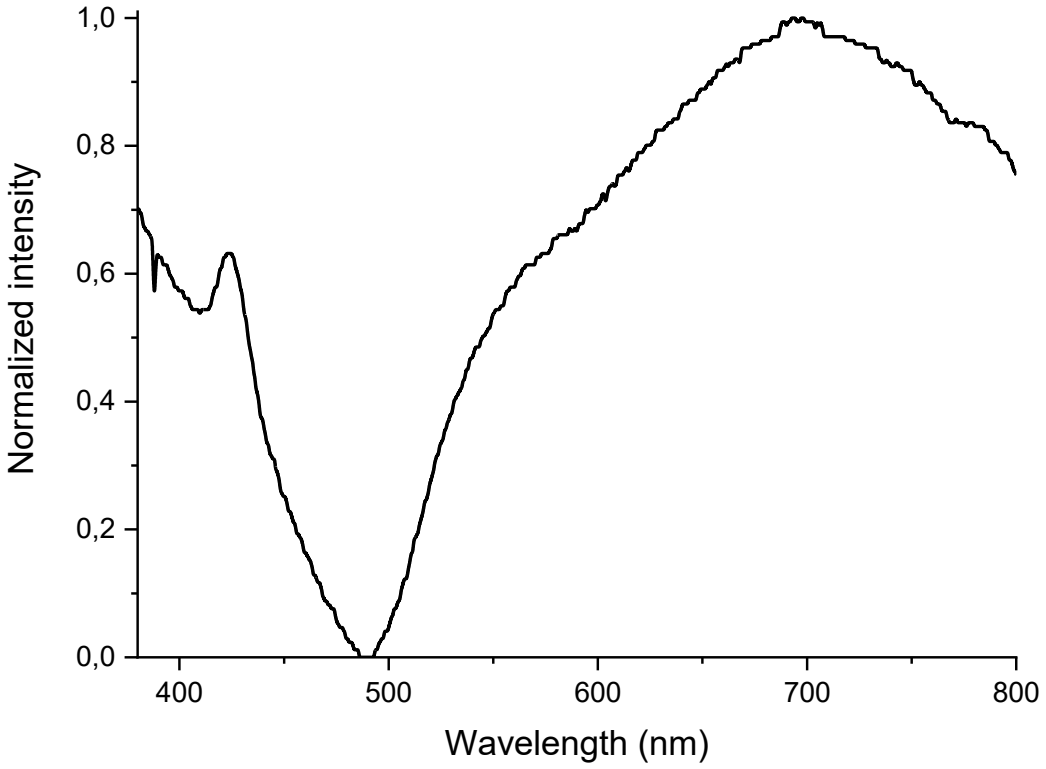

Figure 3.4.14: Uv-Vis spectrum, in water solution, of AuNPs after functionalization with 3-chloro-propanethiol (method 1) and $P(PEG350)_3$.

In order to use the AuNPs@P(PEG350) 3 system in a biological environment, the dimensions were also calculated in PBS solution, in order to simulate the physiological pH. DLS analysis (***Figure 3.4.15***, solid line) indicates a higher R_H average (65 nm). Finally, DLS analysis, performed in PBS solution (***Figure 3.4.15***, dashed line), indicates a R_H average (90 nm) higher than that in water; the size increase can be explained by higher ionic strength of the solvent.

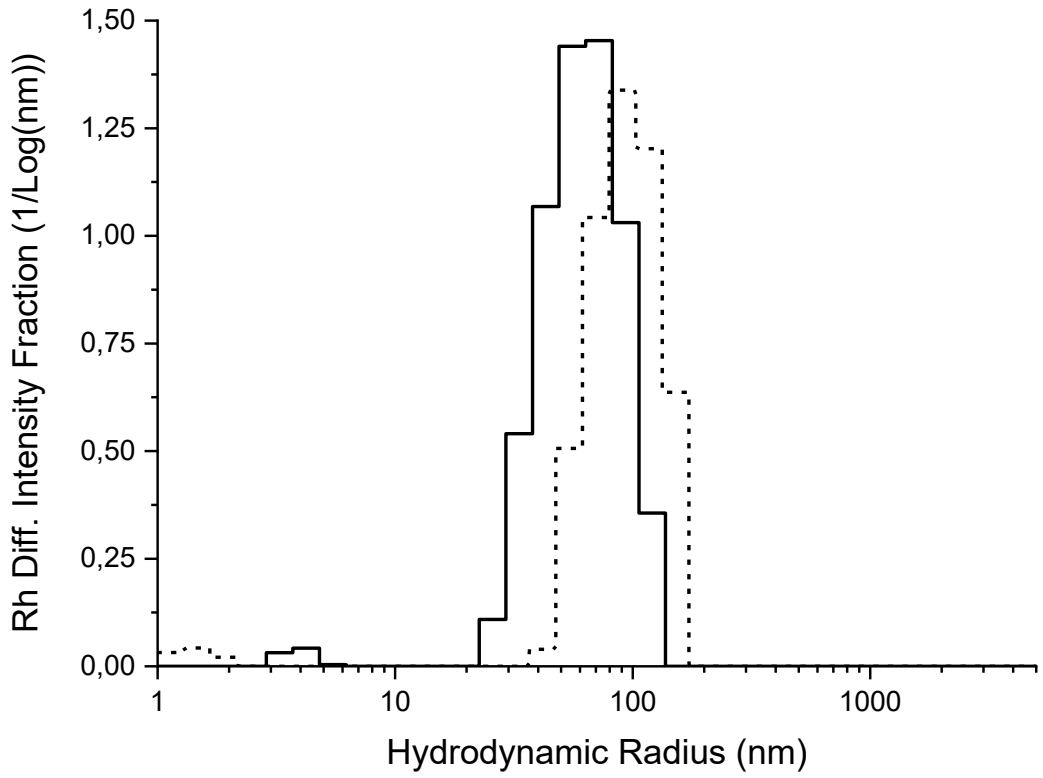

Figure 3.4.15: Size distribution AuNPs after functionalization with 3-chloro-propanethiol (method 1) and $P(PEG350)_3$: in water solution (solid line), and PBS solution (dashed line).

Figure 3.4.16 (right) shows the fluorescence spectra of both $P(PEG350)_3$ and of AuNP@$P(PEG350)_3$ in acetone and in water solution. In particular, the fluorescence spectra of the acetone solutions of $P(PEG350)_3$ and AuNPs@$P(PEG350)_3$ and that of the aqueous solution of AuNPs@ $P(PEG350)_3$ exhibit the same emission band at 654 nm (λ_{exc} = 425 nm).

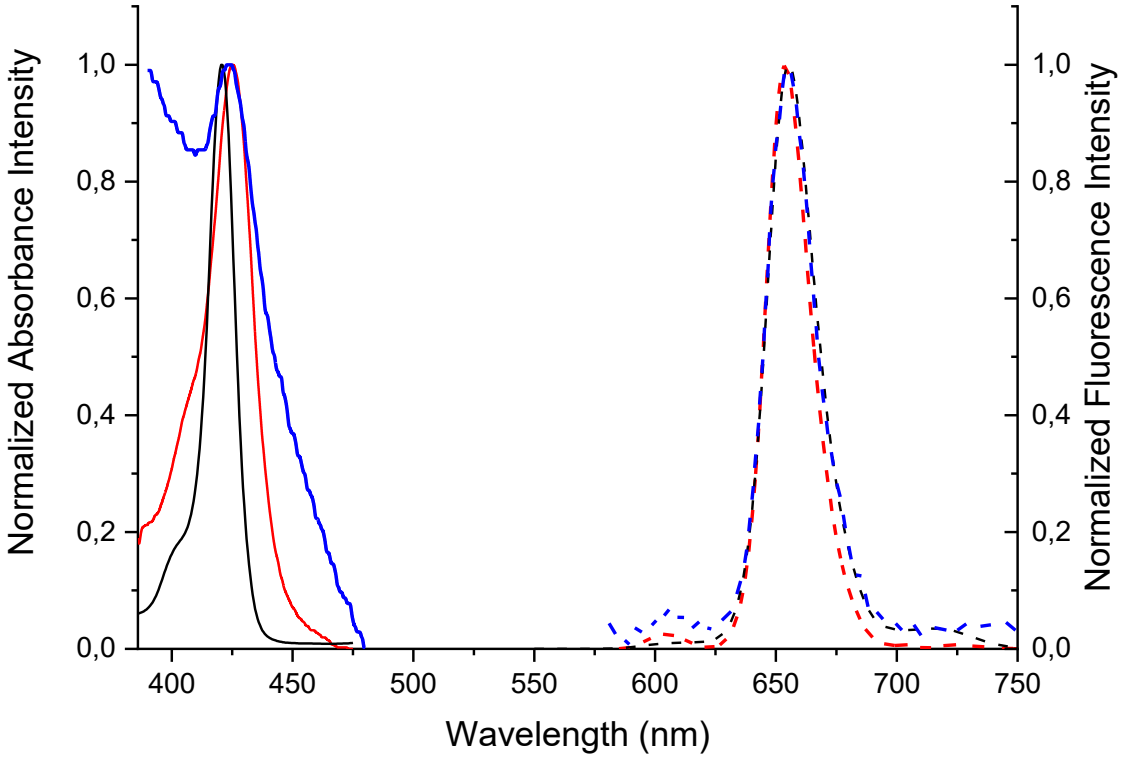

Figure 3.4.16: Normalized Uv-Vis spectra of acetone solution of $P(PEG350)_3$ (solid black line) and $AuNPs@P(PEG350)_3$ (solid red line) and an aqueous solution of $AuNPs@P(PEG350)_3$ (solid blue line). Normalized fluorescence spectra of acetone solutions of $P(PEG350)_3$ (dashed black line) and $AuNPs@P(PEG350)_3$ (dashed red line) and an aqueous solution of $AuNPs@P(PEG350)_3$ (dashed blue line).

As previously described, the characterizations referring to the functionalization reaction of AuNPs@ClPT with $P(PEG750)_3$, using AuNPs@ClPT obtained with the second functionalization method (***see diagram 3.4.7***), are now reported. ***Figure 3.4.17*** shows the Uv-Vis spectrum of the particles, dispersed in acetone.

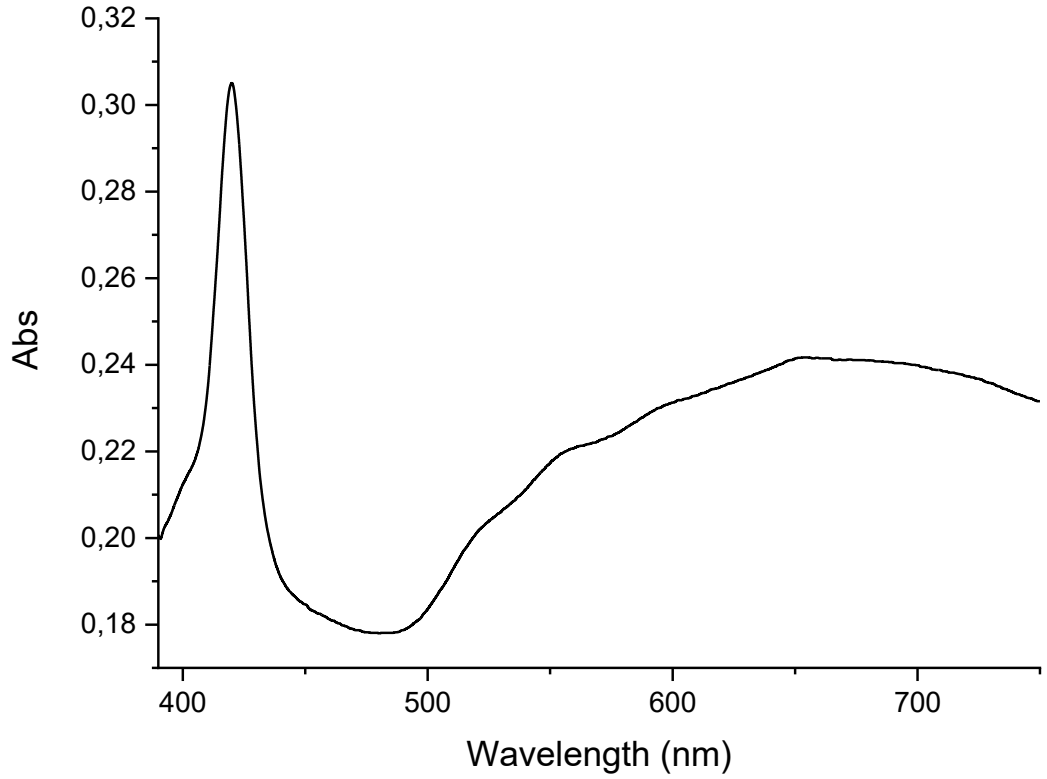

Figure 3.4.17: Uv-Vis spectrum, in acetone solution, of AuNPs after functionalization with 3-chloro-propanethiol (method 2) and $P(PEG750)_3$.

From the Uv-Vis spectrum of ***Figure 3.4.17*** we can notice the presence of the Soret band at 419 nm, a value that indicates the presence of the porphyrin in solution. Also in this case, it is noticeable hump can be found that in the range of the Q-bands, due to the contribution of the SPR of modified AuNPs.

The dimensional analysis obtained by means of DLS is shown in ***Figure 3.4.18***. In particular, the figure shows the comparison between the size distribution before and after the functionalization with $P(PEG750)_3$.

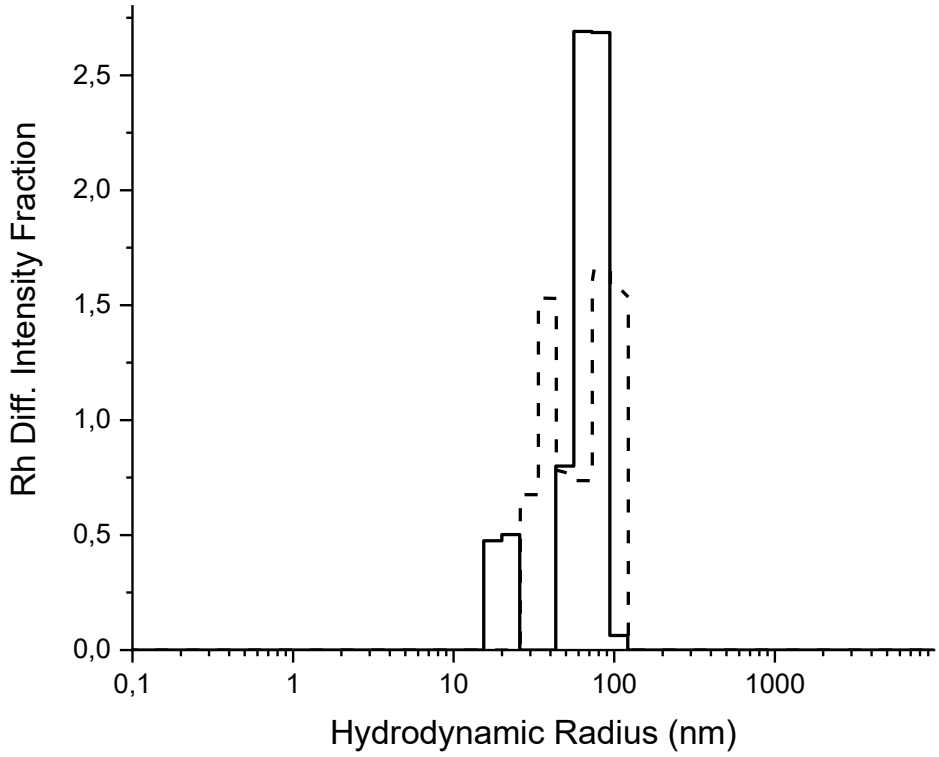

Figure 3.4.18: Size distribution, in acetone solution, of AuNPs after functionalization with 3-chloro-propanethiol (method 2) and P(PEG750)$_3$ (solid line), and AuNPs after functionalization with 3-chloro-propanethiol with method 2 (dashed line).

The DLS spectrum shows a shift of the two distributions at about 70 nm, indicating that the two families of particles have undergone the functionalization reaction with the same intensity.

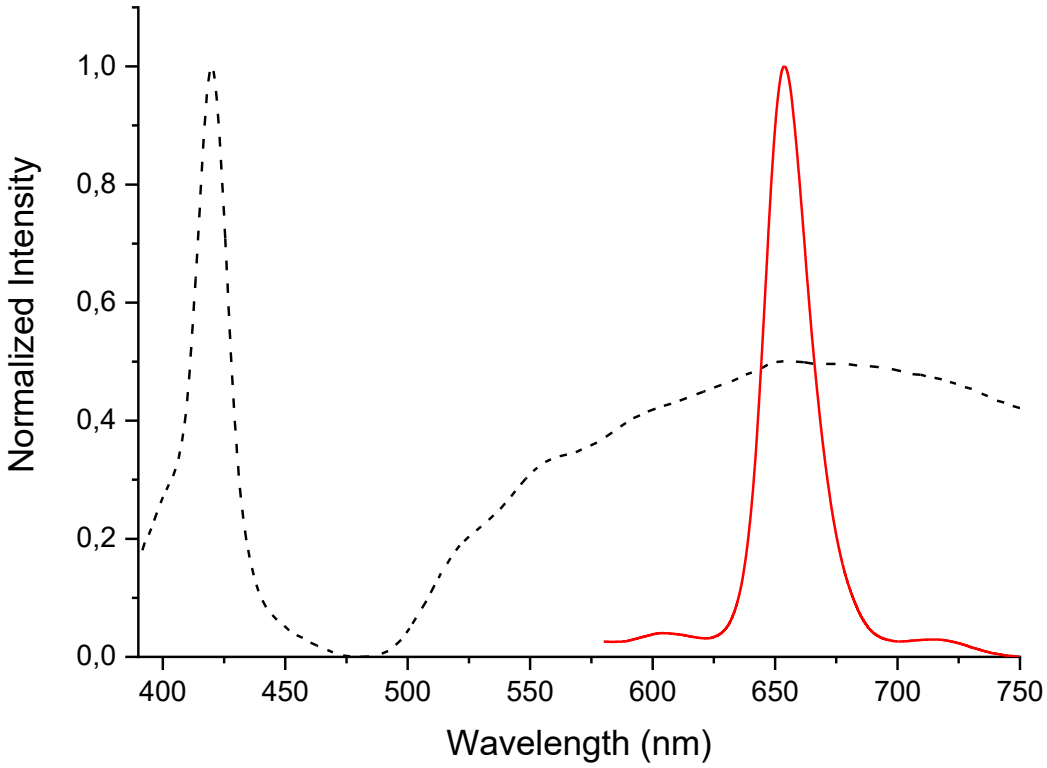

Figure 3.4.19: In black, Uv-Vis spectrum of AuNPs functionalized with 3-chloro-propanediol and $P(PEG750)_3$ in acetone; in red, the corresponding fluorescence spectrum of the same solution (λ_{exc}=419 nm).

The fluorescence spectrum of ***Figure 3.4.19*** shows the typical signal at 654 nm of porphyrinic systems, with small shoulders at values of 604 nm and 714 nm. The fluorescence signal is very intense, which indicates a high amount of porphyrin derivatives on the particles' surface and an equally high density of functionalization.

The same sample was characterized by Uv-Vis (***Fig. 3.4.20***), DLS (***Fig.3.4.21***) and Fluorescence (***Fig.3.4.22***) techniques, after being suspended in water.

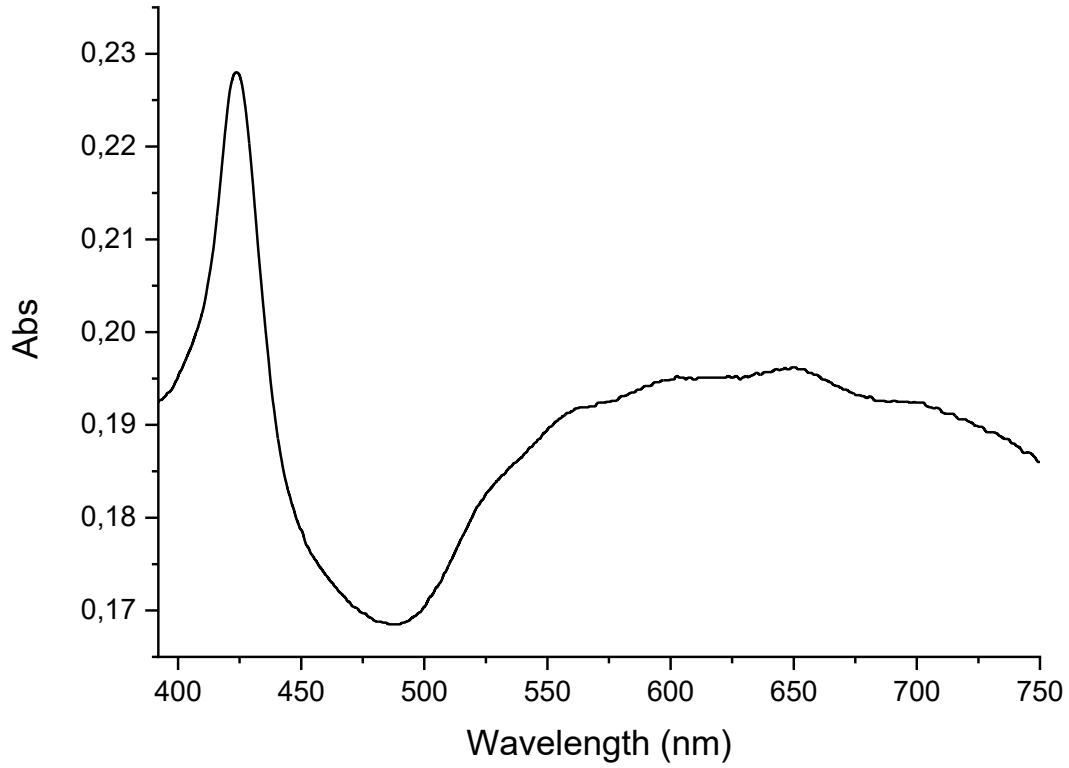

Figure 3.4.20: Uv-Vis spectrum, in water solution, of AuNPs after functionalization with 3-chloro-propanethiol (method 2) and $P(PEG750)_3$.

The Uv-Vis spectrum of ***Figure 3.4.20*** shows, even if with a lower intensity than the same sample in acetone, the peak of the Soret band at 425 nm, typical of this kind of porphyrins in water. The signals deriving from the Q-bands can also be seen, even if partially covered by the contribution of the SPR of modified AuNPs.

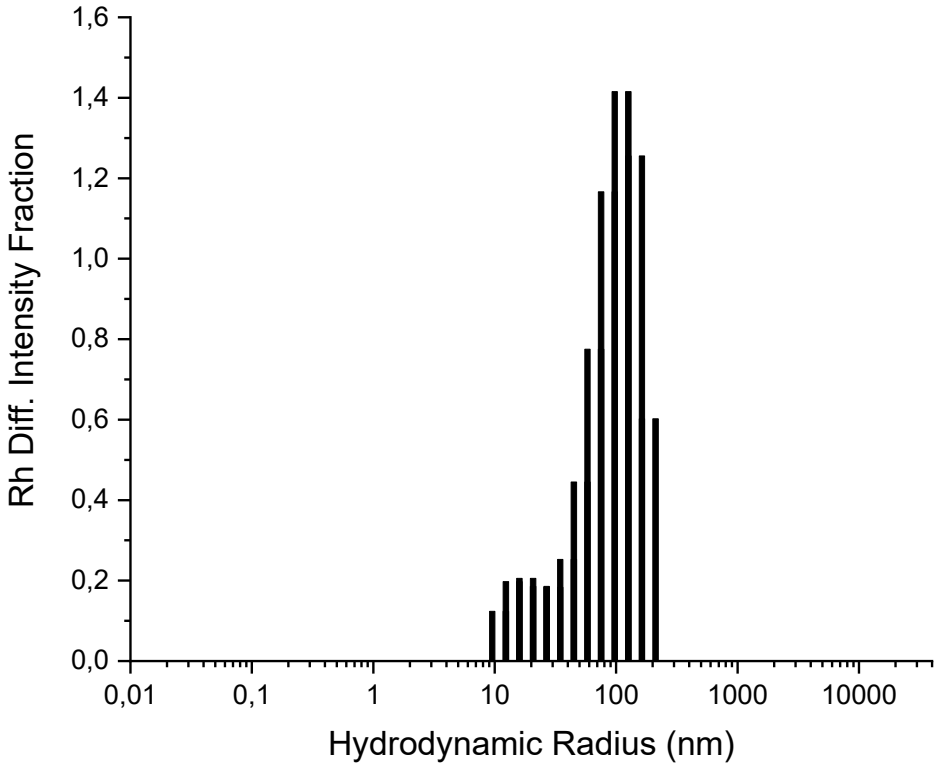

Figure 3.4.21: Size distribution, in water solution, AuNPs after functionalization with 3-chloro-propanethiol (method 2) and $P(PEG750)_3$.

The DLS spectrum of ***Figure 3.4.21*** shows a wider distribution index due of the formation of small aggregates that such systems tend to form in aqueous solution thanks to porphyrin-porphyrin interaction.

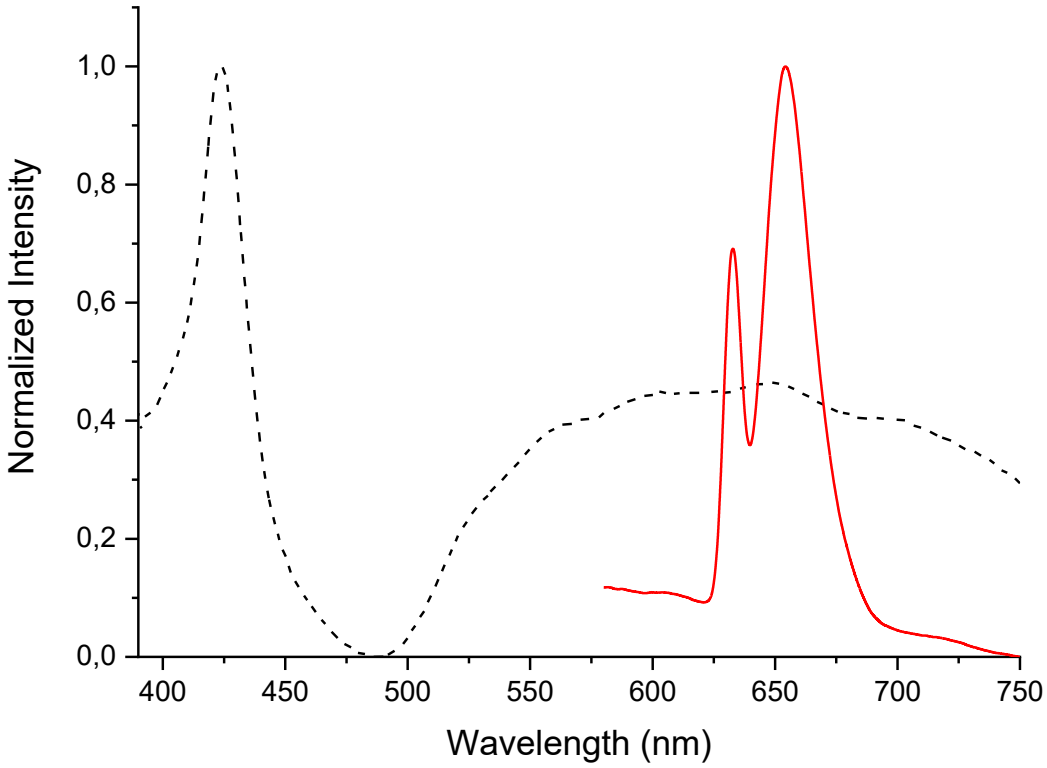

Figure 3.4.22: In black, Uv-Vis spectrum of AuNPs functionalized with 3-chloro-propanediol and $P(PEG750)_3$ in water; in red, the corresponding fluorescence spectrum of the same solution (λ_{exc}=423 nm).

As expected, the fluorescence spectrum of ***Figure 3.4.22*** shows the 654 mn band, typical of these porphyrin systems, and a second peak at 636 nm, due to the presence of an instrumental artefact. In fact, using a filter at 405 nm, placed ahead the detector, the signal at 636 nm disappears (***Figure 3.4.23***).

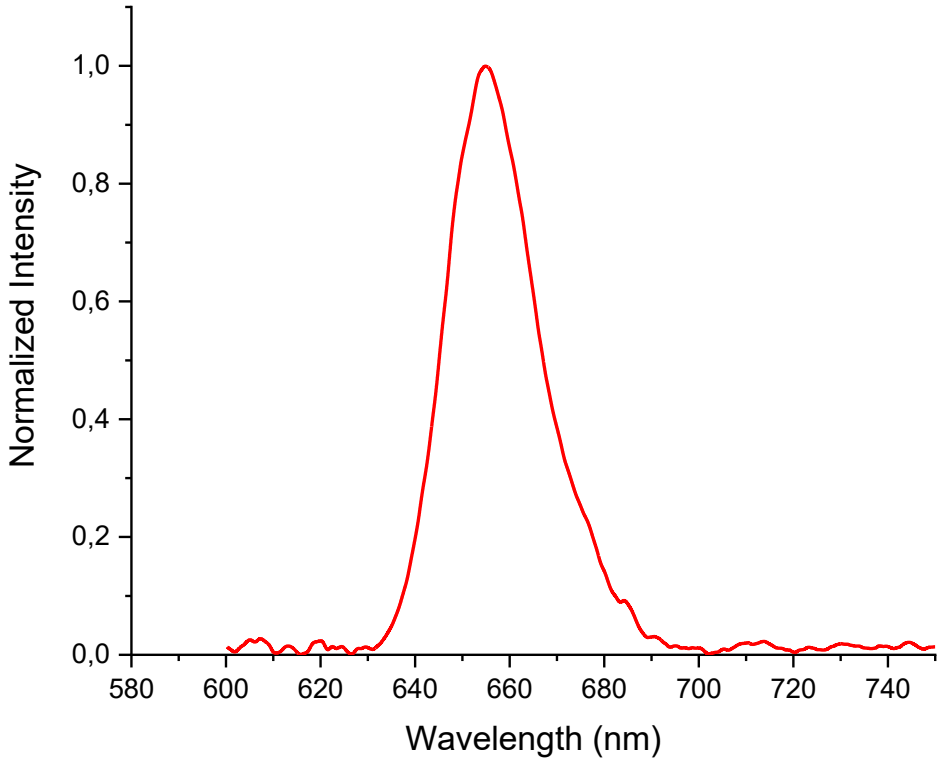

Figure 3.4.23: Fluorescence spectrum of AuNPs functionalized with 3-chloro-propanediol and $P(PEG750)_3$ (λ_{exc}=423 nm). The spectrum was acquired using a 405 nm filter in front of the detector.

[1] Turkevich, J.; Hillier, J.; Stevenson, P.C. Discussions of the Faraday Society, 1951, 11, 55.
[2] Frens, G. Nature Phys. Sci., 1973, 241, 20-22.
[3] He, Y.Q.; Liu, S.P.; Kong, L.; Liu, Z.F. Spectrochimica Acta Part A, 2005, 61, 2861–2866.

Synthesis, functionalization and characterization of Magnetic Nanoparticles

Iron oxide nanoparticles, consisting of maghemite (γ-Fe_2O_3) or magnetite (Fe_3O_4), have attracted much interest due to their widespread electronic and, recently, biomedical applications.

The synthesis of magnetite nanoparticles is schematized in the ***Figure 3.5.1***:

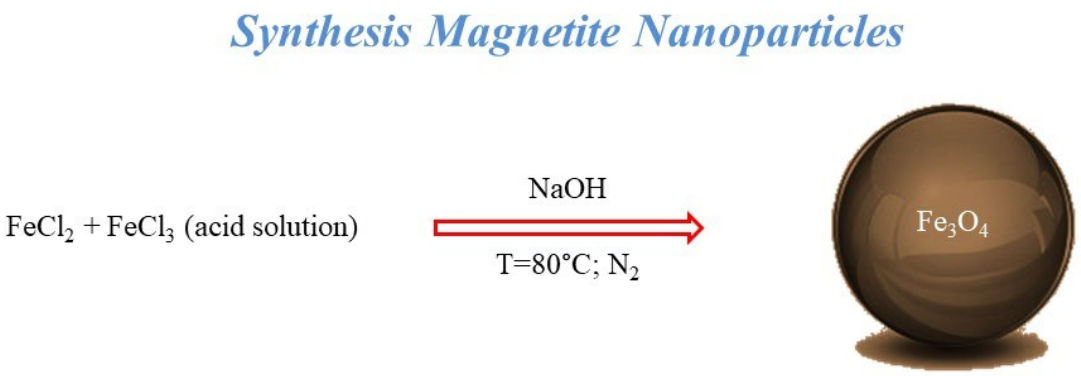

Figure 3.5.1: Synthesis scheme of Fe_3O_4 nanoparticles.

The Fe_3O_4 nanoparticles were prepared by coprecipitation of Fe(II) and Fe(III) chlorides (Fe(II)/Fe(III) ratio=0.5) with 1.5 M NaOH. The black precipitate was collected using a magnet, washed twice with H_2O, twice with 0.1M tetramethylammonium hydroxide (TMAOH), and isolated via centrifugation before being taken up finally in 0.1 M TMAOH.

Briefly, in a 5 mL solution of 0.01M of HCl were dissolved 1.08632 g $FeCl_3 \cdot 6H_2O$ and 0.40282 g $FeCl_2 \cdot 4H_2O$. The solution was added dropwise to 50 mL of a 1.5 M NaOH solution kept with vigorous stirring, under nitrogen flow and at 80°C. A black precipitate formed immediately. The precipitate was isolated via magnetic decantation and washed twice with 100ml of water, then twice with 100ml of 0.1M tetramethylammonium hydroxide pentahydrate. Particles were separated by centrifugation at 6000 rpm for 15 min and the final precipitate was dissolved in 25 mL of 0.1 M TMAOH. The final black solution was stored in air under benchtop conditions for further use.

Figure 3.5.2: synthesis of Fe_3O_4 nanoparticles.

Note: A second synthesis was performed using the process described above. The synthesis was arrested after the washing step with water and, in order to preserve the magnetic particles, they were stored in a vial with 25 cc of water after being subjected to nitrogen flow.

This method of conservation has been used only for the nanoparticles which will be subsequently subjected to silica coating.

The MNPs obtained were characterized by Uv-Vis (***Figure 3.5.3***) and IR spectroscopies (***Figure 3.5.4***), and with thermogravimetric (***Figure 3.5.7***) and DLS analyses (***Figure 3.5.8***).

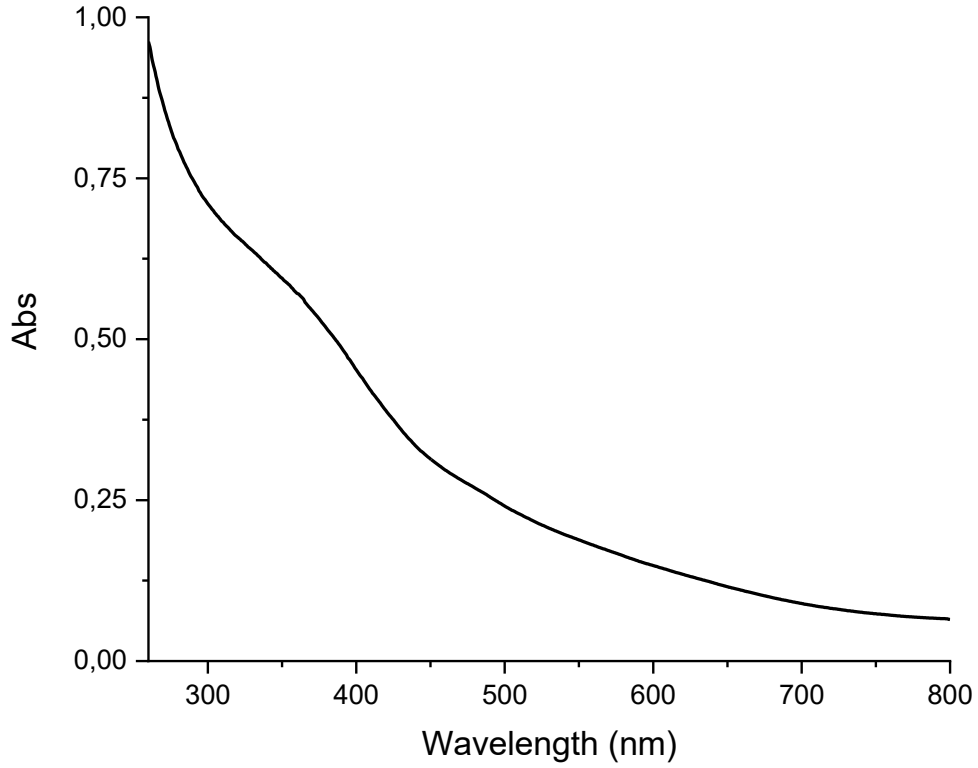

Figure 3.5.3: Uv-Vis spectrum of Fe_3O_4 nanoparticle in water solution.

The Uv-Vis spectrum of Fe_3O_4 nanoparticles does not show any absorption peak, but only a broaded scattered signal along the whole range from 250 to 800 nm.

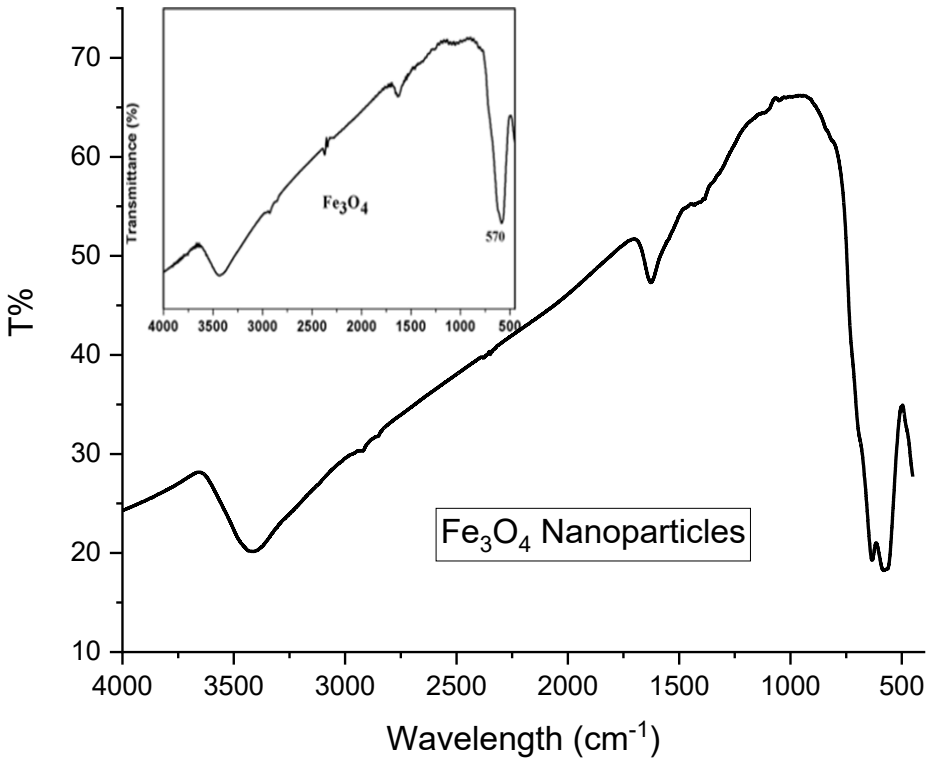

Figure 3.5.4: IR spectrum of the nanoparticles of Fe_3O_4. Inset shows the IR spectrum of the Fe_3O_4 nanoparticles from literature (Mahto, T. K.; Chowdhuri, A. R.; Sahu, S. K. Journal of Appl. Polym. Sci. 2014, 131, vol.19,).

The IR spectrum of Fe_3O_4 nanoparticles (magnetite, ***Figure 3.5.4***) shows, if compared to the one obtained from literature, the typical signals of magnetite nanoparticles at 560 and 637cm^{-1} due to the Fe-O bond in tetrahedral and octahedral position[1, 2]

In order to completely remove any bulk impurities from the nanoparticles, heat treatment was carried out inside a heating mantle at the temperature of 500 °C for 90 minutes in an atmosphere of N_2. Subsequently, the obtained sample was by means of thermo-gravimetric analysis. We can notice a weight loss of 4.76% due to the presence of impurities like H_2O, $FeCl_3$ and $FeCl_2$, incorporated within the MNPs, as it is possible to observe from the IR spectra in ***Figure 3.5.5*** and ***Figure 3.5.6***.

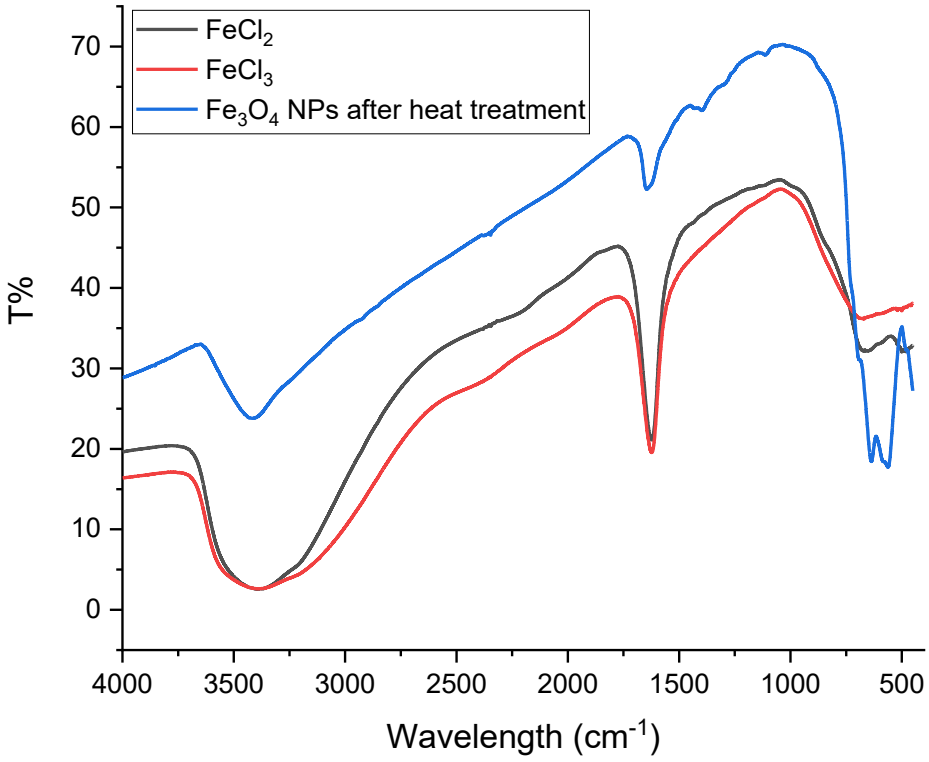

Figure 3.5.5: IR spectra of the nanoparticles of Fe_3O_4 nanoparticles (blue), ferrous chloride (black) and ferric chloride (red).

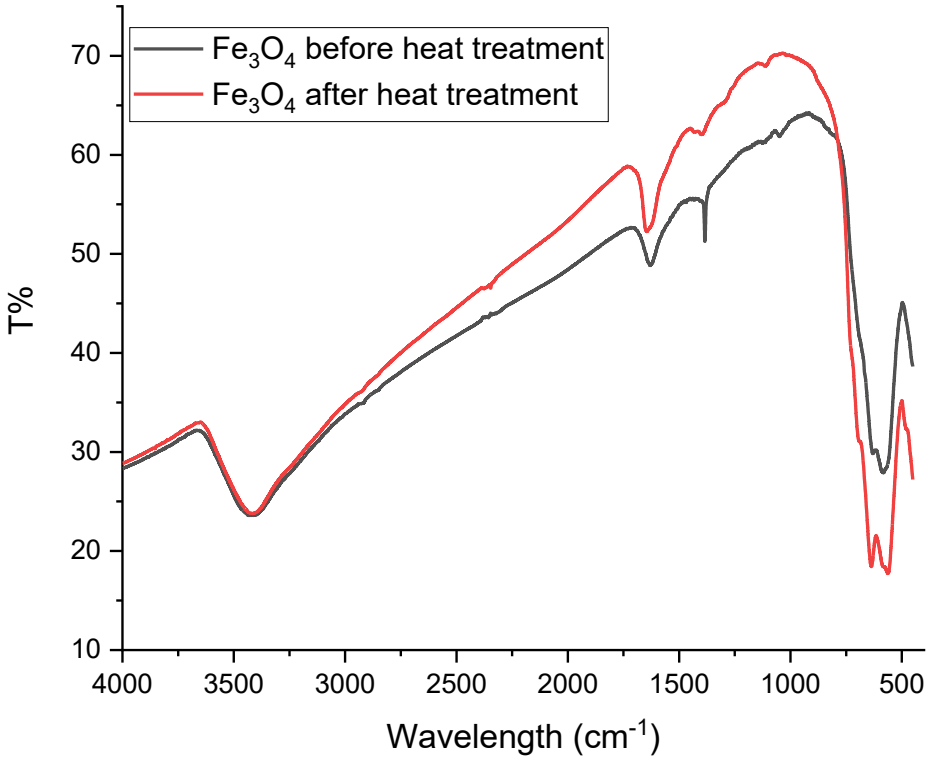

Figure 3.5.6: IR spectra of the nanoparticles of Fe_3O_4 nanoparticles before heat treatment (black) and after heat treatment (red).

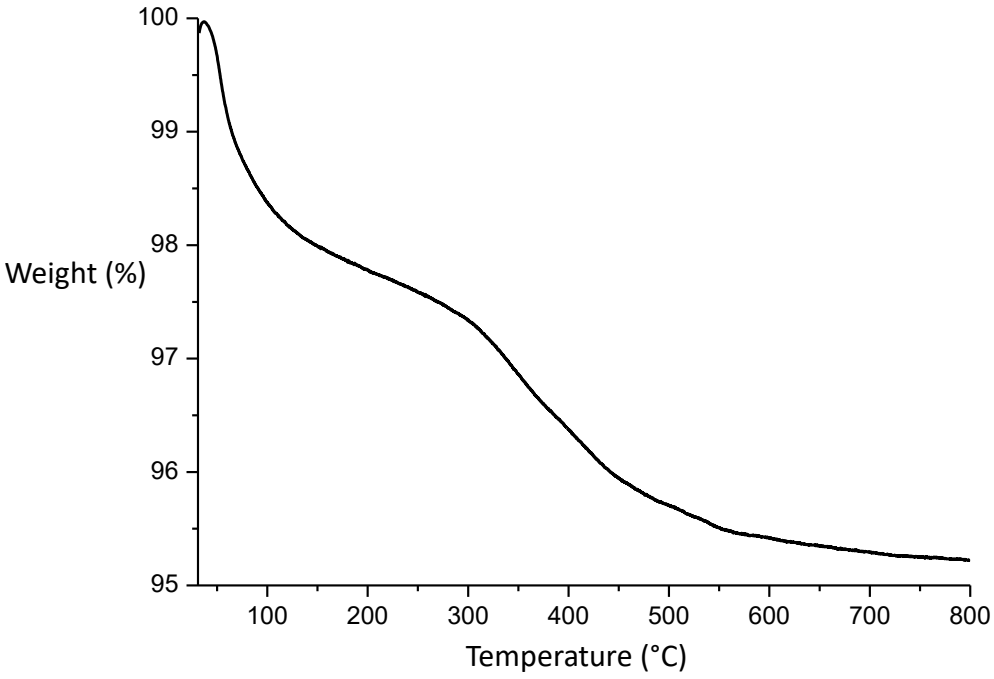

Figure 3.5.7: TGA analysis in N_2 of Fe_3O_4 nanoparticles after treatment at 500 ° C

From the thermo-gravimetric analysis, it is possible to observe two temperature ranges in which there is weight loss. The initial loss, included in the temperature range 0-100 °C, is attributable to the presence of water in the sample; the second one, included in the range between 200-400 °C, is certainly attributable to the presence of impurities like $FeCl_2$ and $FeCl_3$, incorporated during the co-precipitation reaction.

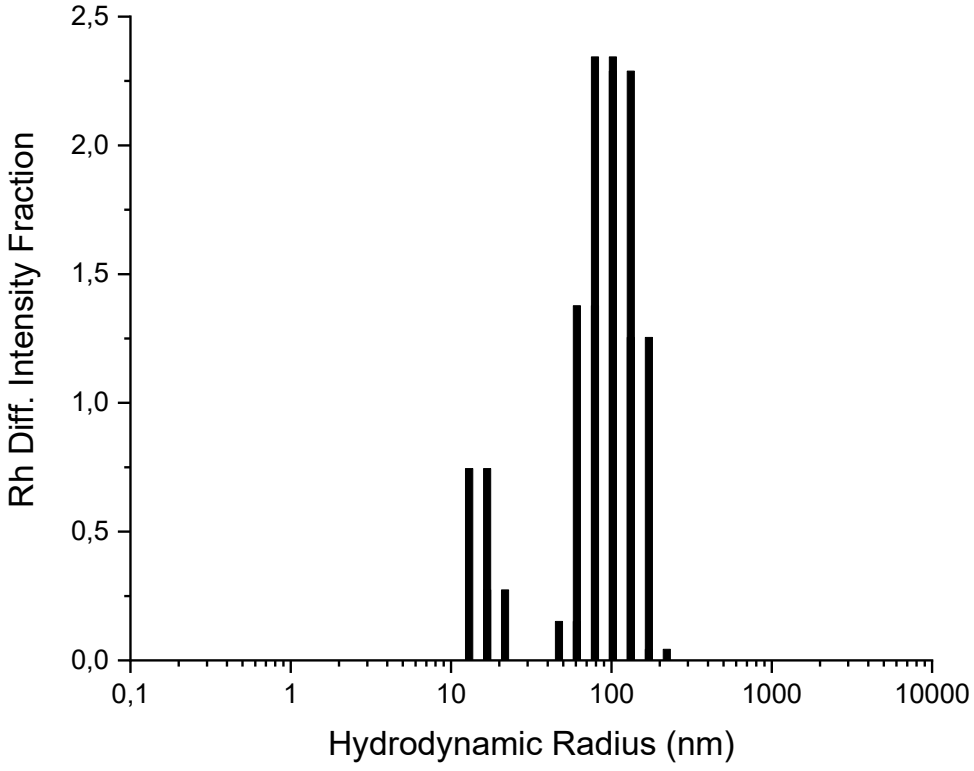

Figure 3.5.8: Size distribution of Fe_3O_4 Nanoparticles in water solution.

The sizes of the magnetite nanoparticles were determined by DLS analysis in water. The graph in ***Figure 3.5.8*** shows two different distributions, the first at around 16 nm and the second at around 105 nm; the latter is due to poor stability over time of nanoparticles which tend to collapse with each other, due to magnetic interactions, forming larger aggregates.

To improve the stability of magnetite nanoparticles over time, it was decided to cover the latter with two different shells, gold and silica, so as to observe which of the two is the best in different aspects, such as ease of synthesis, functionalization capacity, etc.

[1] García, C. P. E.; Rodriguez, G. C. A.; C. A. Martínez, P. C. A. – Inf. Spec. – Mat. Sci., Eng. and Tech. April 2012

[2] Mahto, T.K; Chowdhuri, A.R.;Sahu, S.K. - Journal of Appl. Polym. Sci. 2014, 131,19, 40840

Synthesis, functionalization and characterization of Fe_3O_4@SiO_2 Nanoparticles.

The Fe_3O_4 nanoparticles, synthetized by means of the co-precipitation method as described in the previous chapter, and stored in water dispersion, were used to be covered with a SiO_2 shell, in order to improve the stability and the capacity of functionalizing the surface. Furthermore, silica possesses many advantages, such as uniform size and shape, resistance of acid and alkali, thermal stability and low cytotoxicity. [1, 2]

The synthesis (***Figure 3.6.1***) and functionalization (***Figure 3.6.5***) scheme is shown below:

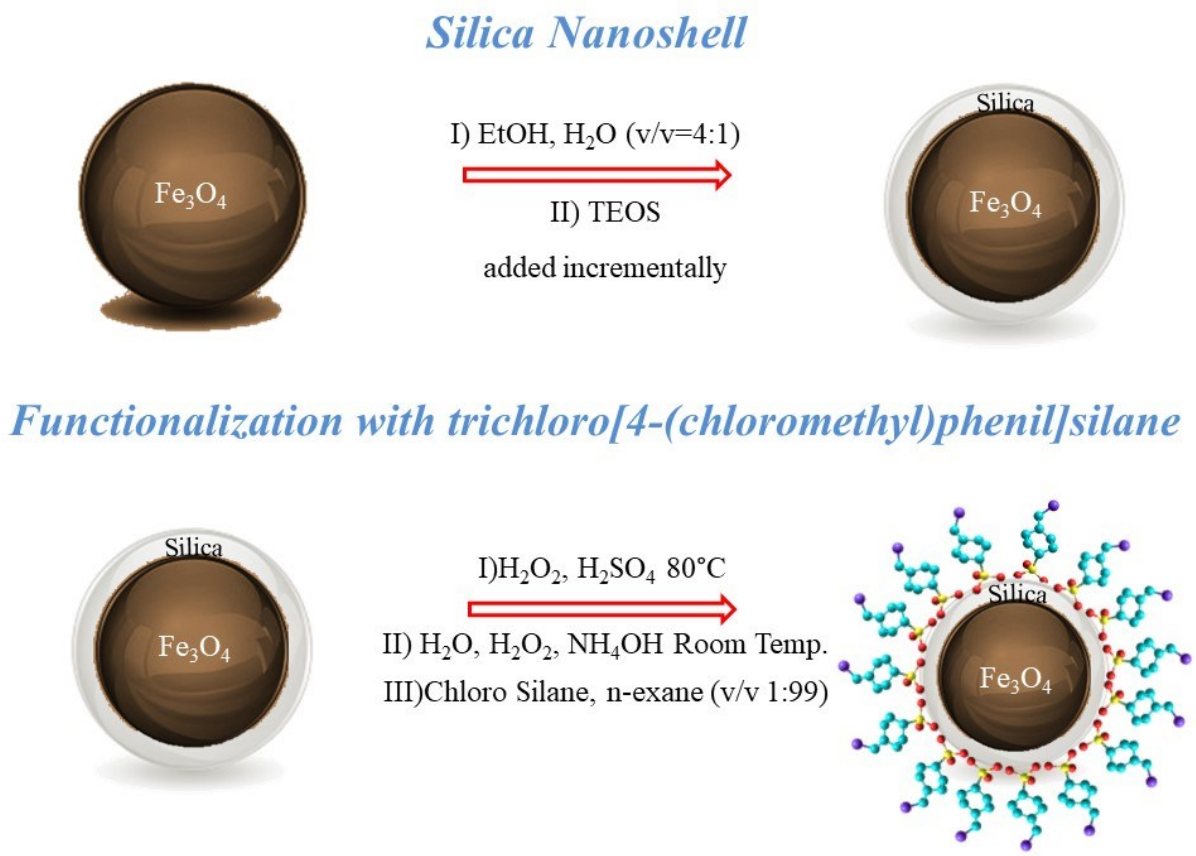

Figure 3.6.1: Synthesis of silica nanoshell on Fe_3O_4 nanoparticles, and functionalization with trichloro[4-(chloromethyl)phenil]silane.

Fe_3O_4@SiO_2 nanoparticles were prepared through a modified Stöber method.[3]

Briefly, 0.0204 gr Fe_3O_4 nanoparticles were dispersed into 25 mL solution containing ethanol and distilled water (V/V = 4:1) and 0.3 mL NH_4OH (30%) under ultrasonication. Then, 0.2 mL TEOS was dropped slowly into the mixture with the reaction stirred, and further stirred

for 6h. Thus, prepared material was achieved by centrifugation and washed with Milli-Q water and ethanol for several times, and dried in vacuum at 70 °C for 7h.

The Fe_3O_4@SiO_2 nanoparticles obtained were characterized by UV-Vis (***Figure 3.6.2***), IR, (***Figure 3.6.3***) and with DLS analysis (***Figure 3.6.4***).

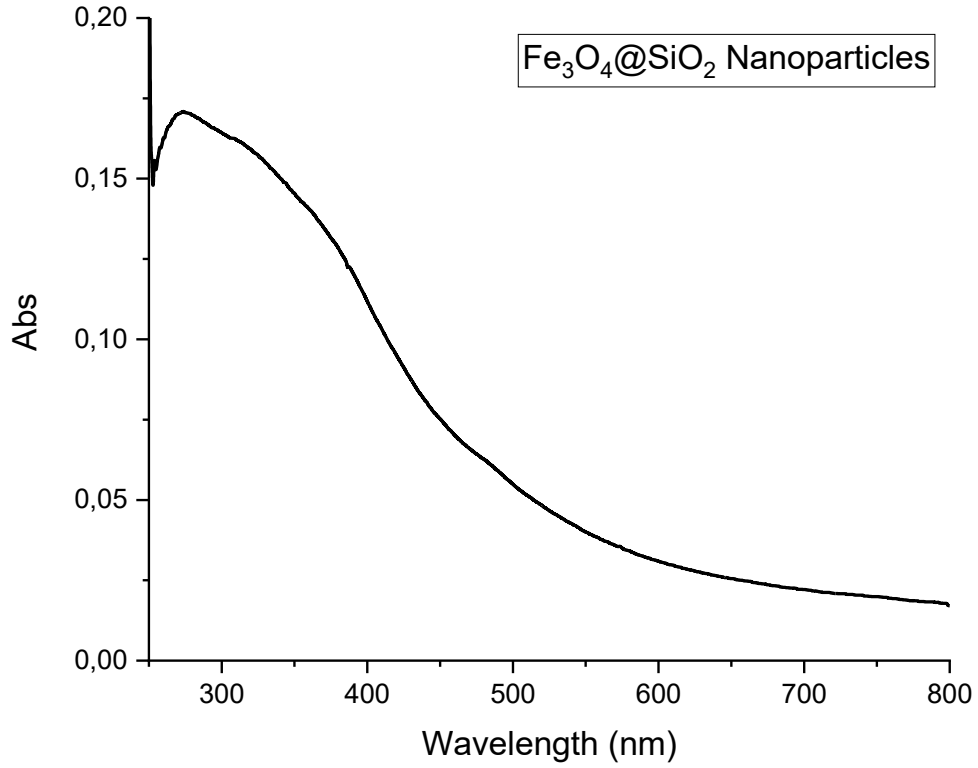

Figure 3.6.2: Uv-Vis spectrum of Fe_3O_4@SiO_2 nanoparticle in water solution.

The Uv-Vis spectrum of the nanoparticles of Fe_3O_4@SiO_2 is very similar to the Fe_3O_4 nanoparticles one. In fact, it does not show any typical absorption signal, but only a broaded signal along a range of wavelengths ranging from 250 to 800nm

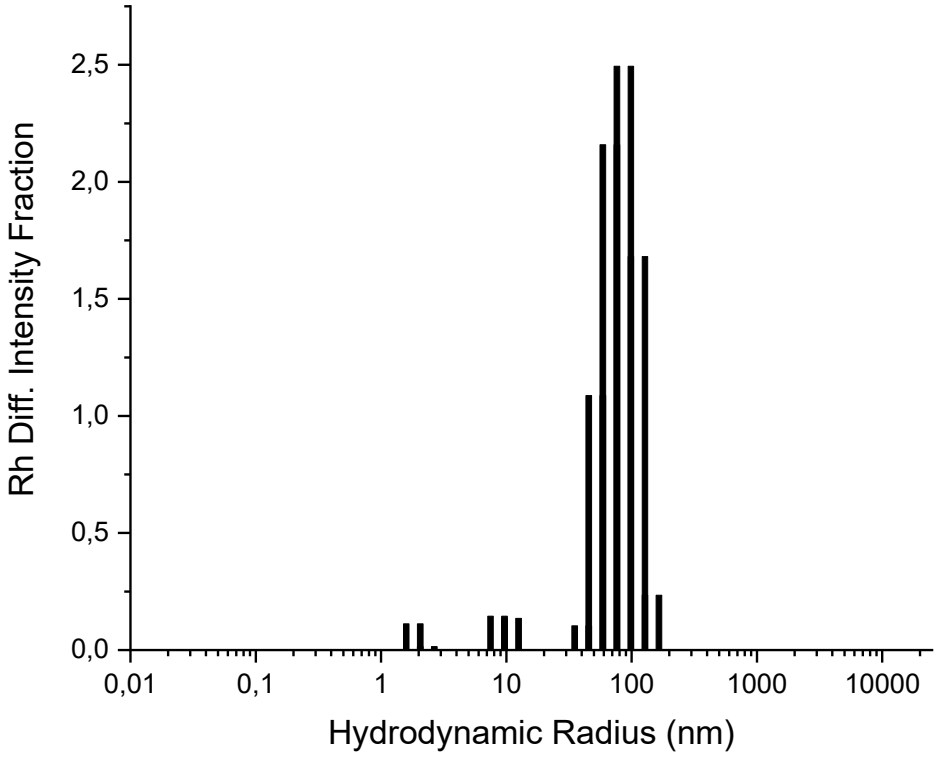

Figure 3.6.3: Size distribution of Fe_3O_4@SiO_2 Nanoparticles in water solution

The dimensions of the Fe_3O_4@SiO_2 nanoparticles were determined by DLS analysis in water. The graph in ***Figure 3.6.3*** shows three different distributions: the first one at around 2 nm, possibly due to the formation of pure silica nanoparticles, the second one at around 10 nm, and the third one at around 85nm. Compared to the size distribution of Fe_3O_4 nanoparticles, the Fe_3O_4@SiO_2 size distribution is slightly diminished, as if nanoparticles systems tend to be more isolated, perhaps, thanks to the silica coating.

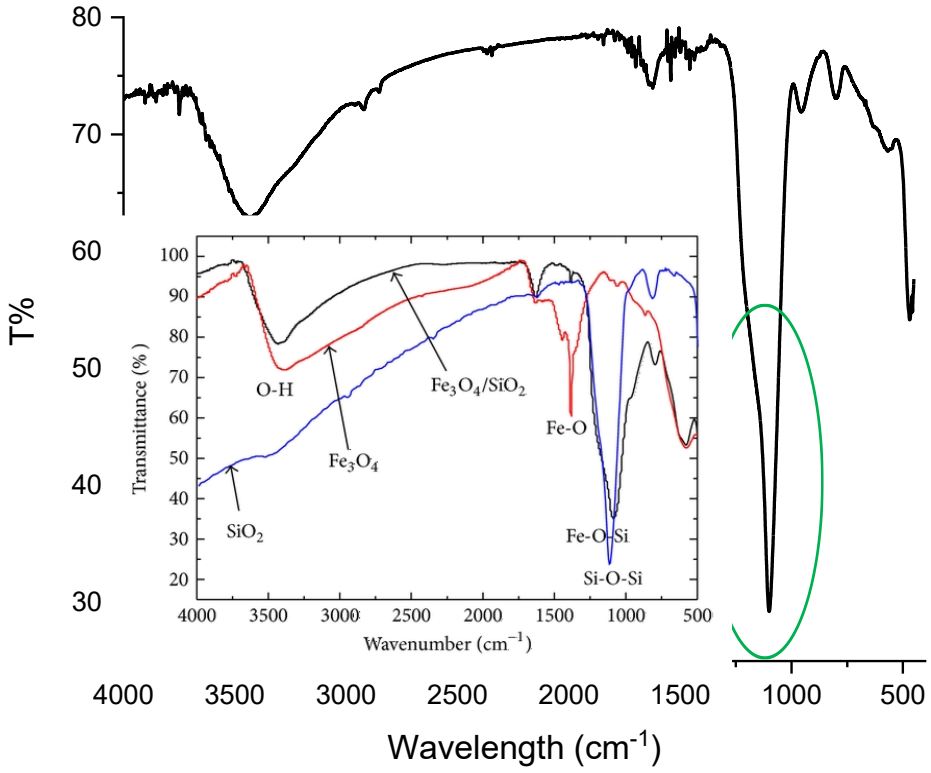

Figure 3.6.4: IR spectrum of Fe_3O_4@SiO_2 nanoparticles. Inset shows the IR spectrum of the Fe_3O_4@SiO_2 nanoparticles from literature where we can clearly see the peak relative to the Fe-O-Si bond, which is very evident even in the experimentally obtained spectrum.

The IR spectrum of Fe_3O_4@SiO_2 nanoparticles (***Figure 3.6.4***) shows, if compared to the one obtained from literature, the typical signals, not only related to the nanoparticles of Fe_3O_4, but above all those related to the bond Fe-O-Si, which indicates the occurred covering of the surface of the magnetic nanoparticles by the silica.

Obtained the nanoparticles of Fe_3O_4@SiO_2, these are treated with a piranha mixture to prepare the surface for a post-functionalization with the chlorosilane.

Briefly, 15mg of nanoparticles, previously taken to dryness and dried in a vacuum oven at 70°C for 24h, are put in a vial and added with 0.3ml of H_2O_2 (30%) and 0.7ml of H_2SO_4 and left to sonicate at 80°C for 1h.

After that, the nanoparticles are separated by centrifugation and washed many times with water. After the washes, 0.715ml of water, 0.143ml of H_2O_2 (30%) and 0.143ml of NH_4OH are added in the vial and left to react at room temperature in sonicator for 35 minutes. Finally, the particles are separated with the magnet and are washed many times with water and left to dry in a vacuum oven at 70 °C for 24h.

Once the surface is prepared, the nanoparticles are suspended in 0.990ml of anhydrous n-hexane (prepared previously). Once the suspension has been obtained, 0.010 ml of chlorosilane are added (all the operations described are performed under constant flow of nitrogen) and all put in to react in the sonicator for about 40 minutes at room temperature.
Once the reaction is complete, the nanoparticles are washed and centrifugated with n-hexane, so as to eliminate the excess chlorosilane. Finally, the particles are transferred to a new vial and placed in a vacuum oven at 50 °C for 24h. The particles thus functionalized are ready for the next step of functionalization with the porphyrin (***Figure 3.6.5***).

$$Fe_3O_4@OSi(phe)CH_2Cl + P(PEG350)_3 \rightarrow Fe_3O_4@OSi(phe)CH_2\text{-}O\text{-}P(PEG350)_3$$

$$Fe_3O_4@OSi(phe)CH_2Cl + P(PEG750)_3 \rightarrow Fe_3O_4@OSi(phe)CH_2\text{-}O\text{-}P(PEG750)_3$$

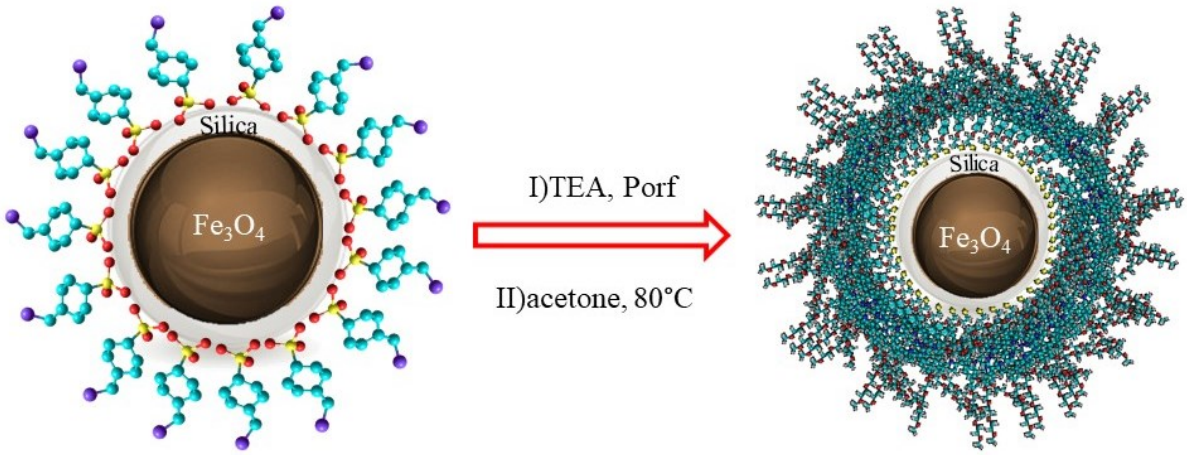

Figure 3.6.5: scheme of the functionalization of $Fe_3O_4@SiO_2@SiCl$ with porphyrins derivatives

Briefly, 0.75mg of $Fe_3O_4@SiO_2@SiCl$ are suspended in 1 mL of acetone. Then, this solution is added with 1µL of triethylamine and 1.01mg of $P(PEG750)_3$ and left to react at 80°C for 24h under sonication.
After 24 hours, the solution is concentrated and left to react for one hour. At the end of the reaction, the nanoparticles are purified by washes with acetone and subsequent centrifugations. Finally, the precipitate is dried in a vacuum oven.
The nanoparticles thus obtained are characterized by UV Vis (***Figure 3.6.6***).

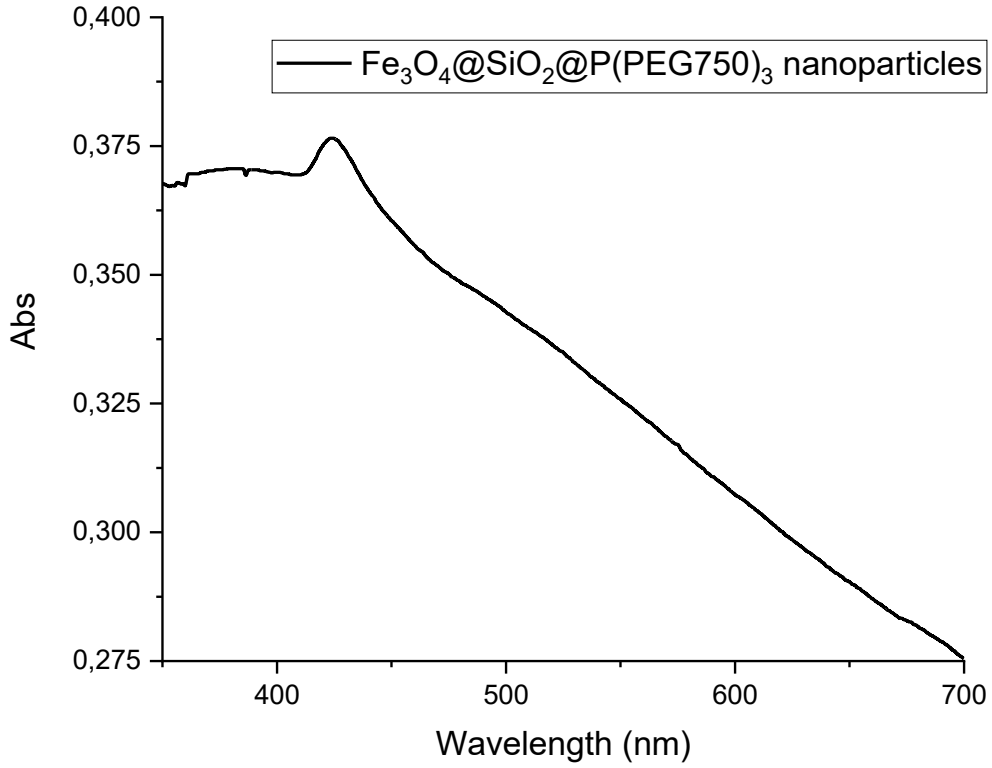

Figure 3.6.6: Uv-Vis spectrum of Fe_3O_4@SiO_2@P(PEG750)$_3$ nanoparticles in acetone solution.

The UV Vis spectrum (***Figure 3.6.6***) clearly shows the typical soret band (at 415 nm) of the porphyrinic systems. The signals related to the Q bands are hidden by the strong scattering of nanoparticle systems.

The system described is still under study to confirm the effective anchoring of the porphyrin on the surface of the nanoparticles, through TEM, STEM and XPS analyzes. The signal obtained through Uv-Vis spectroscopy gives hope for the successful functionalization of the nanoparticles of Fe_3O_4@SiO_2 with P(PEG750)$_3$.

[1] Zhao, Y.; Li, J.; Zhang, S.; Wang, X. RSC Adv. 2014, 4, 32710–32717

[2] Sheng, G.; Alsaedi, A.; Shammakh, W.; Monaquel, S.; Sheng, J.; Wang, X.; H. Li, H.; Huang, Y. Carbon 2016, 99, 123–130.

[3] Stöber, W.; Fink, A.; Bohn, E.; J. Colloid Interface Sci. 1968, 26, 62–69

Synthesis, functionalization and characterization of Fe_2O_3@Au Nanoparticles.

Iron oxide nanoparticles consisting of maghemite (γ-Fe_2O_3) or magnetite (Fe_3O_4) have attracted much interest due to their widespread electronic and, more recently, biomedical applications. In particular, solutions of γ-Fe_2O_3 and Fe_3O_4 particles 7.5-100 nm in diameter look like promising magnetic fluids for targeted drug delivery. The extent of biomedical applicability of these particles depends strongly upon their stability in solutions of physiological pH, as well as the degree to which their surfaces may be chemically functionalized. Iron oxide applicability is notably hindered by the materials' spontaneously oxidizable surfaces; chemical methods to predictably tune surface functionality are still being explored. However, it is well established that Au nanoparticle surfaces may be repeatedly functionalized with thiolated organic molecules. Placement of a functional group on the terminal end of the alkanethiolate imparts further chemical reactivity and the opportunity to create multifunctional, reactive nanoparticles. To maximize the tunability of chemical functionality and, ultimately, biological applicability, a thorough understanding of the magnetic, electronic, and optical properties of core/shell systems as a function of composition is essential.

Literature data show that attempts to overlay Au shells onto freshly synthesized Fe_3O_4 particle surfaces failed to yield any evidence of Au reduction. Specifically, it was observed that freshly prepared Fe_3O_4 nanoparticles (i.e. within 24h of nucleation) failed to obtain an Au shell. However, using Fe_3O_4 nanoparticle solutions that were exposed to air for extended periods (>1 week), sequential addition of $AuCl_4^-$ led to the formation of stable and soluble core/shell nanoparticles. It is well known that long-term exposure of Fe_3O_4 to air results in particle oxidation to form γ-Fe_2O_3 via Fe cation diffusion;[1] [2] these observations suggest that Au^{3+} preferentially reduces onto γ-Fe_2O_3 surfaces rather than Fe_3O_4. For this reason it was decided to use Fe_2O_3 particles to form Fe_2O_3@Au hybrid systems.

A synthesis (***Figure 3.7.1***) (***Figure 3.7.4***) and functionalization (***Figure 3.7.10***) scheme of the nanoparticles of Fe_2O_3 is shown below:

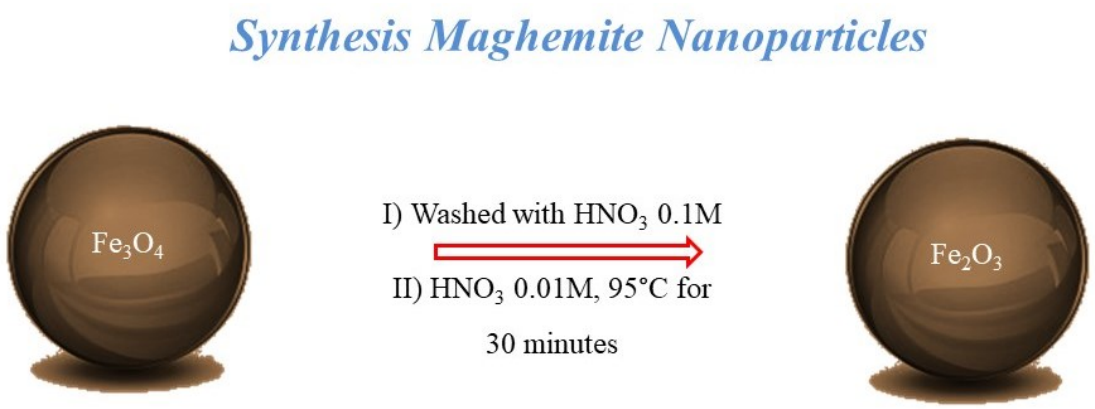

Figure 3.7.1: Synthesis scheme of Fe_2O_3 nanoparticles.

Briefly, in order to synthesize γ-Fe_2O_3 nanoparticles, an aliquot of freshly nucleated Fe_3O_4 particles (see chapter 5) were washed with 0.1 M HNO_3 and isolated by centrifugation. The particles were dissolved in 0.01M HNO_3 and heated with stirring at 90-100 °C for 30 min to completely oxidize the particles to γ-Fe_2O_3.[3]

The solution was cooled to room temperature, centrifuged, and the supernatant separated with a magnet. The isolated particles were washed twice with H_2O and once with 0.1M TMAOH solution, and were suspended in 0.1M TMAOH solution.

In this conditions, the interactions between $N(CH_3)^+$ counterions and adsorbed OH^- anions stabilize the solution and prevent particle's aggregation.[4, 5, 6] The particles suspension were stored in the fridge and remained stable for several months.

The particles thus obtained were characterized by UV-Vis (***Fig. 3.7.2***) and DLS (***Fig. 3.7.3***).

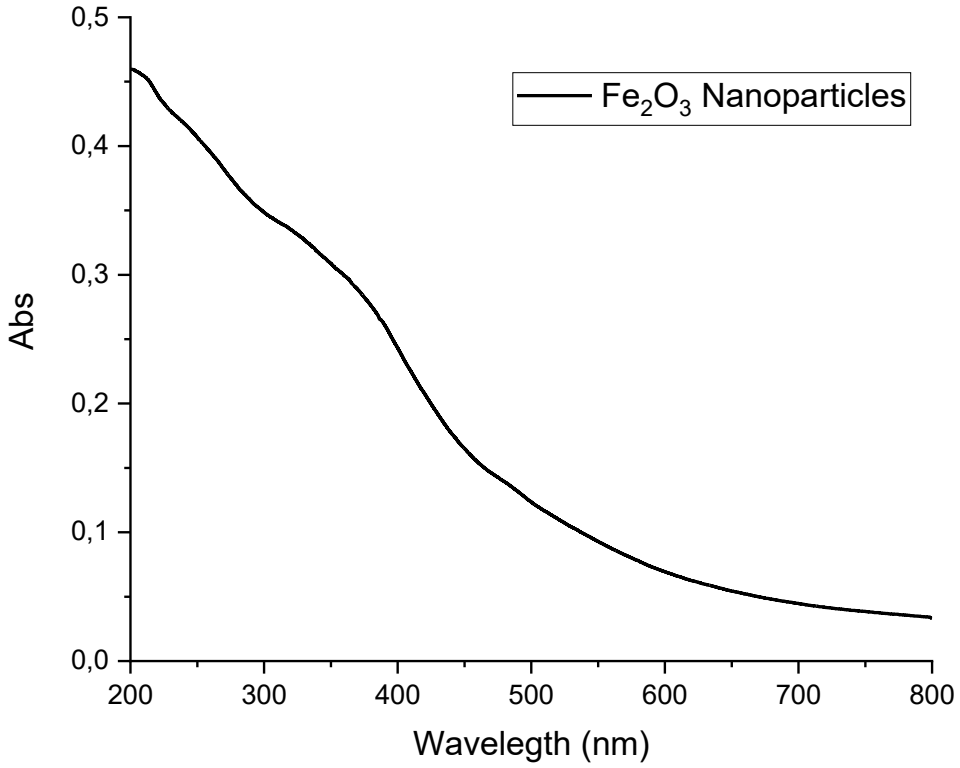

Figure 3.7.2: Uv-Vis spectrum of Fe_2O_3 nanoparticles in water suspension

The Uv-Vis spectrum of the nanoparticles of Fe_2O_3 is very similar to those of the only nanoparticles of Fe_3O_4, in fact it does not show any characteristic absorption signal, but only a broaded signal along a range of wavelengths ranging from 200 to 800nm.

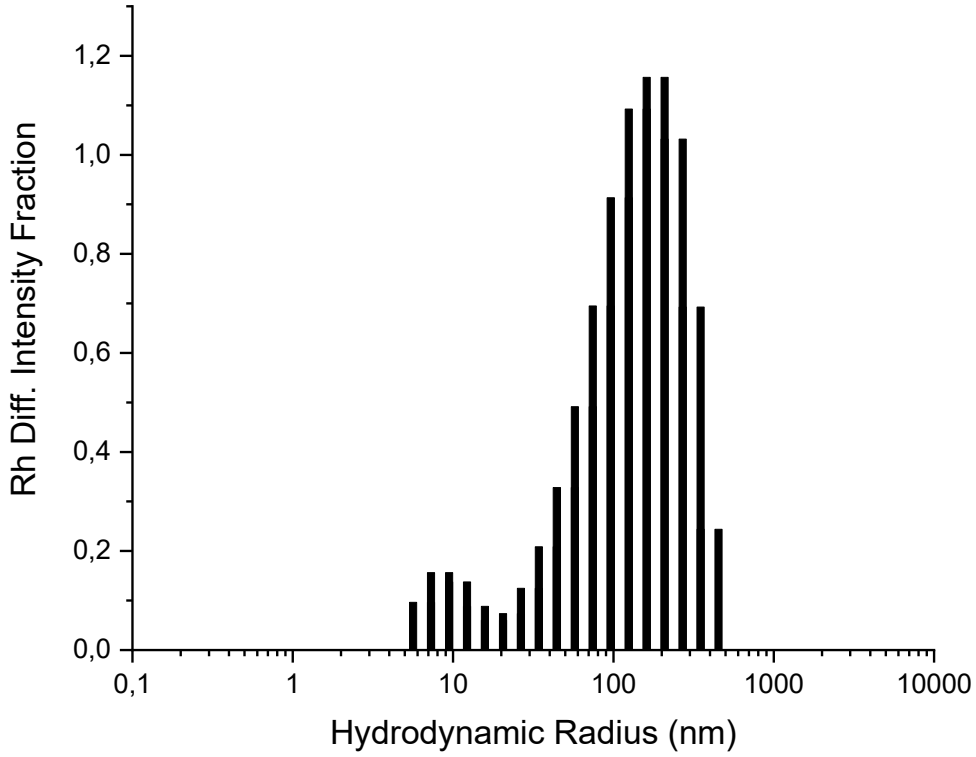

Figure 3.7.3: Size distribution Fe_2O_3 nanoparticles in water solution

The sizes of the maghemite nanoparticles were determined by DLS analysis in water. The graph in ***Figure 3.7.3*** shows two different distributions not well separated, with a R_H average around 150nm. This distribution is, possibly, due to magnetic interactions that create nanoparticles aggregates.

Successively, Au shells were formed by reduction of Au^{3+} onto the Fe oxide surfaces using a modification of Brown and Natan's iterative hydroxylamine seeding procedure[7] (***Figure 3.7.4***).

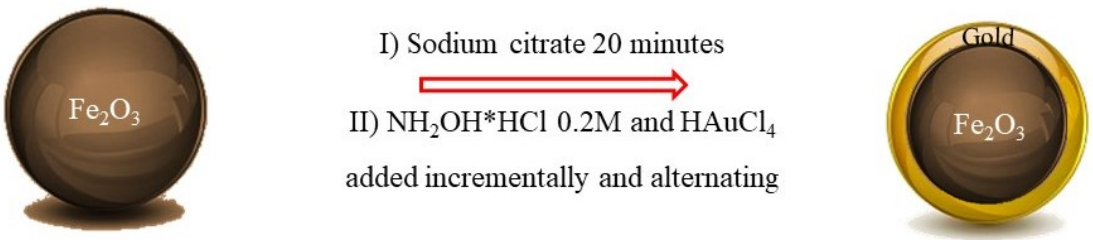

Figure 3.7.4: Synthesis scheme of gold nanoshell on Fe_2O_3 nanoparticles

Briefly, 3.75 ml of γ-Fe_2O_3 nanoparticles solution were diluted into 70 ml of water and stirred with an equal volume of 0.1M sodium citrate for 10 min into sonicator to exchange adsorbed OH^- with citrate anions. After, the solution was transfer into heating plate for other 10 minutes. Into solution of Fe oxide/citrate, aliquots of 1% HAuCl4 were incrementally added (with an interval of at least 10 minutes between each addition) along with an excess of 0.2 M NH_2OH*HCl (see ***table 3.7.5***).

Iteration	***0.2M NH_2OH*HCl (µL)***	***1% $HAuCl_4$ (µL)***
1	***375 µL***	***312.5 µL***
2	***140.5 µL***	***250 µL***
3	***94 µL***	***250 µL***
4	***94 µL***	***250 µL***
5	***140.5 µL***	***250 µL***

Table 3.7.5: Amounts used in iterative seeding of Fe oxide nanoparticles.

After the last addition, the solution is brought to the boiling point and allowed to react for 30 minutes. Finally, it is left to cool at room temperature and subsequently characterized by Uv-Vis (***Fig. 3.7.6***) and DLS (***Fig. 3.7.7***) techniques.

The Uv-Vis spectrum of Fe_2O_3@Au nanoparticles (***Figure 3.7.6***) (solid line) clearly shows, at values of 528nm, the peak relative to the gold plasmon resonance. In the ***Figure 3.7.6*** the two spectra of Fe_2O_3 nanoparticles are compared, before and after the covering with the gold shell.

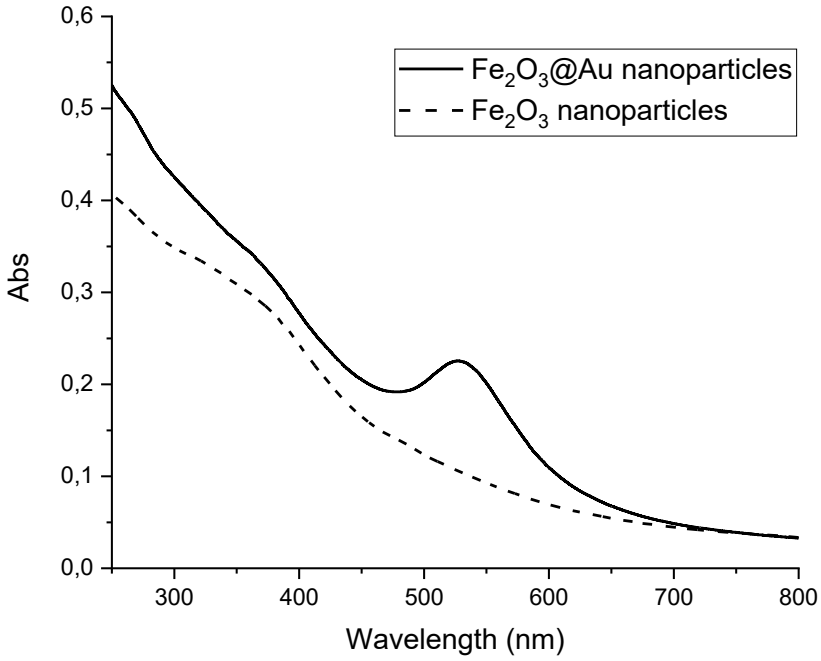

Figure 3.7.6: Uv-Vis spectra of Fe_2O_3 nanoparticles (dashed line) and Fe_2O_3@Au nanoparticles (solid line) in water solution

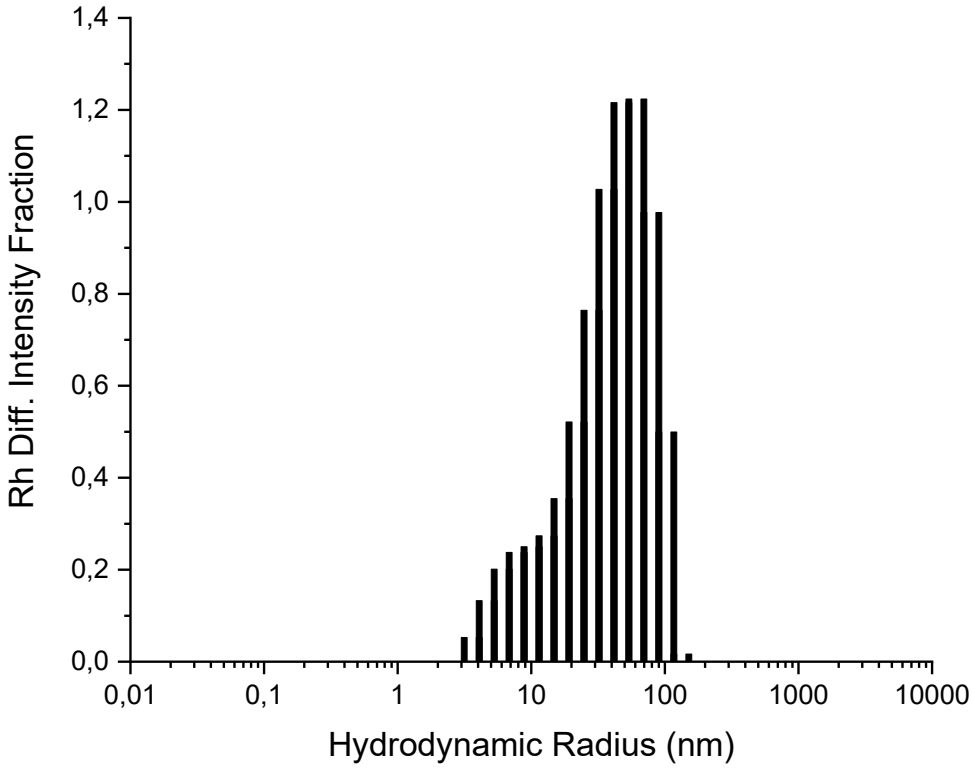

Figure 3.7.7: Size distribution of Fe_2O_3@Au nanoparticles in water solution

The DLS spectrum shows a dimensional distribution shifted at lower values, in particular with a R_H average of about 45nm. This is an indication of the fact that after the coating with gold the particles form aggregates of smaller and more stable dimensions over time.

The next step concerns the functionalization of Fe_2O_3@Au nanoparticles with a thioled linker. The procedures adopted for the functionalization step are a modification of the same described for the AuNPs, known as method 2.

Briefly, 1.21mg of Fe_2O_3@Au nanoparticles were solubilized in 5cc of water and left to sonicate for about 30 minutes. 1 ml of a solution of 3-chloro-propanethiol in ethanol (40µL thiol in 1ml of ethanol) was added into nanoparticles dispersion, and left to react into sonicator at 60°C for 3 hours. The obtained solution, cooled at room temperature, was centrifuged at 5000 rpm for 15 min; the residue was separated from supernatant, sonicated in ethanol and centrifuged for 2 more times. The final product Fe_2O_3@Au@ClPT was maintained under vacuum at 60 °C for 24 h and then suspended in acetone and analyzed by means UV-Vis (***Fig. 3.7.8***) and DLS (***Fig. 3.7.9***) techniques.

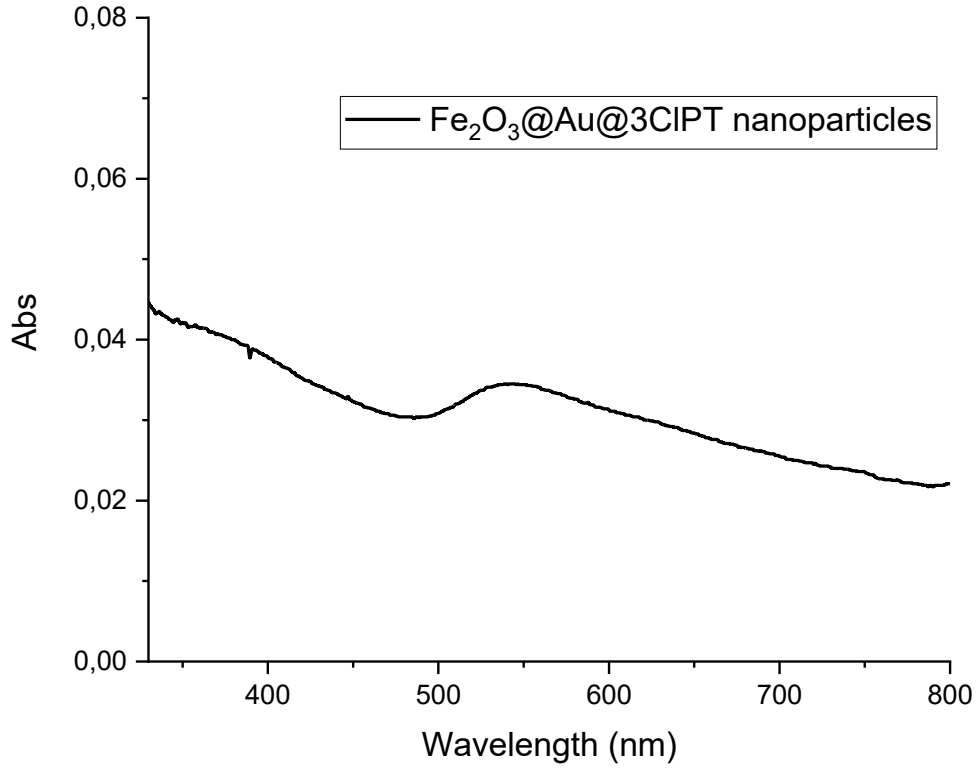

Figure 3.7.8: Uv-Vis spectra in acetone solution of Fe_2O_3@Au@ClPT nanoparticles.

The Uv-Vis spectrum of Fe_2O_3@Au@ClPT nanoparticles (***Figure 3.7.8***) clearly shows, at values of 540 nm, the peak relative to the gold plasmon resonance. The shift of the plasmonic resonance peak value, compared to that of the spectrum in ***Figure 3.7.6***, might be caused by the different solvent used. Furthermore, the low signal intensity is due to the poor suspendibility of the Fe_2O_3@Au@ClPT system in acetone

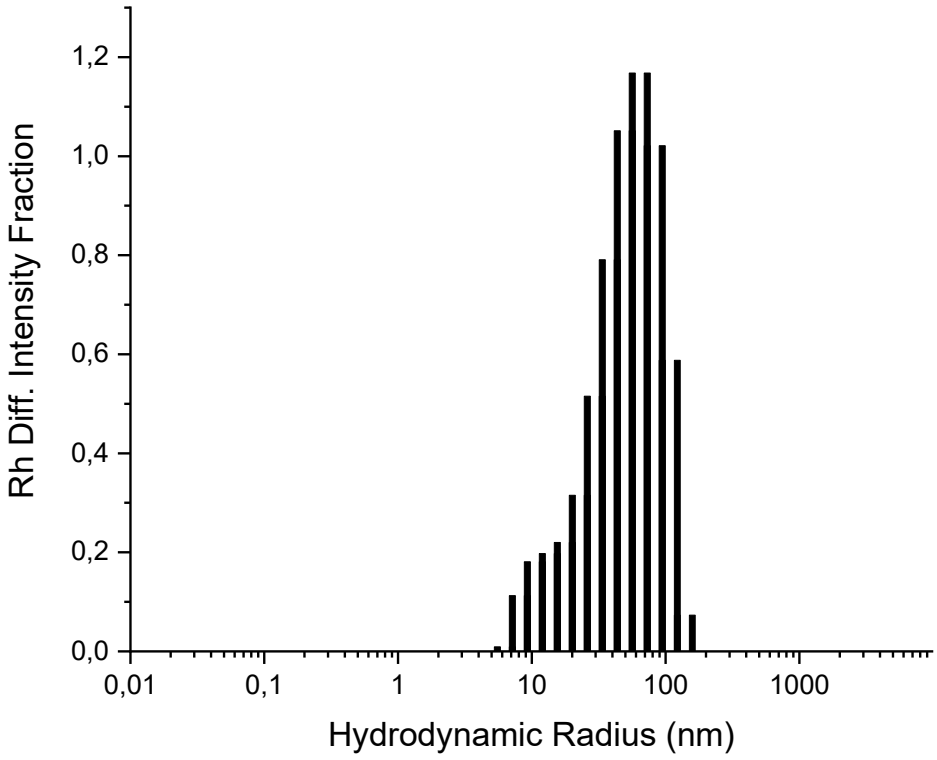

Figure 3.7.9: Size distribution in acetone solution of Fe_2O_3@Au@ClPT nanoparticles.

The DLS spectrum in ***Figure 3.7.9*** shows a size distribution shifted to upper values, in particular with a R_H average of about 55nm (about 10nm in plus respect the nanoparticles without thiol). This is a possible index of the successful functionalization.

The third step of the synthetic process concerned the covalent binding through a nucleophilic substitution reaction of 5,10,15-tri-(p-[ω-methoxy-poly (ethylene oxide)] phenyl}-20-(p-hydroxyphenyl) porphyrin [$P(PEG350)_3$ or $P(PEG750)_3$] at Fe_2O_3@Au@ClPT nanoparticles (***Figure 3.7.10***). The functionalization with the porphyrin provides the same procedure used for Ag and Au nanoparticles. Therefore, for brevity, only the Uv-vis, fluorescence and DLS characterizations will be reported.

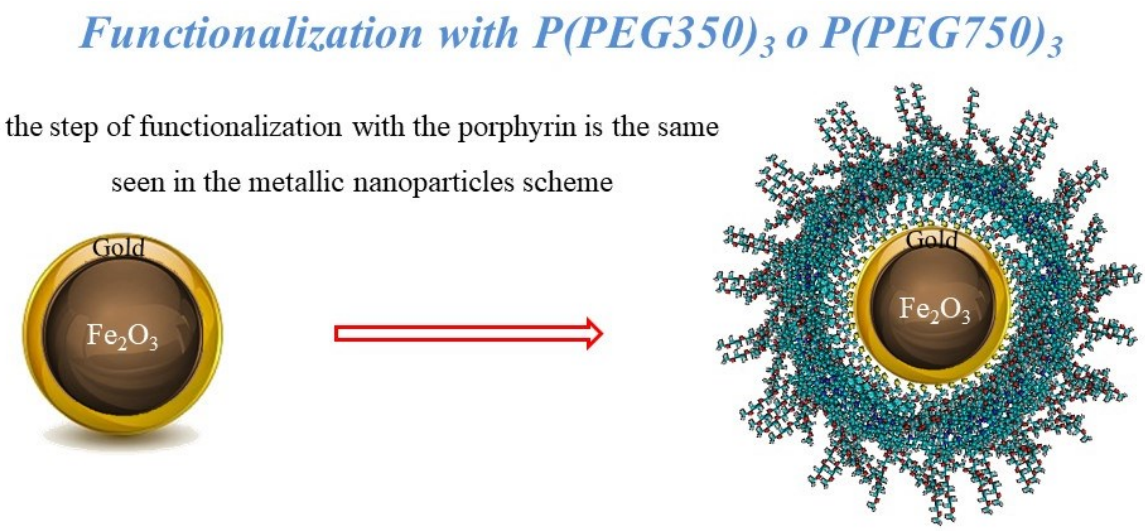

Figure 3.7.10: Synthesis scheme of the functionalization of Fe_2O_3@Au with porphyrins derivatives.

The Uv-Vis spectrum of Fe_2O_3@Au@P(PEG350)$_3$ nanoparticles (***Figure 3.7.11***) (solid line) clearly shows, at values of 420nm, the peak relative to Soret band of porphyrin. In ***Figure 3.7.11***, the two spectra of Fe_2O_3@Au@ClPT and Fe_2O_3@Au@P(PEG350)$_3$ nanoparticles are compared so that the signal relative to the plasmonic peak of the gold is also very well displayed.

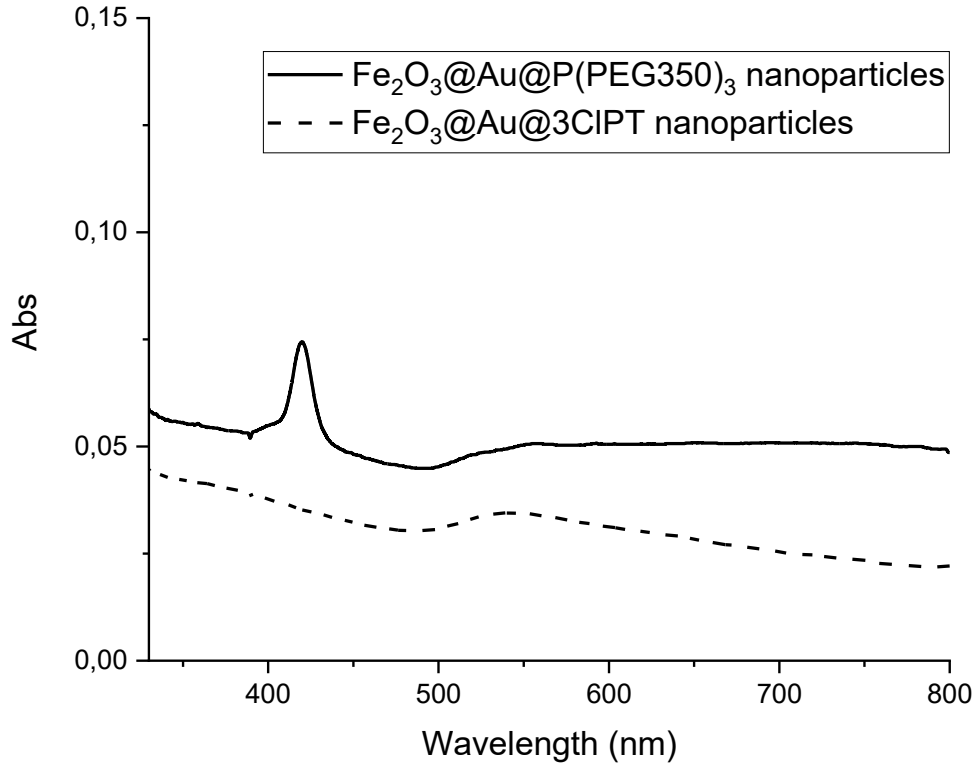

Figure 3.7.11: Uv-Vis spectra of Fe_2O_3@Au@ClPT nanoparticles (dashed line) and Fe_2O_3@Au@P(PEG350)$_3$ nanoparticles (solid line) in acetone solution

[1] Cornell, R. M.; Schwertmann, U. The Iron Oxides; VCH: New York, 1996.
[2] Jolivet, J. P.; Tronc, E. J. Colloid Interface Sci. 1988, 125, 688-701.
[3] Lefebure, S.; Dubois, E.; Cabuil, V.; Neveu, S.; Massart, R. J. Mater. Res. 1998, 13(10), 2975
[4] Massart, R. IEEE Trans. Magn. 1981 17(2), 1247-48.
[5] Bacri, J.; Perzynski, R.; Salin, D. J. Magn. Magn. Mater. 1990 85, 27-32
[6] Kang, Y. S.; Risbud, S.; Rabolt, J. F.; Stroeve, P. Chem. Mater. 1996, 8, 2209-2211.
[7] Brown, K. J.; Walter, D. G.; Natan, M. J. Chem. Mater 2000, 12, 306-313.

Results and Discussion

Chemical and physical characterization of the functionalized nanoparticles.

The present PhD research work focuses on obtaining a new synthetic strategy for the creation of hybrid and multifunctional nanoparticle systems, for applications in the therapeutic field and in particular in cancer therapy.

The interest in the nanoparticles for biomedical application is born from the necessity of reducing the poor pharmacokinetics and inappropriate biodistribution of chemotherapy drugs. Because of their low molecular weight, for example, intravenous antitumor agents tend to have a short circulation time and low concentration in tumors and metastases.

To help the antitumor agents administered to achieve adequate circulation time, appropriate concentration into tumoral cells and to mitigate their accumulation in potentially endangered healthy organs and tissues, nanoscale delivery systems such as liposomes, polymer micelles, polymers, nanogels, and nanocapsules have emerged as an indispensable platform for modern cancer therapys.

Nanoteranostics has recently become one of the main keywords in cancer research, based on the premise that, if cancer grows, it can be hampered during the diagnosis phase, and the subsequent treatment would be much simpler because the growth of cancer is delayed or reduced. The following research project focuses mainly on the field of oncological therapies, where the main purpose of the research is to increase the effectiveness of treatments and decrease the undesirable toxic side effects of current therapies, which indiscriminately influence the cells (both sick and healthy), causing often serious collateral damage.

The project proposes the development of new organic/inorganic hybrid nanosystems having a core-shell-shell structure, consisting of metal (Ag, Au and/or Fe_3O_4@Au) nanoparticles functionalized by a covalent bond with PEGylate porphyrinic systems. The choice to synthesizing these hybrid systems born from the possibility to exploit the different properties of the single parents components, combined in a single complex system, as an example: the magnetite core will provide the paramagnetic properties necessary for use in the targeted distribution of drugs (NP fabrics via magnetic field), in magnetic resonance and magnetic hyperthermia (magnetic NPs can be subjected to an alternating magnetic field, overheat and therefore determine cell death); The gold particles can be used as a heat source in

photothermal therapy (hyperthermia by light stimulation). The nanoscale sizes of the nanosystems (40-100 nm) allow them to work as passive targeting (EPR effect); The organic shell, obtained by functionalization with the PEGylated porphyrins derivatives, induces the necessary water solubility and the biocompatibility of the whole system. Also, thanks to its excellent spectroscopic properties (Uv-Vis absorption and fluorescence), it allows to monitor its presence inside the tissues. Furthemore, the capability of the porphyrin core to generate singlet oxygen, under light irradiation, allows its use as a phototoxic agent (for the photodynamic therapy of tumors).

In this landscape, it is clear that these hybrid nanosystems strongly implements the field of application and efficiency in the biomedical field.

In summary, the scientific objective can be achieved by creating biocompatible intelligent systems that do not require further vectors, but that are themselves able to move into the tissues, in order to recognize, to accumulate, and treat the diseased tissues. These new multi-tasking molecules, therefore equipped with diagnostic and therapeutic properties, fall into the category of theranostic agents.

To better correlate the properties of the hybrid systems with the physical size and the chemical composition, several instrumental characterizations have been conducted.

The sizes of the different samples were evaluated using Uv-Vis and Dynamic Light Scattering, as well as with transmission electron microscopy (TEM) and atomic force microscopy (AFM). In addition, the compositional analysis was performed using X-Ray Photoelectron Spectroscopy (XPS), Energy-Dispersive X-Ray Spectroscopy (EDS) and Scanning Transmission Electron Microscopy (STEM).

To obtain more detailed information on the shape, size and morphology of the functionalized, and non, nanoparticles systems, TEM analyzes were also conducted.

The TEM images of AgNPs samples functionalized both with $P(PEG350)_3$ and with $P(PEG750)_3$ were acquired by examining the corresponding suspensions in acetone and in water (after deposition on the substrate for TEM analysis and solvent removal).

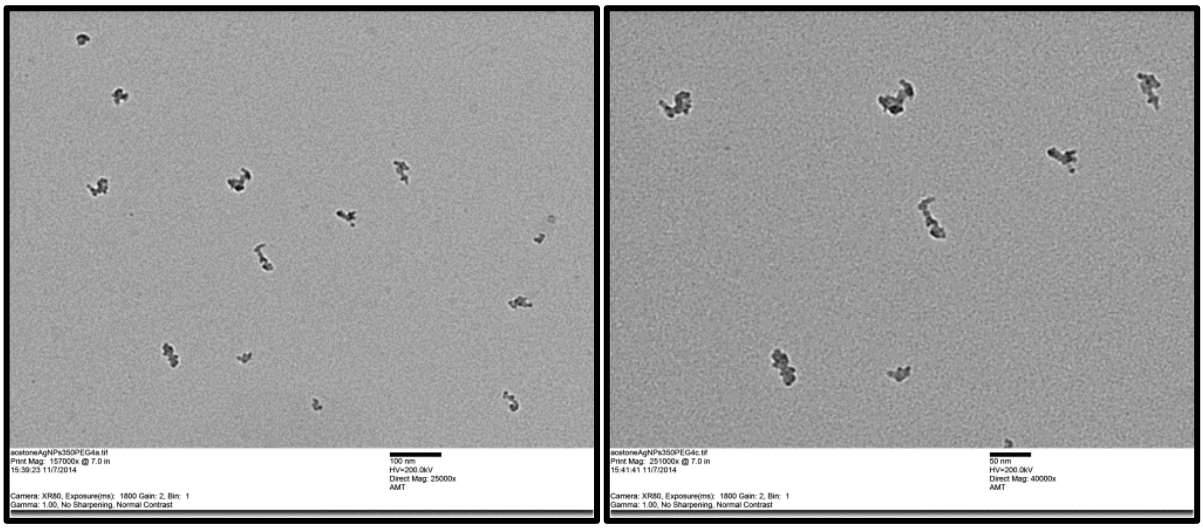

Figure 4.1.1: TEM images of AgNPs@P(PEG350)$_3$ nanoparticles. The sample was deposited by an acetone dispersion.

Figure 4.1.1 shows the TEM image of the sample of silver nanoparticles functionalized with P(PEG350)$_3$ and suspended in acetone. The sizes of the particles were about 50nm.

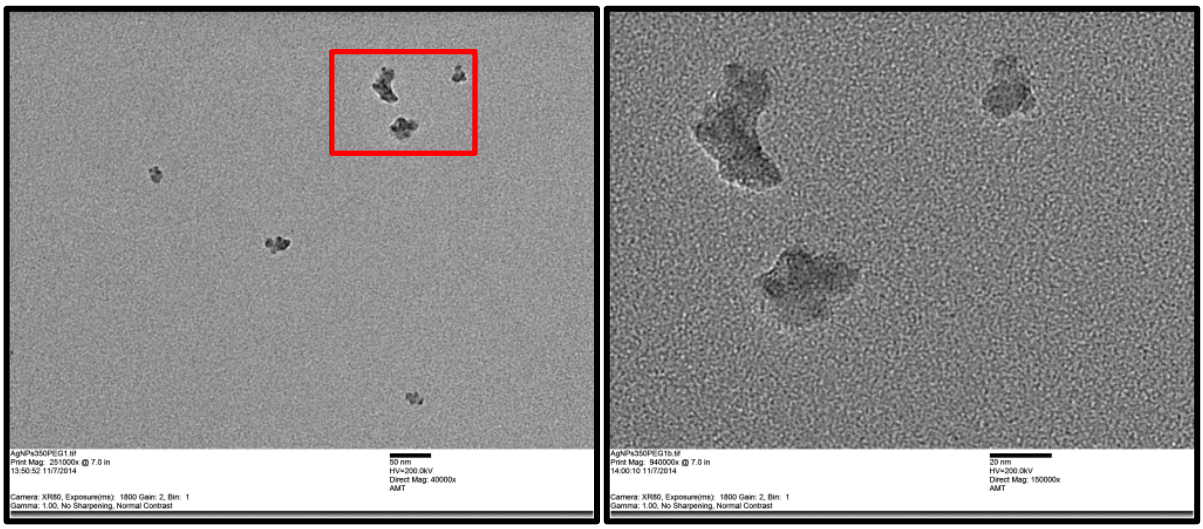

Figure 4.1.2: TEM images of Ag@P(PEG350)$_3$ nanoparticles. The sample was deposited by a water dispersion. On the right, an enlargement of the red box in the figure on the left

Figure 4.1.2 shows the TEM image of the sample of silver nanoparticles functionalized with P(PEG350)$_3$ and deposed by water suspension. The average size of the particles was about 70nm.

Figure 4.1.3 shows the dimensional distributions of the samples of AgNPs@P(PEG350)$_3$ performed by DLS analysis, using acetone (left) and in water (right) respectively. We can notice that the dimensions are comparable to those obtained by TEM microscopy, even if we have to consider that in the first case (***see TEM images***) the dimensions were referend to

aggregates, formed after evaporation of the solvent, while the dimensions obtained through DLS not only considered possible aggregates that formed in solution (due for example to the poor solubility of the systems or to the porphyrin-to-porphyrin interactions), but also the solvation shell of the system under examination. Therefore, the dimensions of the AgNPs@P(PEG350)$_3$ are actually smaller than those calculated with these techniques.

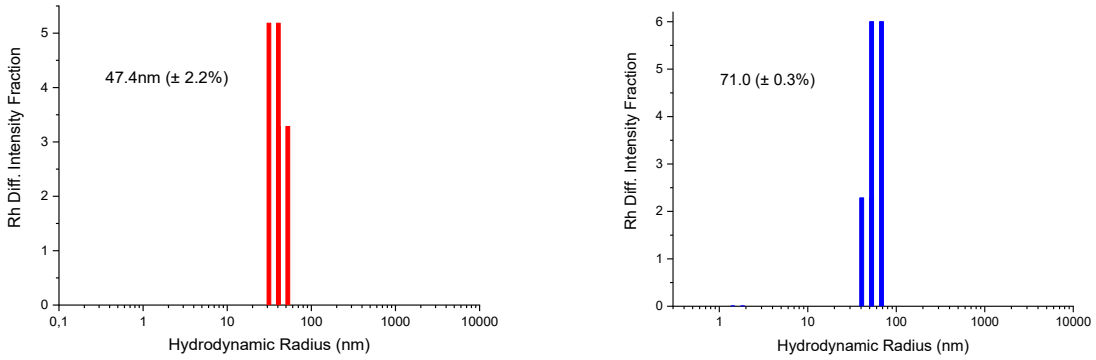

Figure 4.1.3: In red, the size distribution of AgNPs@P(PEG350)$_3$ nanoparticle in acetone, in blue, the size distribution of AgNPs@P(PEG350)$_3$ nanoparticle in water.

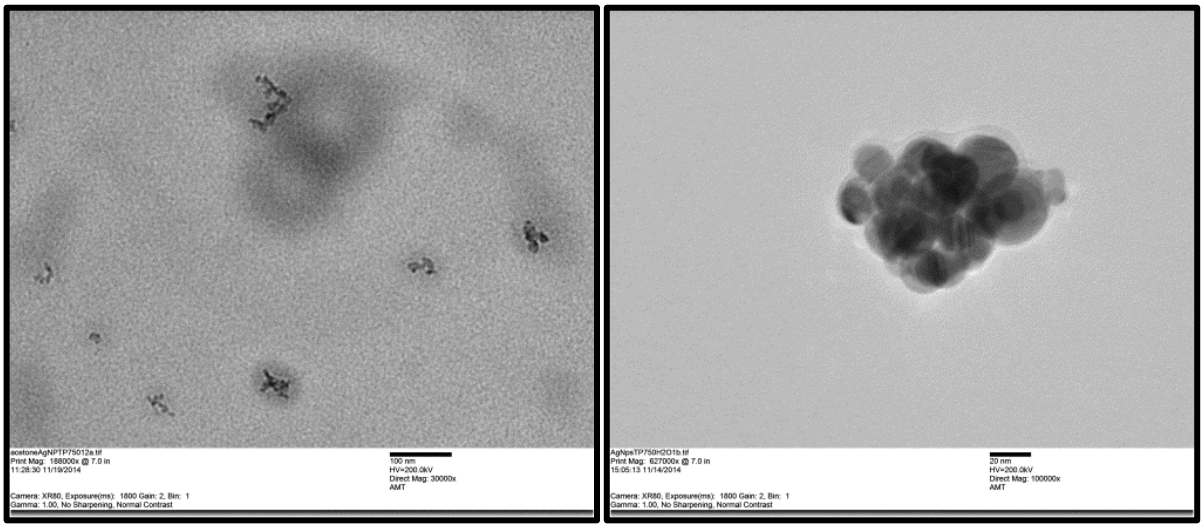

Figure 4.1.4: TEM images of AgNPs@P(PEG750)$_3$ nanoparticles. The sample was deposited by a water dispersion.

As expected, the dimensions of AgNPs@P(PEG750)$_3$ are bigger than AgNPs@P(PEG350)$_3$. In particular, we notice that the nanoparticles with P(PEG750)$_3$ tend to easily aggregate, ***Figure 4.1.4 left***, and the formation of species having dimensions of the order of one hundred nanometers, a value that is very well combined with that obtained with the light scattering (90.6nm ± 5.1%.) analysis (***Figure 4.1.5***). Similar results have been obtained also in the water

tests, finding that the sizes increase to about 120nm for the sample as it is (***Figure 4.1.4 right***) (***Figure 4.1.5***).

Also in this case, the dimensions obtained through the two techniques (DLS and TEM) seem to be comparable. But, as explained above, the obtained dimensions refer to aggregate particle (TEM) or to solution systems, thus including their solvation shell. Actually, the real dimensions of AgNPs@P(PEG750)$_3$ are about 30nm in diameter, as seen from the enlargement in ***Figure 4.1.4*** (right).

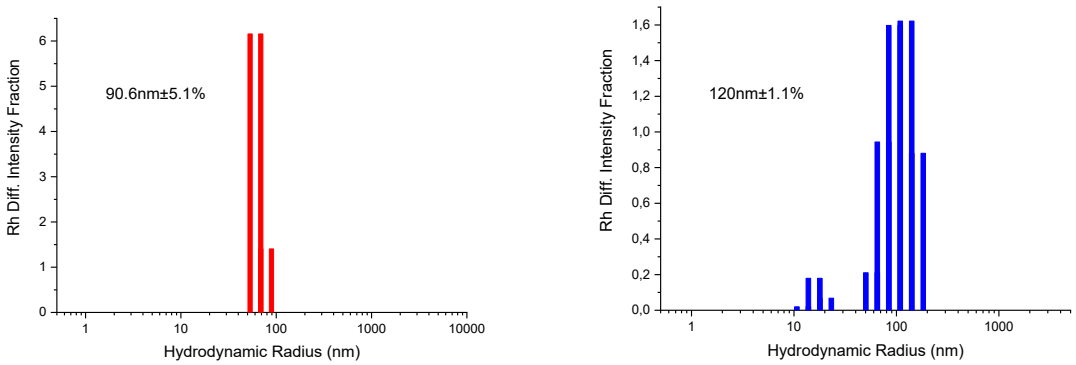

Figure 4.1.5: In red, the size distribution of AgNPs@P(PEG750)$_3$ nanoparticle in acetone, in blue, the size distribution of AgNPs@P(PEG750)$_3$ nanoparticle in water.

The dimensional characterization was also implemented with AFM analysis. Below are the images and dimensional profiles for 3 types of silver samples: AgNPs (***Figure 4.1.6***), AgNPs@ClPT (***Figure 4.1.7***) and AgNPs@P(PEG750)$_3$ (***Figure 4.1.9***)

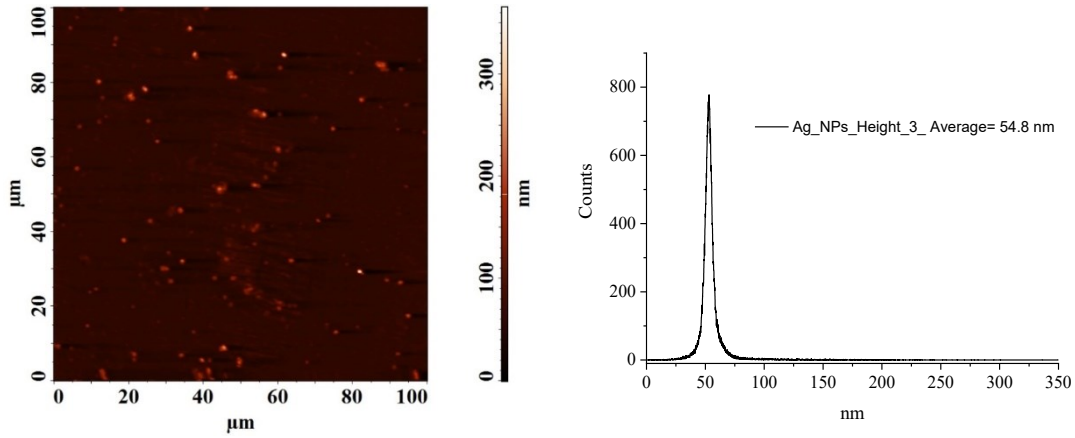

Figure 4.1.6: AFM image of AgNPs nanoparticles (right) and, profile of AgNPs nanoparticles sizes (left)

Figure 4.1.6 shows respectively the image (left) and the sizes profile (right) obtained through AFM, of a sample of AgNPs. The values obtained from the distribution are greater than

expected, both for the plasmonic peak value and for the values obtained by DLS. This is due to the evaporation of the solvent which determining the particle aggregates formation.

Also the dimensions obtained through AFM may or may not agree with those obtained through other techniques, like TEM or DLS, due to the interferences caused by the evaporation of the solvent and by the local concentration of particles, which can create more or less large objects.

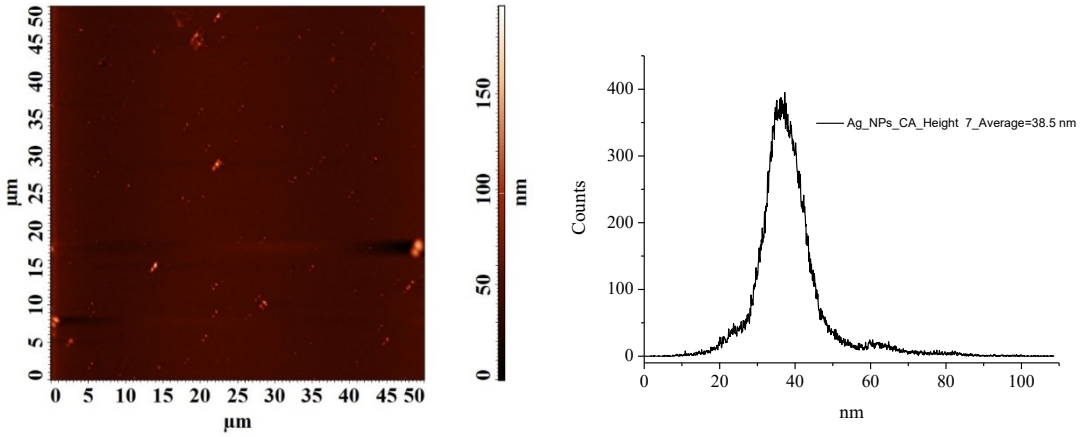

Figure 4.1.7: AFM image of AgNPs@ClPT nanoparticles (right) and, profile of AgNPs@ClPT nanoparticles sizes (left)

Figure 4.1.7 shows the image (left) and the sizes profile (right) obtained through AFM. In the case of AgNPs@ClPT, the values are comparable with those obtained using the DLS technique (***Figure 4.1.8***).

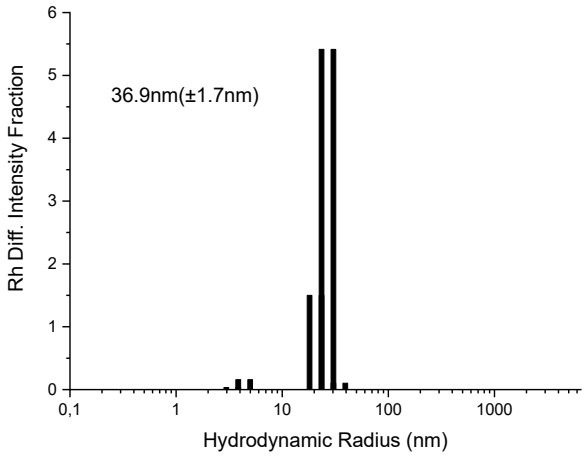

Figure 4.1.8: Sizes distribution of AgNPs@ClPT nanoparticle in acetone solution.

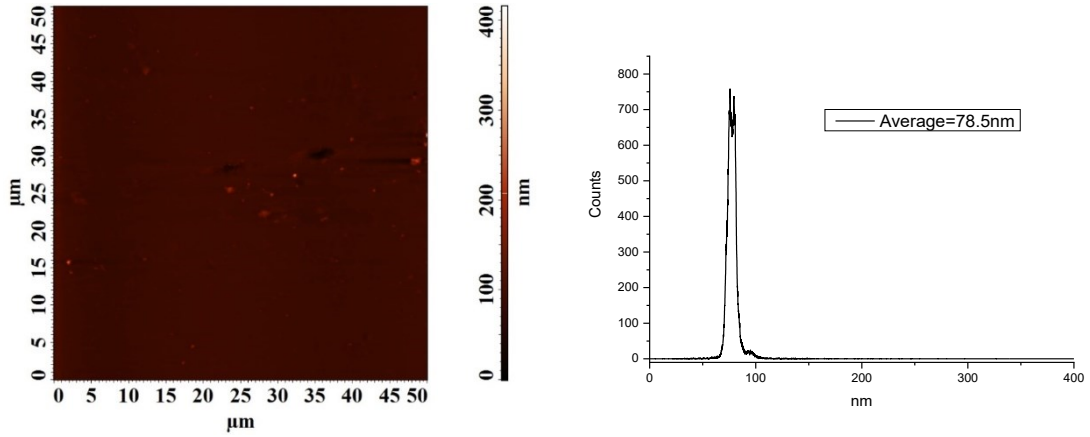

Figure 4.1.9: AFM image of AgNPs@P(PEG750)$_3$ nanoparticles (right) and, profile of the size of the same sample (left).

Figure 4.1.9 shows the image (left) and the sizes profile (right) obtained by AFM technique, respectively, of a sample of AgNPs@ P(PEG750)$_3$. As for the previous one, the dimensions of this sample, obtained from the AFM, are comparable to those obtained by DLS (***Figure 4.1.5***).

The successful functionalization of the nanoparticles with the porphyrin units was verified using three techniques: X-Ray Photoelectron Spectroscopy (XPS), Energy-Dispersive X-Ray Spectroscopy (EDS) and Scanning Transmission Electron Microscopy (STEM). With the XPS technique, which analyzes the core electrons of the individual elements, whether they are isolated or involved in a chemical bond, the kinetic energy value of the electron will be different, allowing to know exactly if the coupling agent or the porphyrin are bounded to nanoparticles.

Through XPS, three samples were analyzed: AgNPs (***Figure 4.1.10***), AgNPs@3CLPT (***Figure 4.1.11***) and AgNPs@P(PEG350)$_3$ (***Figure 4.1.12***).

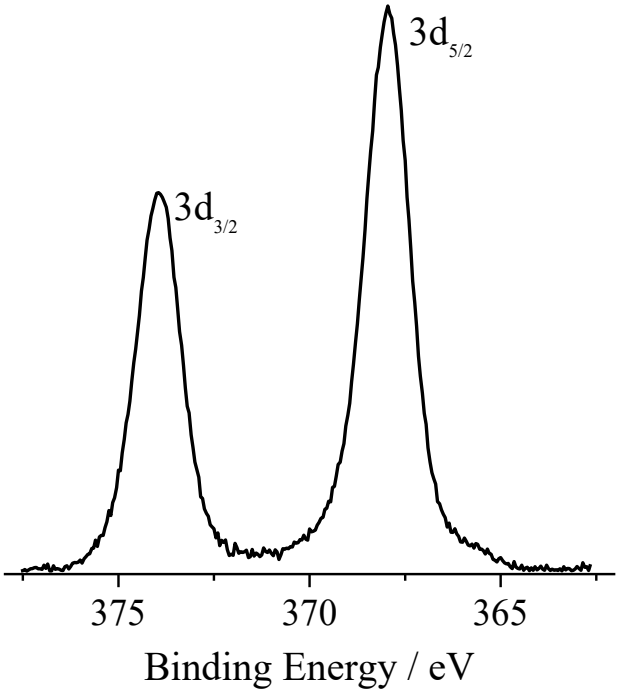

Figure 4.1.10: XPS spectrum of silver nanoparticles. The spectrum shows the presence of the two electrons in the silver 3d orbit with angular momentum (j) of 3/2 and 5/2 respectively.

The XPS spectrum in ***Figure 4.1.10*** focuses the binding energy zone from 365eV to 375eV (within this range, the peaks relative to the two silver electrons fall in the 3d orbitals, respectively with an angular momentum (j) of 3/2 and 5/2). The presence of these two signals indicates the presence of silver in the sample.

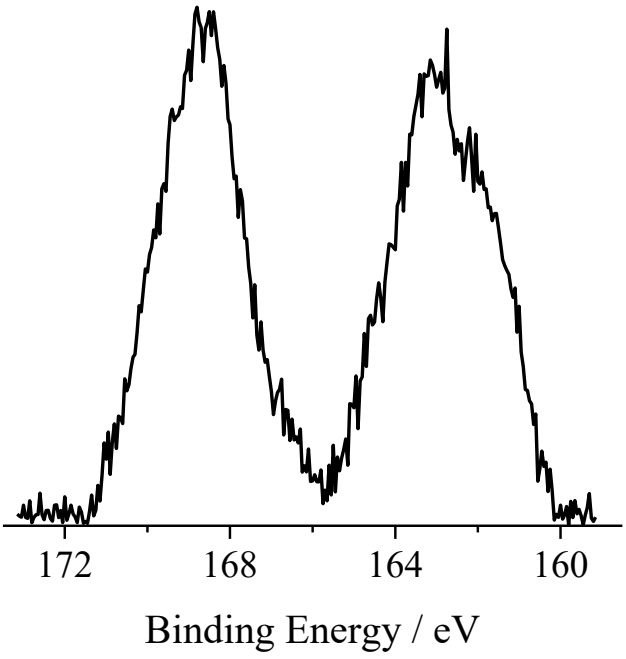

Figure 4.1.11: XPS spectrum of AgNPs@3ClPT. The spectrum shows the zone concerning the sulfur 2p signals.

The spectrum in ***Figure 4.1.11*** shows the binding energy values in the sulfur range. The spectrum is difficult to interpret, because the peak of our interest is in a eV range, from 160 to 164 where, according to the literature, we find both the value of binding energy (162.5eV) of an atom of sulfur bound to gold (but also to silver), and the value of thiol (164eV). Therefore, it is possible to hypothesize that the sample has a large part of thiol linked to the nanoparticle, given that the binding energy value is at the peak maximum, and a small part of free thiol (remained adsorbed on the sample despite the washes). The second peak indicates, according to literature, the presence of sulfates, whose binding values are around 169eV. The presence of sulphates may derive from the glass in which the sample was deposited, or it may be due to oxidation processes of the sulfides (such hypothesis requires further clarification by subsequent experiments).

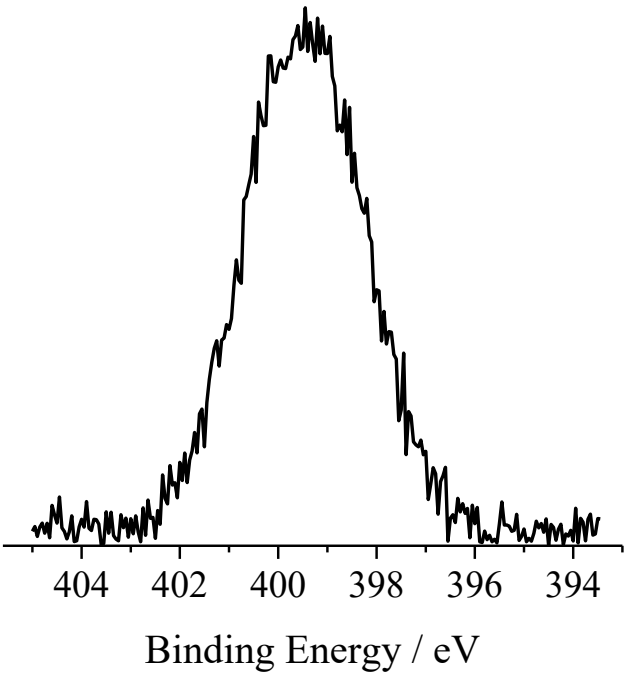

Figure 4.1.12: XPS spectrum of AgNPs@P(PEG350)$_3$. The spectrum range is that of 1s nitrogen.

The XPS spectrum of ***figure 4.1.12*** is related to the nitrogen range. In particular, it is possible to attribute the peak to the pyrrole azotes of the porphyrin, since, according to literature, the binding energy value of a nitrogen bonded to carbon atoms is about 400eV like the one shown in the figure.

A further qualitative analysis of elementary type was made through STEM measurements which indicate the presence of a given element within the sample. ***Figure 4.1.13*** shows the data of regarding AgNPs@P(PEG750)$_3$ sample.

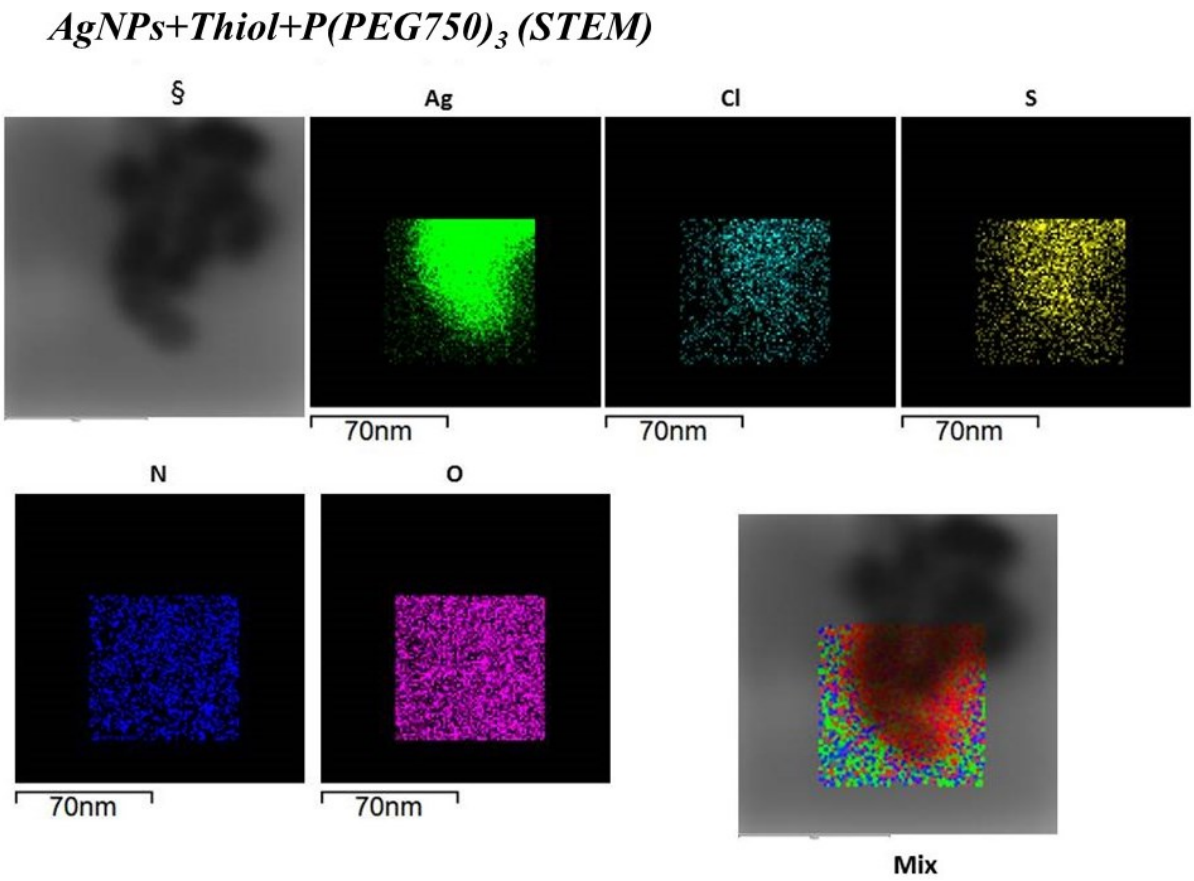

Figure 4.1.13: STEM analysis of AgNPs@P(PEG750)$_3$.

In ***Figure 4.1.13*** we notice the presence of all the elements of our interest within a certain selected area, as shown at the bottom right of the image. It is possible to observe the silver signal, an index of the presence of the nanoparticles, the sulfur and chlorine signals, an index of the presence of thiol linker, and the presence of the nitrogen and oxygen deriving from the porphyrin derivatives P(PEG750)$_3$. To complete the data, the atomic percentage of the individual elements was calculated from the EDS and XPS spectra. The theoretical and experimental atomic percentages of the two techniques for a sample of AgNPs@P(PEG350)$_3$ and AgNPs@P(PEG750)$_3$ are compared in the ***Table 4.1.14*** and ***Table 4.1.15***.

AgNPs+P(PEG350)$_3$	Teoretical	XPS	EDS
C%	74.8	70.7%	29.11%
O%	20.33	21.1	-0.76
N%	3.25	1.9	3.97
S%	0.81		52.31
Cl	0.81	0.2	15.31

Table 4.1.14: Table of atomic percentages for a sample of AgNPs@P(PEG350)$_3$

Also, the ratio between the areas of sulfur and chlorine, obtained with the EDS technique, determines the percentage of 3-chloro-propanethiol functionalized, quantity which amounted to 36.95%.

AgNPs+P(PEG750)$_3$	Teoretical	XPS	EDS
C%	71.8	65.4	83.2
O%	25.13	26.4	0.12
N%	2	0.9	4.42
S%	0.5		10
Cl	0.5	0.2	1.90

Table 4.1.15: Table of atomic percentages for a sample of AgNPs@P(PEG750)$_3$

Also in this case, the ratio between the sulfur and chlorine areas, obtained with the EDS, gives a percentage of 3-chloro-propanethiol functionalized equal to 8.46%. The explanation of this is to be found in the greater steric hindrance of the PEG chains, longer for the P(PEG750)$_3$ compared to the P(PEG350)$_3$.

The same typology of characterizations has been carried out on the samples of gold nanoparticles.

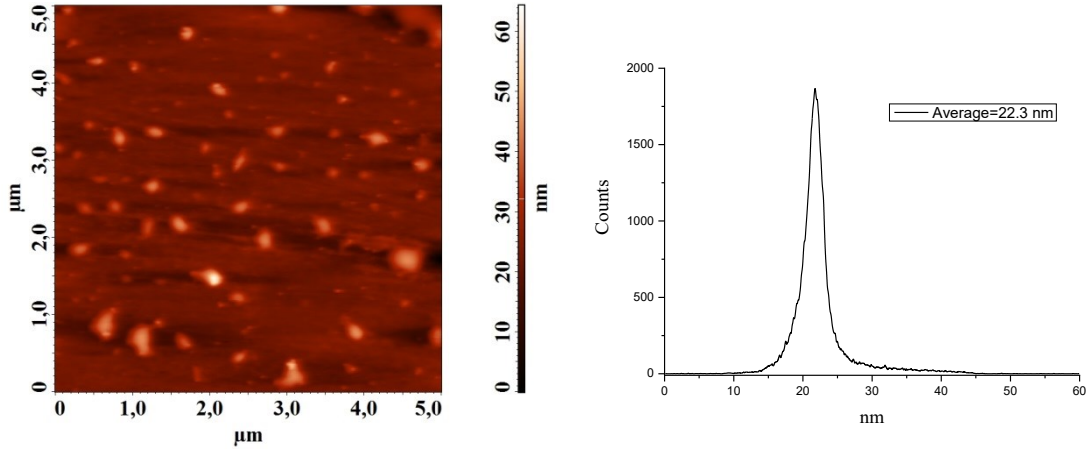

Figure 4.1.16: AFM image of AuNPs (right) and, sizes profile of the same sample (left).

Figure 4.1.16 shows the image (left) and the sizes profile (right) obtained by AFM for the AuNPs sample, respectively. The values shown fit well with those obtained by DLS (***Figure 4.1.17***) and Uv-Vis (***Figure 4.1.17***) as a function of the plasmonic peak value (***Table 4.1.18***).

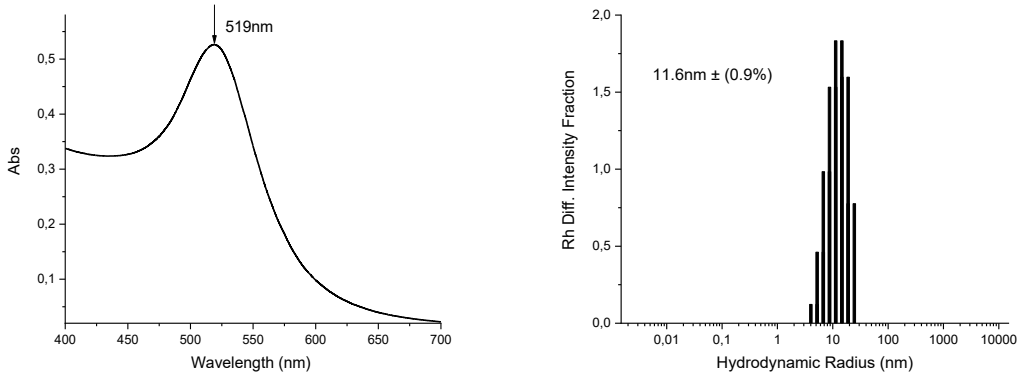

Figure 4.1.17: Uv-Vis spectrum of AuNPs (left) and, size distribution of AuNPs nanoparticles (right).

No.	Mean diameter, *D* (nm)	Color	λ_{max} (nm)				Number of Au atom in a gold nanoparticle
			λ_{ab}	λ_{RRS}	λ_{SOS}	λ_{FDS}	
1	12	Orange–red	520	286	480	310	5.33×10^4
2	19	Red	522	286	480	310	2.12×10^5
3	24	Red	524	286	480	310	4.27×10^5
4	33	Red	528	286	480	310	1.11×10^6
5	41	Red–purple	530	286	480	310	2.13×10^6

Figure 4.1.18: Table correlations color, size and absorption wavelength of AuNPs.

With regard to the plasmon resonance peak values of 400nm, literature data show objects with dimensions of about 12 nm of diameter. Considering the solvation shell, and the wide distribution shown by the analysis to the DLS, we can consider the values of the three techniques that agree with each other.

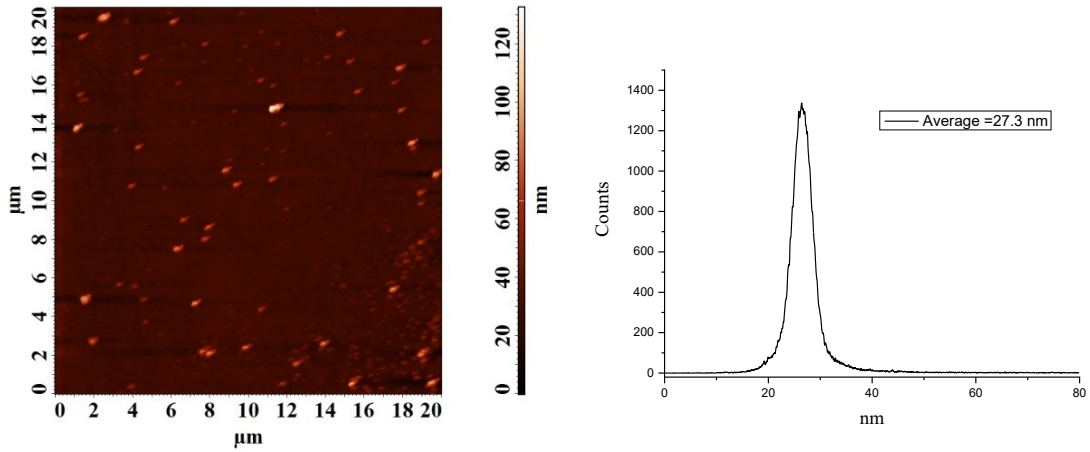

Figure 4.1.19: AFM image of AuNPs@3ClPT (right) and, sizes profile of the same sample (left).

Figure 4.1.19 shows the image (left) and the sizes profile (right) obtained by AFM for the AuNPs@3ClPT sample, respectively. The values shown differ from those obtained by DLS in solution (***Figure 4.1.20***).

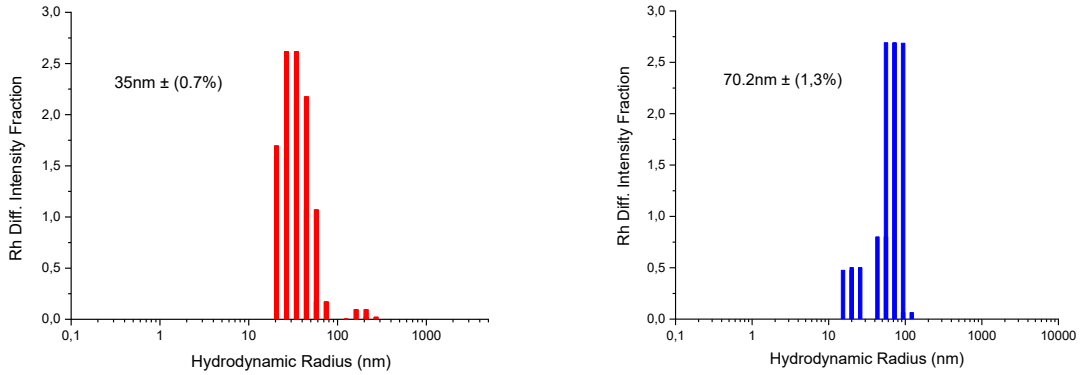

Figure 4.1.20: In red, the size distribution of AuNPs@3ClPT nanoparticle (method 1) in acetone, in blue, the sizes distribution of AuNPs@3ClPT nanoparticle in acetone (method 2).

Figure 4.1.20 shows the two dimensional distributions (method 1 and 2) of the Au@3ClPT nanoparticles. There are some differences in terms of sizes compared to AFM analysis. This can be explained by lipophilic interaction between the nanoparticles in solution and their poor solubility in acetone, which leads to the formation of aggregates.

If we also consider that the DLS technique includes the solvation shell in the measure, we can well explain such large dimensions.

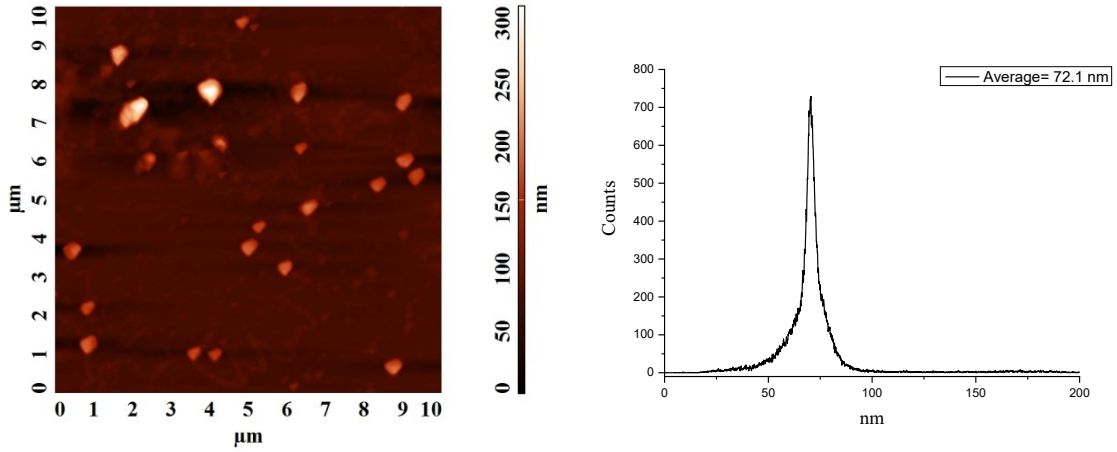

Figure 4.1.21: AFM image of AuNPs@P(PEG350)$_3$ (right) and, sizes profile of the same sample (left).

Figure 4.1.21 shows the image (left) and the sizes profile (right) obtained by AFM for the AuNPs@P(PEG350)$_3$ sample, respectively. The values of the average size deviate from those obtained through DLS (***Figure 4.1.22***), for the reasons discussed above.

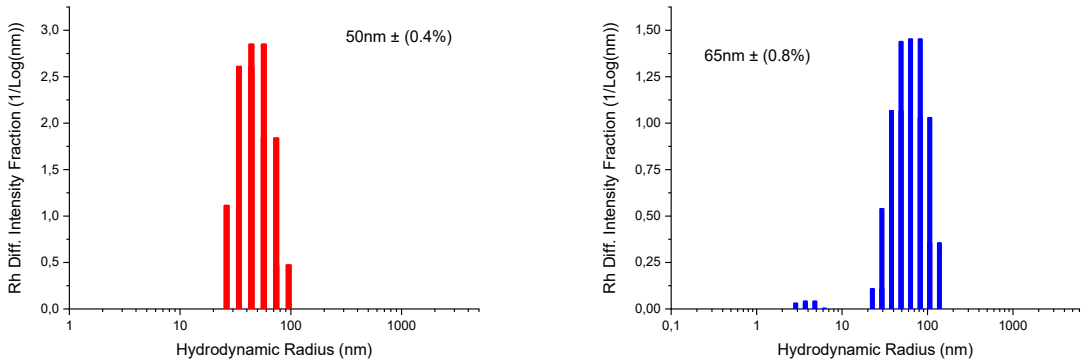

Figure 4.1.22: In red, the size distribution of AuNPs@P(PEG350)$_3$ nanoparticle in acetone. In blue, the size distribution of AuNPs@P(PEG350)$_3$ nanoparticle in water.

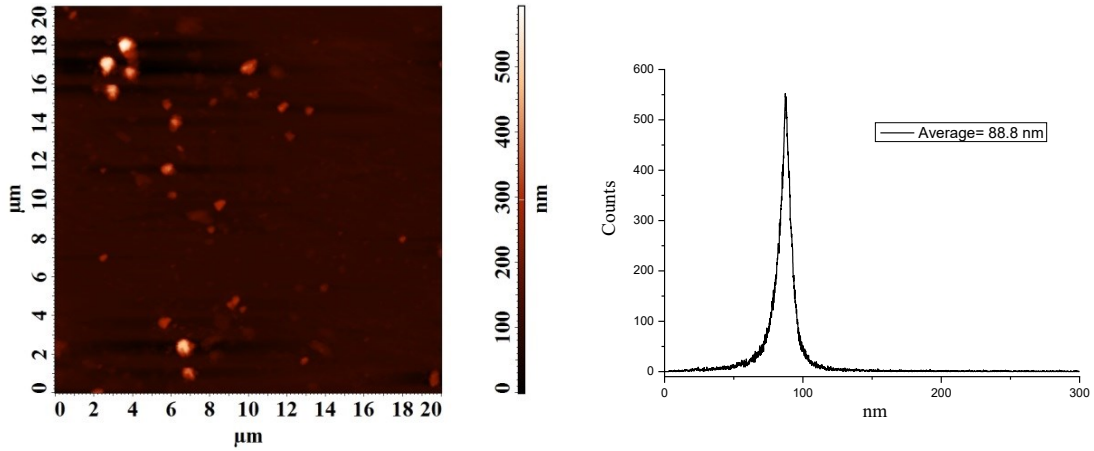

Figure 4.1.23: AFM image of AuNPs@P(PEG750)$_3$ (right) and, size's profile of the same sample (left).

Figure 4.1.23 shows the image (left) and the sizes profile (right) obtained by AFM for the AuNPs@P(PEG750)$_3$ sample, respectively. The values of the average size are comparable with the data obtained through DLS (***Figure 4.1.24***).

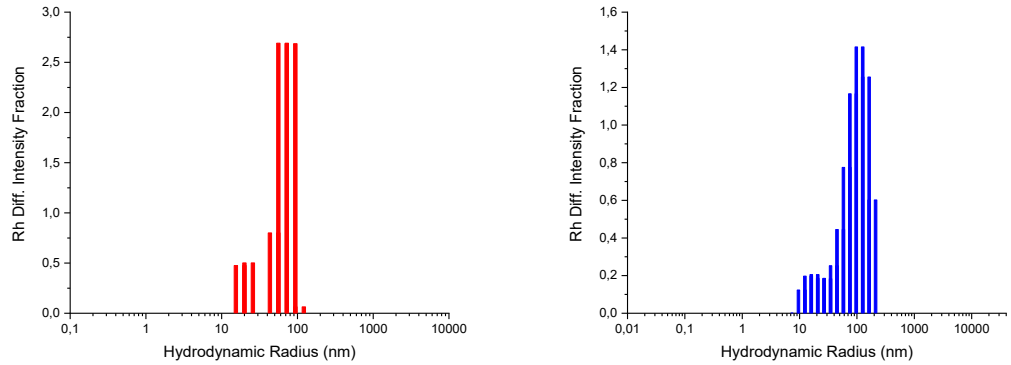

Figure 4.1.24: In red, the size distribution of AuNPs@P(PEG750)$_3$ nanoparticle in acetone, in blue, the sizes distribution of AuNPs@P(PEG750)$_3$ nanoparticle in water

In summary, keeping in mind the considerations made previously, the results obtained through and different techniques are difficult to compare with each other. Observing, however, the trend of the dimensions for each of them, we can notice that there is an increase of these after each functionalization step.

Therefore, it can be assumed that the TEM and AFM images confirm, within the experimental error, the results obtained with the DLS and with those of the UV-Vis.

Also for gold samples, the successful functionalization of the nanoparticles with the porphyrin units was verified using X-Ray Photoelectron Spectroscopy (XPS) (***Figure 4.1.25***), and Scanning Transmission Electron Microscopy (STEM) techniques (***Figure 4.1.26***).

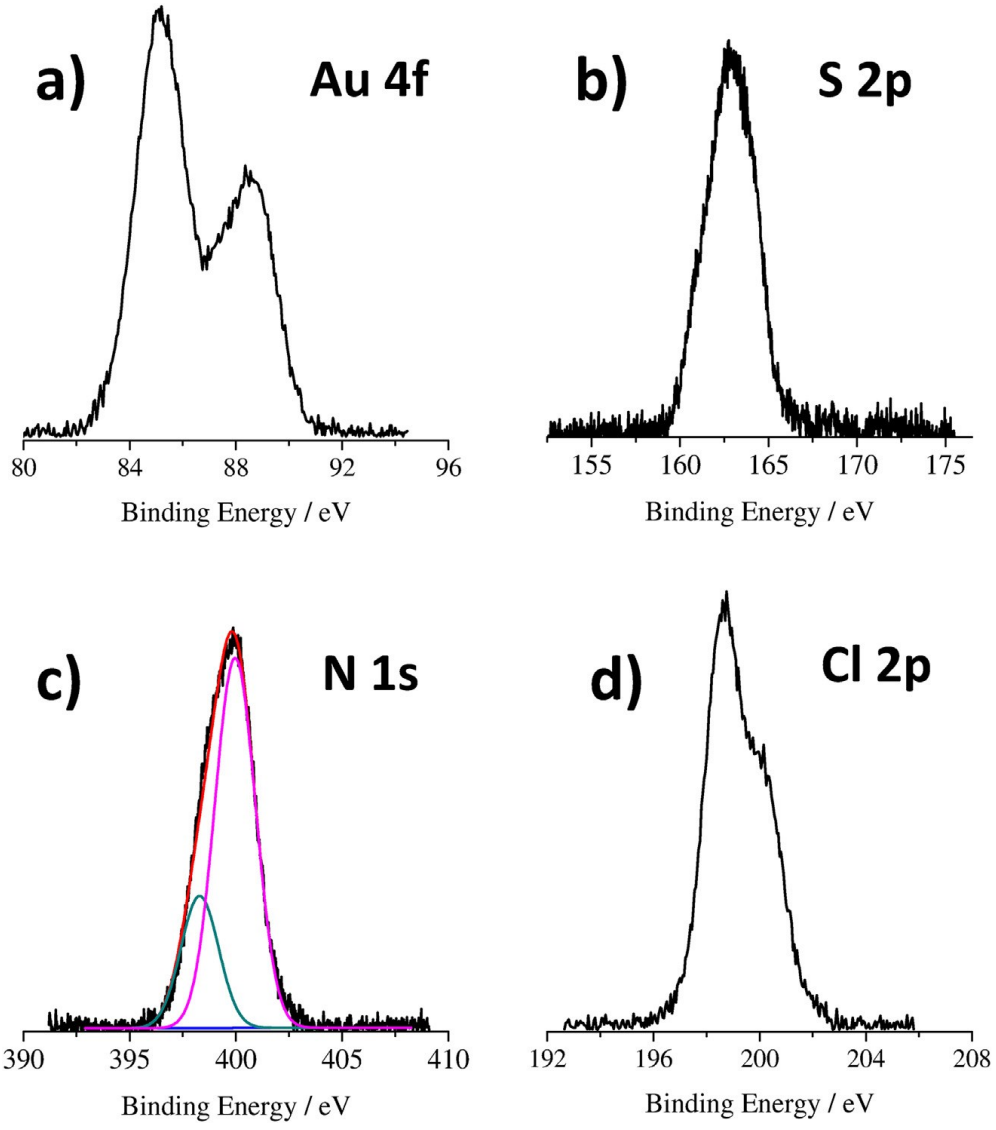

Figure 4.1.25: Al Kα excited XPS of the AuNPs@P(PEG350)$_3$ sample measured in the Au 4f (a), S 2p (b), N 1s c) and Cl 2p (d) binding energy regions, respectively. In the N 1s binding energy region (c), the black line refers to the experimental profile, the dark cyan line refers to the 398.3 eV component, the magenta line refers to the 400.0 eV component, the blue line refers to the background and the red line, superimposed to the experimental profile, refers to the sum of all Gaussian components.

Further experimental evidences, about the $P(PEG350)_3$ binding mode on the functionalized AuNPs surface, were obtained by XPS measurements.[1,2] ***Figure 4.1.25a*** shows the XP spectrum of $AuNP@P(PEG350)_3$ in the Au 4f binding energy (BE) region. The Au $4f_{7/2,5/2}$ spin-orbit components lie at 85.1 and 88.5 eV, respectively.[3, 4, 5]

These values are ~ 0.3 eV larger than those we found for the AuNPs and close to many gold-supported porphyrin systems, thus suggesting a partial oxidation of gold that donates some electron charge to the thiol groups.[4]

Figure 4.1.25b shows the XP spectrum of $AuNP@P(PEG350)_3$ in the S 2p binding energy region. The unique observed peak at 163.0 eV is consistent with the convolution of the S $2p_{3/2},p_{1/2}$ doublet of the thiol group and this value is strongly reminiscent of those already observed for thiolate species bound to the surface of gold.[6 7 8 9 10 11 12 13 14 15 16 17]

No additional peaks have been observed at higher BE thus inferring the absence of any SOx components which, if present, give rise to signals in the 166-170 eV range. Also the peak width at half height of this signal 2.9 eV is in tune with sulfur ligands that bind to gold nanoparticles.

Figure 4.1.25c shows the XP spectrum of $AuNP@P(PEG350)_3$ in the N 1s binding energy region. Only one peak at 400.0 eV is clearly evident with some lower BE asymmetry. The number of N 1s signals in porphyrin-based materials has been the subject of discussion[18 19 20 21 22]. In a few cases, porphyrin molecules exhibit two chemically-inequivalent N 1s core-level signals corresponding to the free iminic (−C=N−), at lower binding energy, and pyrrolic (−CN−), at higher binding energy, nitrogens. In many cases, a broad convolution of these two overlapped signals in the 1:3 intensity ratio has been proposed. This 1:3 intensity ratio seems to be due to the lifting of the D4h symmetry because of the presence of ring substituents or because of the grafting on surfaces.[23] This seems also the case of the present result in which an accurate fitting of the experimental profile indicated the lower intensity component at 398.3 eV, in tune with these previous results.[24 25 26 27 28 29] The possibility of the formation of Au(III)-porphyrin can be ruled out since no XPS evidences of Au(III) was observed. Finally, ***Figure 4.1.25*** shows the XP spectrum of the $AuNPs@P(PEG350)_3$ in the Cl 2p binding energy region. It is worthy of note that the experimental conditions used during these measurements allowed to obtain the two Cl spin-orbit components at 198.7 and 200.0 eV typical of chlorine atoms bound to aliphatic carbons.[30] Atomic concentration analysis performed on this $AuNP@P(PEG350)_3$ system allowed us to carry out some useful data. The 3-chloro-1-propanethiol coupling agent has an identical number of sulfur and chlorine atoms and indeed we observed a Cl/S ratio ¼ 1 in the sulfur functionalized AuNPs. Therefore, after

grafting of the porphyrin molecules, the reduction of this ratio will be indicative of the number of coupling agent molecules that have reacted with the porphyrin molecules. Obviously, the different sizes of these two molecules allows one to forecast just a small deviation of this ratio from unity. In fact, the Cl/S ratio diminished just of the 4% being 0.96. This result suggests that only one out of 25 coupling agent molecules reacts with the porphyrin to get the AuNP@P(PEG350)$_3$ system and this is in total agreement with the calculated sizes of the present coupling agent and porphyrin whose footprints (evaluated with an MM$^+$ method) are 74 and 1830 Å^2, respectively.

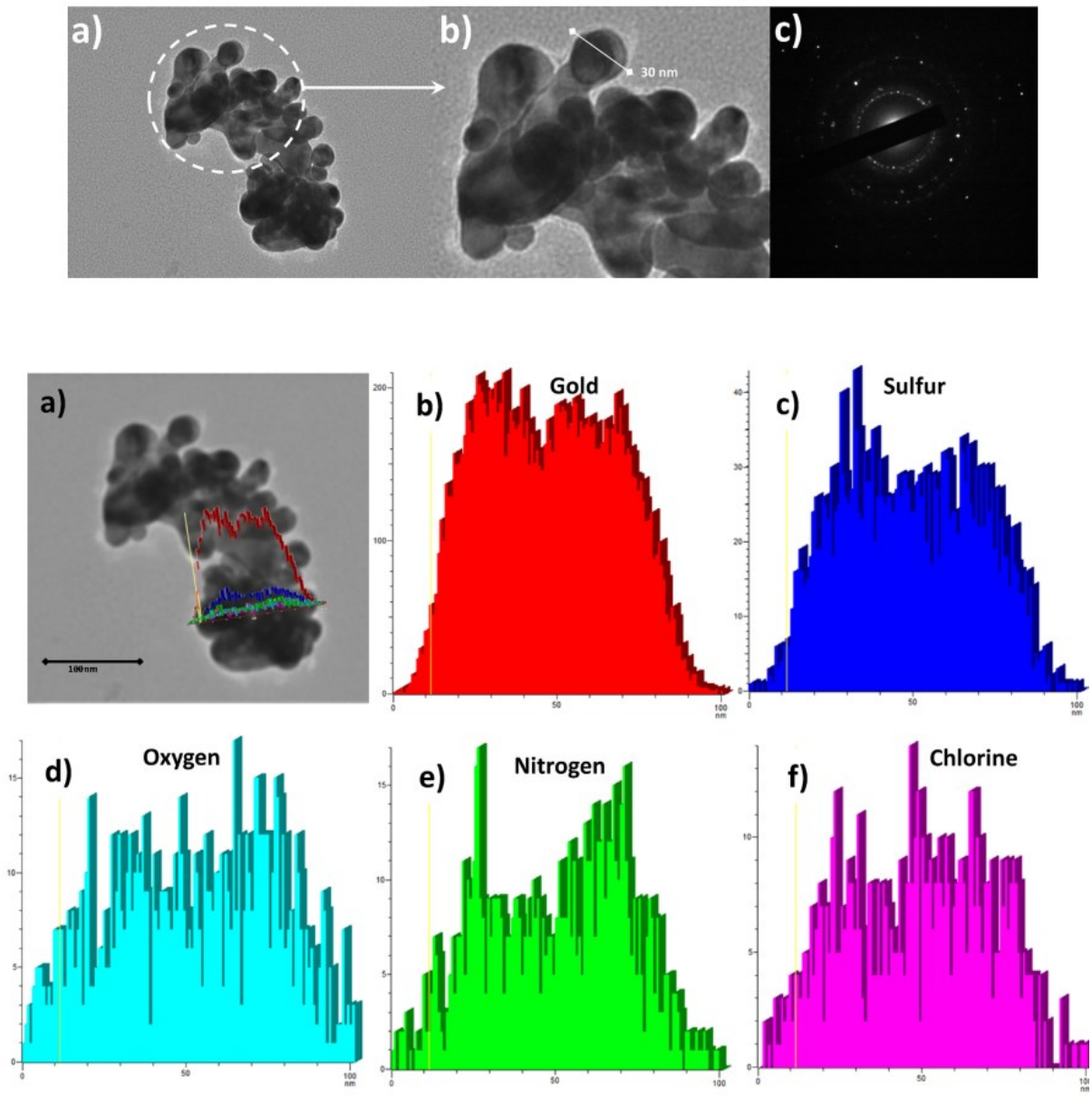

Figure 4.1.26: STEM of AuNP@P(PEG350)$_3$ with linescans displaying total elemental analysis taken at 100 nm scale length (a). Elemental analysis detected by peculiar element emission lines (b-f)

STEM analysis on AuNP@P(PEG350)$_3$, reported in ***Figure 4.1.26,*** shows the sulfur, due to the coupling agent, and also confirms the modification of AuNPs with Porf@PEG, because nitrogen and oxygen signals are also present. Furthermore, the occurrence of the chlorine signal of the ClPT coupling agent suggests the not unexpected, and not complete, AuNP@ClPT chlorine substitution, because of the different sizes of the Porf@PEG and ClPT group.

The percentage of functionalization of gold sample was determined by thermogravimetric analysis in air. The test is based on the evaluation of weight loss of the sample, that can be attributed at organic material which decomposes as the temperature increases (800 ° C).

In particular, the TGA thermogram of AuNP@P(PEG350)$_3$ (***Figure 4.1.27***) indicates a large weight loss, in the range 100-750 °C, of about 70 wt %, attributed to the thermo-oxidation of the linked organic moieties (ClPT and Porf@PEG).

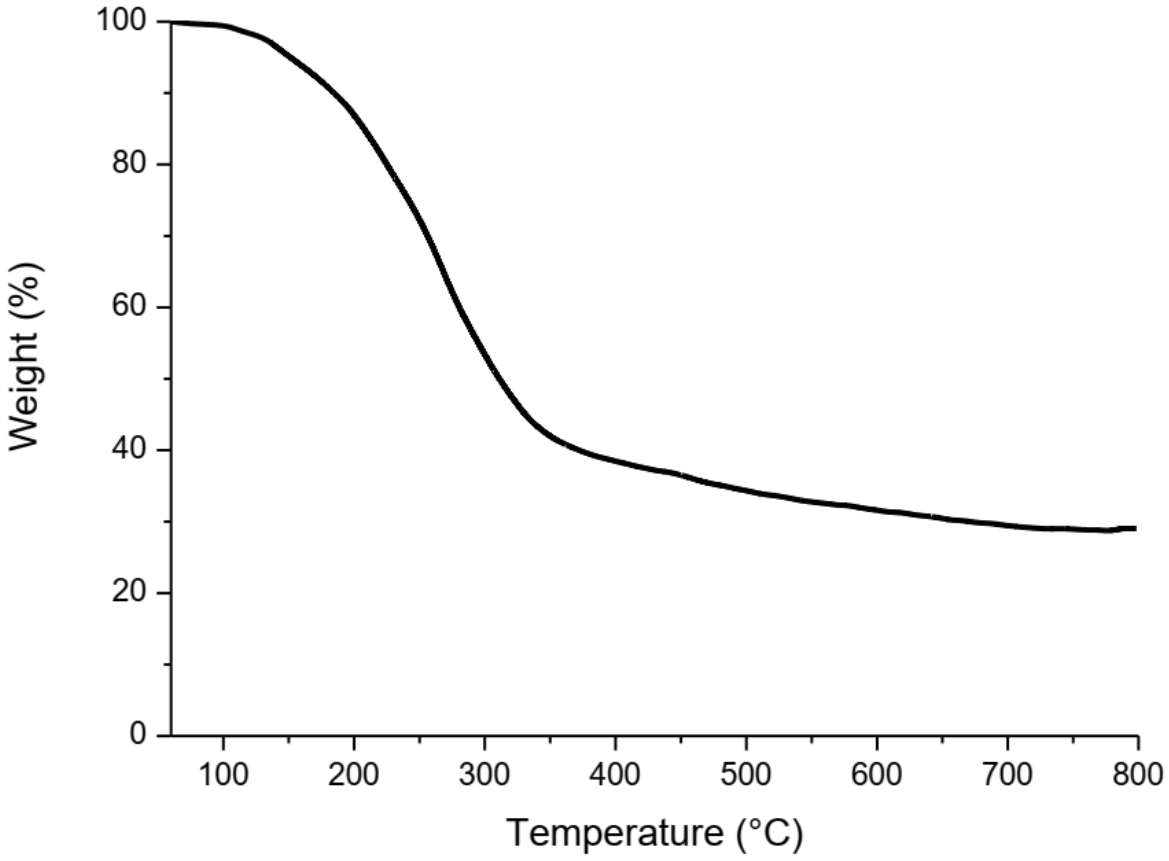

Figure 4.1.27: TGA in air (60 mL/min) of AuNP@P(PEG350)$_3$

Magnetic nanoparticles (MNPs) have demonstrated their potential in a wide variety of biomedical applications, including in tumour hyperthermia. However, highly reactive nature and aggregation affinity of these nanostructures are the main limitations for such applications. To overcome these limitations, those MNPs should be covered with an inert shell in order to protect the magnetic core against chemical alterations. Considering the noble, chemically inert nature of gold, which also has good biocompatibility, we synthetized chemically stable gold-coated Fe_2O_3 (Fe_2O_3@Au) nanoparticles.

The morphology, elemental distribution and the structure of the core-shell nanoparticles were characterized using TEM/STEM and EXD analyses.

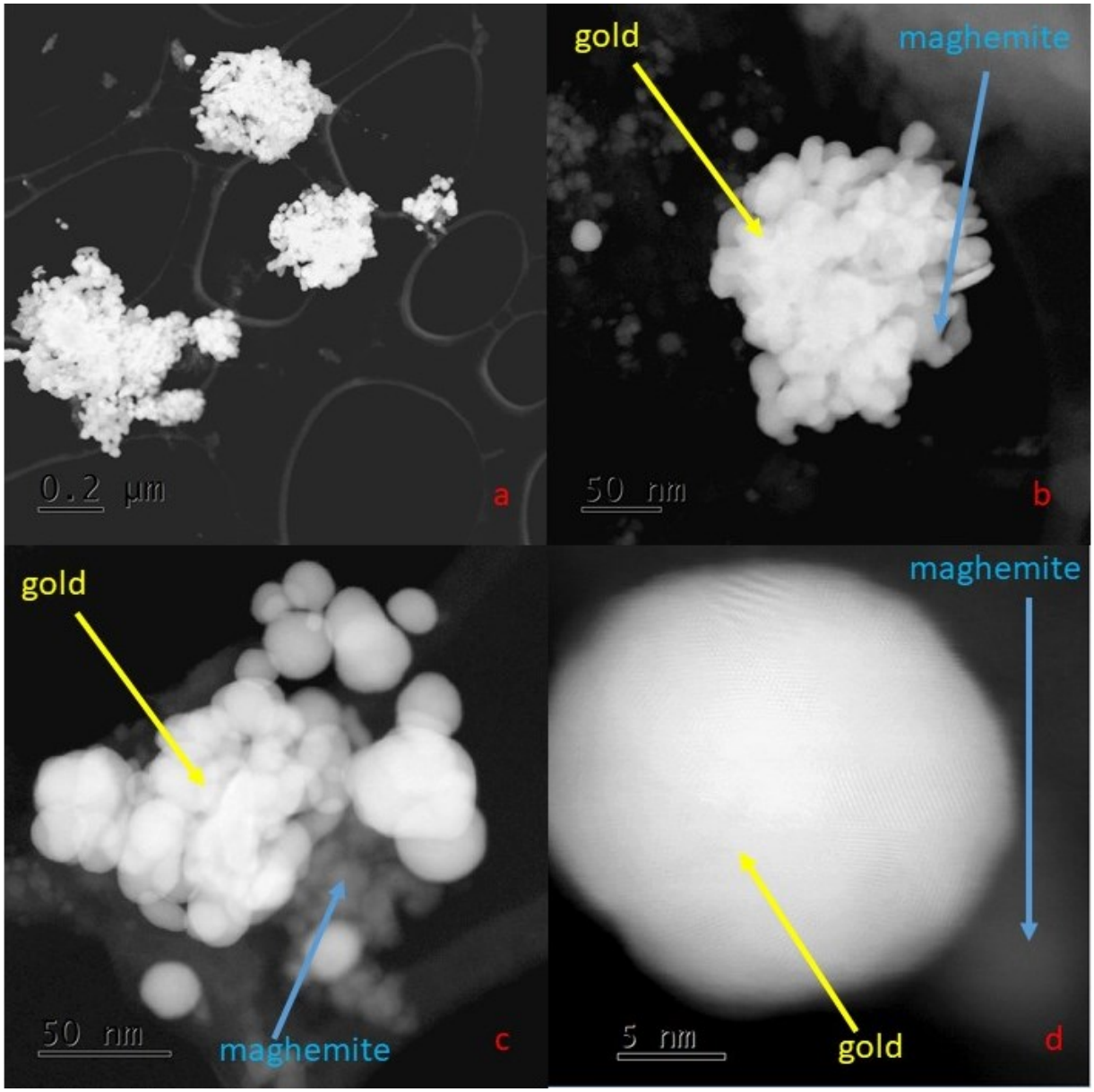

Figure 4.1.28: TEM images of Fe_2O_3@Au@P(PEG350)$_3$ nanoparticles. Brightest areas represent gold (yellow arrows), while darker areas represent maghemite (blue arrows)

Figure 4.1.28 shows the TEM images of the Fe_2O_3@Au@P(PEG350)$_3$ nanoparticles and deposed from a suspension in alcohol solution. We can clearly see the presence of particle aggregates with dimensions that also reach 200nm. These data fit well with the wide distribution obtained by the DLS analysis. The individual systems, however, have dimensions ranging from 20 to 30nm, as can be seen from the enlargement in ***Figure 4.1.28d***. From the TEM images it is possible to clearly observe the presence of gold (light areas) and maghemite (dark areas). These have been confirmed by the EELS (electron energy loss spectroscopy) and ERD analyzes reported in ***Figure 4.1.29***.

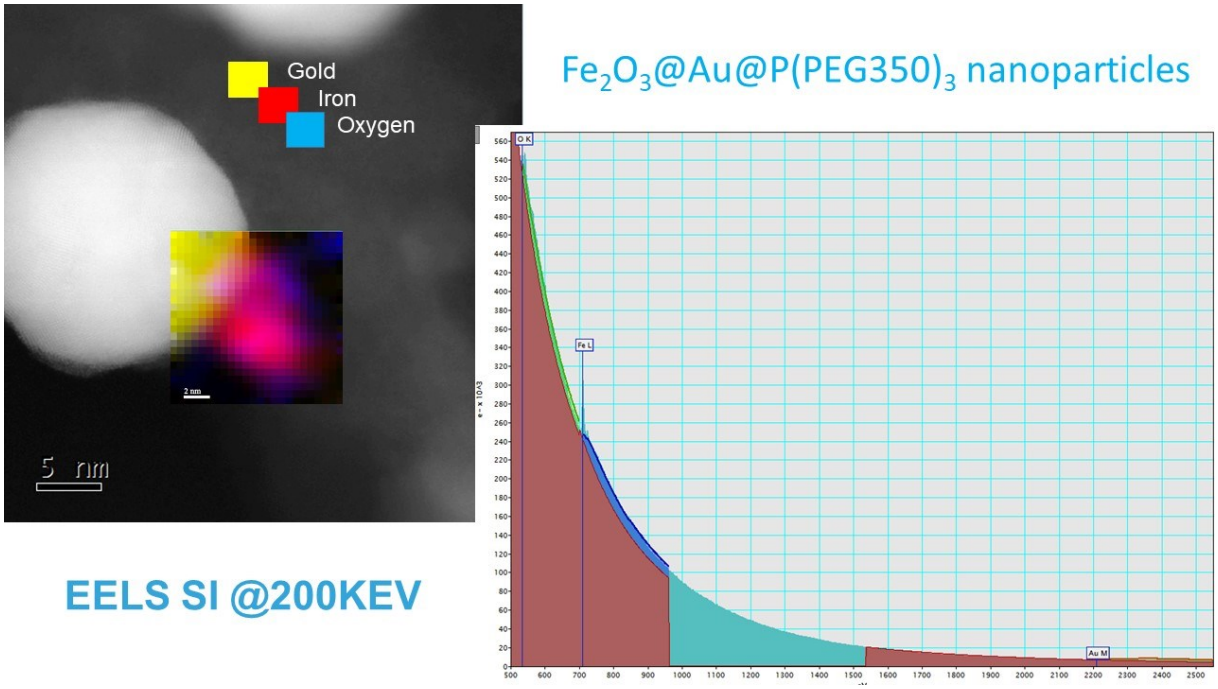

Figure 4.1.29: EELS analysis of Fe_2O_3@Au@P(PEG350)$_3$ nanoparticles.

Figure 4.1.29 shows the EELS analysis carried out on a sample of nanoparticles of Fe_2O_3@Au@P(PEG350)$_3$. The analysis shows the presence of elements such as gold, iron and oxygen obtained from a restricted area of the sample. This confirms the presence of magnetite and the gold shell.

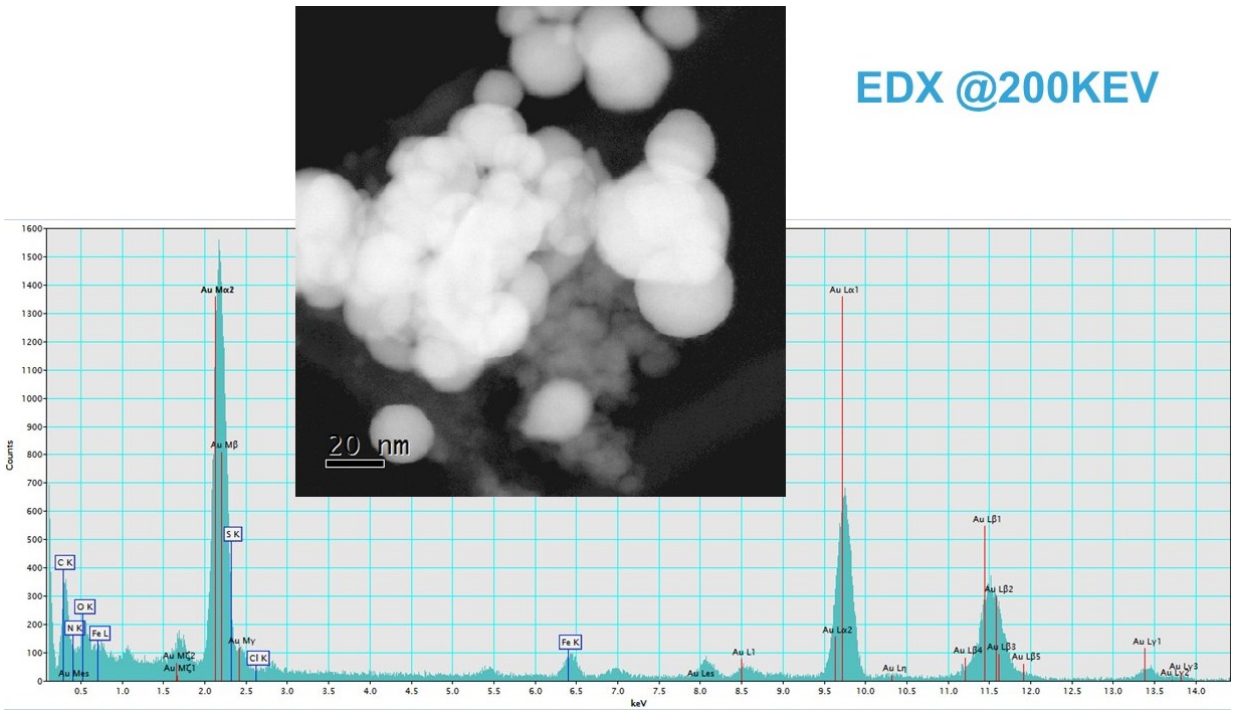

Figure 4.1.30: EDX analysis of Fe_2O_3@Au@P(PEG350)$_3$ nanoparticles.

Figure 4.1.30 shows the EDX analysis performed on a sample of nanoparticles of Fe_2O_3@ Au@P(PEG350)$_3$. The analysis shows the presence of elements such as gold, iron and oxygen, nitrogen, sulfur and chlorine obtained from a narrow area of the sample shown as an insert in the figure. The presence of these elements confirms not only the presence of maghemite and the gold shell, but also the presence of the thioled linker (sulfur and chlorine) and porphyrin (nitrogen).

In summary, it is possible to conclude that the functionalization of the nanoparticles of Fe_2O_3 @Au with the P(PEG350)$_3$ has been successful.

[1] Gulino A. Anal BioanalChem 2013, 405(5), 1479-95.
[2] Briggs, D.; Grant, J.T. Chichester, West Sussex, U.K: IM Publications; 2003
[3] Ohyama, J.; Hitomi, Y.; Higuchi, Y.; Tanaka, T. Top Catal 2009, 52(6-7), 852-9
[4] Kanehara, M.; Takahashi, H.; Teranishi, T. Angew Chem Int Ed 2008, 47(2), 307-10
[5] Penon. O.; Patino, T.; Barrios, L.; Nogues, C.; Amabilino, D. B.; Wurst, K. et al. Chemistryopen 2015, 4(2),127-36
[6] Battocchio, C.; Porcaro, F.; Mukherjee, S.; Magnano, E.; Nappini, S.; Fratoddi, I et al. J Phys Chem C 2014, 118(15), 8159-68
[7] Laibinis, P. E.; Whitesides, G. M.; Allara, D. L.; Tao, Y. T.; Parikh, A. N.; Nuzzo, R. G. J Am Chem Soc 1991, 113(19), 7152-67.
[8] Lu, H. B.; Campbell, C. T.; Castner, D. G.; Langmuir 2000, 16(4), 1711-8.
[9] Zhang, S.; Leem, G.; Lee, T. R. Langmuir 2009, 25(24),13855-60.
[10] Zhou, J. F.; Beattie, D. A.; Sedev, R.; Ralston, J. Langmuir 2007, 23(18), 9170-7
[11] Srisombat, L. O.; Park, J. S.; Zhang, S.; Lee, T. R. Langmuir 2008, 24(15), 7750-4
[12] Wenzler, L. A.; Moyes, G. L.; Raikar, G. N.; Hansen, R. L.; Harris, J. M.; Beebe, T. P. et al. Langmuir 1997, 13(14), 3761-8.
[13] Schoenfisch, M. H.; Pemberton, J. E. J Am Chem Soc 1998, 120(18), 4502-13
[14] Kariuki, N. N.; Luo, J.; Hassan, S. A.; Lim, I. I. S.; Wang, L. Y.; Zhong, C. J. Chem Mater 2006, 18(1), 123-32
[15] Badia, A.; Demers, L.; Dickinson, L.; Morin, F. G.; Lennox, R. B.; Reven, L. J Am Chem Soc 1997, 119(45),11104-5.
[16] Badia, A.; Cuccia, L.; Demers, L.; Morin, F.; Lennox, R. B. J Am Chem Soc 1997, 119(11), 2682-92
[17] Azcarate, J. C.; Addato, M. A. F.; Rubert, A.; Corthey, G.; Moreno, G. S. K.; Benitez, G. et al. Langmuir 2014, 30(7), 1820-6.
[18] Zhang, Z. J.; Hu, R. S.;Liu, Z. F. Langmuir 2000, 16(3), 1158-62
[19] Sarno, D. M.; Matienzo, L. J.; Jones, W. E. Inorg Chem 2001, 40(24), 6308-15
[20] Offord, D. A.; Sachs, S. B.; Ennis, M. S.; Eberspacher, T. A.; Griffin, J. H.; Chidsey, C. E. D et al J Am Chem Soc 1998, 120(18), 4478-87
[21] Yamashige, H.; Matsuo, S.; Kurisaki, T.; Perera, R. C. C.; Wakita, H. Anal Sci 2005, 21(6), 635-9
[22] Chen, M.; Feng, X. F.; Zhang, L.; Ju, H. X.; Xu, Q.; Zhu, J. F. et al. J Phys Chem C 2010, 114(21) ,9908-16
[23] Gulino, A.; Mineo, P.; Bazzano, S.; Vitalini, D.; Fragala, I. Chem Mater 2005, 17(16), 4043-5
[24] Gulino, A.; Bazzano, S.; Mineo, P.; Scamporrino, E.; Vitalini, D.; Fragala, I Chem Mater 2005, 17(3), 521-6
[25] Gulino, A.; Mineo, P.; Fragala, I. NO(2) Inorg Chim Acta 2008, 361(14-15), 3877-81
[26] Gulino, A.; Mineo, P.; Fragala, I. J Phys Chem C 2007, 111(3), 1373-7
[27] Gulino, A.; Lupo, F.; Condorelli, G. G.; Mineo, P.; Fragala, I. Chem Mater 2007, 19(21), 5102-9.
[28] Gulino, A.; Mineo P.; Scamporrino E.; Vitalini, D.; Fragala, I Chem Mater 2006, 18(9), 2404-10
[29] Gulino, A.; Mineo, P.; Scamporrino, E.; Vitalini, D.; Fragala, I. Chem Mater 2004, 16(10), 1838-40
[30] Briggs, D.; Grant, J. T.; Chichester, West Sussex, U.K: IM Publications; 2003.

Theranostic Applications of the obtained hybrid nano-systems

Potential teranostic applications have been tested on two core@shell gold systems. In particular, the AuNPs@P(PEG350)$_3$ system was tested as a potential photosensitizing agent and, moreover, preliminary cell studies were performed.

The second system, AuNPs@P(PEG750)$_3$, has been tested as a pH sensor for unusual environments.

Focusing on P(PEG350)$_3$, as far as the photophysical properties are concerned, time-resolved fluorescence was measured. ***Figure 4.2.1*** shows the fluorescence decay and related fitting, according to the equation shown below (1), for P(PEG350)$_3$ and AuNPs@P(PEG350)$_3$. The fluorescence lifetime of P(PEG350)$_3$ is 8.8 ns, in agreement with the value reported for the analogous four-PEG-branched porphyrin,[1] and with the typical values of metal-free porphyrins.[2 3]

$$I(t) = I_0 \sum_i A_i \, exp^{\left(-t/\tau_i\right)} \qquad (1)$$

The functionalization with AuNPs causes some fluorescence quenching and the decreasing of the porphyrin excited state lifetime with the appearance of two shorter lifetimes (0.2 ns and 5.9 ns with energy contributions of 28 and 72%, respectively) (***Figure 4.2.1***). Such phenomenon can be attributed to energy or electron transfer from the porphyrin excited singlet state to the gold nanoparticles, as previously observed in other porphyrin/gold systems.[4]

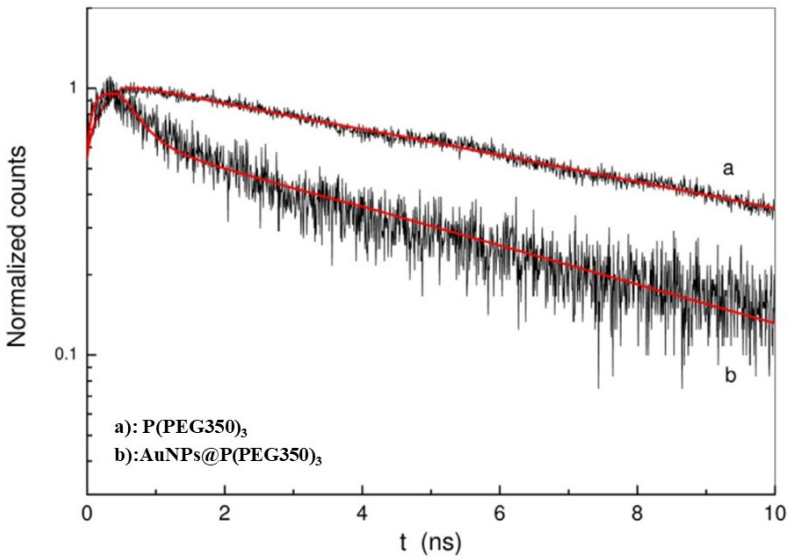

Figure 4.2.1: Fluorescence decay at 660 nm for $P(PEG350)_3$ (curve a) and $AuNPs@P(PEG350)_3$ (curve b). The continuous lines are the curve fits with equation (1).

The $AuNPs@P(PEG350)_3$ was tested as a potential photosensitizer agent, thus verifying the $^1O_2$ formation under irradiation.

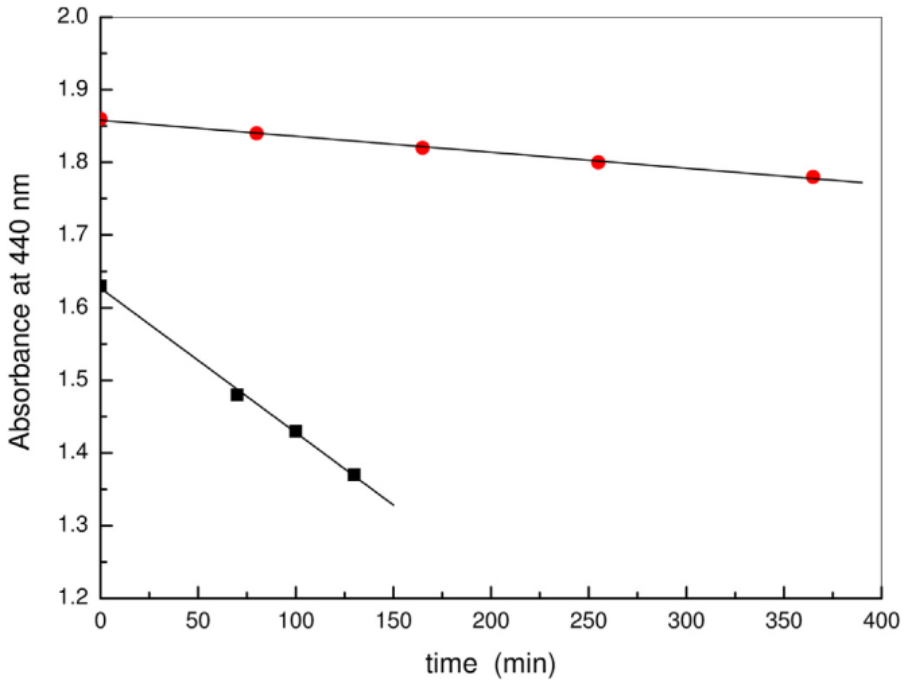

Figure 4.2.2: Change of the absorbance value at 440 nm as a function of irradiation time in the presence of TPPS as standard (squares) or AuNP@Porf@PEG (circles) in aqueous solution. The lines are the linear fit results

Figure 4.2.2 shows the decrease in the RNO absorbance at 440 nm as a function of the irradiation time for AuNPs@P(PEG350)$_3$, or for the 5,10,15,20-tetrakis(4-sulfonatophenyl) porphyrin (TPPS) chosen as a reference. The experimental data were fitted with equation (1) and Φ = 0.22 ± 0.05 was obtained for AuNPs@P(PEG350)$_3$.

$$\phi = \phi_{TPPS} \frac{OD^{TPPS}}{OD^{AuNPs@Porf@PEG}} \frac{\Delta A}{\Delta A^{TPPS}} \qquad (1)$$

In a previous work of my research group[5], it has been measured the singlet oxygen quantum yield (Φ) of a tetra PEGylate porphyrin (similar to the present P(Peg350)$_3$ system) as 0.33 ± 0.05. The observed lower value is due to the different environment experienced by neighboring porphyrins bound to the AuNPs surface with respect to the free porphyrins.[6 7]

Finally, preliminary cellular studies by confocal microscopy were aimed to assess the actual uptake of the AuNPs@P(PEG350)$_3$ nanosystems by the cells, as well as to verify, also in the complex intracellular environment, the maintenance of the emission properties of the porphyrin-functionalized nanoparticles, which are relevant for their performances as photosensitizer

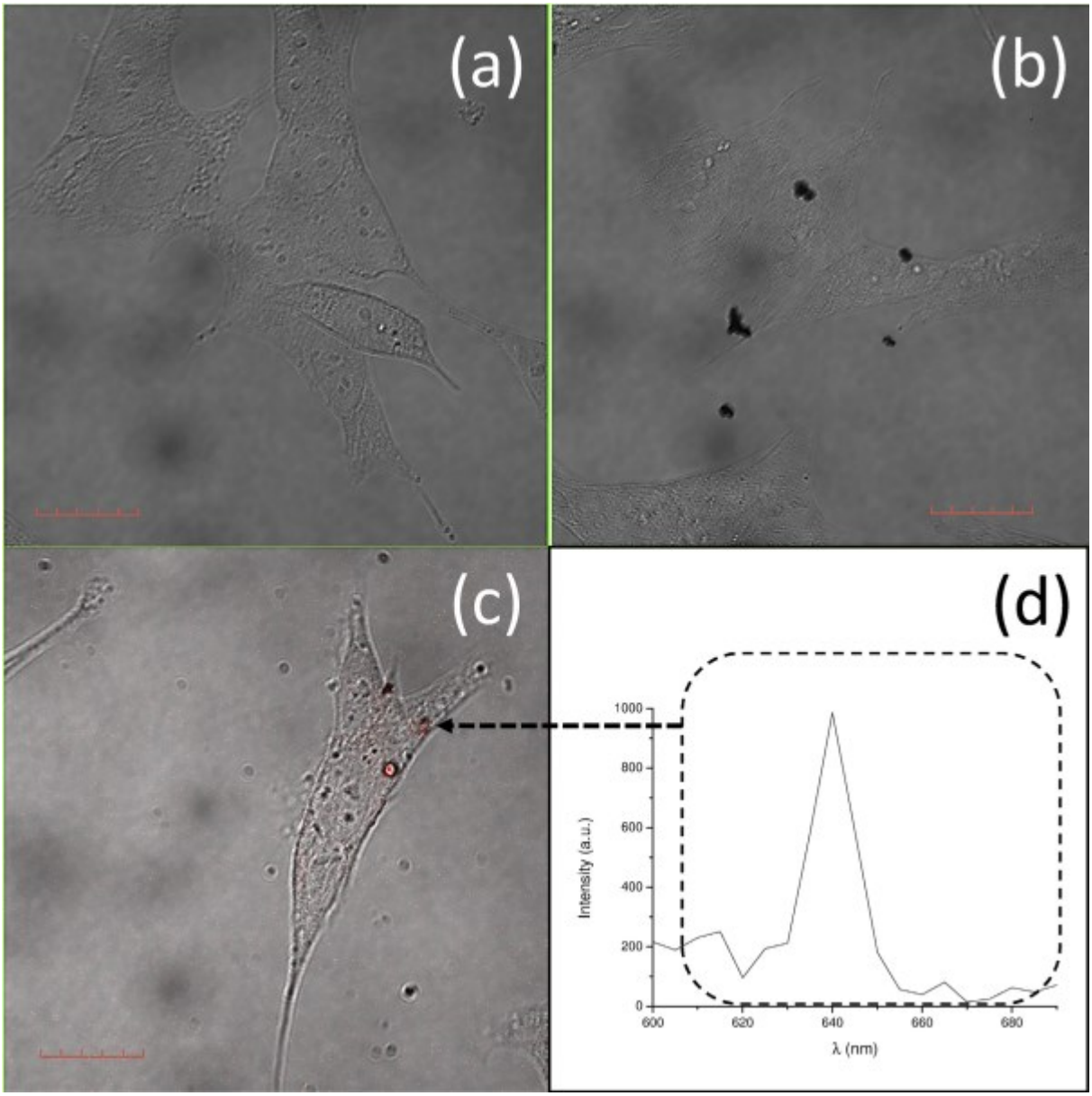

Figure 4.2.3: LSM results of the interaction of AuNPs with SH-SY5Y cells. In a-c: merged fluorescence (in red, $\lambda_{excitation/emission}$ = 543/550-700 nm) and bright field optical micrographs of cells untreated (a) and treated for 2h of incubation time with bare AuNPs (b) or AuNPs@P(PEG350)$_3$ (c). Scale bar = 20 μm. In (d): the fluorescence spectrum collected on the red ROI in panel (c) evidenced by the arrow.

Figure 4.2.3 shows the representative LSM images of human neuroblastoma SH-SY5Y cells, treated with bare AuNPs (***Figure 4.2.3b***) or AuNPs@P(PEG350)$_3$ (***Figure 4.2.3c***), in comparison to untreated cells (***Figure 4.2.3a***). The uptake of AuNP is clearly visible by the presence of dark spots corresponding to nanoparticle aggregates within the cells. Similar intracellular dark features are found in the cells treated with AuNPs@P(PEG350)$_3$, which also display a red fluorescence co-localized with such aggregates. The spectra recorded in correspondence of these regions confirm the porphyrin-related emission (***Figure 4.2.3d***). The

observed shift, of about 10 nm, in comparison to the emission spectra recorded in aqueous solution, can be explained as due to the different solvent environment.

The measurement of pH in diseased tissues has shown that the microenvironment in tumors is generally more acidic than in normal tissues. Major mechanisms which lead to tumor acidity probably include the production of lactic acid and hydrolysis of ATP in hypoxic regions of tumors. For information on this aspect, which binds the acidity of pH and the birth/growth of a tumor tissue, the AuNPs@P(PEG750)$_3$ system has also been studied as a pH sensor, both in organic solvent and in aqueous solution.

As previously described, the AuNPs@P(PEG750)$_3$ system has been characterized through UV-vis absorption, fluorescence spectroscopies and TEM/STEM analyses of the purified particles, to confirm the correct functionalization.

To make a comparison, Uv–Vis and fluorescence measurements were also performed on an aqueous solution of a very similar chemical derivative, the 5,10,15,20-(p-[ω- methoxy-poly(oxyethylene)]phenyl)porphyrin (P). The UV–vis spectrum of AuNPs@P(PEG750)$_3$ (***Figure 4.2.4***) showed a sharp Soret band (black solid line) at about 424 nm, with a red-shift of about 4 nm with respect to the unlinked diluted solution of P (blue solid line), and a bump signal in the 500–800 nm region of the gold nanoparticles plasmon that overlap the porphyrin's Q-bands. A very similar typical emission at about 654 nm was observed in the fluorescence spectra of both AuNPs@P(PEG750)$_3$ (black dashedline) and P (dashed blue line), by excitation of the porphyrin derivatives at 424 nm.

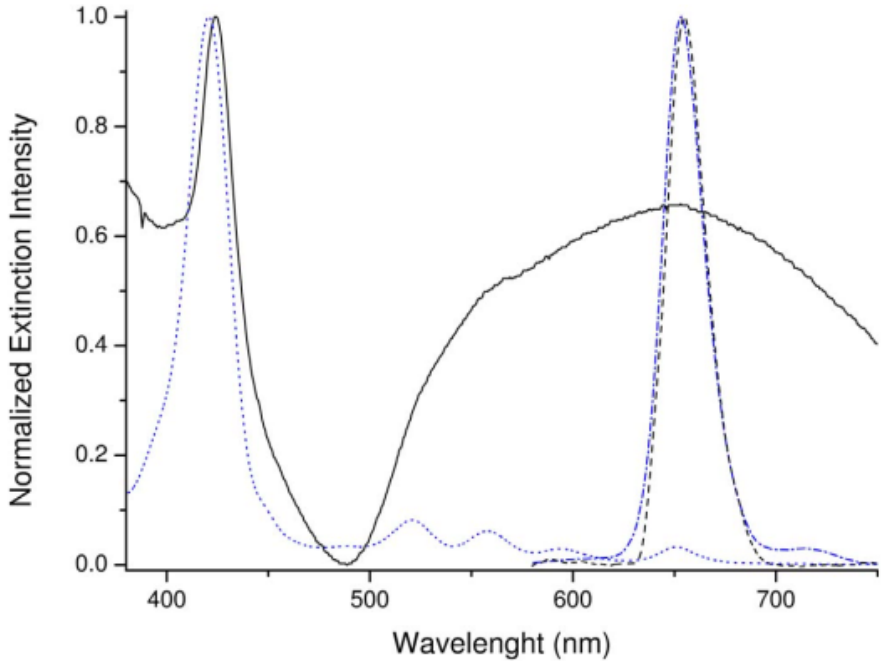

Figure 4.2.4: Normalized Uv–Vis spectra of an aqueous solution of AuNPs@P(PEG750)$_3$ (solid black line) and P (dotted blue line). Also reported the normalized fluorescence spectra of AuNPs@P(PEG750)$_3$ (dashed black line) and P (dotted-dashed blue line) in aqueous solution.

The TEM image of AuNPs@P(PEG750)$_3$ (***Fig. 4.2.5a***) showed a cluster, formed probably by nanoparticles aggregation occurring during the sample drying before the analysis. However, in the aggregate, it is possible to distinguish single nanoparticles with an average size of about 30 nm (***Fig. 4.2.5b***). Moreover, the integrity of the structural/reticular properties of the gold nanoparticles was qualitatively confirmed by the presence of corresponding diffraction pattern (***Fig. 4.2.5c***).

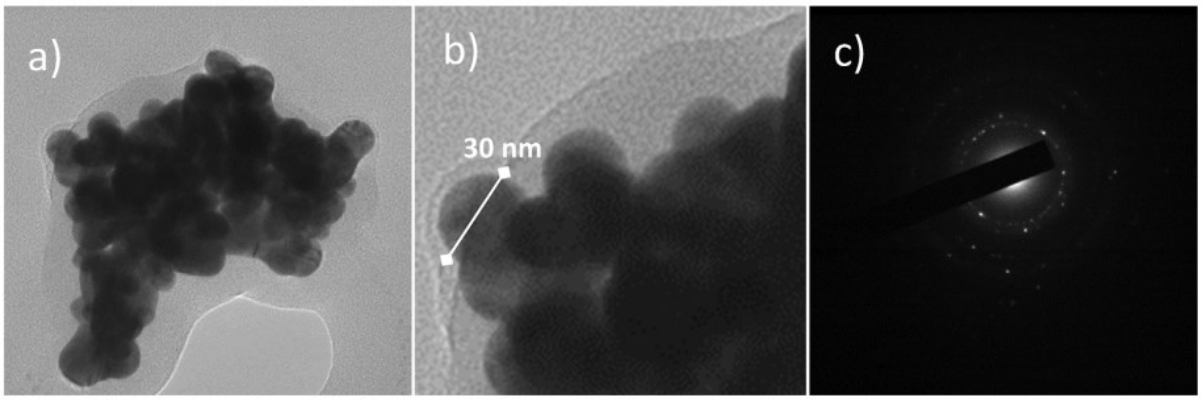

Figure 4.2.5: TEM images of: (a) AuNPs@P(PEG750)$_3$, (b) its magnification and (c) the respective diffraction pattern.

The functionalization of the AuNPs@P(PEG750)$_3$ was also probed by STEM analysis with linescans displaying total elemental analysis taken at 40 nm scale length (***Fig. 4.2.6a***). The emerging of the expected signals of the nitrogen and oxygen due to the PEGylate porphyrin moiety, apart from those of the sulfur and chlorine of the 3-chloro-1-propanethiol spacer and the ubiquitary carbon, allowed us to diagnose the occurred conjugation (Fig. ***Fig. 4.2.6b–g***).

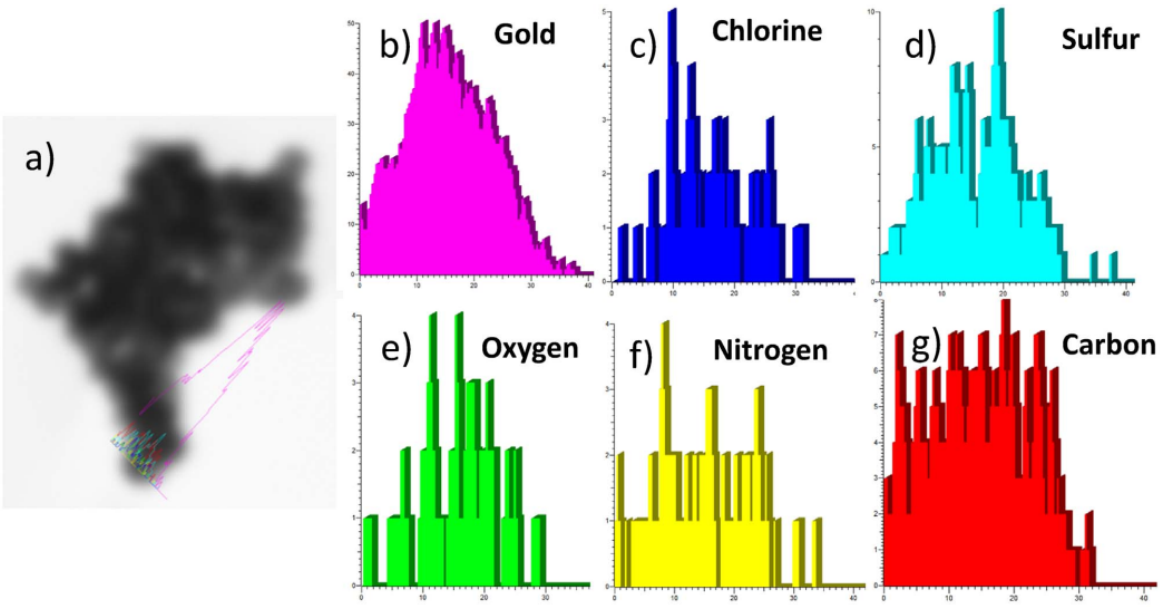

Figure 4.2.6: (a) STEM of AuNPs@P(PEG750)$_3$ with linescans displaying total elemental analysis taken at 40 nm scale length. (b–g) Elemental analysis detected by the peculiar element emission lines.

To verify the AuNPs@P(PEG750)$_3$ capability as a pH sensor, the titration of an aqueous solution containing these nanoparticles was performed monitoring the variation of both the absorption band intensity at 424 nm and that of the emission at 654 nm (exciting at 424 nm). The fluorescence emission spectroscopy was here adopted for its high sensibility and the strong signal variation (decreasing upon treatment with acids) observed along the titration. Examining the results of the Uv–Vis titration, because of the background changes after each acid addition (due to the scattering), a baseline correction procedure was applied. The change of the UV–vis absorbance spectrum of the solution containing the nanoparticles at the different pH values appears in ***Fig. 4.2.7***.

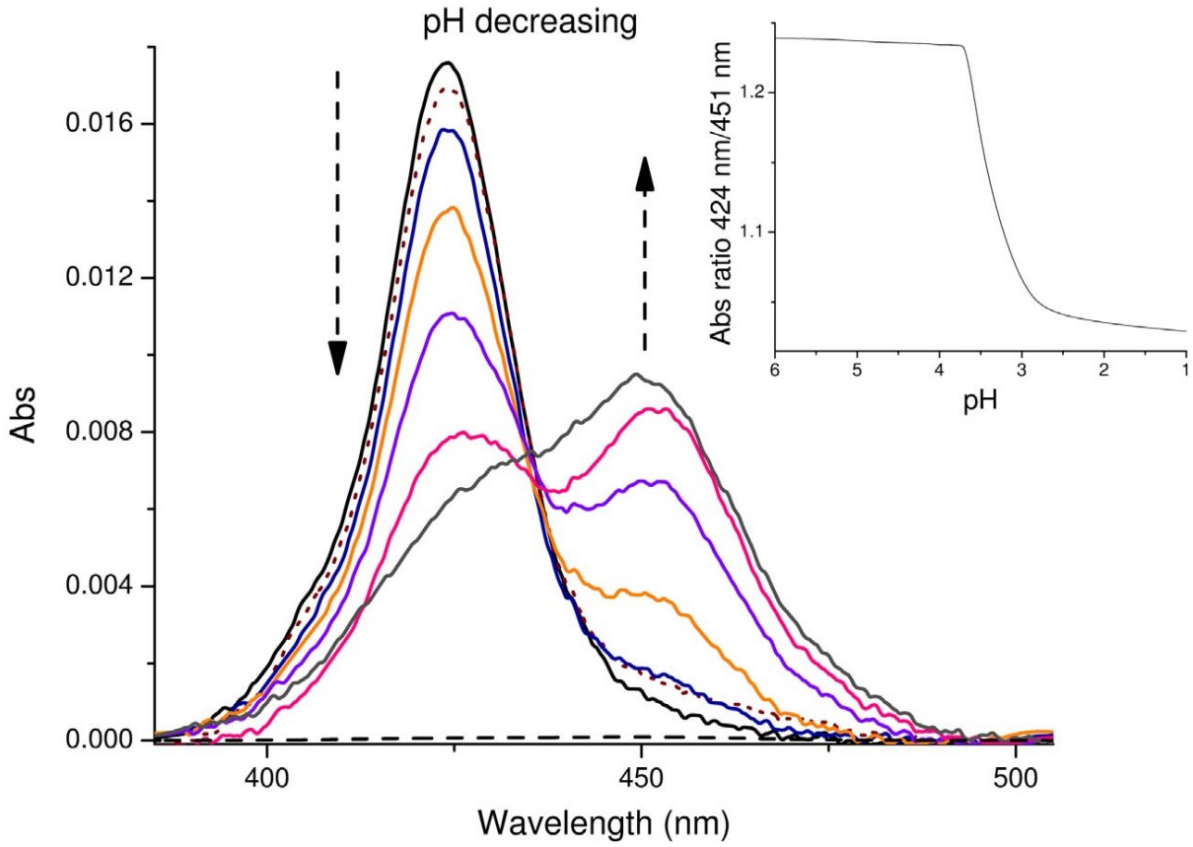

Figure 4.2.7: Uv–Vis spectra of the AuNPs@P(PEG750)$_3$ in aqueous solution at different pH values (pH range, from about 6 to 1). The dotted line refers to the spectrum of the solution of AuNPs@P(PEG750)$_3$ recovered by centrifugation and the following heating at 80 °C under nitrogen atmosphere. The dashed line refers to the spectrum of the solution after AuNPs@P(PEG750)$_3$ elimination by centrifugation at 5000 rpm for 10 min. In the inset, the 424/451 nm intensity ratios as a function of the pH are reported.

It is evident the progressive decrease of the Soret band at 424 nm, whereas a new band at 451 nm grows up. To overcome any problems due to the baseline correction, the Uv–Vis titration curve was obtained directly from the raw data on the basis of the intensity ratios between the bands at 424 nm (free base porphyrin) and 451 nm (protonated porphyrin). In the inset of ***Fig. 4.2.7***, the decrease of the absorbance intensity ratio in function of HCl concentration is evident. Remarkably, after centrifugation and drying at 80 °C (under a N_2 atmosphere), the residue recovered the porphyrin starting Soret intensity, after sonication in water (dotted line in ***Fig. 4.2.7***).

However, to improve the analytic performance of the AuNPs@P(PEG750)$_3$ nanoparticles, experiments monitoring the change of the fluorescence signal (λexc = 424 nm) were also performed.

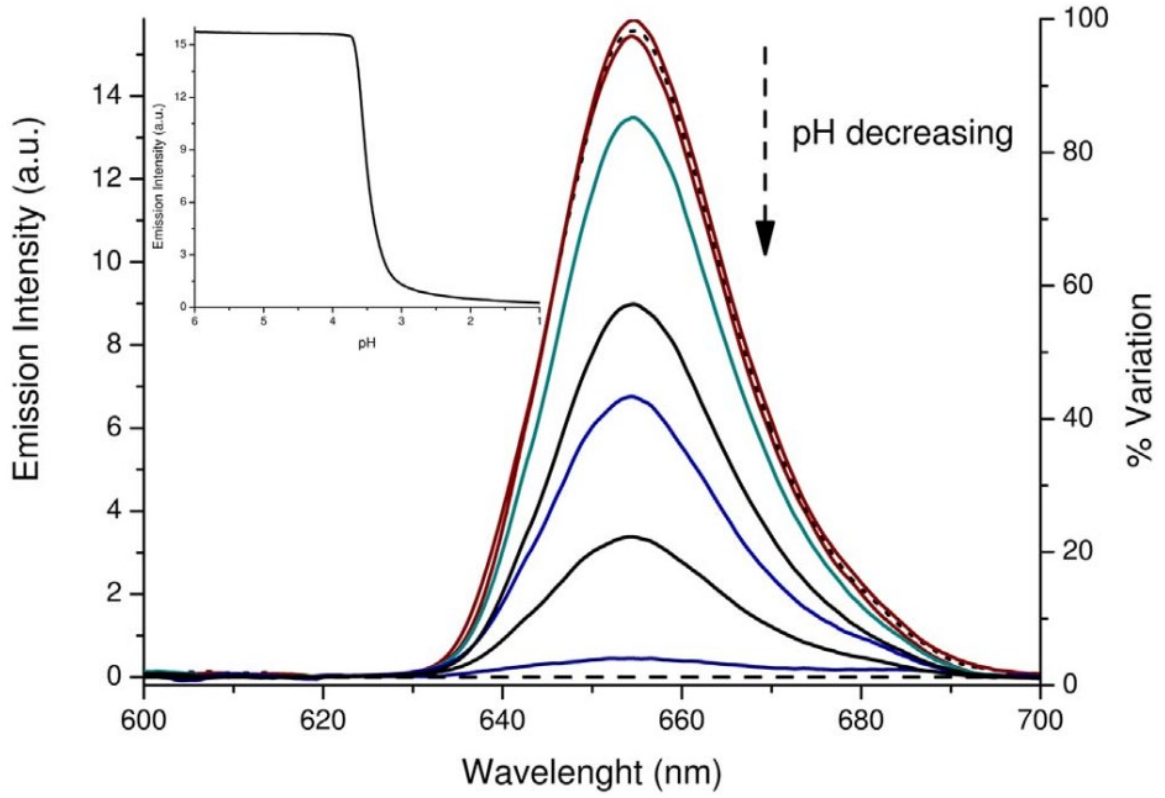

Figure 4.2.8: Fluorescence spectra of the aqueous solution of AuNPs@P(PEG750)$_3$ at pH values of 5.98, 3.93, 3.64, 3.53, 3.47, 3.31, 1.89, corresponding at % emission intensity variation of 100, 98.29, 85.15, 56.60, 42.70, 21.22 and 2.84, respectively. The dotted line refers to the spectrum of the solution of AuNPs@P(PEG750)$_3$ recovered by centrifugation and the following heating at 80 °C under nitrogen atmosphere. The dashed line refers to the spectrum of the solution after AuNPs@P(PEG750)$_3$ elimination by centrifugation at 5000 rpm for 10 min. In the inset, the fluorescence intensity variation as a function of the pH is reported.

Figure 4.2.8 shows the decrease of the fluorescence intensity in function of HCl concentration is evident, and an equivalence point at about pH 3.51 (***Fig. 4.2.8, inset***). These data indicate that the percentage of the residual fluorescence band intensity of the AuNPs@P(PEG750)$_3$ with respect to its initial value can be used to establish the pH value of a solution (***Fig. 4.2.8***).

As a confirmation, a similar behavior was obtained by performing a titration with HCl of a very dilute aqueous solution of P (4×10^{-8} M), a similar molecular system to POH, having four PEG branches with the same average polymerization degree (***Figs. 4.2.9 and 4.2.10***).

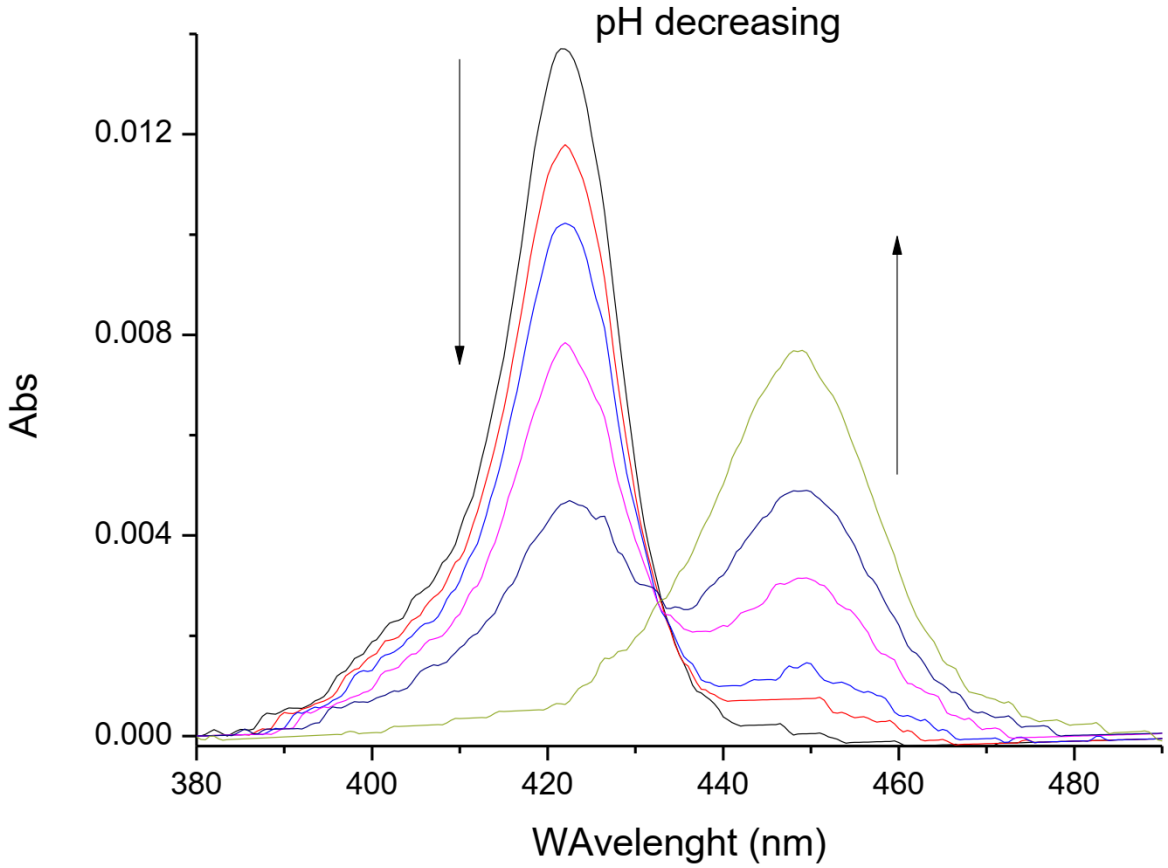

Figure 4.2.9: UV-vis titration with HCl of an aqueous solution (4×10^{-8} M) of 5,10,15,20-(p-[ω-methoxypoly(oxyethylene)]phenyl)porphyrin.

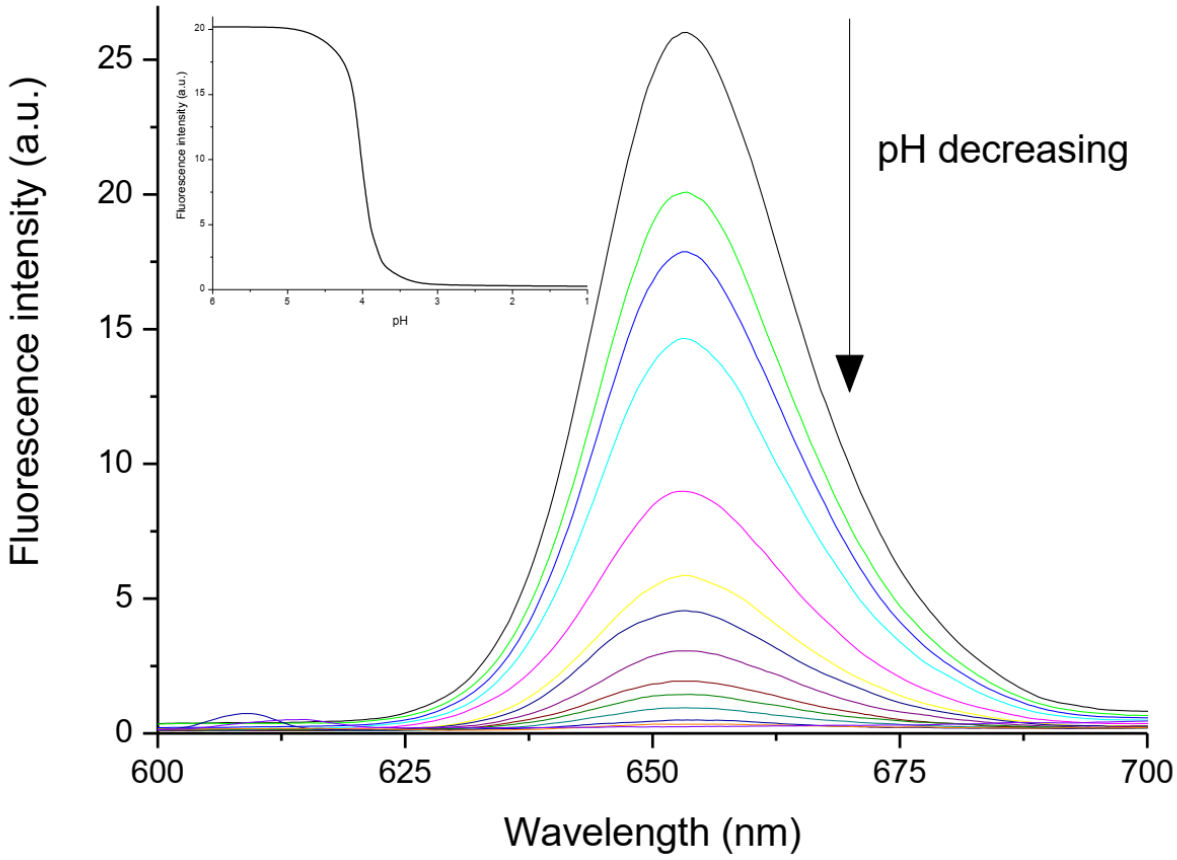

Figure 4.2.10: Spectrofluorometric titration with HCl of an aqueous solution (4×10^{-8} M) of 5,10,15,20-(*p*-[ω-methoxypoly(oxyethylene)]phenyl)porphyrin.

It is noticeable that in this last case the equivalence point resulted at about pH 4.05, then 0.5 pH unit upper to that of AuNPs@P(PEG750)$_3$ (pH 3.51). This difference is probably due to the contribute of gold nanoparticle on the pKb of its bounded porphyrin. The aqueous solution was then centrifuged at 5000 rpm for 10 min to remove the titrated nanoparticles from it; the supernatant, analyzed by Uv–Vis and fluorescence spectroscopies, did not show any appreciable signal due to a AuNPs@P(PEG750)$_3$ residue presence (dashed lines in ***Figs. 4.2.7 and 4.2.8***), whereas the collected residue dried at 80 °C under N_2 flow, used again, showed the recovering of its pH-sensing capability (dotted line in ***Figs. 4.2.7 and 4.2.8***).

Remarkably, several cycles, alternating acid treatments and drying at 80 °C under nitrogen atmosphere and solubilization by sonication, were performed with only slight variations of the performance so indicating the reversible protonation of the AuNPs@P(PEG750)$_3$ nanoparticles (***Fig. 4.2.11***).

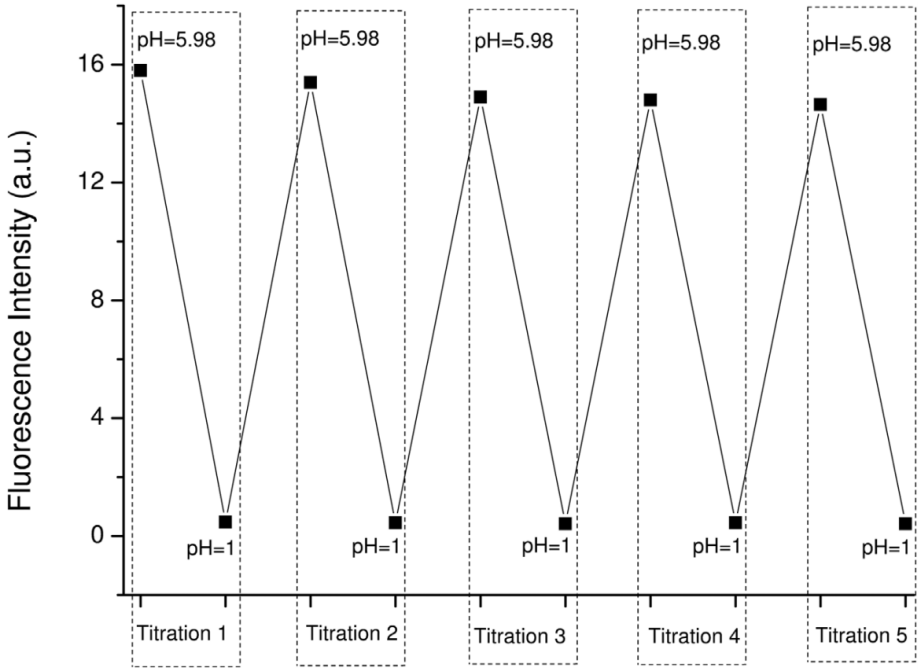

Figure 4.2.11: Representative fluorescence changes of AuNPs@P(PEG750)$_3$ aqueous solution as a result of acid titrations and successive centrifugation and thermal regeneration (80 °C, N_2).

To evaluate possible anion interferences, the nano-optical-pH sensor behavior of AuNPs@P(PEG750)$_3$ was further investigated considering other acids such as HNO_3 and CH_3COOH; however, also in these cases, the behavior was similar to the titration with HCl.

In short, it is possible to confirm that the two systems of gold nanoparticles, functionalized with two different types of PEGylate-derivatives of porphyrins, maintain the spectroscopic properties of the porphyrins.

These properties, coupled with those deriving from nanoparticles, have allowed to obtain a multifunctional system, with properties ranging from photosensitizing capacity to cell penetration to the pH sensor in unconventional environments, with the possibility of use this system again after simple treatments.

[1] Angelini, N.; Micali, N.; Villari, V.; Mineo, P.; Vitalini, D.; Scamporrino, E. Phys Rev E 2005, 71(2), 021915(7pp)
[2] Maiti, N. C.; Ravikanth, M.; Mazumdar, S.; Periasamy, N. J Phys Chem Us 1995, 99(47),17192-7
[3] Castriciano, M. A.; Romeo, A.; Villari, V.; Angelini, N.; Micali, N.; Scolaro, L. M. J Phys Chem B 2005, 109(24), 12086-92.
[4] Kotiaho, A.; Lahtinen, R.; Lehtivuori, H.; Tkachenko, N. V.; Lemmetyinen, H. J Phys Chem C 2008, 112(27), 10316-22.
[5] Mineo, P.; Faggio, C.; Micali, N.; Scamporrino, E.; Villari, V. Rsc Adv 2014, 4(37), 19389-95.
[6] Venediktov, E. A.; Tulikova, E. Y.; Maizlish, V. E. Russ J Gen Chemþ 2012, 82(6), 1145-52
[7] Kubat, P.; Lang, K.; Kral, V.; Anzenbacher. P. J Phys Chem B 2002, 106(26), 6784-92.

Conclusion

In conclusion, various synthetic methods have been developed and have allowed the surface functionalization of inorganic nanoparticles (gold, silver, magnetite@silica and magnemite@gold) using different types of linkers, such as 3-chloro-propanediol and/or Trichloro[4-(chloromethyl)phenyl]silane, which allowed the covalent bonding (by etherification raction) of PEGylate porphyrin groups to obtain the NP@Porf@PEG nanosystems.

The synthetic steps were monitored, from the point of view of optical and dimensional properties, by means of UV-vis, steady-state and time-resolved fluorescence, DLS, AFM and TEM/STEM measurements. The amount of organic layer bound to the NPs surfaces was determined by thermogravimetric or EDS analysis. STEM and XPS investigations allowed a straightforward chemical characterization of the engineered hybrid organic-inorganic structures.

Preliminary studies on the theranostic properties were carried out on two systems with a core@shell structure of gold nanoparticles. As we have seen in the first case, we studied the photosensitizing properties of the porphyrin through the RNO test, and we obtained excellent results. Secondly, the internalization and localization properties on neuroblastoma cell lines have been studied, obtaining excellent results in this case.

Finally, the second system has been studied as a pH sensor, with the objective of exploiting this property to use it in biological fluids, or better, on diseased tissues; this way, it is possible to monitor the birth and growth environment of a tumor.

The results obtained were excellent in this case too, also because the system can be reused several times through simple centrifuges and thermal regeneration at 80 ° C.

With regard to all the other synthesized nanoparticles systems, such as silver, magnetite, magnetite@silica and maghemite@gold, the covalent binding of porphyrins derivatives on the NPs surface has been demonstrated. The main objective of future studies is to evaluate their possible theranostic applications, first of all the antibacterial activity of silver nanoparticles derivatives.

In synthesis, upon validation of the functioning of the system, and therefore of the project itself, the synthesis strategy can be adapted to functionalize and/or co-functionalize the nanoparticles also with active targeting agents (folic acid, oligopeptides, biotine, etc.) to limit the accumulation exclusively in diseased tissues endowed with specific receptors, further implementing the targeting properties described above.

Therefore, the results obtained during my PhD research work, could be a fundamental starting point in order to developing systems for theranostic applications, exploiting both the nanoparticles and the porphyrin derivatives properties, thus to obtain multifunctional platforms for biomedical applications.

Appendix

Instrumentation

UV-Vis spectra were recorded at room temperature by a Shimadzu Model 1601 spectrophotometer, in quartz cells using acetone or water as a solvent.

Fluorescence spectra were recorded by a Jasco FP-8200 spectrofluorimeter, in quartz cells using acetone or water as a solvent at T = 25.0 ± 0.1 C. A long pass filter was placed along the emission path.

Thermogravimetric analysis (TGA) was performed from 50 to 800 °C temperature range, by means of Pyris TGA7 (Perkin-Elmer). The sample was placed in a platinum pan, kept at 30 C under a 60 mL/min air flow until balance stabilization and subsequently heated (scan rate of 10 C/min). A baseline, recorded with empty platinum pan (in the same measurement conditions), was subtracted from each thermogram before data analysis.

^{1}H-NMR spectra (acquired at 27 °C with a spin lock time of 0.5s) were obtained on a ^{UNITY}INOVA instrument (Varian) operating at 500 MHz and using VNMR for acquisition and spectra processing. Samples were dissolved in CD_2Cl_2 and the chemical shifts expressed in ppm by comparison with the CH_2Cl_2 residue signal.

MALDI-TOF mass spectra were acquired by a Voyager DE (PerSeptive Biosystem) using an acquisition protocol reported elsewhere.[1] [2] [3] The Trans-3-indoleacrylic acid (IAA) was used as MALDI matrix. Mass spectrometer calibration and average molecular mass determination were performed as reported in previous cases. [4]

X-ray photoelectron spectra (XPS) were measured on the as prepared sample at 45 take-off angles relative to the surface plane with a PHI 5000 Versa Probe II system (base pressure of the main chamber $1*10^{-8}$ Pa). Samples were excited with a monochromatized Al-Kα X-ray radiation using a pass energy of 5.85 eV. Spectra calibration was achieved by fixing the main C 1s peak at 285.0 eV. No relevant charging effects were observed. The XPS peak intensities were obtained after Shirley background removal. Atomic concentration analysis was performed by taking into account the relevant atomic sensitivity factors. The instrumental energy resolution was ≤0.3 eV. Deconvolution of the N 1s spectrum was carried out by fitting the spectral profile with two symmetrical Gaussian envelopes after subtraction of the background. This process involves data refinement, based on the method of the least squares fitting, carried out until there was the highest possible correlation between the experimental spectrum and the theoretical profile. The residual or agreement factor R defined by R=

$[\sum(F_{obs} - F_{calc})^2 / \sum(F_{obs})^2]^{1/2}$ after minimization of the function $\sum(F_{obs} - F_{calc})^2$ converged to values of 0.03.

Nanoparticles sizes were determined by means of a miniDAWN Treos (Wyatt Technology) multi-angle light scattering detector, equipped with a Wyatt QELS DLS Module. The measurements were performed at 25 C using solutions previously filtered with 0.2 mm filter. Size distributions were obtained by using the Wyatt software (ASTRA 6.0.1.10).

Fluorescence lifetime measurements were carried out by using a home-made apparatus based on time-correlated-single-photoncounting. A Ti:Sa laser (Spectra Physics MaiTai DeepSee) with duplication system (Radiantis Inspire Blue) is used as source and the detecting system is based on a monochromator (Oriel Cornerstone 1/8 m) and a microchannel-plate photomultiplier (Hamamatsu R1645U-01, 200 ps rising-time) operating in single-photon counting regime. Pre-amplification, constant fraction discrimination, synchronization of the laser pulse and acquisition of fluorescence decay curves are realized by means of EG&G electronic devices.[5] [6]Laser wavelength was set at 500 nm with power of about 300 mW and fluorescence decays were collected at 660 nm. The collected data were analyzed using the nonlinear least-squares iterative reconvolution procedures, obtaining an instrumental resolution of about few tens of picoseconds. Curve fitting was performed by using multiexponential decay law:

$$I(t) = I_0 \sum_i A_i \, exp^{(-t/\tau_i)}$$

where I is total fluorescence decay curve, I_0 is the intensity at time zero, and A_i and τ_i are, respectively, the relative amplitude and lifetime of the ith component, under the condition $\sum_i A_i = 1$.

The amount of $^1O_2$ produced by the nanosystem was determined by a standard method based on the bleaching reaction of pnitroso-N,N'dimethylaniline (RNO).[7] The sensitizer AuNP@Porf@PEG was dissolved, with imidazole (10 mM) and RNO (50 mM), in buffered solution (50 mM of PBS). Higher concentration of RNO than phosensitizer ensures that time dependence of absorbance at 440 nm is essentially due to photochemical reaction of RNO. The solution was irradiated by a green LED lamp (wavelength range 500-550 nm) with a power density of 3.3 mW/cm^2. In order to extract the quantum yield of $^1O_2$ formation, Φ, for AuNP@Porf@PEG, a solution of TPPS (5,10,15,20-tetrakis(4-sulfonatophenyl)porphyrin) was subjected to the same experimental conditions and used as standard reference (FTPPS = 0.62).[8] The following relation[8] is then used:

$$\phi = \phi_{TPPS} \frac{OD^{TPPS}}{OD^{AuNPs@Porf@PEG}} \frac{\Delta A}{\Delta A^{TPPS}}$$

where ΔA is the absorbance change at 440 nm and $OD^{AuNP@Porf@PEG}$ the optical density in the irradiation wavelength range for AuNP@Porf@PEG solution, ΔA^{TPPS} and OD^{TPPS} being the values measured for the standard reference in the same experimental conditions.

Human neuroblastoma SH-SY5Y cells were grown in DMEM-F12 (1:1) medium, supplemented with 10% foetal bovine serum (FBS), 1% penicillin/streptomycin, 2 mM L-glutamine and maintained in a humidified incubator at 37 C in 5% CO_2 atmosphere. At confluence, cells were split on glass bottom Petri dishes (WillCo Wells, glass diameter of 22 mm) and placed in the incubator. The day after cells were treated with bare and functionalized nanoparticles at a final concentration of AuNPs of $2*10^{-9}$ M, as determined by UV-Vis spectra. After 2 h of incubation time, cells were washed with phosphate buffer saline solution (10 mM PBS, 37 °C, pH = 7.4) and fixed. Confocal imaging was performed with an Olympus FV1000 confocal laser scanning microscope (LSM), equipped with diode UV (405 nm), multiline Argon (457 nm, 488 nm, 515 nm), green and red HeNe (543 nm, 633 nm) lasers. An oil immersion objective (60xOPLAPO) and spectral filtering system was used. The detector gain was fixed at a constant value and images were taken, in sequential mode, for all the samples, at random locations throughout the area of the well. For LSM-spectroscopy, the spectral filtering was set on beam split mode and sequences of xy-lambda scans were acquired at an interval each from the other of 5 nm. Emission spectra were reconstructed from selected regions of interest (ROIs) on the recorded images.

AuNPs@Porf@PEG and AgNP@Porf@PEG morphology were investigated at University of Exeter (UK) using a TEM, JEM2100 LaB6, operating at 200 Kv, and a digital Scanning transmission electron microscopy (STEM) equipped with BF & DF STEM Detectors plus SE/BSE detector. TEM and STEM samples were prepared by placing ten drops of the sample dispersed in H2O (~0.5 mg/mL) by sonication (10 min in an ultrasound bath) on 300 mesh holey-carbon coated copper grids.

Fe_2O_3@Au@P(PEG350)$_3$ morphology were investigated at CNR-IMM (CT) using a TEM, JEOL ARM200 F Cs-corrected, operated at 200 keV; the images were acquired both with a Jeol High Angle Annular Dark Field (HAADF) and a Gatan Annular Bright Field (ABF) detector.

[1] Montaudo, G.; Scamporrino, E.; Vitalini, D.; Mineo, P. Rapid Commun Mass Sp 1996, 10(12), 1551-9
[2] Vitalini, D.; Mineo, P.; Scamporrino, E. Macromolecules 1997, 30(18) ,5285-9.
[3] Scamporrino, E.; Maravigna, P.; Vitalini, D.; Mineo, P. Rapid Commun Mass Sp 1998,12(10), 646-50
[4] Mineo, P.; Vitalini, D.; Scamporrino, E.; Bazzano, S.; Alicata, R. Rapid Commun Mass Sp 2005, 19(19), 2773-9.
[5] Angelini, N.; Micali, N.; Villari, V.; Mineo, P.; Vitalini, D.; Scamporrino, E. Phys Rev E 2005, 71(2), 021915 (7pp)
[6] Mazzaglia, A.; Valerio, A.; Villari, V.; Rencurosi, A.; Lay, L.; Spadaro, S. et al. New J Chem 2006, 30(11), 1662-8
[7] Mosinger, J.; Micka, Z. J Photoch Photobio A 1997, 107(1-3), 77-82.
[8] Venkatesan, R.; Periasamy, N.; Srivastava, T. S. P Indian as Chem Sci 1992, 104(6), 713-22.